Anisotropic Work-Hardening and Strain Path Effects in an AlMn Alloy

Steven VAN BOXEL

Examencommissie:
Prof. dr. ir. Hugo Hens, voorzitter
Prof. dr. ir. Paul Van Houtte, promotor
Prof. dr. ir. Bert Verlinden, promotor
Prof. dr. ir. Bart Blanpain, assessor
Prof. dr. Marc Seefeldt, assessor
Prof. dr. ir. Jin Won (Maria) Seo, assessor
Dr. Wolfgang Pantleon
(Risø-DTU, Denemarken)
Dr. Edgar Rauch
(CNRS-Grenoble INP, Frankrijk)

Proefschrift voorgedragen
tot het behalen van de
graad van Doctor in de
Ingenieurswetenschappen

December 2010

Arenberg Doctoraatsschool, W. de Croylaan 6, 3001 Heverlee, België

ISBN 978-94-6018-284-6
D/2010/7515/123

Voorwoord

Het schrijven van een doctoraat is een buitengewoon lastige opdracht gebleken, waarbij de strijd tegen de om de hoek sluimerende wanhoop het moeilijkste aspect is geweest. Gelukkig stond ik er niet alleen voor en zijn er daarom velen die ik wil bedanken voor hun erg op prijs gestelde steun en zwaar op de proef gestelde geduld.

Mijn oprechte dank gaat eerst en vooral uit naar mijn promotoren, prof. Paul Van Houtte en prof. Bert Verlinden. Hun inzichten, kritische kijk en begeleiding hebben niet alleen de richting gewezen voor mijn doctoraatsproject, maar hebben ook hun stempel gedrukt op mijn persoonlijke ontwikkeling als onderzoeker en als mens. Ik had me geen betere promotoren kunnen dromen.

Een huizenhoog dankjewel ben ik verschuldigd aan prof. Marc Seefeldt, zonder wiens aanstekelijke enthousiasme, deskundige inbreng en blijvende steun dit doctoraat nooit eenzelfde mate van diepgang zou hebben gekregen. Zonder hem zou deze thesis er nooit zijn kunnen komen. Beste Marc, bedankt voor alles en dat is in dit geval onnoemelijk veel en nog veel meer.

I would also like to thank the other members of my jury, dr. Edgar Rauch, dr. Wolfgang Pantleon, prof. Maria Seo, prof. Bart Blanpain and prof. Hugo Hens for their valuable comments on the manuscript and the interesting discussions during the preliminary defense which have lead to numerous improvements to the text.

Jeg vil også gerne udtrykke min store taknemmelighed til Dorte Juul Jensen og Wolfgang Pantleon fra Risø-DTU. Jeres moralske opbakning har betydet meget for mig. Jeg var aldrig kommet i mål, uden vores ugentlige møder. Jeg står i evig gæld til jer.

Anand Krishna Kanjarla should definitely not be overlooked in this preface. It has been an extreme pleasure sharing an office with this gem of a person, being able to discuss anything, at any time. My insights in plasticity of metals have been largely extended due to our interactions. Anand, my dear friend, thank you so much.

Jozefien en Frederik, bureau- en lotgenoten, bedankt voor het delen van lief en leed, bedankt voor de steun op persoonlijk, technisch en praktisch vlak.

Many thanks need to be expressed as well to my other office mates (Enze, Liang, Sampath and Gijs), the remaining ASTROnauts (Bert, Shen, Artur, Xiahua, Steven, Philip, Stijn,...) and all the usual suspects of the alma lunches and other aspects of the MTM culture for creating such a nice work environment.

Mijn dank gaat verder uit naar het technisch personeel van MTM, in het bijzonder Jo Mariën en Louis Depré, dat betrokken is geweest bij de ontwikkeling van de afschuiftester. Mensen die het kunnen weten hebben dit toestel geroemd als “a fine piece of equipment”.

I would like to express my gratitude towards Bjørn Holmedal of NTNU in Trondheim, Norway. During my short visit, he managed to transfer a huge amount of knowledge on work-hardening in texture models to me. A special thanks remains to be given to prof. Monique Gaspérini and dr. Paolo Flores for explaining and demonstrating the shear tester devices in Paris and Liège respectively.

Bedankt aan al mijn vrienden, Michel, Annemie, Gert, Marijke, Jozefien, Jan, Frederik (ook voor de pasta), Veerle, Jeroen, Marieke, Tine, Karel, Sofie, An, Leen, Bert (zij het sporadisch, altijd een waar genoegen), voor hun steun, geloof en vertrouwen. Ook wil ik eenieder van CampusToneel, en in het bijzonder Jan en Chris, bedanken voor de geweldige repetities, voorstellingen, weekends en al het overige. Jullie slaagden er steeds in om even alle doctoraatsgerelateerde beslommeringen uit mijn hoofd te krijgen.

Gert, Marijke en Wouter, mijn huisgenoten, bedankt voor het creëren van een gezellige thuis na de uren.

Jeg vil gerne sige tak til alle fra AFM-M4D på Risø-DTU, især til mine kontorkammerater Jette og Jacob. Tak for at bevare troen på mig, når i spurgte om min ph.D.’s tilstand. Selvom svaret igen og igen var, at den ikke var helt færdig endnu. Tak for at spørge om det alligevel og for støtten til mig.

Mange tak til Claudia, Michael, Neil, Alison, Anna og alle andre på hold 399. Jeg har følt mig rigtig hjemme i det nye og uforståelige land, da jeg mødte jer. Det var en af de vigtigste grunde til, at jeg kunne gennemføre min ph.D. Tak til Lars for at undervise os i Dansk på en enestående måde.

Dank aan mijn familie, mijn lieve broer en zus, schoonbroer en schoonzus. Bedankt om er te zijn in de moeilijke momenten, deel nu zeker mee in de vreugde! Dit jaar eindelijk een Kerstfeest zonder doctoraatsbekommernissen en laten we dat zo houden tot misschien ooit Elise of Thomas dezelfde weg op zouden gaan.

Tot slot wil ik mijn ouders uitdrukkelijk bedanken voor hun onvoorwaardelijke en onuitputtelijke steun. In cruciale tijden zijn jullie het geweest die mij weer op weg hebben geholpen. Mama en papa, bedankt voor alles!

Steven

December 2010

Abstract

The anisotropy of the flow stress is an important material property which strongly influences the strength and forming limits of a workpiece in various industrial forming processes. It has been demonstrated in the literature that the intragranular substructure contributes considerably to this anisotropy. Mechanical tests that realise an abrupt change of the strain path after a certain amount of prestraining provide a direct way to assess the evolution of the anisotropy with strain. The mechanical response that follows after such a strain path change (SPC) is moreover very informative about the substructure, since the observed transient hardening behaviour is thought to be determined by the same micro scale mechanisms that lead to the formation of the substructure. A clear understanding of the involved microstructural mechanisms is however still missing. Furthermore, changes of the strain path often occur in modern forming processes.

The mechanical behaviour of an aluminium-manganese alloy during strain path changes is first characterised in an experimental study. In order to obtain a comprehensive data set of different types of SPC tests at different amounts of prestrain, a device to perform tests in simple shear has been developed. Various SPC tests are realised by combining deformations to different levels of prestrain through cold rolling or simple shear and subsequent straining in simple shear. The contributions to the anisotropy of the substructure and of the texture are separated through a multilevel approach which takes the measured evolution of the texture into account. Observed trends for the different SPC are discussed in the light of the possible microstructural mechanisms that are generally considered to determine work hardening and the formation of the substructure.

A new multiscale model is developed which accounts for the different contributions to work hardening and anisotropy on their most appropriate length scales. The contributions to the anisotropy stemming from the substructure are modelled at the meso scale through the values of the critical resolves shear stresses of the different slip systems of the individual grain orientations. The transient work hardening effects after strain path changes are modelled by the gradual softening of slip systems that become less active after an SPC and a two stage hardening regime for active slip systems that were active in the opposite slip direction prior to the SPC. The capabilities of the model and the influence of the model parameters are discussed by examples of an individual orientation subjected to specific deformation modes.

The mechanical behaviour for different strain path changes as predicted by the model is compared to experimental results. Since the used texture model does not capture the texture evolution of the alloy reasonably accurate, the comparison between model and experiments is based on properties that characterise the influence of the substructure. For the extreme cases of strain path changes the model results correspond very well to the experimental results. For intermediate strain path changes, such a correspondence is however not always observed. The evolution with prestrain can only be captured within a limited strain interval, indicating that the evolution equation within the model for the substructural anisotropy during monotonic straining is not yet advanced enough to capture the true behaviour. The capabilities of the model are summarised and compared to those of earlier models aimed at predicting the hardening behaviour after strain path changes.

Samenvatting

De anisotropie van de vloeispanning is een belangrijke materiaaleigenschap die de sterkte en de vervormingslimieten van een werkstuk tijdens verscheidene industriële vormgevings processen sterk beïnvloedt. In de literatuur is aangetoond dat de intragranulaire substructuur aanzienlijk bijdraagt tot deze anisotropie. Mechanische testen die een abrupte verandering van het vervormingspad na een zekere mate van voorvervorming bewerkstelligen, maken het mogelijk om de evolutie van de anisotropie op een directe manier te analyseren. De mechanische respons die volgt na zo een verandering van het vervormingspad geeft bovendien ook informatie over de substructuur, omdat aangenomen wordt dat het vastgestelde overgangsgedrag in de vervormingsversteviging bepaald wordt door dezelfde mechanismen op de microschaal die ook leiden tot de vorming van de substructuur. Deze microstructurele mechanismen worden momenteel nog niet duidelijk begrepen. Bovendien komen veranderingen in het vervormingspad ook vaak voor tijdens moderne vormgevingsprocesses.

In een experimentele studie wordt het mechanisch gedrag van een aluminium-mangaan legering tijdens veranderingen van vervormingspad gekarakteriseerd. Om een volledige dataset met verschillende types van vervormingspadverandering bij verschillende voorvervormingen te bekomen, is een apparaat ontwikkeld dat monsters in eenvoudige afschuiving kan vervormen. Verschillende veranderingen van vervormingspad worden gerealiseerd door voorvervormingen door koudwalsen en eenvoudige afschuiving te combineren met een verdere vervorming door eenvoudige afschuiving. De bijdragen tot de anisotropie van enerzijds de substructuur en anderzijds de textuur worden van elkaar gescheiden door de experimenteel opgemeten evolutie van de textuur in rekening te brengen. De vastgestelde tendenzen voor de verschillende veranderingen van vervormingspad worden besproken in het licht van de mogelijke microstructurele mechanismen die algemeen beschouwd worden de vervormingsversteviging en de vorming van de substructuur te bepalen.

Een nieuw meerschalenmodel wordt vervolgens ontwikkeld dat de verschillende bijdragen tot de vervormingsversteviging en de anisotropie in rekening brengt op de voor hen meest aangewezen lengteschaal. De bijdragen tot de anisotropie gerelateerd aan de substructuur worden gemodelleerd op de mesoschaal aan de hand van de waarden van de kritisch geresolveerde schuifspanningen voor de verschillende glijsystemen van individuele korrelorientaties. Het overgangs-

gedrag in de vervormingsversteviging na veranderingen van het vervormingspad wordt gemodelleerd door enerzijds een geleidelijke verzachting van de glijsystemen die minder actief zijn na de verandering van het vervormingspad en anderzijds een versteviging in twee stappen van actieve glijsystemen die actief waren in de tegenovergestelde richting voor de verandering van het vervormingspad. De capaciteiten van het model en de invloed van de modelparameters worden besproken aan de hand van voorbeelden van een individuele korrelorientatie die onderworpen wordt aan specifiek gekozen vervormingsmodes.

Het mechanisch gedrag voor verschillende veranderingen van vervormingspad zoals voorspeld door het model wordt vergeleken met de overeenkomstige experimentele resultaten. Omdat het gebruikte textuurmodel de evolutie van de textuur voor de gebruikte legering niet accuraat genoeg benadert, wordt de vergelijking tussen model en experimenten gedaan aan de hand van grootheden die enkel de invloed van de substructuur beschrijven. Voor de meest uitgesproken veranderingen van vervormingspad wordt een zeer goede overeenkomst tussen model en experimentele resultaten bekomen. Voor tussenliggende veranderingen van vervormingspad is dit echter niet altijd het geval. De evolutie met de mate van voorvervorming kan alleen maar voorspeld worden in een beperkt vervormingsinterval. Dit wijst erop dat de modelvergelijking die de substructurele anisotropie tijdens een monotone vervorming beschrijft niet geavanceerd genoeg is om het werkelijke gedrag te simuleren. De capaciteiten van het model worden samengevat en vergeleken met die van eerdere modellen die eveneens het verstevigingsgedrag na veranderingen van vervormingspad beschrijven.

List of symbols

x	scalar value
$\dot{x}$	time derivative/rate of x
$\overline{x}$	average value of x
$\mathbf{x}$	vector/tensor
$\hat{\mathbf{x}}$	vector with unit length
x_{ij}	component of tensor
i, j	indices of vector, matrix or tensor with dimension 3
p, q	indices of vector, matrix or tensor with dimension 5
α, β	as subscript : indices of vector, matrix or tensor with dimension 12 or 24
	as superscript : indicating a certain slip system
P	as superscript : indicating a certain slip plane
r	as superscript : indicating a certain relaxation, can be either 1 or 2
$\mathbf{x} \cdot \mathbf{y}$	single-contracted (dot) product between $\mathbf{x}$ and $\mathbf{y}$
$\mathbf{x} : \mathbf{y}$	double-contracted (double dot) product between $\mathbf{x}$ and $\mathbf{y}$
$\lVert \mathbf{x} \rVert$	norm of the vector or tensor $\mathbf{x}$

The Einstein summation convention is used throughout the thesis text e.g., it however only applies on indices (subscripts) and not on specific slip systems or slip planes (superscripts)

$\mathbf{a}$	dislocation interaction matrix
$\hat{\mathbf{b}}^{\alpha}$	vector of unit length parallel to the Burgers vector of slip system α

b	length of the Burgers vector
b_1	modelling constant controlling the evolution zith strain of the λ^{α}
b_2	modelling constant controlling the initial softening rate after a cross type strain path change
c_1	modelling constant controlling the evolution with strain of the π^{α}
c_2	modelling constant controlling the evolution with strain of the back stress after a slip system reversal
$\cos\theta$	Parameter of Schmitt to quantify the abruptness of a strain path change
$\mathbf{E}$	straining mode $\mathbf{E} = \dot{\boldsymbol{\varepsilon}} / \lVert\dot{\boldsymbol{\varepsilon}}\rVert$
$\mathbf{F}$	deformation gradient tensor
f	volume fraction of dislocation walls
$\mathrm{f}(g)$	orientation distribution function
G	shear modulus
$\mathbf{H}$	latent hardening matrix in latent hardening model of Kocks
$\mathbf{h}$	hardening matrix describing latent hardening
H	hardening matrix of substructural anisotropy model
$H^{\alpha\beta}$	component of hardening matrix H, describing the contribution of a slip system β to the hardening of a slip system α
$H_{//}$	component of H for self an coplanar hardening
H_X	component of H for hardening of intersecting slip systems
$H_{\leftrightarrow}$	component of H for hardening of slip systems with the opposite slip direction

h^{α}	hardening anisotropy factor for a slip system α
h_{ref}	weighted average of the hardening anisotropy factors of all slip systems, with the slip rates as the weighting factors
j	dislocation flux
$\mathbf{K}^{r}$	velocity gradient of a simple shear relaxation
K	proportionality constant of the Kocks work hardening model
$\mathbf{L}$	macroscopic velocity gradient tensor
$\mathbf{l}$	local velocity gradient of a single grain
$\mathbf{l}^{\alpha}$	velocity gradient tensor of slip system α
$\mathbf{l}_{k}$	overall velocity gradient of a boundary segment
L_{R}	annihilation length of the Kocks work hardening model
l^{α}	hardening anisotropy factor of the straining mode before a strain path change for a slip system α
$\mathbf{M}$	anisotropy tensor due to texture in Teodosiu-Hu model
$\mathbf{M}^{\alpha}$	Schmid-matrix of a slip system α
M	Taylor factor
$\hat{\mathbf{n}}^{\alpha}$	normal vector of unit length to the slip plane of slip system α
n	modelling parameter influencing the relative importance of highly active slip systems in contributing to the hardening of other slip systems
n	total number of discrete orientations taken into account in the macro scale model
$\hat{n}_{k}$	normal to grain boundary segement plane
$\mathbf{P}$	polarity tensor in Teodosiu-Hu model
R	isotropic hardening contribution in Teodosiu-Hu model

$\mathbf{S}$	anisotropy tensor due to substructure in Teodosiu-Hu model
$\mathbf{S}_L$	part of $\mathbf{S}$ representing the hardening contributions of slip systems that has become latent
S	total number of (decoupled) slip systems per orientation taken into account in the meso scale model
S_D	scalar part of $\mathbf{S}$, representing the hardening contributions of slip systems that are active
T	temperature
$\dot{W}$	rate of plastic work dissipation
$\mathbf{X}$	back stress tensor in Teodosiu-Hu model
α	proportionality constant in Taylor equation for the flow stress
β-fibre	group of crystallographic orientations which are interconnected in orientation space, starting from the copper orientation over the S orientation to the brass orientation. These orientations are typically the dominant orientations in a cold rolled face centred cubic single phase material
Γ	overall amount of dislocation slip
$\dot{\Gamma}$	sum of slip rates
$\dot{\Gamma}^P$	sum of slip rates of the slip systems coplanar to a slip plane P
Γ_{pre}	microscopic prestrain
γ	macroscopic shear strain
γ_0	strain shift necessary to make the stress-strain curve after transient hardening behaviour coincident with the monotonic one

γ_1	amount of strain between a strain path change and the first inflexion point of the transient hardening behaviour
γ_2	amount of strain between a strain path change and the second inflexion point of the transient hardening behaviour
γ_3	amount of strain between a strain path change and the end of the transient hardening regime
$\dot{\gamma}^{\alpha}$	shear strain rate/slip rate of slip system α
$\dot{\gamma}^{r}$	shear strain rate/slip rate of a relaxation
$\boldsymbol{\varepsilon}$	true strain
$\dot{\boldsymbol{\varepsilon}}$	true strain rate
$\dot{\boldsymbol{\varepsilon}}/\lVert\dot{\boldsymbol{\varepsilon}}\rVert$	straining mode
ε_{vm}	von Mises equivalent strain, $\varepsilon_{vm} = \sqrt{2/3\,\varepsilon_{ij}\varepsilon_{ij}}$
$\dot{\varepsilon}_{vm}$	von Mises equivalent strain rate, $\dot{\varepsilon}_{vm} = \sqrt{2/3\,\dot{\varepsilon}_{ij}\dot{\varepsilon}_{ij}}$
θ	microscopic hardening rate
	disorientation angle
	angular difference between straining modes
θ_0	microscopic hardening rate at zero stress
	hardening rate at end of prestraining
θ_1	hardening rate at the first inflexion point of the transient hardening regime
θ_2	hardening rate at the second inflexion point of the transient hardening regime
θ_3	hardening rate at the end of the transient hardening regime
θ_A	parameter of phenomenological micro scale model with the dimension of a hardening rate

θ_B	parameter of phenomenological micro scale model with the dimension of a hardening rate
$\tilde{\theta}_{ms}$	averaged microscopic hardening rate during monotonic straining, derivative of $\tilde{\tau}_{ref}$ with $\overline{\Gamma}$
θ_{ref}	derivative of τ_{ref} with Γ as described by the micro scale hardening model for monotonic strain paths
θ_{sub}	true derivative of τ_{ref} with Γ which can become different from θ_{ref} after strain path changes
κ	parameter in the model of Estrin and Mecking describing the relative importance of particle hardening compared to forest hardening
λ^{α}	necessary slip rate of a slip system α to maintain its previous anisotropy contribution during further deformation
π^{α}	current polarity variable of slip system α
ρ	dislocation density
ρ_f	dislocation density associated with forward straining in the model of Rauch
$\rho_{f,0}$	initial value of ρ_f just after a strain path reversal
ρ_r	dislocation density associated with part of the substructure that dissolves after a strain path reversal in the model of Rauch
$\boldsymbol{\sigma}'$	deviatoric stress tensor
σ_0	macroscopic scalar value of the yield stress
σ_{eq}	flow stress corresponding to a certain equivalent strain rate, conserving the rate of energy dissipation
τ	critical resolved shear stress
τ^{α}	critical resolved shear stress of a slip system α

τ_0	initial microscopic slip resistance
τ_1	stress at the first inflexion point of the transient hardening regime
τ_2	stress at the second inflexion point of the transient hardening regime
τ_3	stress at the end of the transient hardening regime
τ_{III}	stage III, saturation stress
τ_A	parameter of phenomenological micro scale model with the dimension of stress
τ_B	microscopic saturation stress in phenomenological micro scale model
τ_I	isotropic contribution to the critical resolved shear stress in the models of Peeters and Holmedal
τ_L^α	latent hardening contribution to the critical resolved shear stress of a slip system α in the model of Holmedal
τ_P^α	contribution to the critical resolved shear stress of a slip system α due to the polarity of the substructure in the model of Holmedal
τ_R^α	softening contribution to the critical resolved shear stress of a slip system α due to previous slip activity in the reverse direction in the model of Holmedal
τ_n	normalisation factor for the back stress
τ_{ref}	weighted average of critical resolved shear stresses of all slip systems, with the slip rates as the weighting factors
$\tilde{\tau}_{ref}$	weighted average of τ_{ref} of the individual grains with the M -factors of the grains as weighting factors
τ_{sat}	microscopic saturation stress

$\tau_{wd}^{P,\alpha}$	contribution to the critical resolved shear stress of a slip system α by the immobilised dislocations in a dense dislocation wall on a slip plane P in the model of Peeters
$\tau_{wp}^{P,\alpha}$	contribution to the critical resolved shear stress of a slip system α by the polarised dislocations at a dense dislocation wall on a slip plane P in the model of Peeters
$\Delta\tau$	permanent hardening/softening at the end of the transient hardening regime
φ_1	first Euler angle according to the Bunge convention
Φ	second Euler angle according to the Bunge convention
φ_2	third Euler angle according to the Bunge convention
Φ_{wp}^{P}	dislocation flux through the family of dense dislocation walls on a slip plane P in the model of Peeters
$\dot{\mathbf{\Omega}}$	macroscopic rate of rigid body rotation
$\dot{\boldsymbol{\omega}}_l$	local lattice spin of a single grain

List of abbreviations

A-Lamel	advanced Lamel model
bcc	body-centred cubic
CP	commercially pure
CPFEM	crystal plasticity finite element method
DDW	dense dislocation wall
EBSD	electron backscattered diffraction
FC	full constraints
fcc	face-centred cubic
FEM	finite element model/method
GBSODF	grain boundary segment orientation distribution function
GNB	geometrically necessary boundary
IDB	incidental dislocation boundary
IF	interstitial free
LEDS	low energy dislocation structures
LHR	latent hardening ratio
MB	microband
MODF	misorientation distribution function
ND	normal direction
ODF	orientation distribution function
PSN	particle stimulated nucleation
RD	rolling direction
RVE	representative volume element
SD	shear direction
SEM	scanning electron microscope
SFE	stacking fault energy

SPC	strain path change
SPN	shear plane normal
SPIF	single point incremental forming
TD	transverse direction
TEM	transmission electron microscope
ULg	Université de Liège
XRD	X-ray diffraction

Table of contents

1

General introduction

Deep drawing of sheet metals has many industrial applications for both conventional steels and non-ferrous metals used as structural components. Varying examples for this can be named like e.g. deep drawn car body parts, stringers for aircraft fuselages, parts of ship hulls, drinking cans, train components, etc. For many of these applications a main design aim is to combine a high strength with a low weight of the component. Due to the high ductility of most metals one way of obtaining this is by strengthening the material through deformation imposed by various forming processes, which includes the final shaping process as well. An important aspect of ductile deformation is that the strength becomes anisotropic, meaning directionally dependent. This can be both an advantage and a disadvantage. The anisotropy depends on the material, its thermomechanical history, the deformation process and the strain path which is imposed. With further improvements of the current designs it will become more and more important to take the material anisotropy and its evolution during shaping into account in order to get the best performance from the used material.

At present the anisotropic response of the material during complex shaping processes cannot be accurately predicted yet, not even for single phase metallic materials for which the strengthening mechanisms are best understood. If such accurate predictions would become feasible, they would enable to exploit the anisotropic behaviour to a much larger extent in order to improve the performance of the material within its application. This work would like to contribute to achieving the long term goal of accurate predictions for complex shaping processes by exploring the material behaviour of planar samples subjected to abrupt changes in the directionality of the deformation process (strain path changes), by efforts in both experimental characterisation and deformation modelling.

The behaviour of metallic materials during deformation processes is determined by many different parameters working on different length scales. Of course, the imposed shape change and the loading configuration of the work piece (application scale) are of chief importance, but the material response – which depends on a complicated interplay of its various constituents on different length scales – also influences the resulting shape (e.g. elastic spring back causing deviations from the required shape) and strength of the work piece.

Materials science endeavours to understand the relationships between the characteristic material features on the different length scales and the observed material response. The comprehension of particular aspects can be utilised to predict how a material will behave if it is subjected to certain conditions. If this can be done with a sufficient accuracy, the tools developed to predict the material behaviour can be applied to optimise the material specifications needed to advance the performance of the material, e.g. to make it stronger in the directions that are expected to take the highest loads. Materials science attempts to improve the way materials are utilised by exploiting the internal material characteristics.

Due to the complex nature of material behaviour, the most widely used approach to improve materials is that of trial and error[1]. Sufficient experimental evidence can often lead to the formulation of a mathematical model, describing the influence of a few parameters on a material property. If the parameters of the model do not have a physically understood nature, the model is called *phenomenological*, if the parameters can be derived from physical characteristics of the material, it is called a *physically based* model. In general the physically based models have a wider applicability and result in more insight in the material processes they describe. They are, however, much more difficult to formulate. Almost all material models are partially phenomenological.

Nowadays, most models are implemented in computer programs. This enables to combine different models and to extend the number of parameters and the number of properties which can be predicted. The applicability of such computer programs is quite naturally restricted by the amount of sophistication which is built into them.

If different submodels working on different length scales are combined into one computer code, the resulting model is called a *multiscale model*. The different length scales are connected by the fact that some parameters (input) of the submodels are derived from the predicted properties (output) of other submodels.

---

[1] Of course, trial should not be perceived here as a random guess, but as a motivated search towards the optimal solution.

In case that a certain submodel 'A' has a field variable 'α' as its output, there are two ways of coupling this output to other length scales. In a *hierarchical* scale transition, the integrated average of α over the field, as obtained by submodel A is passed on to the connected submodels. The averaging over the field is called a homogenisation step. Alternatively in an *embedded* scale transition, the submodels which depend on the field variable α will call submodel A for each integration point, providing A with specific input in order to obtain a local value of α, which the submodels then use to calculate the fields of other properties. In both cases, the equilibrium condition between input and output can be pursued by iteratively converging towards the imposed conditions.

At the cost of highly increased complexity and number of needed computing operations, multiscale modelling offers a whole set of consistent results on all involved length scales, as well as an interesting framework to study interdependences of various material characteristics on different length scales. Because of this second feature, it is possible to separate different influences on a single variable, which can be hard or even impossible to achieve by experimental validation.

The aim of this thesis is to gain insight in the development of anisotropy and the effects of abrupt changes of the strain path during cold deformation of an aluminium-manganese alloy. The chosen material will be characterised during experimental tests achieving different types of strain path changes at different amounts of deformation. Based on the gained insights of the experimental work a multiscale model with the focus on the work hardening effects during strain path changes will be developed.

1.1 Length scales in plastic deformation

For the plastic deformation of metallic materials, six different length scales are particularly relevant.

The smallest length scale which has a resolvable influence on the material response is the length scale of the crystal lattice structure or *atomistic scale* (1-10 Å). The arrangements of atoms in a specific lattice structure as well as the presence of interstitial and/or substitutional atoms as well as vacancies in that lattice structure determine how elementary deformation processes can occur in the material. Stacking fault energy (SFE) and lattice friction are important parameters for dislocation dynamics which can be changed by altering the lattice arrangement.

At the second length scale, the *nano scale* (1-10 nm), the creation, interaction and storage of individual lattice defects (e.g. dislocations, solute concentrations,...) should be considered. These lattice defects are very important for plastic deformation since they mediate the deformation. The interaction of these defects determines the strengthening of metals.

The third length scale (*micro scale*) deals with the spatial distributions of the lattice defects (e.g. cell boundaries, dense dislocation walls and twin boundaries which are all built up out of a large number of (partial) dislocations) and how they evolve with further deformation. The physical dimension of this length scale typically ranges from 10 nm to 100 nm.

The next hierarchical level is the *meso scale* (1-100 µm). This is the typical scale of individual grains. The effects of the interactions between grains and of the dislocation substructure on the stress vs. strain relation are of main importance here. Also the effects due to the presence of precipitates and different phases, are situated at this length scale. This level will be the focus of the present work.

The *macro scale* (typically 1-10 mm) includes the effects of distributions of individual quantities of the meso scale, like crystallographic and morphological texture, phase distribution, grain size distribution, grain boundary misorientation distribution, ... The considered material volume at this length scale should represent all intrinsic material characteristics, it is therefore often called a representative volume element (RVE).

The *application scale* is the scale of the actual work piece (1 cm-100 m). Here the influences of the shape of the work piece and the loading configuration as well as their evolutions during the forming process are considered.

It is worth noting that the above mentioned division in different length scales is somewhat arbitrary and is not clearly reflected in all possible materials. It should be regarded as an exercise to set the ground for the modelling methodology.

1.2 Concepts in plasticity

The principle aim in deformation modelling is to find correspondence between the displacement field and the stress field resulting from certain boundary conditions through the constitutive behaviour of the material. The boundary conditions can be both applied loads and/or imposed displacements. A displacement field generally consists of two parts, the translation of the rigid body and the deformation[2]. Only the deformation part is relevant in relation to the material behaviour. The material model should therefore define a constitutive relation between stress and strain, which is the symmetric measure of deformation. The asymmetric part of the deformation, the rigid body rotation, is unrelated to the stress and follows from the imposed boundary conditions.

Stress and strain are both symmetric tensorial quantities of rank 2 which need 6 independent values to generally describe a certain state. Since elastic deformations are small and do not have a permanent character, they are often neglected in plastic deformation modelling. It is also often assumed that plastic deformation of metals cannot result in volume changes, since most micromechanical processes that accommodate the plastic deformation do not change the interatomic distances. The trace of the plastic strain tensor therefore sums up to zero, reducing the number of independent values of the strain tensor to 5. For the stress tensor only the deviatoric part, of which the sum of its diagonal terms is also zero, is of importance for plasticity. The constitutive behaviour of metals is therefore a 5 dimensional problem. Also in this work the elastic deformation will be neglected. Unless explicity mentioned, deformation and strain will from here on be referring to plastic deformation and plastic strain.

A very important characteristic of a material for the modelling of deformation processes is the *flow stress*. This is the stress level that needs to be imposed by the loading device in order to have the deformation going on. A crucial feature for metallic materials is that this flow stress increases with increasing strain, which is called *work hardening*. This effect prevents that local flaws would lead to localisation of the deformation.

On the microstructural level plastic deformation and work hardening can be understood as a consequence of the combination of glide, multiplication and storage of linear lattice defects, called dislocations, which is the most widely observed microstructural mechanism for plastic deformation in metals. Whenever the stress during elastic deformation reaches a critical level, called the *yield stress*, plastic deformation becomes possible by glide and multiplication of dislocations. For dislocations to be moved on their slip plane a critical value of the resolved shear stress τ_{crss} (3) has to be reached. The resolved shear stress on a slip plane can

---

[2] Within this work ‘deformation’ is considered as the combination of shape change (straining) and rigid body rotation and it is fully characterised by the deformation gradient tensor $\mathbf{F}$.

[3] The subscript ‘crss’ will be omitted in the rest of the text. τ will always be refering to the critical value of the resolved shear stress, unless explicitely stated otherwise.

be calculated by describing the stress tensor in the reference system of the slip system. This procedure is the basis of the generalised Schmid law that calculates which slip systems will be active under a given stress state. The movement of dislocations through the crystal lattice facilitates the permanent displacement of atoms to equilibrium positions other than their initial positions and therefore allows a permanent change of the shape of the work piece. After some travel length the dislocations will get stored due to interaction with local obstacles. The flow stress to keep the deformation going on will increase with further straining since the stored dislocations act as obstacles for the subsequent mobile dislocations.

The slip of dislocations is bound to the lattice structure. Dislocations glide on specific crystallographic planes in specific crystallographic directions. For the face-centred cubic (fcc) lattice structure the slip planes and directions are the $\{111\}$ and $\langle 110 \rangle$ respectively, resulting in 12 possible *slip systems*. For the body-centred cubic (bcc) lattice structure the slip planes can be, depending on the material, either $\{110\}$, $\{112\}$ or $\{123\}$ planes and the slip directions are $\langle 111 \rangle$, resulting in 48 possible slip systems. Due to the geometrical nature of these slip systems, whether a grain can or cannot deform under a given stress state largely depends on the crystallographic orientation of the grain. The yield stress and also the flow stress for single crystals are therefore anisotropic. Also in polycrystals the orientation and spatial distributions of available slip systems can cause a certain degree of anisotropy. The preferential occurrence of orientations is reflected in the *crystallographic texture*. The texture of a material is consequently an important characteristic to evaluate the anisotropy of the yield stress.

Not only does the crystallographic orientation distribution have an effect on the anisotropy. Another important cause of anisotropy stems from the intragranular *substructure* built up by the dislocations stored during deformation. For reasons not yet well understood dislocations group themselves in distinct configurations which, due to their morphology and their influence on the local stress field, also cause anisotropy. This contribution to the overall anisotropy generally increases with increasing strain. The effects of this intragranular anisotropy are most obvious if a sudden change in strain path occurs. At a sudden change of strain path other slip systems need to be activated to accommodate the deformation. The newly activated dislocations have to interact with the existing substructure formed during prestraining.

1.3 Strain path changes

The strain path of a deformation process can be represented by the evolution of the incremental strain $d\boldsymbol{\varepsilon}$ during the deformation. The true strain $\boldsymbol{\varepsilon}$ is the integral of this incremental strain over the strain path which is equal to the integral of the strain rate $\dot{\boldsymbol{\varepsilon}}$ over the time interval:

$$\boldsymbol{\varepsilon} = \int d\boldsymbol{\varepsilon} = \int \dot{\boldsymbol{\varepsilon}} dt \,. \tag{1.1}$$

A strain path is constant over a time interval if the direction of the strain rate, also called the *straining mode,* $\dot{\boldsymbol{\varepsilon}} / \|\dot{\boldsymbol{\varepsilon}}\|$ is constant over that time interval. Any change in the straining mode implies a *strain path change* (SPC). In many deformation operations these strain path changes are small and occur gradually so that possible effects on the hardening anisotropy can be neglected. In some more complex forming operations (e.g. deep drawing) the strain path changes can be very abrupt and the substructural anisotropy will have a major influence on the resulting strength of the work piece. A parameter to quantify the abruptness of a strain path change has been proposed by Schmitt et al. [1985], which calculates the cosine of the angle between the straining modes prior and after the SPC,

$$\cos\theta = \frac{\dot{\boldsymbol{\varepsilon}}_1}{\|\dot{\boldsymbol{\varepsilon}}_1\|} : \frac{\dot{\boldsymbol{\varepsilon}}_2}{\|\dot{\boldsymbol{\varepsilon}}_2\|} \,. \tag{1.2}$$

This parameter ranges between -1 and 1. If it is 1, both straining modes are equal and there is no change in the strain path. If it is -1, the straining modes are opposite and there is a strain path reversal. Micromechanically this can be achieved by reversing the slip directions. For a strain path reversal it is expected that the same slip systems still will be active but with dislocations moving in the opposite direction. For a value of the Schmitt-parameter of 0, the straining modes are orthogonal, which is the largest possible difference without a partial reversal of the strain path in the first straining mode. On the micromechanical level an orthogonal SPC is expected to activate a completely new set of slip systems.

Combinations of experimental tests realising either a strain path reversal or an orthogonal SPC are therefore very informative about the anisotropy of the substructure. Strain path change experiments having a strain reversal are often called *Bauschinger tests*, while tests with an orthogonal strain path change are often referred to as *cross tests*. Results of these types of tests will be discussed in this thesis from a mechanical, textural and substructural point of view to assess the problem of substructural anisotropy and to feed the multiscale model with calibration and validation data.

1.4 Approach

The presented research falls into two distinct parts. In the *experimental part*, the mechanical evolution with strain of the selected aluminium alloy is characterised. In the *modelling part*, a new multiscale model for the prediction of the mechanical behaviour under an arbitrary strain path is presented and discussed.

The main objective of the experimental part is to obtain an integral data set characterising the mechanical behaviour of the same material under different strain path changes. Such complete data sets are rarely found in scientific literature, while they are essential for advancing the understanding of mechanical anisotropy. The outcome of this study will be utilised in an assessment of the developed multiscale model. It might as well be useful for all other models that deal with the anisotropy of prestrained aluminium or with the mechanical response during strain path changes.

For the purpose of conducting strain path change experiments, a new test apparatus has been designed and built to perform deformation in simple shear. In combination with other existing deformation tests, like e.g. conventional cold rolling or uniaxial tension a variety of strain path changes can be obtained.

The objective of the modelling part is to explore how accurate the experimental results can be predicted based on theoretical considerations and assumptions derived from both the literature and the experimental part. A multiscale approach is chosen because this enables to treat the different aspects of material anisotropy at their most appropriate length scale. If the model is successful, this also enables to study the possible correlation between the two main processes contributing to the overall anisotropy of the flow stress, being the texture evolution and the intragranular substructure development, since this correlation is poorly understood and difficult to assess by experimental means.

A second aim of the presented model is to reduce the number of experiments needed to obtain a reasonably accurate prediction of the anisotropy of prestrained materials. To characterise the anisotropy of a material experimentally in order to predict the yield stress for all straining modes occurring in complex deformation processes, many different experiments have to be conducted, which is very costly. For some straining modes the yield stress might not even be possible to obtain directly via an experimental test. The texture of a material on the other hand can be obtained by a dedicated diffraction measurement on a single sample. Much ongoing research in the field of mechanical material science is therefore dedicated to the prediction of the anisotropy from a known texture. For prestrained materials or for deformation processes where abrupt strain path changes occur, the texture alone is not sufficient to characterise the anisotropy, since the intragranular substructure in the prestrained material also contributes to the anisotropy. A model which combines both texture and substructure evolution might offer a solution.

The insights obtained from the experimental results and the modelling work might be instrumental to tackle engineering problems where strain path changes could have an important influence on the flow stress. In spring back and failure predictions of complex deformation processes a close estimate of the flow stress at the end of the strain path is of crucial importance. In the ongoing research on the single point incremental forming (SPIF) rapid prototyping technique [Eyckens et al.; 2007a] which imposes very complex strain paths on the material, the prediction of the local flow stress turns out to be a tough task.

A possible application of a successful multiscale model for mechanical behaviour during strain path changes could be to implement it inside finite element models (FEM) and to activate it only for elements where an abrupt change of strain path is obtained or expected. Even with the current computation speeds a full integration of this type of models will for most problems turn out to be too computationally demanding.

1.5 Overview of text

In the following chapter, an overview of the existing literature on strength and anisotropy of metallic materials will be presented. The focus here will lay mainly on the anisotropy which is caused by the intragranular dislocation substructure and how that affects the work hardening behaviour after abrupt strain path changes.

In the third chapter, the experimental techniques and results are presented, in order to obtain a comprehensive data set on a widely used deep drawing aluminium alloy, including different sorts of strain path changes at different amounts of prestrain.

A multiscale model for work hardening during cold deformation will be presented in chapter 4. This model aims to predict the work hardening anisotropy and the transient hardening behaviour after an SPC.

In chapter 5, predictions by the multiscale model will be discussed in reference to the experimental data of chapter 3 and the overall performance will be compared to earlier strain path change hardening models.

Chapter 6 concludes this work by recapitulating the main achievements and conclusions of the thesis and putting forward some suggestions for further study into this subject.

2

Literature survey

Modelling material behaviour during complex deformation processes involves finding appropriate evolution equations for the material parameters that affect the mechanical behaviour. Material subjected to plastic deformation will become intrinsically different from its initial state. The changes are situated on almost all length scales in a wide variety of properties, but there is one material property which encompasses the influence of all these changes on the macro scale level, namely the flow stress. This is the stress level that is required to continue the deformation. If only one straining mode operates during the deformation, the flow stress tensor gets very often reduced to a single equivalent scalar value[4]. Whenever multiple straining modes are present, also the 'directionality' or anisotropy of the flow stress regarding the straining mode (the direction of the strain) is required for a full description of the flow stress. The anisotropy of the flow stress is usually represented by the flow surface, which is a 5 dimensional hyper surface in the deviatoric stress space, representing all stress states where the deformation will become plastic. The main problem from the materials science point of view in deformation modelling is to get a good description of the flow surface and how it evolves with ongoing deformation.

There are many possible sources of anisotropy in a material. For polycrystalline materials one of the main sources is the crystallographic texture, which already has been discussed in paragraph 1.2. Preferential alignment of grain shapes or different phases as well as contingent clustering of different phases or grain sizes can also induce a certain degree of anisotropy. All these influences are collected under the term morphological texture. At moderate strains only slight changes of the morphological texture are to be expected and therefore it will not be discussed

---

[4] In that case also the strain is reduced to an equivalent scalar value.

further on. Crystallographic and morphological texture represent distributions of characteristics which are situated on the meso scale and should therefore be treated as characteristics of the macro scale.

At the meso scale the main contribution to the overall anisotropy stems from the dislocation substructure morphology. Due to its complex nature it is not yet understood how it exactly contributes to the anisotropy. All dislocations and dislocation interaction products are perturbations of the crystal lattice and therefore have a local displacement field and corresponding elastic stress field around them. The interaction of all the local stress fields of the stored dislocations in the substructure will have a contribution to the anisotropy of the grain. Today's characterisation techniques are not yet advanced enough to directly measure the stresses at such a small scale. Most of the knowledge on the anisotropy due to the substructure comes from theoretical considerations based on the observed morphology. The literature review will mainly focus on what is known about the intragranular substructure.

At the micro scale the interactions of individual dislocations with the increasing number of stored dislocations will cause an increase of the flow stress which due to purely geometrical considerations also happens in an anisotropic way. To activate an inactive slip system a higher shear stress is needed than to keep an active slip system active, since the dislocations of the inactive slip system have to cut the dislocation forest of stored dislocations of the active slip system. This is known as latent hardening. At very low levels of strain where no substructure has yet been formed, this effect can be clearly observed. At a higher amount of strain it becomes inseparable of the previously discussed effect of the substructure on the anisotropy.

The literature review starts with the general framework of anisotropy and work hardening in paragraph 2.1. Here the basics on how to calculate texture evolution and its influence on anisotropy as well as how dislocation interactions lead to work hardening and anisotropy will be discussed. In paragraph 2.2 the experimental and modelling results on the intragranular substructure are reviewed. The effects on the stress field are discussed and some conclusions for further work presented. Paragraph 2.3 discusses the effects on work hardening behaviour during abrupt strain path changes, since they clearly show the influence of the substructure on the anisotropy. The corresponding observed changes in substructural morphology are also treated. Finally some models which include a substructural contribution to model anisotropy are reviewed in paragraph 2.4.

2.1 General framework: Anisotropy and work hardening in metallic materials

Anisotropy and work hardening have in the past decades generally been treated separately in material science. While anisotropy has been predominantly an issue in applied mechanics, the fundamental research in work hardening has been driven by experimental results where anisotropy has no significant influence. A relatively straightforward combination of both aspects has proven to work well for many engineering applications. Only for complex applications, like failure prediction and the study of processes with non-monotonic strain paths, a more integrated treatment of both aspects is required.

In this paragraph, the widely used phenomenological approach for anisotropy and work hardening in applied mechanics is presented first. Then the Taylor type models for texture evolution are introduced and it is described how they can be used to obtain a yield locus. After that the micromechanical mechanisms involving dislocation interactions that lead to work hardening will be discussed. Finally the hardening anisotropy as a result of these dislocation interactions is reviewed.

2.1.1 Phenomenological description of an anisotropic flow surface

The yield locus plays a crucial role in describing the material flow behaviour in modelling of complex deformation processes. As the locus of all deviatoric stress states where plastic flow can occur, it reflects the anisotropy of the yield stress for a material with a certain thermo-mechanical history. Using the rule of normality which prescribes that the straining mode $\dot{\boldsymbol{\varepsilon}}/\|\dot{\boldsymbol{\varepsilon}}\|$ (cf. paragraph 1.2) should be perpendicular to the yield locus, the yield locus can be used to derive the constitutive relation between stress and strain rate [Hill; 1950]. Many mathematical formulations which approximate the actual materials anisotropic yield locus have been proposed since the pioneering work of Hill. The recent book by Banabic et al. [2000] gives an extensive overview of phenomenological yield locus descriptions coming from the field of continuum mechanics. These descriptions generally have six to nine parameters which need to be calculated from experimentally obtained yield stress values.

One of the most challenging questions is how the flow surface (of which the initial state is equal to the yield locus) evolves with further deformation. In

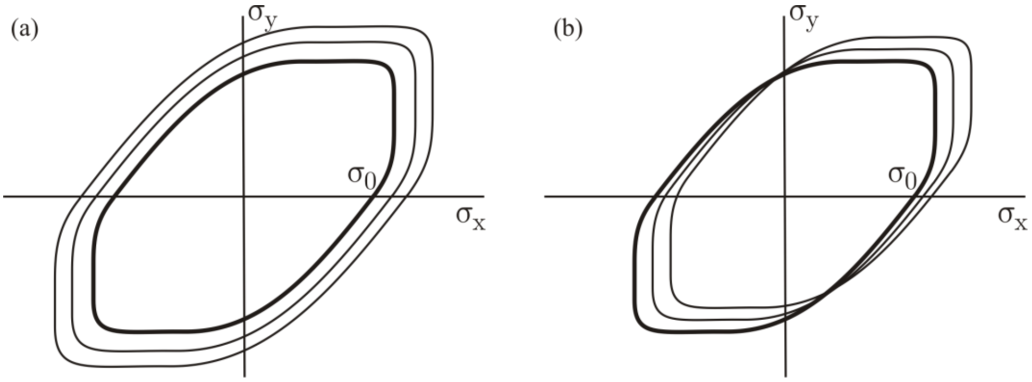

Fig. 2-1 : Schematic example of hardening mechanisms implemented for phenomenological yield locus descriptions. (a) Isotropic hardening. (b) Kinematic hardening.

continuum mechanics two main mechanisms are proposed: isotropic and kinematic hardening [e.g. Asaro and Lubarda; 2006]. Isotropic hardening changes the parameter of the flow surface description which is characteristic for the size of the flow surface, usually the flow stress in the rolling direction of a plate sample σ_0. It increases (or decreases in case of softening) the size of the whole flow surface in a proportional way in all directions (fig. 2-1 (a)), retaining the shape of the flow surface. In case of kinematic hardening the flow surface is shifted in a certain direction in the stress space, while the size and the shape of the flow surface are unaltered, so that the flow stresses close to the direction of the shift are now made larger at the cost of the flow stresses in the opposite directions (fig. 2-1 (b)). Both hardening modes are often combined to obtain a more general hardening behaviour. Nevertheless, due to the complex nature of all microstructural processes involved causing hardening and changes in the anisotropy which also affect the shape of the flow surface, combined isotropic and kinematic hardening as such is often insufficient in describing the true anisotropic hardening behaviour.

2.1.2 The influence of texture on anisotropy

One of the main causes of the anisotropy of the flow stress is the texture of the material (cf. section 1.2). Therefore an interesting approach is to calculate the yield locus from the texture [e.g. Van Houtte and Van Bael; 2004]. Since the evolution of the texture for a certain deformation increment can be calculated using crystal plasticity models, also the evolution of the flow surface with deformation can be estimated.

a) The Taylor model of crystal plasticity

One of the most successful basic crystal plasticity models is the full constraints (FC) Taylor model proposed by G.I. Taylor in 1938 [Taylor; 1938]. A mathematically more elaborated formulation can be found in e.g. [Kocks; 1970] and [Gil Sevillano et al.; 1980]. It starts from the assumption that all grains deform under the same deformation gradient tensor $\mathbf{F}$ as the deformation applied macroscopically while the plastic work dissipation $\dot{W}$ is minimised. In this way all grains deform in a compatible way. Since the stress is assumed to be homogeneous throughout the individual grains, stress equilibrium is not guaranteed at the grain boundaries. The model further assumes that the deformation is accommodated by homogeneously distributed slip on certain crystallographic planes (with plane normals $\hat{\mathbf{n}}^{\alpha}$, depending on the slip system α) in certain crystallographic directions ($\hat{\mathbf{b}}^{\alpha}$), resulting in a simple shear deformation for each slip system. Microscopically this translates into the deformation by dislocation glide on equally spaced slip planes. For incremental calculations the applied deformation can be represented by the velocity gradient tensor $\mathbf{L}$, which is constant in deformation processes like e.g. rolling, wire drawing and simple shear:

$$\dot{\mathbf{F}} = \mathbf{L} \cdot \mathbf{F} . \tag{2.1}$$

The velocity gradient of a slip system α can be written as

$$\mathbf{l}^{\alpha} = \left(\hat{\mathbf{b}}^{\alpha} \otimes \hat{\mathbf{n}}^{\alpha} \right) \dot{\gamma}^{\alpha} \quad \text{or} \quad l_{ij}^{\alpha} = \left(\hat{b}_i^{\alpha} \hat{n}_j^{\alpha} \right) \dot{\gamma}^{\alpha} \tag{2.2}$$

with $\dot{\gamma}^{\alpha}$ being the shear strain rate of the slip system (further called slip rate). The overall velocity gradient of a single grain $\mathbf{l}$ is the combined slip activity of all systems added together with the rate of lattice spin $\dot{\boldsymbol{\omega}}_l$:

$$\mathbf{l} = \sum_{\alpha} \left(\hat{\mathbf{b}}^{\alpha} \otimes \hat{\mathbf{n}}^{\alpha} \right) \dot{\gamma}^{\alpha} + \dot{\boldsymbol{\omega}}_l . \tag{2.3}$$

Fig. 2-2 illustrates this equation for a single slip system presented in the reference frame of the crystal lattice. The symmetrical (which equals the macroscopically imposed strain rate tensor $\dot{\boldsymbol{\varepsilon}}$) and asymmetrical (equal to the rate of rigid body rotation $\dot{\boldsymbol{\Omega}}$) part of equation (2.3) are

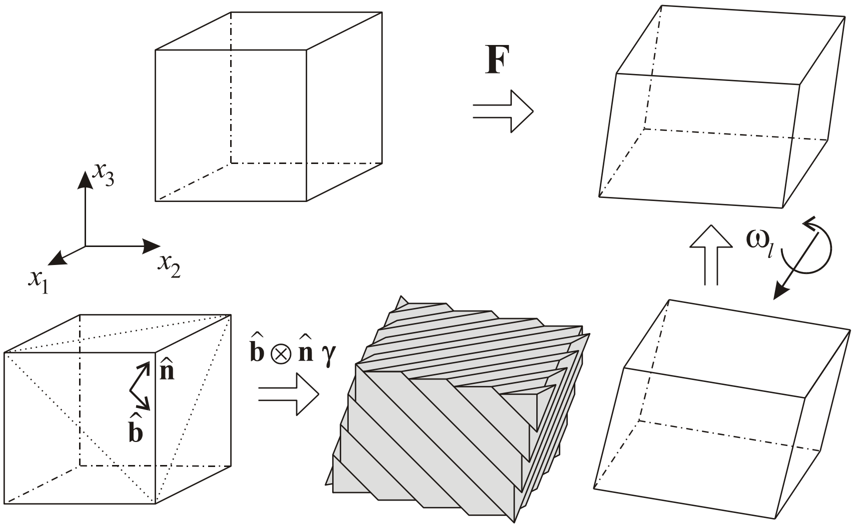

Fig. 2-2 : Illustration of equation (2.3) in a reference frame attached to the initial orientation of the crystal lattice for a deformation gradient tensor $\mathbf{F}$ which can be accommodated by single slip on the system $(1\,1\,1)\left[0\,1\,\bar{1}\right]$ and a small lattice rotation $\boldsymbol{\omega}_l$.

$$\dot{\boldsymbol{\varepsilon}} = \sum_{\alpha} \mathbf{M}^{\alpha} \dot{\gamma}^{\alpha} \quad \text{with } \mathbf{M}^{\alpha} = \frac{1}{2}\left(\hat{\mathbf{b}}^{\alpha} \otimes \hat{\mathbf{n}}^{\alpha} + \hat{\mathbf{n}}^{\alpha} \otimes \hat{\mathbf{b}}^{\alpha}\right) \text{ and} \tag{2.4}$$

$$\dot{\boldsymbol{\Omega}} = \sum_{\alpha} \frac{1}{2}\left(\hat{\mathbf{b}}^{\alpha} \otimes \hat{\mathbf{n}}^{\alpha} - \hat{\mathbf{n}}^{\alpha} \otimes \hat{\mathbf{b}}^{\alpha}\right)\dot{\gamma}^{\alpha} + \dot{\boldsymbol{\omega}}_l \,. \tag{2.5}$$

For equation (2.4) a solution has to be found for the slip rates $\dot{\gamma}^{\alpha}$, which in a small strain increment can be approximated by constant values, that comply with $\dot{\boldsymbol{\varepsilon}}$, under the condition of a minimised rate of plastic work dissipation :

$$\dot{W} = \sum_{\alpha} \tau^{\alpha} \left|\dot{\gamma}^{\alpha}\right| = \min, \tag{2.6}$$

where τ^{α} are the critical resolved shear stresses of the slip systems. The found slip rates $\dot{\gamma}^{\alpha}$ can be used in equation (2.5) to find the rate of lattice spin $\dot{\boldsymbol{\omega}}_l$ to update the grain's orientation to use in the calculation of the next increment. The deviatoric stress tensor $\boldsymbol{\sigma}'$ of the grain can be found with the condition that the resolved shear stress $\mathbf{M}^{\alpha} : \boldsymbol{\sigma}'$ should be equal to the critical resolved shear stress

τ^{α} for all active slip systems and lower than τ^{α} for all non active slip systems. Van Houtte [Van Houtte and Aernoudt; 1975, Van Houtte; 1988] has designed a solution algorithm based on the linear programming technique to solve the foregoing equations in an efficient way. The Taylor factor M, linking a certain scalar equivalent of the macroscopic strain rate with the microscopic slip rate (cf. equation (A.1)), which is difficult to obtain experimentally, can also be calculated with the Taylor-type models. For a single grain also the following equation holds:

$$\sigma_{eq} = M\tau_{ref}\,, \tag{2.7}$$

with σ_{eq} the flow stress corresponding[5] to the chosen scalar equivalent of the strain rate that defines M (e.g. $\dot{\varepsilon}_{11}$ for tensile tests and uniaxial and plane strain compression test, $\dot{\varepsilon}_{12}$ for simple and pure shear tests or the von Mises strain rate $\dot{\varepsilon}_{vm}$ for more complex straining modes), and τ_{ref} the weighted average of τ^{α} with the slip rates $\dot{\gamma}^{\alpha}$ as the weighting factors[6]. It follows from equation (2.7) that M also links the macroscopical flow stress σ_{eq} with the (micro)structural resistance against dislocation slip τ_{ref}. M only depends on the straining mode $\dot{\boldsymbol{\varepsilon}}/\|\dot{\boldsymbol{\varepsilon}}\|$ and the orientation of the grain. The average Taylor factor $\overline{M}$ for the complete set of grains depends accordingly only on the straining mode and the texture of the material.

b) Further developments in Taylor type modelling

Several variants to the FC Taylor model have been proposed, mainly to introduce a certain degree of stress equilibrium at the grain boundaries. One approach has been to introduce overall stress equilibrium by self-consistent modelling, where the stress state of an individual grain in an iterative calculation over all grains is forced into equilibrium with the stress state of the matrix having the average properties of the rest of the grains [Molinari et al.; 1987, Lebensohn and Tomé; 1993]. Randomly appointing grain orientations to integration points in finite element simulations using the generalised Schmid law as the constitutive material

---

[5] The corresponding flow stress to a certain equivalent of the strain rate should conserve the rate of energy dissipation: $\sigma_{eq}\dot{\varepsilon}_{eq} = \boldsymbol{\sigma} : \dot{\boldsymbol{\varepsilon}} = \dot{W}$.

[6] Some derivations related to M and clarifications on the chosen definitions for τ_{ref}, σ_{eq} and $\dot{\varepsilon}_{eq}$ can be found in appendix A.

law has also been used to obtain better texture predictions [Kalidindi et al.; 1992, Delannay et al.; 2006]. Both methods can be applied to all straining modes, but are unfortunately computationally very intensive and for the moment therefore impractical for industrial applications. The Lamel model [Van Houtte et al.; 1999], the GIA model [Engler et al.; 2005] and the advanced Lamel model [Van Houtte et al.; 2005] impose equilibrium of the shear stresses acting on the grain boundaries, while compatibility of the shear strains is kept. These models are computationally less demanding than the previously described ones and result in equally good texture predictions. The Lamel model can only be used for rolling deformation and is therefore not suited for general yield locus calculations.

c) Yield locus calculation with crystal plasticity models

To derive yield loci from the texture one complication has to be overcome. In the Taylor-type models the deformation is imposed, whereas yield loci are defined in the deviatoric stress space. One way to solve this problem is to calculate the plastic potential as a function of the straining mode and to invert it into deviatoric stress space to obtain the yield locus [Arminjon and Bacroix; 1991, Van Houtte; 1994]. In this method, attention should be paid to the convexity of the plastic potential, to avoid irregularities in the yield locus [Van Houtte and Van Bael; 2004, Van Houtte et al.; 2009]. Maudlin et al. [1996] proposed an alternative method where a piece-wise linear representation of the yield surface is obtained by taking the inner envelope of a set of hyper planes. Each hyper plane is defined as the normal plane to an imposed strain rate at its corresponding yield stress point. The imposed strain rates are selected by randomly probing strain rate space.

Calculating the yield locus from an experimentally obtained texture using crystal plasticity models is an effective method to incorporate the materials anisotropy into modelling of industrial forming operations. Further improvement of these models could be achieved if the evolution of the flow surface with local strain could be incorporated. A first step in this direction has been to account for isotropic and kinematic work hardening, mostly by phenomenological equations on the macro scale [Asaro and Lubarda; 2006]. A further refinement of the applied models incorporating isotropic and anisotropic hardening at more appropriate length scales – closer to the micromechanical sources of work hardening and hardening anisotropy – should result in better anisotropy predictions [Peeters; 2002]. In the remaining sections of this chapter the focus will be therefore on the micromechanical contributions to work hardening.

2.1.3 Work hardening as result of dislocation interaction processes

Extensive research has been done on the micromechanical causes of (isotropic) work hardening. Several dependences of the flow stress of metallic materials on microstructural parameters like grain size, dislocation density and precipitate size and chemical characteristics like alloying content have been experimentally obtained, as well as the dependence of flow stress on temperature and strain rate. A comprehensive overview of all these dependences can be found in [Gil Sevillano; 1993].

a) The work hardening evolution for single phase materials

For single phase materials, the main contribution to work hardening comes from the increase of the forest dislocation density during deformation. The elementary slip process via dislocation glide is hindered by the existence of “forest” dislocations intersecting the glide plane that need to be cut by the mobile dislocations. To overcome these and other obstacles a certain value of the shear stress has to be resolved on the slip plane in order to expand existing dislocations loops and to let them eventually cut the forest dislocations. For a broad range of materials, substructures, temperatures and strain rates the following dependence of this critical resolved shear stress τ to the (forest) dislocation density ρ has

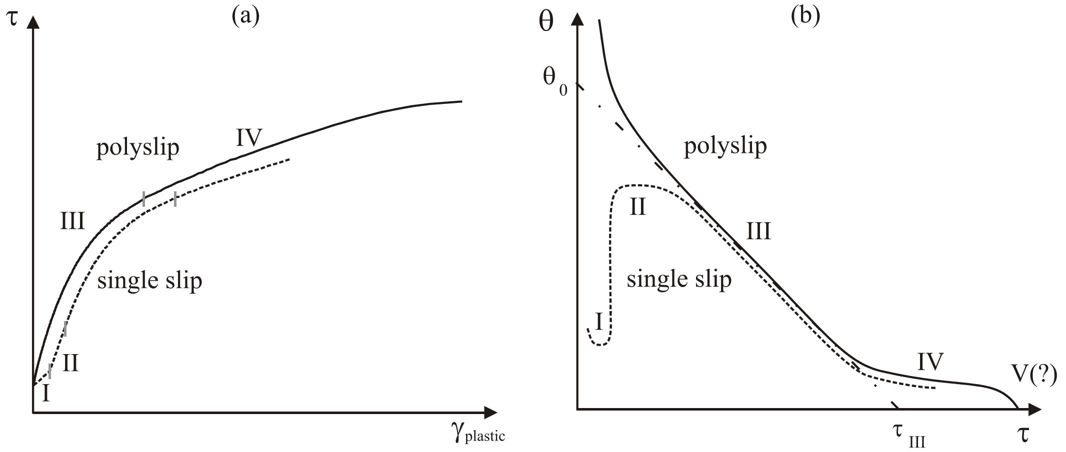

Fig. 2-3 : Schematic sketch of flow stress versus strain (a) with the corresponding hardening rate versus flow stress curve (b), illustrating the hardening stages for single crystals deformed in single slip and polyslip. After [Kocks and Mecking; 2003].

been experimentally obtained for all hardening stages:

$$\tau = \alpha G b \sqrt{\rho}\,, \tag{2.8}$$

where G is the shear modulus and b the length of the Burgers vector. α is a proportionality factor about 0.2 to 0.5 and is slightly dependent on strain rate and temperature [Kocks and Mecking; 2003]. A schematic sketch of the evolution of τ with the overall amount of dislocation slip Γ as a representation of the strain together with the corresponding hardening curve (hardening rate $\theta = d\tau/d\Gamma$ as a function of τ) is shown in fig. 2-3.

For single crystalline materials oriented for single slip deformation, four stages in the work hardening behaviour are observed. Initially there is a short stage of low hardening (stage I), followed by a stage with a high athermal hardening (stage II). In stage III, the hardening rate gets linearly reduced with increasing stress, almost to the point of stress saturation τ_{III}. A fourth stage is observed at large strains which is characterised by a slowly decreasing hardening rate, extending the point of stress saturation to a much higher stress level. Some researchers even have reported a stage V with a downward deviation of the hardening curve to a saturation stress, but it is still under discussion whether this is a true stage in hardening or an artefact due to material failure [Kocks and Mecking; 2003].

b) Dislocation mechanisms for work hardening

The dislocation mechanisms responsible for the described succession of hardening stages have been the subject of debate for more than 30 years, a wider consensus on this subject seems to have been established only rather recently.

Stage I hardening is a result of the formation of dislocation dipoles formed by mutual attraction of dislocations of opposite signs on parallel slip planes. Also multipoles of edge dislocation segments will be formed after the passing of obstacles via double cross slip (fig. 2-4). These multipoles will trigger secondary slip due to the build-up of internal stresses in the multipolar arrangements [Gil Sevillano; 1993]. This secondary slip will slightly reorient the material volume inside the multipoles. Because of the difference in the stress states inside and outside the multipoles, the multipoles become large non-impenetrable obstacles for primary slip resulting in the sudden rise in the hardening curve and the onset of stage II hardening. The hardening rate θ_{II} in stage II is observed to be independent of temperature and strain rate.

The transition to stage III starts when the annihilation of stored dislocations by massive cross slip or climb of dislocation segments becomes effective [Nabarro; 1989]. These mechanisms are thermally activated, so that the onset of stage III is temperature and strain rate dependent. A simple, but widely supported model for stage III hardening has been proposed by Kocks [1976]. It starts from equation (2.8) to express the hardening rate as a function of the dislocation density and its evolution with strain:

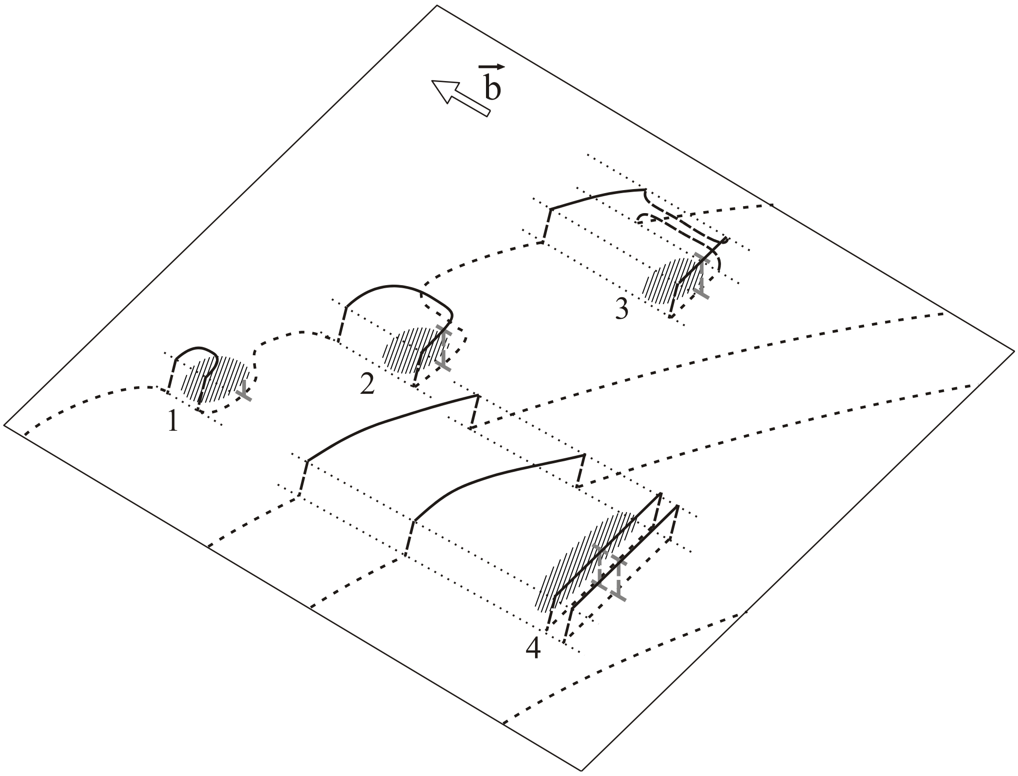

Fig. 2-4 : Schematic representation of the formation of dislocation multipoles during stage I of work hardening. If a dislocation loop encounters an obstacle (hatched regions), the screw segment will pass it via a double cross slip operation (1). The edge segment on the primary slip plane which is blocked by the obstacle might trap the edge segment on the parallel slip plane to form a dipole (2). Annihilation via cross slip behind the obstacle releases the dislocation loop from the obstacle but results in a double jog for the further expanding dislocation loop and a prismatic dislocation loop as debris at the obstacle (3). After several dislocation loops have passed the obstacle with the same mechanism, edge dislocation multipoles remain as debris at the obstacle (4). For details cf. [Jackson; 1985].

$$\theta = \frac{d\tau}{d\Gamma} = \frac{\alpha G b}{2\sqrt{\rho}} \frac{d\rho}{d\gamma} \tag{2.9}$$

The evolution equation of ρ can be expressed as the sum of a dislocation storage term and a dislocation annihilation term:

$$\frac{d\rho}{d\gamma} = \frac{d\rho^{+}}{d\gamma} + \frac{d\rho^{-}}{d\gamma} = \frac{1}{Kb}\sqrt{\rho} - \frac{L_R}{b}\rho . \tag{2.10}$$

Combining equations (2.9) and (2.10) results in:

$$\theta = \frac{\alpha G}{2K} - \frac{L_R}{2b}\tau = \theta_0 \left(1 - \frac{\tau}{\tau_{III}}\right), \tag{2.11}$$

with θ_0 the hardening rate at $\tau = 0$ and τ_{III} the saturation stress of stage III.

The storage of mobile dislocation segments is assumed to be proportional to $\sqrt{\rho}$, which follows from the assumption that the average area a dislocation segment can sweep before it is stored, is inversely proportional to the number of stored dislocations it encounters. K is a proportionality constant. The annihilation of stored dislocations is assumed to be proportional to the density of stored dislocations ρ, since dislocation segments have to recombine via cross slip or climb. L_R represents the average length of dislocation line per unit length which gets annihilated at annihilation sites [Kocks; 1976].

The assumption of the proportionality between the storage of mobile dislocation segments with $\sqrt{\rho}$ has been related to the “principle of similitude” [e.g. Kocks and Mecking; 2003]. This principle is based on the experimentally observation that the microscopically observed length scales of dislocation configurations are inversely proportional to the flow stress. It states that the microstructure will stay self similar with a decreasing length scale during deformation. One of the consequences of the principle of similitude is a constant athermal contribution to the hardening rate, irrespective of the applied stress, which can be easily verified by inserting the assumption $d\rho^{+}/d\gamma \propto \sqrt{\rho}$ into equation (2.9). This athermal hardening contribution is similar to the constant hardening rate of stage II and corresponds to:

$$\theta_0 = \frac{\alpha G}{2K} . \tag{2.12}$$

The assumption of an average annihilation length L_R which remains constant with increasing dislocation density as proposed by Kocks is more difficult to justify. The good agreement with experimental observations nevertheless indicates that recovery processes scale with ρ, whatever the physical mechanisms involved may be. The temperature and strain rate dependence of stage III hardening is governed by the thermal influence on the recovery term and translates into a strong dependence of the saturation stress τ_{III} of equation (2.11) on temperature and strain rate.

The hardening mechanisms of stage IV are still under discussion. Several models, all based on somewhat different physical mechanisms, will be discussed in section 2.2.3.b.

c) Evolution of the hardening in polycrystals

The hardening of polycrystalline samples does not show stage I and stage II hardening (fig. 2-3). The boundary restrictions exerted by the differently oriented grains on each other enforce the activation of multiple slip systems directly from the start of the deformation. Therefore annihilation processes can occur at the dislocation multipoles and thus stage III hardening is observed from the onset of deformation [Gil Sevillano; 1993]. The short initial stage with a very high but rapidly decreasing work hardening rate (fig. 2-3) can be attributed to the interaction of dislocations with grain boundaries or precipitates [Estrin and Mecking; 1984]. The hardening mechanisms (from stage III on) active in polycrystals are the same as for single crystals, therefore the further evolution of the hardening curve is also the same.

2.1.4 Anisotropy as a result of slip system interactions

Since forest hardening is believed to be the most important hardening mechanism (cf. section 2.1.3.a), it seems natural to assume that dislocation slip itself leads to an anisotropic work hardening.

For single crystals in single glide this has been extensively studied for fcc materials [Kocks; 1964, Jackson and Basinski; 1967, Franciosi et al.; 1979]. The latent hardening ratios (LHR) of all possible kinds of slip system combinations have been measured by first activating a primary slip system and after some strain changing the deformation path to activate a secondary system.

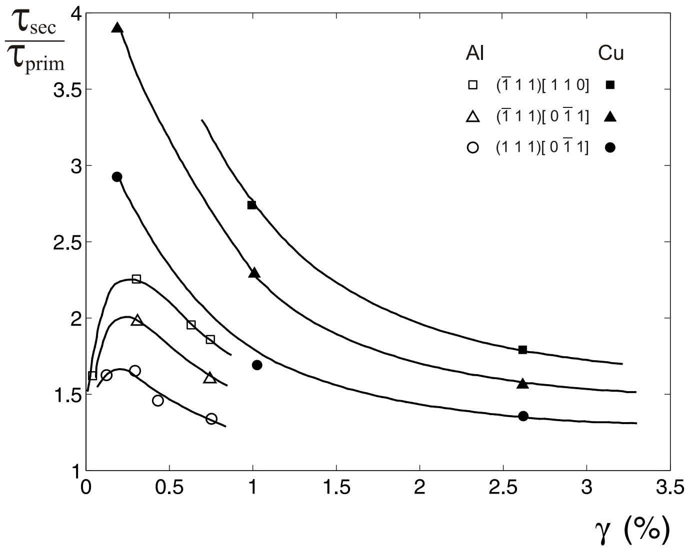

Fig. 2-5 : Latent hardening ratios (LHR) of secondary slip on different slip systems after primary slip on $(1\,1\,1)[\bar{1}\,0\,1]$ for Copper and Aluminium. From [Franciosi et al.; 1979].

$$\text{LHR} = \frac{\tau_{sec}}{\tau_{prim}}, \tag{2.13}$$

with τ_{prim} and $\tau_{\sec}$ the critical resolved shear stresses of the slip system active just before and after the change of the straining path respectively.

As can be seen from fig. 2-5 the LHRs can be subdivided for every material into three groups, depending on the type of dislocation interaction product (no junction, glissile junctions or sessile junctions). The three LHR curves show a maximum value at low strains with a decline to a stable value at higher strain. The exact type of junction depends on the geometry of the two participating dislocation segments, including the glide direction and the angle of the Burgers vector with the dislocation line [Shenoy et al.; 2000]. Hirth [1961] has reviewed all 24 possible interactions (12 slip systems with 2 possible glide directions) from a theoretical point of view. There are some discrepancies between the theoretical strength of some interactions and the found LHR, mainly because no dependence on the slip direction within a slip system has been reported in the experimental studies. The most striking difference however comes from the analysis for the interaction of critical slip systems[7]. This interaction should, according to Hirth, result in strong barriers to further slip, where in latent hardening experiments a similar LHR is found as for coplanar and collinear slip systems interactions which form no junctions at all and correspond to the lowest curve of LHR values.

A good correspondence between the analysis of Hirth and the measured LHR can be found for the conjugated slip systems[8], which can form sessile Lomer-Cottrell locks and therefore have the highest LHR. All dislocation interactions that can form jogs on the primary dislocation correspond to the second curve of LHR values, in which the theoretical analysis of Hirth and the experimental data also correspond for at least one glide direction of an activated secondary slip system.

Franciosi and Zaoui [1982] made a theoretical analysis of the hardening rates from single crystals oriented for multislip and could accurately predict which combination of slip systems will be activated in a situation where 6 or 8 systems are equally stressed, but only three or two are found experimentally to become active. To explain this they needed to incorporate latent hardening into a generalised Schmid law.

The observed latent hardening can be formally described by introducing a hardening matrix $\mathbf{h}$ defined by :

$$d\tau^{\beta} = \sum_{\alpha} h_{\beta\alpha} d\gamma^{\alpha} \tag{2.14}$$

in which the hardening of a slip system is made dependent on the slip activity on other systems. For describing the obtained LHR curves of fig. 2-5 an expression for the self hardening coefficient $h_{\alpha\alpha}$ should be used which describes the observed hardening of the primary slip system, while the expressions for the various non diagonal components of $\mathbf{h}$ should result in the observed LHR dependence on strain of the primary system. Frequently the initial maxima of the LHR curves are neglected and constant ratios larger than 1 between the off diagonal and diagonal terms of $\mathbf{h}$ are assumed, which corresponds to the observed stable LHR values after some small strain [Asaro; 1983].

---

[7] Critical slip systems are secondary slip systems that have their Burgers vector perpendicular to the Burgers vector of the primay slip system. e.g. $\left(\bar{1}\,1\,1\right)[1\,0\,1]$ and $\left(\bar{1}\,\bar{1}\,1\right)[1\,0\,1]$ for $(1\,1\,1)\left[\bar{1}\;0\,1\right]$.

[8] Conjugated slip systems are secondary slip systems that are not collinear or coplanar and have a {110}-plane as symmetry plane with the primary system. e.g. $\left(\bar{1}\;\bar{1}\;1\right)[0\,1\,1]$ and $\left(\bar{1}\,1\,1\right)[1\,1\,0]$ for $(1\,1\,1)\left[\bar{1}\;0\,1\right]$.

An alternative approach is to model the slip systems interactions in a more direct way, adapting equation (2.8) to incorporate slip systems interactions, based on an interaction matrix $\mathbf{a}$ expressing how strong dislocations will be hindered by the interaction with the forest of dislocations stored on any other slip systems.

$$\tau^{\beta} = Gb\sqrt{\sum_{\alpha} a_{\beta\alpha}\rho^{\alpha}} \tag{2.15}$$

From a theoretical point of view, $\mathbf{a}$ should be constant for a large strain interval. For equivalent interactions, a single value for $a_{\beta\alpha}$ should be used, resulting in 6 different values in $\mathbf{a}$, corresponding to self hardening, coplanar systems, collinear systems, critical systems, conjugate systems and one for all other interactions resulting in glissile jog formation. If appropriate values for the $\mathbf{a}$ matrix are selected, this approach can reasonably well predict the evolution of the LHR for single slip [Franciosi et al.; 1979].

Kocks and co-workers [1991] have derived a latent hardening model equation, similar to equation (2.14), but having a simple evolutionary law of the elements of the hardening matrix $\mathbf{h}$. They start from the Taylor equation for the flow stress (equation (2.8)) and by attributing the hardening of a slip plane to the increase of the density of intersecting forest dislocations, the following equation is found:

$$d\tau^{P} = \frac{(\alpha Gb)^{2}}{2\tau^{P}}\, d\rho_{f}^{P} \tag{2.16}$$

with τ^{P} the critical resolved shear stress of slip plane P and ρ_{f}^{P} the density of dislocations intersecting plane P. Since hardening is only attributed to the forest density, the critical resolved shear stresses of coplanar slip systems will always remain equal. The increase of the forest density on a plane P is equal to the sum of the increases of the dislocation line length Λ^{α} on all slip systems α intersecting plane P :

$$d\rho_{f}^{P} = \sum_{\alpha} Y_{P\alpha}\, d\Lambda^{\alpha} \tag{2.17}$$

with $\mathbf{Y}$ a matrix having 0 terms for coplanar slip systems and 1 for all other ones.

The increase of dislocation line length can come from two mechanisms, one being direct storage which is related to the shear rate on the slip system α, and one related to the relaxation of the forest structure in order to get into an arrangement of lower energy. The latter mechanism is assumed to be controlled by the interaction types between participating dislocation densities and depending on the direct storage terms. The overall increase of dislocation line length is :

$$d\Lambda^{\alpha} = \sum_{\beta} R_{\alpha\beta} d\Lambda_{D}^{\beta} \tag{2.18}$$

with $\mathbf{R}$ the relaxation matrix having unity terms for coplanar interactions and higher values for other types of interactions, and $d\Lambda_{D}^{\beta}$ the increase of dislocation length due to direct storage :

$$d\Lambda_{D}^{\beta} = \frac{\sqrt{\rho_{f}^{\beta}}}{bK} d\gamma^{\beta} = \frac{\tau^{\beta}}{\alpha G K b^{2}} d\gamma^{\beta} \tag{2.19}$$

Combining equations (2.17), (2.18) and (2.19) results in :

$$d\tau^{P} = \theta_{0} \sum_{\beta} \frac{\tau^{\beta}}{\tau^{P}} H_{P\beta} d\gamma^{\beta} \text{, with } H_{P\beta} = Y_{P\alpha} R_{\alpha\beta} . \tag{2.20}$$

θ_{0} is the hardening rate for single slip (cf. equation (2.12)), which can be replaced by a general hardening rate θ to incorporate recovery effects as well.

The elements of the matrix $\mathbf{H}$ are dependent on the type of slip systems interaction and are constant during a large strain interval in contrast to the values of $\mathbf{h}$ in equation (2.14).

Bassani and co-workers [Bassani; 1991, Wu et al.; 1991] have questioned the correctness of the obtained LHR values and the resulting features of $\mathbf{h}$ having off diagonal components larger than 1, by arguing that secondary slip in single crystals oriented for single slip already occurs before the crystal has reoriented itself into a position needed for the activation of a secondary slip system, although the observed shear rate of the secondary system remains initially very low. According to their analysis, the latent hardening needs to be smaller than the self hardening, and the observed LHR values are due to a very high initial self hardening of the secondary slip system. The initial yield stress of a secondary system is even lower than the flow stress of the primary system. The self hardening of active slip systems in their analysis has to be dependent on the strain accommodated on the other slip systems. This approach indeed has somewhat different results in the initial stage of the LHR curves, which is difficult to assess experimentally, but for single crystalline materials these differences do not have any relevance for somewhat larger strains.

The contribution of latent hardening to the anisotropy of polycrystalline fcc materials is thought to be low, since commonly at least three out of four slip planes are simultaneously active. There might nevertheless be an influence via the texture evolution, since different critical resolved shear stresses for the different slip systems have a pronounced influence on which slip systems get activated in case that more than five slip systems are equally stressed. In Taylor type texture models (cf. 2.1.2), if the critical resolved shear stresses are assumed to be equal on all slip systems, for every imposed deformation either 6 or 8 slip systems will be equally stressed [Hill; 1950]. In this case the set of equations (2.4), (2.6) is undetermined, resulting in the so called Taylor ambiguity. A second requirement on the shear rates has to be imposed to come to a single set of shear rates and to obtain the lattice spin via equation (2.5) [Van Houtte; 1988, Delannay; 2001]. By introducing latent hardening, the set of equations (2.4),(2.6) always has a single solution depending on the latent hardening law used [Peeters et al.; 2001a], therefore the latent hardening law can influence the texture evolution [Franciosi; 1985, Schmitt et al.; 1985]. Kocks et al. [1991] reported e.g. differences in modelled compression textures, while Bassani [1991] has shown the influence of latent hardening on the texture evolution in uniaxial tension.

2.2 Formation of intragranular substructure

During deformation an intragranular substructure is formed by the stored dislocations. This substructure can have different morphologies depending on material parameters (e.g. SFE and friction stress), microstructural parameters (e.g. grain size and grain orientation) and process parameters (e.g. imposed straining mode, temperature, strain rate). As has been demonstrated for low carbon steel by Raphanel et al. [1986] and for aluminium by Juul Jensen and Hansen [1990], there exists a contribution to the work hardening anisotropy which cannot be explained by texture evolution and classical latent hardening alone, especially at moderate prestrains. Most likely this contribution stems from the substructure. The substructure typically consists of dislocation free zones which are called cells, surrounded by a network of stored dislocations, the cell walls, which accommodate small lattice misorientations between the neighbouring cells. On top of that, long elongated boundaries of very high dislocation density having larger misorientations are also observed.

In this paragraph first experimental observations of substructures in aluminium will be discussed, followed by a discussion on the works dedicated to explain the formation of the substructure and the consequences for the internal stress state. In the next paragraph the importance of the substructure for work hardening transients during strain path changes will be discussed.

2.2.1 Experimental observations of substructure

a) Cell structures

Early observations of substructure have been thoroughly reviewed by Gil Sevillano et al. [1980]. The works they refer to deal with transmission electron microscopy (TEM) observations of cell structures and the analysis of the evolution of the characteristic parameters describing them. One of these works [Schuh and von Heimendahl; 1974] extensively reports on the evolution of the dimensions of the cells and the disorientation[9] over cell boundaries during cold rolling of aluminium. From their analysis it is concluded that cells are formed early on in the process of deformation and that the formation of new cells due to creation of new cell walls predominates in the low and moderate strain region ($\varepsilon_{vm} < 1.5$)[10]. Some annihilation of existing cell walls also occurs at moderate strains ($\varepsilon_{vm} > 0.4$), especially of walls parallel to the rolling plane. At high strains the cell dimensions remain constant, in spite of macroscopically expected shape changes. This is thought to be a consequence of continuous annihilation of cell walls. The disorientation over cell walls lies between 1° and 3° and increases slightly with strain.

Very similar results have been found for various other cell forming materials [Gil Sevillano et al.; 1980]. The observed morphology of cell structures most likely does not contribute to the anisotropy of the flow stress, since the cells are reasonably equiaxed.

b) Cell blocks, dense dislocation walls and microbands

A second level of grain subdivision has been extensively discussed over numerous articles, mainly by the Materials Research Division of the Risø National Laboratory of Denmark. Most of this work focuses on commercially pure aluminium deformed at room temperature in tension and cold rolling. A recent comprehensive overview was published in 1999 [Hansen and Juul Jensen; 1999].

---

[9] The disorientation is the misorientation having the smallest angle out of the set of symmetrical equivalent misorientation descriptions.

[10] ε_{vm} is the von Mises equivalent strain, which is obtained as $\varepsilon_{vm} = \sqrt{2/3\varepsilon_{ij}\varepsilon_{ij}}$

On top of the cell structure discussed in the previous section, a grain subdivision in cell blocks is proposed. The cell blocks are separated by dense dislocation walls (DDWs) or microbands (MBs)[11]. DDWs are sharp dislocation rotation boundaries having a higher dislocation density and a larger disorientation than cell boundaries. MBs are narrow bands composed of parallel elongated cells also having a large disorientation across them. It is often argued that the cell blocks separated by DDWs and MBs have a different set of active slip systems [Bay et al.; 1989]. One possible explanation for the observed alternating disorientation over successive DDWs (cf. fig. 2-6) is that the different cell blocks would have a different set of less than five slip systems active (as required by equation (2.4)) in order to reduce the number of energetically costly dislocation cutting processes [Bay et al.; 1992]. The assembly of all cell blocks will still comply with the macroscopically imposed deformation. This has been further supported by analysis of the excess dislocation content at the DDWs [Wert et al.; 1995]. However, an experimental proof is still missing. Due to the different active slip systems at both sides, DDWs and MBs are often called geometrically necessary boundaries (GNBs) while cell boundaries have been termed incidental dislocation boundaries (IDBs).

The morphology of the DDW and MB structures depends on grain orientation and straining mode. In deformation in tension, three types of morphologies are observed [Hansen and Huang; 1998]. Type I grains have the tensile axis close to

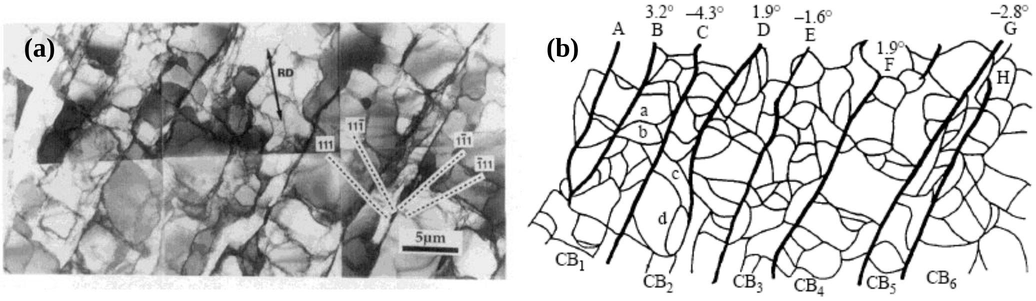

Fig. 2-6 : (a) TEM image of the interior part of a grain of type B in 10% cold rolled aluminium in the longitudinal plane. (b) Sketch of the DDWs and cell boundaries of image (a), the disorientation over the DDWs is indicated. From [Liu et al.; 1998].

---

[11] For microbands the definition of Hu [1963] is used throughout the text. Microbands can also refer to thin elongated tramline like bands parallel to the slip plane mainly observed in copper [Bourelier and Le Héricy; 1963].

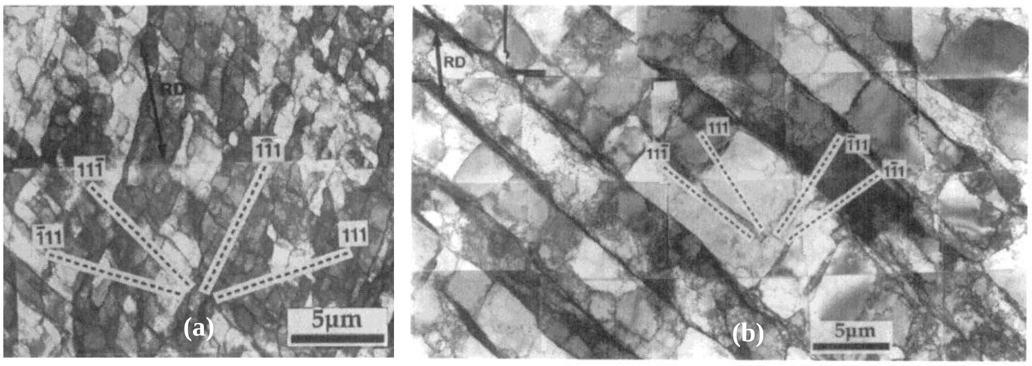

Fig. 2-7 : TEM images of the longitudinal plane of interior part of grains of type A (a) 50% cold rolled aluminium with two sets of straight DDWs parallel to $(1\bar{1}1)$ and $(11\bar{1})$ (b) 30% cold rolled aluminium with one set of somewhat less straight DDWs parallel to $(11\bar{1})$. From [Liu et al.; 1998].

⟨114⟩[12] and show one set of straight DDWs parallel to a {111} plane. Type II grains have a ⟨100⟩ direction close to the tensile axis and do not have DDWs, only equiaxed cells. Type III grains can have all other orientations and have one set of DDWs which is not aligned with a crystallographic plane. For cold rolling, two types of substructure morphologies are reported [Liu et al.; 1998]. Grains of type A (cf. fig. 2-7) have one or two sets of DDWs oriented along $\{111\}$ planes. Grains of type B (cf. fig. 2-6) have much more curved DDWs which are not oriented along {111} planes. Grains oriented close to Goss and S are of type A and show very straight and elongated DDWs while grains with an orientation near Cube are predominantly of type B. All other orientations are mostly of type A with somewhat less straight DDWs parallel to a {111} plane. It is still a matter of debate whether the DDWs for some orientations are aligned with a crystallographic plane or not [Winther et al.; 2000, Humphreys and Bate; 2006].

A study using electron backscattered diffraction (EBSD) on the orientation dependence of subdivision by Delannay et al. [2001] shows that grains with an orientation close to Cube develop large orientation gradients, which orientations along the β-fibre (Copper, S, Brass) do not display.

---

[12] The ⟨114⟩ denomination is merely an indication of the position in the standard triangle derived by the author and has not been proposed as such by Hansen and Huang.

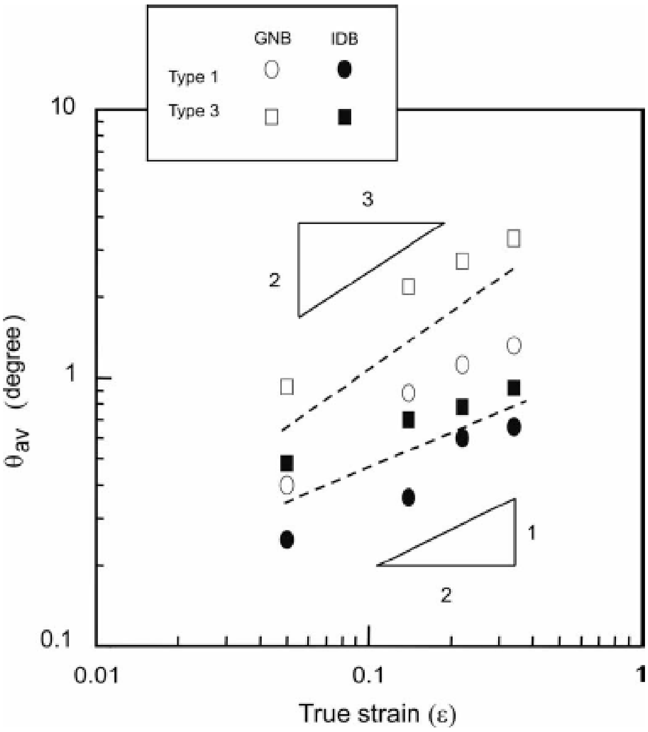

Fig. 2-8 : Log-log plot of average disorientation over IDBs and GNBs as a function of strain for aluminium deformed in tension, indicating a power law with exponent 1/2 and 2/3 respectively. From [Hansen et al.; 2006].

The average disorientation over IDBs and GNBs differs significantly, as well as their evolution with strain. A power law for both is obtained having a somewhat different value for the exponent (cf. fig. 2-8). Hughes and co-workers [1997] observed that scaling of the disorientation distribution applies, at least if both populations of IDBs and GNBS are treated separately. Scaling means that a single probability distribution function applies if the disorientation are normalised with the average value (cf. fig. 2-9). Pantleon and Hansen [2001] identified the Rayleigh distribution as the most probable function for fitting the experimental data. This disorientation distribution can be obtained theoretically by assuming that two slip systems of which the rotation axes of the plastic spins are perpendicular to each other, account for the excess dislocation density of the boundaries in a statistically equal manner (cf. section 2.2.2.b). This is another indication for the hypothesis that less than five slip systems are active in the different cell blocks of the grains.

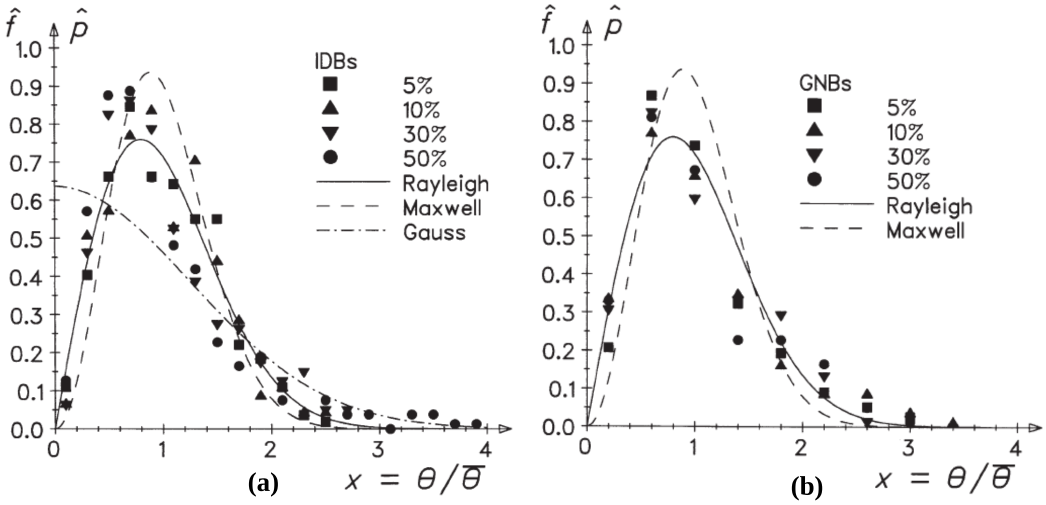

Fig. 2-9 : Normalised disorientation distribution of IDBs (a) and GNBs (b) of cold rolled aluminium, The Gauss, Rayleigh and Maxwell distribution functions are shown for comparison. From [Pantleon and Hansen; 2001].

Few results have been published on the dependence of the GNB-IDB substructure morphology on the grain size. In fine grained pure copper deformed in uniaxial tension, Huang and Hansen [2004] observed the same three types of substructures as in samples with larger grains, however the GNB wall spacing is significantly smaller for the fine grained sample. Feaugas and Haddou [2007] extensively report on the influence of grain size on substructure morphology in nickel and austenitic stainless steel deformed in uniaxial tension. They observe, in contrast to Huang and Hansen, a dependence of the morphology on the grain size. Below a critical value of the grain size, dependent on the SFE, all observed grains are of type II. Moreover no influence of the grain size on the GNB or IDB wall spacing could be statistically demonstrated. A significantly larger spread of the cell wall thickness has been observed for smaller grains. Feaugas and Haddou explain their observations by the influence of intergranular long-range internal stresses arising from plastic strain compatibility requirements at grain boundaries. Since intergranular long-range internal stresses promote multiple slip (more than 2 slip systems simultaneously active) in the early stages of deformation, the substructure will resemble the one of large grains oriented for multiple slip, which is type II, having only IDBs.

A similar observation has been made in an EBSD study on 40% cold rolled aluminium by Van Boxel et al. [2004] where small grains are not likely to show GNB structures, while large grains clearly do.

2.2.2 Models for substructure formation

No consensus has been found yet on the physical backgrounds of substructure formation. Several possibilities have been proposed and tested out in various models. In many cases only the subdivision into cells is considered and not into cell blocks, because the latter, in spite of 25 years of experimental observations, is not yet broadly acknowledged (cf. [Pantleon; 2005]).

In this section four different approaches will be discussed. The first approach focuses on dislocation interaction mechanisms that could initiate the formation of cell walls while the actual dislocation patterning is regarded as a naturally evolving consequence of these mechanisms. In the second approach, statistical fluctuations in the dislocation density or density flux are considered as the cause for dislocation patterning. The third, more recent approach, called dislocation dynamics simulations, tries to predict cell formation by the simulation of thousands of individual dislocations acting under an externally applied stress field. In the fourth approach the stability of a homogeneous deformation is tested by a bifurcation analysis in a continuum mechanics framework. As a result a heterogeneous deformation turns out to be a more stable solution under certain conditions. The length scale of the heterogeneity of the bifurcation is in accordance with the typical length scale of experimentally observed substructures.

a) Dislocation interaction mechanisms

Several authors have proposed dislocation interaction mechanisms for the formation of cell walls. Here, two will be discussed.

Kocks (reviewed in [Kocks and Mecking; 2003]) explains the formation of cells on the basis of pinning points scattered over the glide plane of an active dislocation source. These pinning points are e.g. Lomer-Cottrell locks formed by interaction of primary dislocations with pre-existing forest dislocations. These pinning points or groups of them can be circumvented by subsequent dislocation loops by bowing around them and leaving concave dislocation loops behind. These concave loops are stabilized by interactions with dislocations of secondary slip systems and increase the local critical resolved shear stress. The resistance to dislocation motion on a glide plane is then determined by the stress necessary to let a dislocation percolate through the arrangement of pinning points. Places where these pinning points are somewhat clustered are hard zones and form the core structure of the future cell structure which is formed by entanglement of dislocations initiated at the hard zones.

Jackson [1985] proposed a mechanism for cell formation where cells are formed due to the activation of secondary slip in multipolar edge dislocation structures for reasons of stress relaxation [Kuhlmann-Wilsdorf and Comins; 1983]. These multipolar edge dislocation structures form by a succession of double cross slip events (cf. section 2.1.3.b and fig. 2-4). The secondary slip activated in the multipolar structures induces an orientation difference and therefore transform the multipoles into dislocation cell walls.

This mechanism conforms well to the controversial hypotheses of “low energy dislocation structures” (LEDS). This hypotheses states that dislocation structures nearly minimise the free energy per unit length of dislocation line, among all configurations accessible to the dislocations under the constraints of applied stress and dislocation mobility [Kuhlmann-Wilsdorf; 1992]. In the mechanism of Jackson, the free energy is minimised by the relaxation of the stresses in the multipoles by activation of secondary slip. The LEDS concept corresponds to the application of the second law of thermodynamics to plastic deformation. Herein lies some controversy [Kubin; 1993, Nabarro; 2001], because plastic deformation is a thermodynamically open and dissipative system which is brought far from equilibrium, since 90% of the mechanical work is dissipated as heat. It should be treated as such, which is not the case for the LEDS hypothesis. Moreover, plastic deformation is a highly irreversible process.

b) Statistical fluctuations in dislocation density fluxes

One of the earliest models for grain subdivision treats cell formation in analogy with spinodal decomposition of solid solutions [Holt; 1970]. The total interaction energy between a set of screw dislocations is calculated and a minimum is sought for this energy by introducing periodic perturbations of the local dislocation density. It turns out that a perturbation with a wave length proportional to the average elastic interaction radius between dislocations gives the most stable solution. Although this model has been strongly criticised for many deficiencies and errors [Mughrabi; 1983, Kubin; 1993], it has shown the potential of statistical fluctuations in dislocation density to account for cell formation.

In their stage IV work hardening model, Argon and Haasen [1993] noted that, although the average dislocation flux should be continuous due to compatibility requirements, random local fluctuations will result in a gradual monotonic increase of lattice disorientation between cells with increasing shear strain.

A mathematical model for obtaining the average disorientation over cell walls and cell block walls has been proposed by Pantleon [1998, 2001]. A difference of the dislocation flux coming from one side of a wall with the flux of dislocations with opposite sign coming from the other side, results in an increase of the disorientation over the boundary. In case of GNBs, an imbalance of slip system activity at both sides of the boundaries results in an additional increase of disorientation,

$$\frac{d\theta}{dt} = Pb\Delta j + b\Delta\Gamma j \tag{2.21}$$

with θ the disorientation angle, P the immobilization probability, b the length of the Burgers vector, Δj the difference in the dislocation fluxes, $\Delta\Gamma$ the imbalance parameter for slip system activity at GNBs and j the total dislocation flux. The first term reflects the increase due to the difference in the dislocation flux, while the second term only applies to GNBs. If a Gaussian white noise in the bias of the dislocation fluxes Δj and for GNBS a Gaussian distribution with vanishing mean and standard deviation σ_{imb} for the imbalance parameter $\Delta\Gamma$ is assumed, a Gaussian distribution for the disorientation angle distribution is obtained with average $\langle\theta\rangle = 0$ and mean square

$$\langle\theta^2\rangle = \frac{Pb}{d^*}\gamma + \sigma_{imb}^2\gamma^2, \tag{2.22}$$

with d^* a disorientation correlation length along the boundaries [Pantleon; 2004]. In case of two equally active slip systems with perpendicular rotation axes the combined Gaussian distributions for θ result in the experimentally observed Rayleigh distribution (cf. fig. 2-9) with mean:

$$\bar{\theta} = \sqrt{\pi/2}\sqrt{\langle\theta^2\rangle}. \tag{2.23}$$

For IDBs the evolution of $\bar{\theta}$ results in a square root dependence with strain, while for GNBs a more complex evolution is obtained:

$$\bar{\theta} = \sqrt{\frac{\pi}{2}}\sqrt{\frac{Pb}{d^*}\gamma + \sigma_{imb}^2\gamma^2}. \tag{2.24}$$

The obtained equations describe well the observed dependences of disorientation with strain discussed in section 2.2.1.b (fig. 2-8). However, no information on the cell and cell block sizes can be obtained in this way.

Hähner and Zaiser [Hähner and Zaiser; 1999, Hähner; 2002] have proposed a model, based on statistical dislocation density fluctuations in symmetrical double slip with separate evolution equations for the mobile and stored dislocation densities. A standard Gaussian white noise introduced in the local mobile dislocation fluxes leads to a steady-state solution for the distribution spectrum of the total dislocation density of the following form:

$$p_s\left(\rho\right)=\mathcal{N}\rho^{-0.5\left(1-4/\sigma^2\right)}\exp\left(-\frac{4}{\sigma^2}\sqrt{\rho}\right), \tag{2.25}$$

with σ^2 the noise intensity and $\mathcal{N}$ a normalisation factor. A plot of the obtained normalised probability distribution functions for different values of the noise intensity σ^2 is shown in fig. 2-10. A peak intensity at unity means that the total dislocation density is uniformly distributed over the sample, while a high probability for ρ equal to zero, means that a large fraction of the material volume has a negligible amount of dislocations, corresponding with the cells, while a considerable part of the remaining fraction should have a dislocation density higher than the volume average, corresponding to the cell walls. If σ^2 is larger than 4, equation (2.25) becomes hyperbolic, resulting in a high stability for dislocation patterning into cells and cell walls. In the formulation of their model, Hähner and Zaiser link the noise intensity σ^2 to the strain rate sensitivity of the flow stress, where a low strain rate sensitivity (or a high stress sensitivity of the strain rate) acts as a driving force for cell formation. The value of σ^2 is also increased by allowing for easy dynamic recovery, which is in agreement with experimental observations that cell formation starts at stage III, where dynamic recovery becomes fully effective. Hähner [2002] therefore attributes the patterning to a high level of local strain-rate fluctuations enabling the system to probe new dislocation configurations, while recovery contributes to the structural stabilization of the patterns.

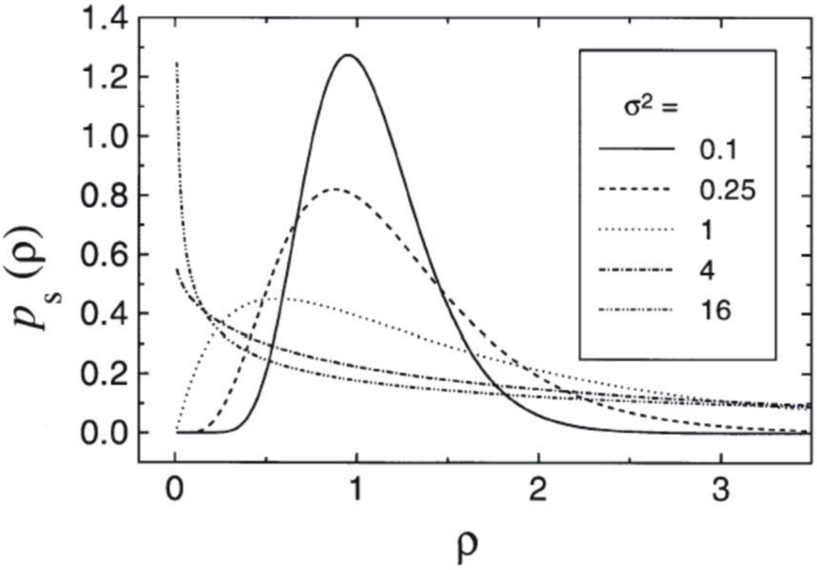

Fig. 2-10: Probability distribution function of the dislocation density obtained in the stochastic model of Hähner and Zaiser (cf. equation (2.25)). From a noise intensity σ^2 larger than 4, dislocation free regions (cells) are becoming stable as seen from the hyperbolic dislocation density spectra. From [Hähner and Zaiser; 1999].

The obtained probability distribution function of the dislocation density can be correlated to a cell size distribution. Out of the modelling framework, a fractal distribution of the cell size is obtained, governed by the minimum cell size $\lambda_{\min}$ and the fractal dimension $D = 1 + 4/\sigma^2$:

$$p_s(\lambda) = D\lambda_{\min}^{D}\lambda^{-(D+1)} \quad \text{for} \quad \lambda > \lambda_{\min} . \tag{2.26}$$

The model description has been found to be in good agreement with TEM observations on copper and copper-manganese single crystals deformed in tension [Zaiser and Hähner; 1999].

c) Dislocation dynamics simulations

Dislocation dynamics simulations study the interactions and group behaviour of large numbers of dislocations by calculating the stress field composed of the local internal stress due to the presence of the individual dislocations and the external stress arising from boundary conditions. The Peach-Köhler force acting on every individual dislocation is calculated and relations between effective stresses and dislocation velocities are defined for dislocation glide, cross-slip and climb. The formation of reaction junctions by the intersection of two dislocations of different Burgers vector is modelled as well. These simulations enable to model complex dislocation interactions and group behaviour from the basic mechanics of individual dislocations, which have been well established since the 1950s, but have a high computational cost. All local dislocation interactions like immobilization, mutual trapping, annihilation, and for 3D simulations also cross slip and multiplication, arise as natural consequences of the simulation set-up.

Kubin [1993] reviews the results of some early 2D dislocation dynamics models, which can already predict slip propagation due to cross slip and the onset of dislocation patterning. The early 2D dislocation models are however limited since dislocation multiplication and junction formation has to be accounted for by artificial criteria. Also the screw or edge character of the involved dislocations has to be imposed. Cross slip therefore is only achievable in simulations with screw dislocations. The glide geometry of crystal lattices only enables specific orientations under specific loading conditions to be simulated in 2D. One other main drawback of 2D simulations is the absence of bow-out stresses and line tension characteristic for the dislocation line configuration. 3D dislocation dynamics can take all this into account, but are computationally extremely demanding and therefore limited in material volume and achievable strain [Madec et al.; 2002a]. A new approach is to extend the 2D models by artificially including line tension, junction formation and dissolution and dislocation multiplication based on insights of the 3D models [Benzerga et al.; 2004, Gómez García et al.; 2006].

The advantage of dislocation dynamics is that some characteristics of dislocations like e.g. the possibility to cross slip or the activation of multiple slip systems can be included or excluded in the modelling framework, in order to study the relative importance of different mechanisms for pattern formation and work hardening. Important observations made in these works, include the following:

1. Including only short range interactions is sufficient to obtain dislocation patterns [Madec et al.; 2002a, Gómez García et al.; 2006], disapproving the idea of energy minimisation due to self screening of long range stresses advocated by the LEDS principle [Kuhlmann-Wilsdorf; 1992].

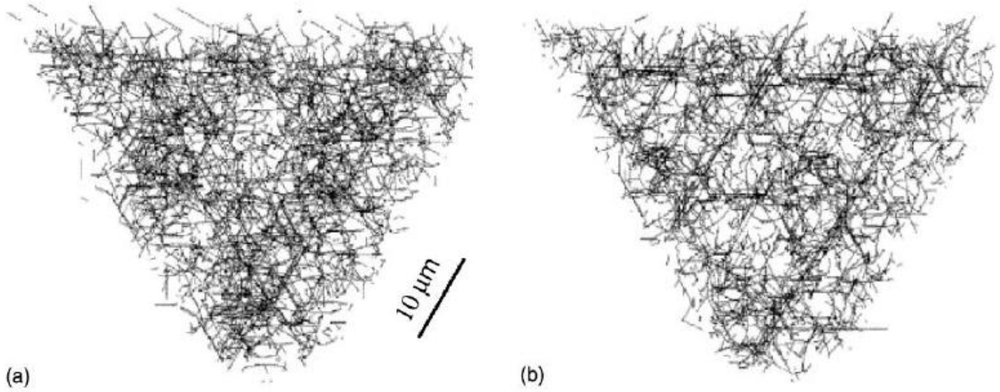

Fig. 2-11 : 2D slice of a 3D dislocation dynamics simulation of a FCC single crystal under uniaxial tension to a strain of 0.002. A cellular substructure forms even if cross slip is deactivated (a). The cell structure has however much sharper cell walls if cross slip is made possible (b). From [Madec et al.; 2002a].

2. Cross slip strongly favours the emergence of clean cellular substructures [Madec et al.; 2002a], approving the stabilization of dislocation patterns via dynamic recovery (cf. fig. 2-11).
3. Reaction junctions are mainly situated in cell walls [Kubin; 1993] and can be eliminated under certain stress conditions [Shenoy et al.; 2000] as well as by thermal assistance [Argon; 2002].
4. The Taylor equation for the flow stress (equation (2.8)) generally applies irrespective of the formed substructure [Madec et al.; 2002a, 2002b].
5. Activity on a slip system results in a very high hardening of the collinear slip system, to the extent that collinear systems are unlikely to be simultaneously active [Madec et al.; 2003].

Apart from the computational cost, another drawback of all dislocation dynamics simulations at their current state is that no lattice rotations are taken into account. Disorientations over cell walls can therefore only be estimated from the excess dislocation content of the walls, which has only been done by Benzerga et al. [2004], resulting in average disorientations in agreement with experimental data. Unfortunately no cross slip is taken into account in this work, resulting in dislocation patterns unlike any of the other works.

d) Substructure formation due to the instability of homogeneous plastic deformation

Sedláček and co-workers [2001] proposed an alternative approach to substructure formation, by performing a bifurcation analysis of the homogeneous deformation field.

A continuum mechanics description of a single crystal deforming under plane strain compression is used. Fcc lattices oriented for symmetric double slip are considered allowing for two slip systems to become active. The material reorientation due to dislocation slip is also taken into account. In their formulation a continuous stream function describes the velocity field and rate independent constitutive equations are used, taking anisotropic work hardening into account. In this formulation both strain compatibility and stress equilibrium are guaranteed. The stream function is disturbed with a planar wave function with an infinitesimal amplitude. An analysis of the stability of the bifurcation is performed on the general formulation of the continuum mechanics model, resulting in conditions for the modelling parameters to make the bifurcation stable. If slip geometry and material reorientation both are taken into account, an instability of the homogeneous deformation field is obtained if latent hardening is stronger than self hardening. The predicted type of instability is internal buckling which results in GNB structures resembling cell wall structures. A qualitative reasoning for the occurrence of an instability due to high latent hardening is that a small disturbance of the deformation field can result in a higher activity on one of both slip systems, making the most active slip system more favourable. Due to the wave form of the bifurcation function this instability will periodically reoccur, alternated by regions where the other slip system is more favourable. Disorientations over GNBs arise as a consequence of this instability.

In a follow-up paper by Kratochvíl et al. [2007], a statistical mechanics description of the collective behaviour of dislocation has been incorporated in this continuum mechanics framework, enabling to predict the wave vector controlling the bifurcation function and introducing a length scale into the model so that in principle average cell sizes and cell wall disorientations could be calculated.

2.2.3 *Internal stress state, work hardening and anisotropy of dislocation substructures*

The previous models for substructure formation allow to derive some consequences for the internal stress state, the work hardening and the anisotropy.

One of the main questions is whether long range stresses influence the shear resistance and if so, how these long range stresses can arise. This question is not answered consistently by the above models and is still a subject of debate.

a) Internal stress state

In the percolation model of Kocks [Kocks and Mecking; 2003], an internal stress field arises from the fact that the hard zones are not sheared (encircled by stabilized concave loops) and therefore have a high forward internal stress, which has to be compensated by a back stress in the cell interiors[13]. This back stress is lower because of the larger volume fraction of cells in respect to cell walls. A polarisation of the microstructure is another consequence, since dislocations of positive sign are stored at one side of the hard zones and the dislocations of negative sign at the opposite side [Kocks et al.; 1980]. Nevertheless Kocks and Mecking expect that this internal long range stress field is of very little importance for work hardening and consequently they estimate the relative contribution to the shear resistance of the cell walls and the cells (first term and second term in equation (2.28)) to be equal throughout the deformation.

Mughrabi [1983, 1987] comes to a similar internal stress field due to patterning, based on different grounds. The internal stress and strain field of an existing cell structure is analysed, taking also the elastic strains into account. For the reason of strain compatibility at the interfaces between cells and cell walls it is required that

$$\gamma_{el,w} + \gamma_{pl,w} = \gamma_{el,c} + \gamma_{pl,c} . \tag{2.27}$$

Due to the high dislocation density of the cell walls, the flow stress is much higher in the walls, resulting in higher elastic stresses and strains in the walls than in the cells. The plastic strain mismatch must be accommodated by glide dislocations at the interface, while the elastic stress mismatch attributes to an internal stress field similar to that of Kocks, with forward stresses in the cell walls and back stresses in the cell interiors. The main difference with the model of Kocks is that the walls should deform plastically, leading to the well known composite model of deforming cell structures:

$$\tau = f\tau_w + (1-f)\tau_c = f\alpha_w Gb\sqrt{\rho_w} + (1-f)\alpha_c Gb\sqrt{\rho_c} , \tag{2.28}$$

---

[13] Forward stress and back stress refer to internal residual stresses which are respectively in the same and in the opposite direction as the imposed stress.

with f the volume fraction of cell walls. This equation has been experimentally substantiated by peak profile analyses of X-ray diffraction (XRD) measurements on copper crystals, revealing that the largest contribution to the flow stress stems from the cell interiors ($(1-f)\tau_c / f\tau_w > 1$), which leads to the conclusion that the long range stresses do influence the shear resistance.

Zaiser and Hähner [1999] obtain very similar internal stress fields in their stochastic model based on dislocation density fluctuations, while they do not need to explicitly make a difference between cell walls and cell interiors. If they however define cell interiors as dislocation free regions, as observed in TEM work, the contribution to the slip resistance in these regions can only come from bow out stresses that act on individual dislocations. For the cell walls still a forest mechanism is considered. Their analysis leads to an alternative formulation for equation (2.28):

$$\tau = f\tau_w + (1-f)\tau_c = f\tau_w + (1-f)\frac{2-D}{D-1}\frac{f}{(1-f)}\tau_w = \frac{f}{D-1}\tau_w, \qquad (2.29)$$

with f the volume fraction of walls and D the fractal dimension as defined in section 2.2.2.b. Since τ_c in this model is a function of the cell size, it can be expressed as a function of f, τ_w and D, taking the fractal cell size distribution of equation (2.26) into account. Since in this model f is increasing with further strain, the relative importance of the contribution of the cell walls becomes larger. This approach is in accordance with the conclusions of Mughrabi and resolves the problem of the assumed forest hardening in the cell interiors of equation (2.28), which is questionable in the light of the TEM measurements presented in section 2.2.1.

Dislocation dynamics simulations [Madec et al.; 2002a] support the finding of Mughrabi that a long range stress field does exist in a dislocation cell structure. However, it turns out of 3D dislocation dynamics simulations that this long range stress field does not play an important role in cell patterning and work hardening (at least not in the initial stages of cell formation). This was concluded from a comparison of the substructure and the work hardening curve obtained from simulations including long range stress fields with those of simulations with a limited spatial stress field for each individual dislocation line segment. Cell structures obtained with the two methods turn out to have the same appearance while the stress strain curves differ only slightly.

b) Stage IV work hardening

Many stage IV work hardening models are based on Mughrabi's composite model (equation (2.28)), where an extra mechanism accounts for the persisting low work hardening rate after stage III when dislocation storage and dynamic recovery are in equilibrium (cf. equation (2.10)). Two examples of such mechanisms are: an imposed decrease of f, resulting in a small but persistent hardening contribution of the cell interiors [Estrin et al.; 1998] and the hardening due to continuous creation of new cell boundaries (keeping f constant), while the disorientation over cell boundaries and the cell dislocation density are saturated [Nes; 1998]. The main problem with these models as well as with the model of Mughrabi is that the dislocation density in the cell interior is much larger than those observed experimentally in TEM investigations.

Argon and Haasen [1993] were the first to attribute the hardening of the cell

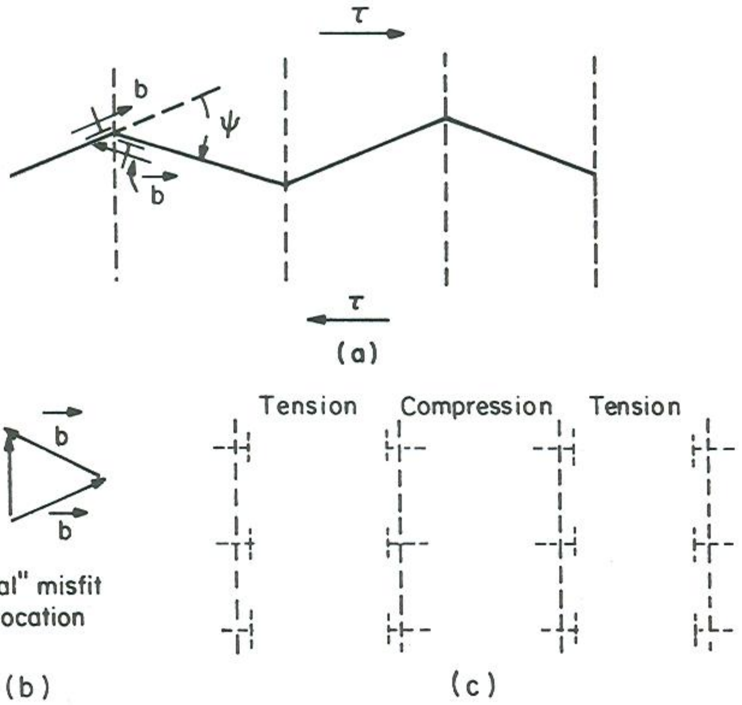

Fig. 2-12 : Long range stress field due to interaction of dislocations with cell wall having a disorientation. (a) Interaction of two dislocations of glide planes misoriented with angle ψ . (b) Virtual misfit dislocation as reaction product of the Burgers vectors. (c) The sum of the stress fields of the misfit dislocations results in a long range stress field.

interiors to the increasing disorientation of the cell boundaries, which results in an additional long range stress field on top of the long range stress field of the cell structure as described by Mughrabi. This can be imagined by an array of sessile misfit dislocations which are left behind if dislocations of opposite sign are stored at the two sides of a cell wall with a certain disorientation (cf. fig. 2-12). The stress field of these misfit dislocations will attribute to an increased slip resistance in the cell interiors, which according to Argon and Haasen has been falsely interpreted as due to a dislocation density in the cell interiors which has never been observed. In their model stage IV hardening is also predicted, since the hardening of the cell interior continues even if dislocation storage and recovery are in equilibrium at the cell walls.

It should be noted that the long range stress field due to the disorientations over cell walls as advocated by Argon and Haasen is different in nature from the previously discussed long range stress field due to composite nature of a cellular structure. In the initial stages just after cell formation, when disorientations are small, the overall long range stress field will stem from the composite nature, while with increasing strain the long range stress field will be increasingly influenced by the disorientations in the substructure. Since dislocation dynamics in their current state do not take disorientations into account, this kind of simulations therefore disregards their influence on the long range stress field.

Pantleon [2004] derived a different dependence of work hardening on the cell boundary disorientation. From his analysis, it follows that the disorientation due to statistical differences in the dislocation flux (first term of equation (2.22)) contributes to type III work hardening, while the disorientation due to differences in the shear rates, causes a mechanism which dominates in stage IV hardening. Stage IV hardening is therefore caused by the local imbalance of dislocation slip associated with GNB structures (resulting in the second term of equation (2.22)).

c) Anisotropy

The influence of the substructure formation on the flow stress anisotropy has not (yet) been considered in publications on models for substructure formation, although the internal stress state due to dislocation pattern formation is regarded as an important aspect for the flow stress anisotropy in the literature on strain path changes (cf. paragraphs 2.3 and 2.4). One exception is the reversal of the applied stress. Both Kocks and Mecking [2003] and Mughrabi [1983] motivate their models for the internal stress state by the observation of the Bauschinger effect. The lower yield stress in the opposite direction as compared to the flow stress obtained in the prestrain is explained by the assistance of the back stress exerted by the dislocation ensembles stored at the cell walls on the dislocations in the cell interiors. For other changes of the strain path Juul Jensen and Hansen [1990] studied the different possible causes of the flow stress anisotropy in cold rolled aluminium. They concluded that texture and latent hardening due to slip system interactions alone could not explain the degree of anisotropy experimentally observed. Their suggestion to take the anisotropy due to elongated GNBs into account has been developed further by Winther [Winther et al.; 1997, Winther; 2005]. A much better prediction of the anisotropy of the flow stress could be obtained if the critical resolved shear stress of a slip system is modelled with a Hall-Petch relation governed by the average distance between the GNBs on the slip plane. More advanced models for flow stress anisotropy including a substructural contribution have been developed in the framework of strain path change models and will be discussed in paragraph 2.4.

2.2.4 Conclusions

The formation mechanisms of the substructure and its influence on the anisotropy still remain unclear, despite extensive characterisation and modelling efforts. Certainly the lack of in-situ bulk characterisation methods with sufficient resolution to provide direct observations of the phenomenon has made it difficult to assess the presented possible explanations.

In a recent paper, Jakobsen et al. [2006] however have presented such a method with results on the tensile deformation on copper up to a strain of 4.2%. The technique uses diffraction of high energy synchrotron radiation measured on both a near and far field detector. With this technique the formation and dynamics of the cell structure at low deformation can be directly observed. The main observations are that dislocation cells emerge and disappear in and out of a background of dislocations and that the observed cells are always free of dislocations. The observation that the cell structure is constantly completely renewed and does not evolve in a progressive way, is a completely new insight which is not reflected in the theories and models which have been developed up till now. The stochastic nature of the cell structure is only captured by the model of Zaiser and Hähner [1999]. The observation of dislocation free cells contradicts the composite theory as proposed by Mughrabi [1983] and all work hardening models derived from it that require forest dislocations inside of cells. Whether these observations still occur at larger deformations and in other metals is not demonstrated, yet it is known that the same hardening mechanisms are active [Gil

Sevillano; 1993]. What the effect on the dynamics of GNB structures is, has however not yet been directly observed in-situ.

The main conclusions for work hardening of the presented overview are:

1. All observations and modelling efforts support the validity of the Taylor equation for the flow stress (equation (2.8)).
2. Disorientations over cell walls and GNBs will contribute to work hardening resulting in stage IV behaviour. A long range stress field exists due to disorientations over the dislocation boundaries (fig. 2-12). The studies with dislocation dynamics that do not find an effect of long range stresses, also do not account for orientation differences.
3. The cells are nearly free of dislocations and do not directly contribute to work hardening.
4. The storage of dislocations in a substructure goes along with polarisation. Dislocations of opposite sign are stored at both sides of the dislocation walls.

The influence of the substructure on anisotropy is the topic of the next paragraph on strain path changes.

2.3 Substructure during strain path changes

A direct way to evaluate how the anisotropy of the flow stress evolves during straining of a material, is by interrupting a series of tests with the same straining mode at different amounts of prestrain and subsequently testing the prestrained samples in a second straining mode. This is equivalent to performing the same strain path change test at different levels of prestrain (cf. section 1.3). The ratio of the reyielding stress of the new straining mode to the flow stress at the end of the prestrain gives a valuation of the anisotropy[14] of the flow stress at the end of the prestraining in the direction of the second straining mode.

The obtained macroscopic anisotropy ratio during SPC tests contains both textural and substructural contributions to the anisotropy. To analyse the substructural

---

[14] It should be noted that most SPC tests require unloading the material, while this unloading does not necessarily happen in industrial processes where SPC occur (e.g. deep drawing). Although in principle, both types of anisotropy can be different due to microplastic effects during unloading and reloading, this difference is however likely to be small.

contribution to the flow stress, the textural contribution needs to be removed first. According to equation (A.13) the macroscopic anisotropy ratio becomes:

$$\frac{\overline{\sigma_2}}{\overline{\sigma_1}} = \frac{\overline{M_2 \tau_2}}{\overline{M_1 \tau_1}} = \frac{\overline{M_2}}{\overline{M_1}} \frac{\tilde{\tau}_2}{\tilde{\tau}_1}, \tag{2.30}$$

with $\tilde{\tau}$ the weighted average of the τ_{ref} of the individual grains with the *M*-factors as the weighting factors (cf. [Tomé et al.; 1984] and appendix A). Under the assumption that $\tilde{\tau}_{ref}\left(\overline{\Gamma}\right)$ is a good approximation of the average hardening curve of the individual grains, the anisotropy ratio can be split into the product of a textural anisotropy ratio $\overline{M_2}/\overline{M_1}$ and a substructural anisotropy ratio $\tilde{\tau}_2/\tilde{\tau}_1$. Both the textural anisotropy ratio and the overall anisotropy ratio depend on the strain rate equivalent chosen to define the *M*-factor of each straining mode (cf. equation (A.1)). In order to find the relative importance of textural anisotropy and the substructural anisotropy it would be appropriate to use the same strain rate equivalent for both straining modes (e.g. the von Mises equivalent $\dot{\varepsilon}_{vm}$), although this might require the use of equivalent stress values which are not directly measured. It has to be noted that the use of a certain equivalent strain rate results in a somewhat different overall anisotropy ratio than if a certain equivalent definition is used for both measured stresses. The average *M*-factors of equation (2.30) can only be obtained by a crystal plasticity model (cf. section 2.1.2) using a measured texture of the material as the input, although many researchers often assume an approximate value.

For the characterisation of the strain path changes, three extreme cases can be distinguished, being reloading in the same straining mode, reverse loading and cross loading (cf. section 1.3). The three cases correspond to a Schmitt-parameter $\cos\theta$ (equation (1.2)) of 1, -1 and 0 respectively. On the micro scale level this translates into the reactivation of the same slip systems in the same direction or in the opposite direction for the same and the reverse straining mode respectively and in the activation of a completely different set of slip systems for cross loading [Schmitt et al.; 1985]. It is generally assumed that all other strain path changes will show a mixture of these extreme cases.

The interaction of dislocations of the active slip systems after the SPC with the existing substructure built up during the prestrain will reveal the substructural contribution to the anisotropy. Through the transient behaviour (cf. supra) these interactions will also have an effect on the subsequent evolution of both the substructural and textural anisotropy. Therefore not only the reyielding stress (determining the anisotropy of the substructure of the prestrain) will be discussed, but also the subsequent hardening after the SPC.

In this paragraph, first the observed mechanical transient behaviour during strain path changes will be discussed as well as its dependence on several material and processing parameters. Then the findings regarding the corresponding substructural evolution during a change of strain path will be described. Finally the possible mechanisms explaining the transient behaviour are discussed and some remaining unsettled questions are addressed.

2.3.1 Mechanical behaviour after strain path changes

After an abrupt SPC, work hardening can evolve very differently compared to the monotonic straining case (fig. 2-3 (b)). Usually the hardening behaviour will return to the monotonic behaviour after a certain amount of straining. The initial part where the work hardening behaviour is different is called the work hardening transient. Since the microstructural mechanisms that enable plastic deformation and cause work hardening are governed by the acting local stress on the level of the individual grains (cf. section 1.2), the end of the transient (return to monotonic work hardening) can only be obtained from the microscopic work hardening curve (θ versus τ), where the effects of crystallographic texture are eliminated. If there is a return to monotonic behaviour, then the microscopic work hardening curve has to coincide with the curve of a monotonic deformation test. Unfortunately most works on SPC tests do not include the conversion from the obtained macroscopic stress strain curve to the microscopic hardening curve. To make a clear distinction, within this section σ and ε are referring to the macroscopic stress and strain (including other anisotropy contributions like e.g. texture), while τ and γ are representing the microscopic counterparts.

a) Work hardening transients

For $\cos\theta = 1$, tension tests on commercially pure (CP) aluminium which are interrupted and continued after unloading and reloading of the sample show that the same work hardening behaviour is observed as in a monotonic test without interruption after a very short transient behaviour with a somewhat lower yield stress and a higher initial work hardening rate [Barlat et al.; 2003].

For Bauschinger tests ($\cos\theta = -1$) a wide transient, both in stress and strain, is observed [e.g. Hasegawa and Yakou; 1980, Rauch and Schmitt; 1989, Hu et al.; 1992]. Fig. 2-13 shows a schematic representation of the stress-accumulated strain curve and the corresponding hardening rate-stress curve of a Bauschinger test compared to a monotonic test. The yield stress τ_y after strain reversal is lower than the flow stress at the end of prestraining τ_{pre}. This stress asymmetry during path reversal is known as the Bauschinger[15] effect. The subsequent hardening behaviour shows a high initial hardening rate which rapidly decreases below the hardening rate θ_{tb} corresponding to the same stress in a monotonic test. After some strain the hardening rate reaches a minimum which corresponds to a first inflexion point at (γ_1, τ_1) in the stress strain curve. The hardening rate increases again towards a second inflexion point at (γ_2, τ_2) and returns then to the monotonic hardening behaviour at (γ_3, τ_3). From this point on the hardening curve θ-τ is generally assumed to equal the monotonic hardening curve. This corresponds to a parallel τ-γ curve, which can be obtained by translating the

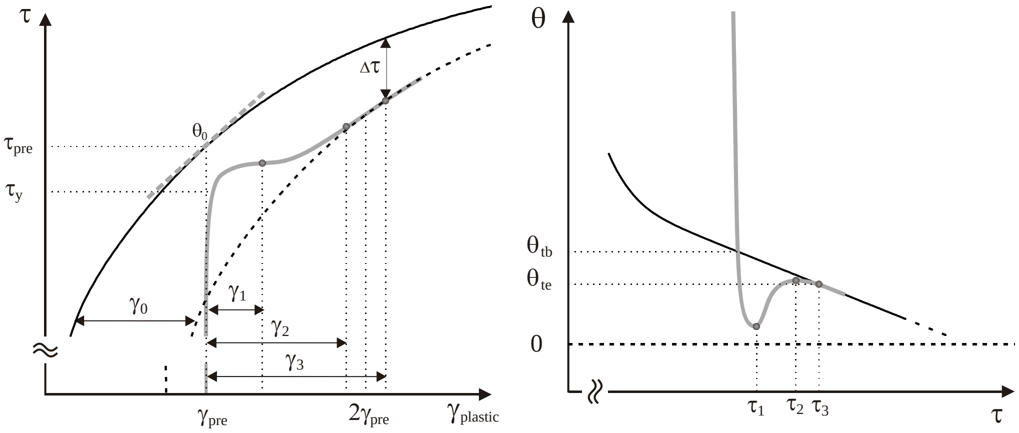

(a) **(b)**

Fig. 2-13 : Schematic representation of transient work hardening behaviour during a Bauschinger test (grey) compared to monotonic hardening curve (black). (a) Stress-accumulated strain curve. (b) Corresponding hardening rate-stress curve.

---

[15] Named after the German scientist Johann Bauschinger (1834-1893) who studied the effect in construction steels.

monotonic curve by a strain of γ_0 (as indicated by the dashed line in fig. 2-13). If the hardening rate θ after yielding drops to 0, an extended plateau of work hardening stagnation over a strain interval is regularly observed instead of a single inflexion point [Hasegawa and Yakou; 1974]. In some cases work softening is reported [Strauven and Aernoudt; 1987, Barlat et al.; 2003]. Not all authors observe this return to the monotonic hardening behaviour [e.g. Zandrahimi et al.; 1989, Li and Bate; 1991], but it should be noted that these works do not attempt to separate textural effects by evaluating the macroscopic σ-ε curve in stead of a microscopic τ-γ curve and in most cases have a limited strain interval of homogeneous deformation after the SPC, due to the use of uniaxial tension as the second deformation mode.

The transient behaviour during cross tests ($\cos\theta = 0$) is very similar to that of Bauschinger tests. The two main differences are that the yield stress τ_y is generally larger than the prestrain flow stress τ_{pre} and that after sufficient prestraining, work softening is commonly observed [e.g. Wagoner and Laukonis; 1983, Rauch and Schmitt; 1989]. Fig. 2-14 illustrates the typical behaviour compared to the monotonic hardening curve of the second straining mode. Also in this case two inflexion points and a point of return to the monotonic behaviour can in principle be defined. In practice the second inflexion point is often very close to the monotonic curve and in case of work softening the first inflexion point occurs immediately after yielding, making γ_3 the only relevant parameter to

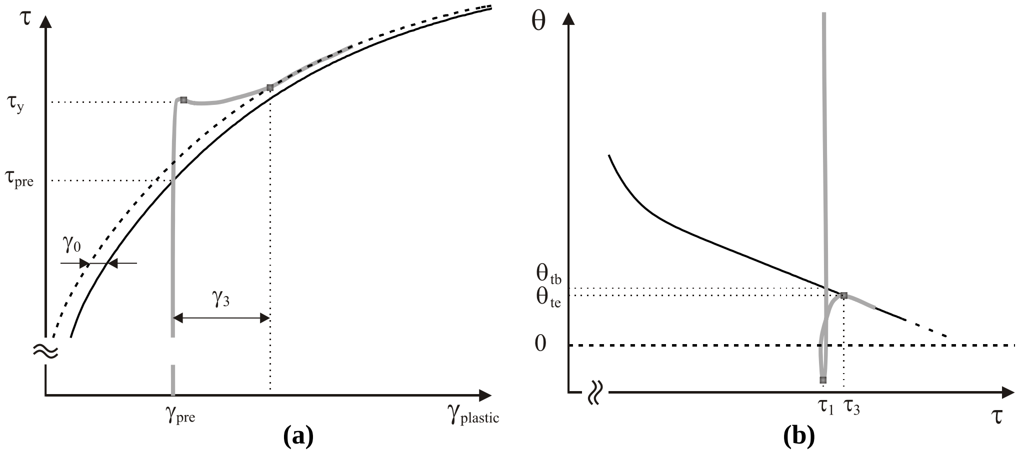

Fig. 2-14 : Schematic representation of transient work hardening behaviour during a cross test (grey) compared to monotonic hardening curve (black). (a) Stress-accumulated strain curve. (b) Corresponding hardening rate-stress curve.

characterise the transient. In this case the return to the monotonic behaviour can also be presented by a shift of the reference curve along the γ-axis. In fig. 2-14 this curve is presented by a dashed line. The displacement γ_0 can be either positive or negative.

The above presented parameters to characterise the transient work hardening behaviour during SPC tests, are merely one way to describe the hardening evolution. A variety of parameter sets are used by different authors and these are usually impossible to interrelate. Some differently defined parameters often bear the same name as well as implied physical meaning. Many reports e.g. discuss the amount of permanent hardening/softening $\Delta\tau$ as the difference between the stresses of the monotonic stress strain curve and the one after the SPC transient, but for the amount of strain used to define $\Delta\tau$ different values are proposed. These include e.g. the strain where no residual back stresses are observed any more using XRD [Wilson; 1965, Bate et al.; 1982], the double amount of the prestrain [Yakou et al.; 1985] or the strain where the work hardening curve starts to coincide with the monotonic curve [Aernoudt et al., 1987]. This last definition seems the most appropriate regarding the underlying microstructural hardening processes. The corresponding difference in accumulated strain γ_0 reflects the additional/deficient deformation that is imposed to obtain the same material strength.

Although qualitative conclusions are similar regardless of the chosen definition, the most diversely defined parameter is the yield stress at the SPC. This is problematic since it has to be used to distinguish between the relative contributions of different sources of anisotropy. Most reports use the classical 0.2% strain offset [e.g. Juul Jensen and Hansen; 1990] or a peak value if softening occurs [Wagoner and Laukonis; 1983], but it is argued that due to the much wider zone of micro plasticity, especially in case of strain reversal, a back extrapolated yield stress is more appropriate to use [Aernoudt et al., 1987, Rauch and Schmitt; 1989]. This back extrapolation is done either linearly [Raphanel et al.; 1986, Li and Bate; 1991], logarithmic [Laukonis and Ghosh; 1978] or parabolic [Bate et al.; 1982].

b) Influence of process and material parameters on the transient

The use of different parameters to characterise the work hardening transients during SPC makes it hard to compare results of different researchers on a quantitative level. The influence of process and/or specific material parameters on the work hardening transient can therefore only be obtained from dedicated studies on this subject and not by assembling all available results in a large matrix study. Due to the common use of the uniaxial tensile test as at least one of the involved straining modes, the strain intervals for which an analysis based on the assumption of homogenous and uniform straining can be applied are rather limited. The introduction of the simple shear test for this kind of research by Raphanel et al. [1987a], has overcome the problems of strain localisation due to necking, yet a systematic study over a large range of strains seems to be lacking. A lot of research has been published regarding Bauschinger tests and the transient behaviour after strain reversal. For other types of SPC the transient behaviour is rarely studied. Most literature on this subject limits itself to the yield stress at the SPC and the ultimate tensile strain if a uniaxial tension test is used as second strain mode.

In spite of these limitations the following summary of the conclusions in the literature regarding the hardening transient during SPC can be given:

1. Similar transient behaviour for different single phase cubic metals.
2. Initial stress difference $\left|\tau_{pre} - \tau_y\right|$ increases with increasing prestrain γ_{pre}.
3. Yield stress τ_y at SPC is a function of Schmitt parameter $\cos\theta$
4. Anisotropy due to texture is not sufficient to explain higher τ_y
5. Length of transient depends on temperature T, prestrain γ_{pre} and strain rate $\dot{\gamma}$
6. Coherent and semi-coherent precipitates increase Bauschinger effect but reduce cross effect.

All statements will be shortly discussed in the following paragraphs.

Wilson [1965] and Yakou et al. [1985] have compared the transient behaviour of different single phase cubic metals during Bauschinger tests. The characteristic behaviour of fig. 2-13 is a general phenomenon in pure fcc and bcc metals. Zandrahimi et al. [1989] found hardening transients during cross type SPC for a wide range of fcc and bcc single phase cubic metals. The most pronounced transients are observed in materials having a high SFE like low carbon steel and aluminium.

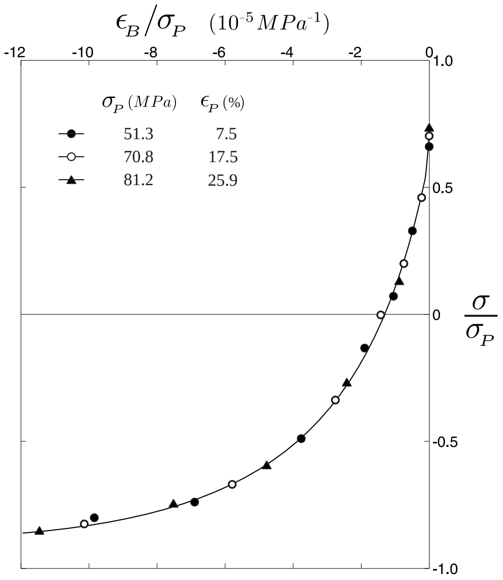

Fig. 2-15 : Normalised stress - normalised strain curves during strain reversal of three Bauschinger tests with different prestrains on aluminium with the prestress as normalising factor [Hasegawa et al.; 1986].

Much research has been dedicated to the influence of the prestrain ε_{pre} in Bauschinger tests. Hasegawa et al. [1986] conclude that the normalised stress – normalised strain curve is a unique curve for different prestrains if the prestrain stress σ_{pre} is used as the normalisation factor at least for the micro plasticity and yielding regime (fig. 2-15). This implies that the reyielding stress σ_y is related to σ_{pre} by a constant so that the stress difference $\sigma_{pre} - \sigma_y$ increases with σ_{pre} and therefore also with ε_{pre}. Based on data of different steels [Strauven and Aernoudt; 1987, Hu et al.; 1992] the same tendency turns out to hold for much higher prestrains.

Christodoulou et al. [1986] on copper and Hu et al. [1992] on mild steel, both performed an extensive analysis of their transient curves, showing that the length of the transient both in strain (defined by γ_3 in fig. 2-14) as well in stress (defined by $\tau_3 - \tau_y$ in fig. 2-14) first increases and then decreases with γ_{pre}, the maximum in stress occurring at a much lower γ_{pre} than the maximum in strain. The maximum of the difference in work hardening between the transient regime and

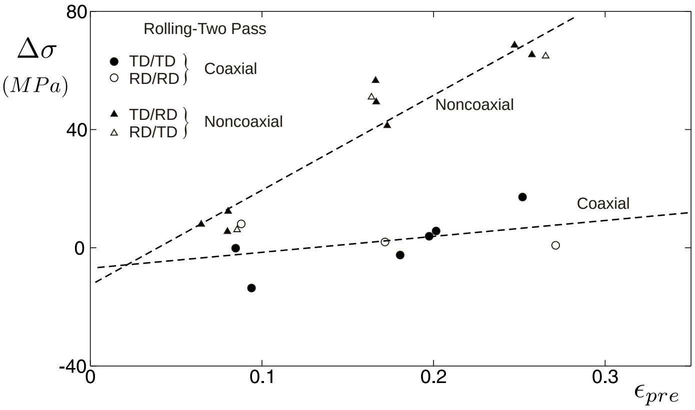

Fig. 2-16 : Influence of prestrain on stress difference after SPC, defined as $\tau_y - \tau_{pre}$ in fig. 2-14, for rolling followed by uniaxial tension for Al killed steel [Wagoner and Laukonis; 1983]. Two different types of SPC are achieved: rolling followed by tension along the rolling axes (coaxial, $\cos\theta \approx$ 0.86) and rolling followed by tension along the transverse axes (non-coaxial, $\cos\theta \approx$ 0). RD (rolling direction) and TD (transverse direction) denote the reference axes of the hot rolling step prior to annealing and cold rolling.

the monotonic reference curve also first increases and then decreases with increasing prestrain [Christodoulou et al.; 1986].

For other types of SPC it is not easy to find such extensive analyses of the transient regime. Mainly the increase of $\sigma_y - \sigma_{pre}$ with increasing ε_{pre} is reported [e.g. Lloyd and Sang; 1979, Rauch and Schmitt; 1989, Wilson and Bate; 1994]. Wagoner and Laukonis [1983] observed for aluminium killed steel a linear increase of this difference with ε_{pre} (fig. 2-16). Rauch and Schmitt [1989] report the length of the transient to equal at least three quarters of the prestrain. For very large prestrains initial flow localisation is observed during cross tests [Rauch and G'Sell; 1989].

The dependence of σ_y on the “abruptness” of the SPC has been characterised for low carbon steel by Raphanel and co-workers [1986, 1987a, 1987b, Schmitt et al.; 1994]. For prestraining in uniaxial tension, it was found that σ_y is related to the Schmitt parameter $\cos\theta$ regardless of the straining mode of the second strain path. Both uniaxial tension and simple shear into different directions have been used as second straining mode. Schmitt et al. [1994] have compiled all this data into a single plot (fig. 2-17). Zandrahimi et al. [1989] have observed a similar but

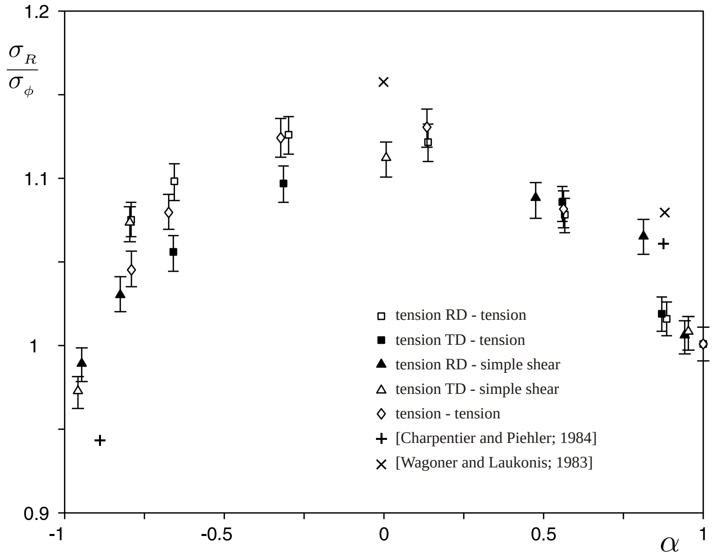

Fig. 2-17 : The ratio of the yield stress and the prestrain stress as a function of the Schmitt parameter at a prestrain of ε =0.14. Compilation of data on low carbon steel from different strain path combinations by Schmitt et al. [1994].

less pronounced dependence for CP aluminium, for low SFE fcc materials the dependence is however not clear.

The relative contribution of texture to the anisotropy can be estimated based on the Taylor factor calculation from the measured texture of the prestrained material (cf. section 2.1.2.a). For low carbon steels prestrained to $\varepsilon = 0.15$ Raphanel et al. [1986] estimate the textural contribution to be one third of the observed anisotropy. By increasing τ_{crss} of non-active slip systems in the prestrain straining mode with 10%, the correct dependence of σ_y / σ_{pre} on $\cos\theta$ can be obtained. Juul Jensen and Hansen [1990] and Li and Bate [1991] applied the same technique for SPC on aluminium concluding that texture effects and latent hardening due to dislocation forest cutting (cf. section 2.1.4) alone are not sufficient to explain the observed anisotropy and hardening transients. The formation of the substructure and its evolution during SPC therefore are likely to have a significant influence on the hardening anisotropy. Rauch et al. [1999, Lopes et al.; 1999] on the other hand found that although similar structural processes are occurring in low carbon steel and aluminium, strain softening can be explained by the textural evolution in the case of aluminium for an SPC with $\cos\theta = -0.5$ but not in the case of steel for an SPC with $\cos\theta = 0.5$.

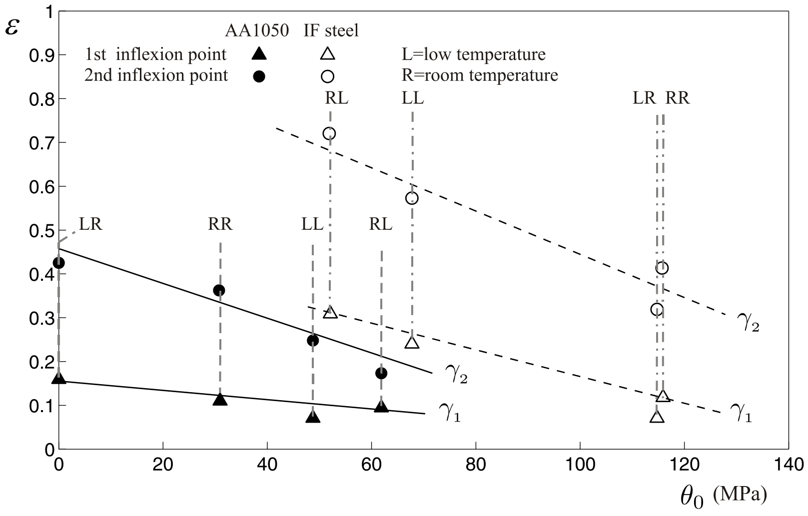

Fig. 2-18 : Influence of prestrain and second strain temperature on the transient work hardening behaviour of aluminium and IF steel [Vincze et al.; 2005]

The influence of temperature T on the transient of Bauschinger tests has been characterised for aluminium by Hasegawa and Yakou [1974]. The length of the plateau of the hardening stagnation first increases and then decreases with increasing deformation T. The maximum length increases with prestrain and occurs at a lower temperature as the amount of prestrain gets higher. Rauch [1997] and Vincze et al. [2005] studied the influence of the deformation temperature on the transient of both the deformation before and after strain reversal on IF steel and CP aluminium. As shown in fig. 2-18, regardless of the temperature, the strain to the inflexion points is correlated to the intrinsic hardening rate θ_0, which is the hardening rate that would occur if the deformation was continued instead of reversed at the same accumulated amount of shear strain (cf. fig. 2-14 (a)). For fcc metals this means that the length of the transient will increase with increasing temperature, while for bcc metals the length of the transient will decrease.

The length of the work hardening transient also increases with decreasing strain rate $\dot{\varepsilon}$ [Rauch and Thuillier; 1993]. The comparison of cross test results under quasi static and impact conditions for different materials enabled Hasebe et al. [1999] to deduce a clear dependence on SFE for fcc materials. For materials with a high SFE like aluminium there is a negative correlation between the length of the transient and the strain rate $\dot{\varepsilon}$. With decreasing SFE this correlation becomes less pronounced and for low SFE fcc materials like copper a positive correlation is observed. For bcc materials like steels, having a very high SFE, a strong negative correlation should be expected, but no strong correlation is observed [Hasebe; 2003]. This leads Hasebe to the conclusion that different mechanisms are controlling the transient work hardening effects in fcc and bcc materials.

Solute atoms and precipitates in commercially used alloys can have a large influence on the work hardening transient during SPC. Wilson [1965] analysed the influence of different types of precipitates on strain reversal both for various steels and aluminium alloys. The overall conclusion is that the permanent softening $\Delta\tau$ increases with the volume fraction of precipitates and the fineness of its dispersion. The shape of the precipitates and their structural correlation with the matrix have an influence as well. In addition to the results of Wilson, Bate et al. [1982] show that in semi-coherent precipitates with high aspect ratios, about 80% of the forward flow stress is related to the stress needed to overcome the back stress exerted by the elastically deformed precipitates on the matrix. A large back stress leads to a large Bauschinger effect during strain reversal. Rauch et al. [2002] on the other hand report the absence of the characteristic work hardening transient in a reverse test on an Al-Mg-Si alloy (AA6022-T4) which has a high solute content and small precipitates.

One of the earlier works on cross tests [Lloyd and Sang; 1979] reports a hardening transient in both CP aluminium (AA1100) and a Al-Mn alloy (AA3003), but the absence of the cross effect in a Al-Cu (AA2036) and a Al-Mg (AA5182) alloy. Wilson et al. [1990] and An [2001] compared the cross effect of respectively an Al-Cu-Mg alloy (AA2014) and an Al-Mg-Si-Mn alloy (AA6082) after different aging treatments, resulting in different precipitation configurations. The influence of the structural correlation of the precipitates with the matrix is most clear in the study by An. Four different aging treatments of AA6082 result in four different matrix-precipitate configurations. For non-coherent precipitates the work hardening transient has the same characteristics as depicted in fig. 2-14. If the alloying elements are in solid solution, a work hardening transient is still observed, but the drop of the work hardening rate below the monotonic curve is not as large and the transient occurs in a much wider strain interval. If only coherent precipitates are present, a higher yield stress is still observed, but the transient in the work hardening rate has vanished, while for semi-coherent precipitates the cross effect is absent.

All these effects will be linked to the evolution of the substructure during the strain path change in the next section in order to find out how the substructure has an influence on the work hardening anisotropy.

2.3.2 Substructural evolution during strain path changes

During the transient work hardening behaviour following an SPC, drastic changes in the dislocation substructure are observed. One of the current hot topics in work hardening research is whether these changes are causing the transient hardening or whether these changes are a mere manifestation of some more general phenomena which also cause the transient hardening behaviour in most metals [Rauch; 2005]. This discussion will be addressed in the next section. Here the observed changes during strain reversal and orthogonal strain path changes will be presented.

a) Strain reversal

The substructure evolution during the transient regime of work hardening after strain reversal in polycrystalline aluminium has been extensively studied by Hasegawa and co-workers using TEM [1975, 1986]. They discovered that the well developed cell structure typical for uniaxial tension (cf. section 2.2.1 and fig. 2-19 (a)) first partially dissolves during reverse straining via uniaxial compression and that with further reverse straining a new substructure similar to the one of the prestrain is rebuilt [Hasegawa et al.; 1975]. This finding has been confirmed for other metals and alloys that form a cellular substructure (e.g. copper [Christodoulou et al.; 1986], low carbon steel [Rauch and Schmitt; 1989], certain aluminium alloys [Dirras et al.; 1999]). Fig. 2-19 (c) shows the partially dissolved substructure after a pseudo-Bauschinger test ($\cos\theta = -0.7$) of which fig. 2-19 (a) can be considered as the substructure prior to the strain reversal. The comparison of fig. 2-19 (c) with fig. 2-19 (a) clearly illustrates the dissolution process. Hasegawa et al. [1975] also measured the average dislocation density of the TEM foils using the intersection method and found that the dislocation density drops during the dissolution of the cells (a decrease of about 16% in the early stage of reversed deformation) and increases again when the new substructure is built up, showing that the dissolution process is accompanied with dislocation annihilation.

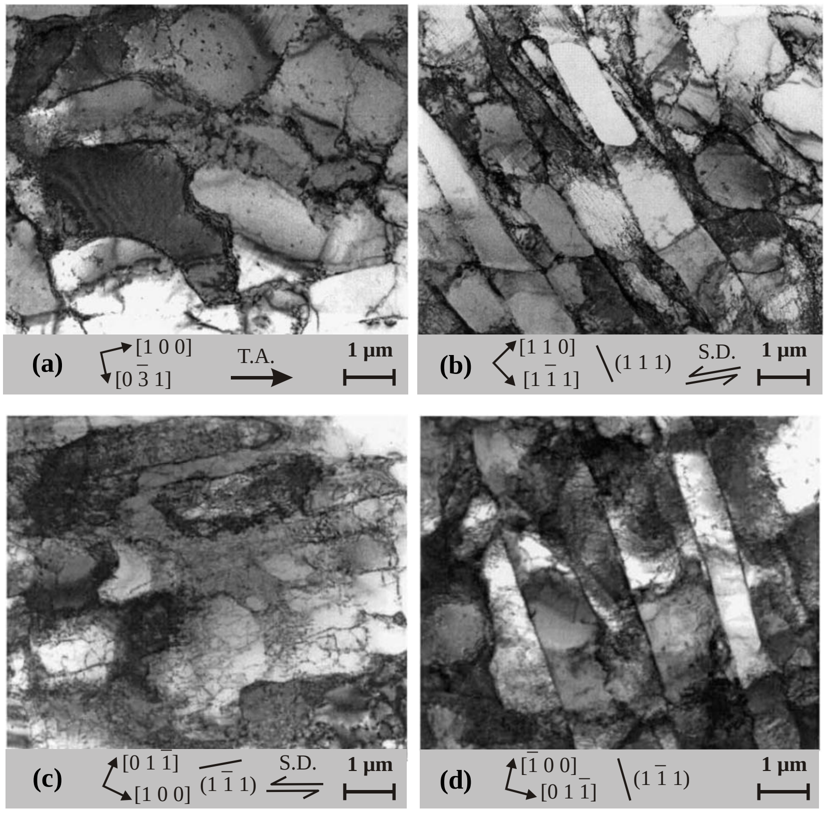

Fig. 2-19 : TEM images of typical dislocation structures developed during plastic deformation in AA1050 after strain paths including uniaxial tension and simple shear. T.A. denotes tensile axis and S.D. shear direction. (a) Uniaxial tension up to ε =0.14. (b) Simple shear up to ε_{eq} =0.15. (c) Pseudo Bauschinger test (cosθ= -0.85), uniaxial tension with ε =0.14, followed by simple shear with ε_{eq} =0.15. (d) Cross test (cosθ= 0), uniaxial tension with ε =0.14, followed by simple shear with ε_{eq} =0.15. From [Barlat et al.; 2003].

Alloys that do not show permanent softening or the transient hardening behaviour during strain reversal, like aluminium alloys with a relatively high content of Mg (> 5 wt%), also do not develop a cellular substructure [Hughes; 1993, Dirras; 1997, Rauch et al.; 2002]. Gaspérini and co-workers [2001] reported however some dissolution of microbands and dislocation walls during strain reversal in AA5182 in the recrystallised state. This dissolution is nevertheless not accompanied by permanent softening or a transient hardening regime. Another extraordinary result from the same paper is that a similar Bauschinger test on the

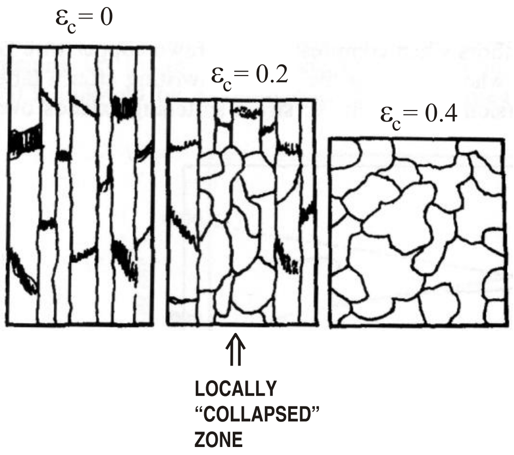

Fig. 2-20 : Schematic representation of substructure evolution during strain reversal of highly deformed ferritic steel. From [Strauven and Aernoudt; 1987].

H19 hardened state material (90% cold rolled, ε_{vm} =1.9) clearly shows permanent softening and transient hardening if the shear direction is parallel to the rolling direction. The corresponding microstructural observation also indicates dissolution of microbands and dislocation walls. If the shear direction is taken at 60° of the rolling direction no permanent softening or transient hardening is observed.

At very large prestrains in drawn steel wires, a completely different substructural evolution during strain reversal is observed [Strauven and Aernoudt; 1987]. The elongated subgrains of the prestrain are not transformed back into more equiaxed subgrains in a geometrical way. Regions of elongated cells successively collapse into regions of more equiaxed cells and so replace the elongated subgrain walls with a much more irregular wall structure (cf. fig. 2-20).

b) Orthogonal strain path change

During an orthogonal SPC the pre-existing substructure gets transformed into a different substructure which is characteristic for the new straining mode. This transformation can be accommodated in different ways.

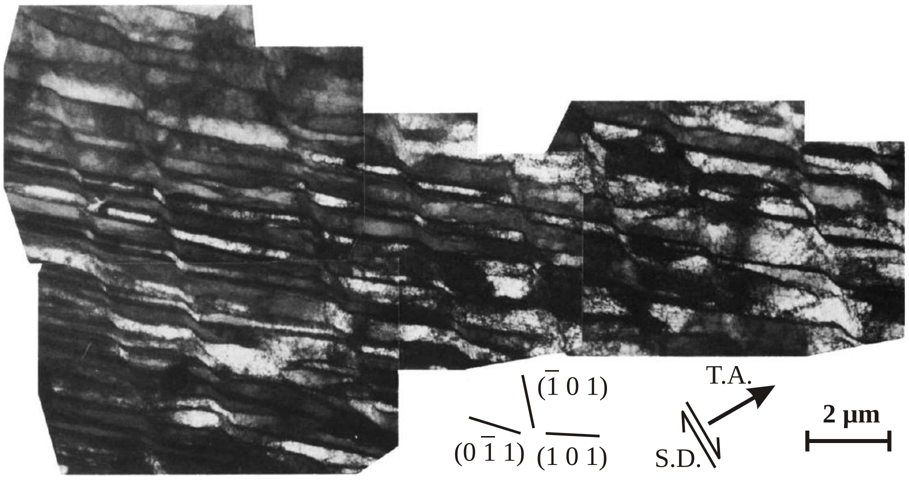

Fig. 2-21 : TEM image of the microstructure obtained at the stress minimum during a cross test on low carbon steel. Prestrain in uniaxial tension ε =0.20, successive strain in simple shear ε_{12} =0.12. From [Rauch and Thuillier; 1993].

Rauch and Schmitt [1989] analysed with TEM the substructure of mild steel predeformed in uniaxial tension and successively deformed in simple shear. They observed regularly spaced thin microbands parallel or normal to the shearing direction that cut through the pre-existing microband structure from the tensile deformation (fig. 2-21). With increasing strain the spacing between the new microbands becomes smaller and at strains higher than the prestrain they become severely curved. Analysis of the large displacement of the DDWs by this cutting process reveals that almost all deformation is accommodated by the microbands [Rauch and Thuillier; 1993, Nesterova et al.; 2001]. The appearance of these microbands does occur in 30% to 40% of all grains [Rauch and Schmitt; 1989] and is strongly dependent on the grain orientation [Nesterova et al.; 2001]. Wilson and Bate [1994] found evidence in IF steel that at some boundaries microbands existing in one grain trigger the creation of microbands in the neighbouring grain, which may continue throughout the whole grain or become diffused within a short distance from the boundary. However, in none of the discussed papers a description has been made of the substructure of the grains that do not form these microbands. The strain localisation on the meso scale level in microbands does not lead to strain localisation on the macroscopic level for moderately prestrained samples, despite of the macroscopically observed work softening. For high prestrains macroscopic strain localisation has been observed to occur in mild steels during shear tests [Rauch and G'Sell; 1989].

In AA3004 aluminium Gaspérini and co-workers [1996] have found two different types of substructural evolution during cross tests on two sets of samples having similar textures but different substructures. One set of samples was highly deformed (90% cold rolled, ε_{vm} =1.9), while the other set was cold rolled in the same way, but received a long annealing treatment. The substructure of the cold rolled sample contains densely spaced DDWs while the annealed sample contains equiaxed cells with sharp boundaries. During shearing, initially new DDWs form in both substructures, but only in the highly deformed cold rolled samples does this lead to the formation of localised microbands cutting through the existing substructure that accommodate all the strain. In the recovered samples the existing substructure gets gradually replaced by a substructure with many DDWs parallel or perpendicular to the shearing direction, typical for shear deformation. No strain localisation has been observed in these samples. In both cases there is a stagnation of the work hardening observed.

This gradual transition has also been observed by Barlat et al. [2003] during cross tests after moderate tensile prestrains up to ε = 0.14 (fig. 2-19 (d)). Mechanical tests show the transient work hardening behaviour as discussed in section 2.3.1.a.

From these results, it can be concluded that the substructural evolution during orthogonal strain path changes is somewhat different for steel (bcc) and aluminium (fcc). In steel, in-grain strain localisation via the formation of microbands takes place after any amount of prestrain, while in aluminium this behaviour is only observed after large prestrains. At lower prestrains a gradual transition to a new substructure is observed.

2.3.3 Proposed mechanisms during strain path changes

Based on the observed substructural evolution during strain path changes some possible mechanisms are proposed to explain the transient behaviour. In the next section a mathematical approach is presented from the modelling point of view.

First the possible mechanisms operating during a strain path reversal will be discussed and then the work hardening mechanisms during a cross type SPC are reviewed.

a) Strain reversal

As mentioned by e.g. Rauch et al. [2002], due to the two inflexion points (at γ_1 and γ_2 in fig. 2-13(a)), at least two competing physical mechanisms should be active during the work hardening transient after an SPC on top of the mechanisms that cause the monotonic work hardening. One of these should cause work softening, while the other one should lead to (extra) hardening. The relative importance of both will vary with increasing strain and leads to the characteristic behaviour in the work hardening curve as discussed in fig. 2-13. These mechanisms as such only influence the trajectory of the work hardening curve and do not necessarily have anything to do with the lower initial flow stress after the SPC. Therefore the cause of the Bauschinger effect has to be explained as well.

Feltner and Laird [1967a,b] ascribe the Bauschinger effect of copper during large strain cyclic tests, to the long range stress field of the dislocation substructure which will assist the reverse motion of dislocations. This effect gradually disappears after many cycles, which is attributed to the hardening by an increasing amount of secondary obstacles resulting in a substructure with a symmetric resistance to dislocation flow.

Hasegawa and co-workers have interpreted their observations in the framework of the percolation model of Kocks as reviewed in section 2.2.2.a. An important aspect in their analysis is the effect that an intermediate recovery treatment has on the substructure and the work hardening transient during a strain reversal test. The transient regime becomes significally shorter after a short recovery treatment between the unloading and the reloading [Hasegawa et al.; 1975] and even tends to completely disappear after longer heat treatments at low levels of prestrain [Hasegawa and Yakou; 1980]. This, as well as the fact that the recovery rate is increased by applying a forward stress [Hasegawa et al.; 1982] is explained by Hasegawa et al. [1986] as a consequence of the polarisation of the substructure (cf. section 2.2.3.a) which is inherent to cell formation as explained by the percolation model [Kocks et al.; 1980]. During stage I recovery (cell boundary sharpening) the interior forward stress in the cell walls is regarded as the driving force for the annihilation of the polarised dislocations and therefore the sharpening of the cell boundaries. During strain reversal it is assumed that the polarised dislocations get remobilised in the opposite direction, explaining the observed dissolution of the substructure, which is called untangling. This untangling becomes easier with increasing reverse strain, since the polarised dislocations at the surfaces of the dislocation walls have been blocking the polarised dislocations entangled somewhat deeper in the wall structure. This effect causes the softening contribution in the transient hardening regime. It will gradually disappear because of the limited availability of polarised dislocations. The substructure however gets rebuilt with the different polarisation on the unpolarised debris of the old structure, which explains the extra hardening in the work hardening transient. Due to the fact that recovery diminishes the polarity of the substructure, the effects of annealing treatments before reverse loading are explained as well within this framework.

This theory on work hardening during strain path reversal has been widely supported for more than 20 years. One aspect of the work hardening transient is however not captured by this theory, which is the initial high hardening rate just after reyielding. Besides the analogy with work hardening after type I static recovery, pointed out by Christodoulou et al. [1986] and the somewhat speculative explanation by Barlat et al. [2003] that this is likely due to the reorientation of the internal stresses caused by grain incompatibilities and dislocation pile-ups, no explanatory reference to this has been found in literature.

At least the implication of the foregoing theory, that the characteristic work hardening behaviour during strain reversal tests as depicted in fig. 2-13 requires a dislocation cell substructure, has been proven wrong by the experimental results of Rauch and co-workers [Rauch; 1997, Vincze et al.; 2005]. All reversal tests on pure aluminium AA1050 and IF steel on either -120 °C and 20 °C show this transient behaviour irrespective of whether the material is predeformed at -120 °C or 20 °C [Vincze et al.; 2005]. The IF steel predeformed at -120 °C however does not develop a cell structure due to the poor mobility of screw segments at that temperature. According to the authors the changes in the substructure morphology as described in section 2.3.2.a cannot be responsible for the transient work hardening behaviour as implied by the theory of the percolation model. The transient effect is however correlated to the dislocation density stored during prestraining [Rauch; 1997]. Vincze et al. [2005] therefore advocate that the nature of the individual dislocations (whether they are created before or after the strain reversal) defines this behaviour. The remobilisation and rapid annihilation of dislocations stored before the strain reversal then realise the work softening, while the creation of new dislocations brings about the work hardening. These principles have been further worked out in a work hardening model [Rauch et al.; 2007] which will be discussed in more detail in the next section.

A shared vision in the reasonings of both Hasegawa-Kocks and (although not explicitly stated as such) Rauch, is that the dislocation storage during deformation, regardless whether this storage is temporary or definite, requires the separation of dislocations of opposite sign to prevent dislocation annihilation.

This separation requires some sort of obstacles which can be either large and complex like cell walls (Hasegawa-Kocks), but also DDWs and precipitates, or small like dislocation interaction products and dislocation entanglements. Whenever the strain path is reversed the dislocations stored during the prestraining have then a different polarity (Hasegawa-Kocks) or different nature (Rauch) to the dislocations which are produced by the current straining mode.

b) Cross type of SPC

Basinski and Jackson in their work on copper single crystals with ‘alien’ substructures [1965a-c] already explored what the effect of an existing substructure is on the hardening of newly activated slip systems. They call a substructure alien to a certain slip system, if the slip system has not contributed to the build-up of this substructure. Their tests show that after yielding a high flow stress and a low hardening rate occur and that the existing dislocation structure formed during prestraining, becomes unstable. An initial localisation of the activated slip system in narrow slip bands, which indicates a preferential multiplication of dislocations on an already operative slip plane, is also observed. After the whole crystal is filled with slip, it behaves as if no prestrain has occurred. Because these observations do not depend on the exact relationship between the activated slip system and the slip system(s) of the prestraining, Basinski and Jackson conclude that “the particular interaction between individual dislocations is not important to determine whether a substructure is alien or not” [1965c]. These observations already contain the basic elements of most theoretical considerations which would be published subsequently regarding transient effects during cross type strain path changes: the influence of the substructure on the flow stress of non active slip systems (latent hardening leading to substructural anisotropy), the slip localisation and substructure instability leading to a low hardening rate and the return to the monotonic workhardening behaviour if the substructure is completely replaced. Unfortunately, no other works regarding strain path change transients on single crystals, where dislocation dynamics can be studied from known activities of specific slip systems, seem to have been published since.

Because polycrystalline samples, both mechanically and microstructurally, show a very similar behaviour during various SPC test as described by Basinski and Jackson, Lloyd and Sang [1979] refer to their concept of the alien substructure for several aluminium alloys as did Wagoner and Laukonis [1983] for aluminium killed steel. The alien substructure gets replaced by dissolution and reformation processes into a new structure characteristic to the current straining mode. According to Wagoner and Laukonis [1983], this requires an activation stress, explaining the initial higher flow stress which gradually returns to the expected monotonic flow stress. The absence of this transient behaviour in certain aluminium alloys (AA2036, AA5182) is explained by the more homogeneous dislocation structures observed after prestraining in these samples [Lloyd and Sang; 1979], which are supposed to have a more isotropic resistance to dislocation flow irrespective of the activated slip systems, compared to the substructures with diffuse cell walls.

Based on the more rigorous analysis of the substructure evolution during cross type SPC test on mild steels by Rauch and Schmitt [Rauch and Schmitt; 1989] (see also section 2.3.2.b), it is concluded that all slip is concentrated in the narrow microbands that cut through the existing microstructure. The softening and localisation occurs because of the disappearance of obstacles in the slip plane, itself due to the breaking up of the existing substructure within the microband [Rauch and Thuillier; 1993]. Since dislocation annihilation is thermally activated, applying a higher strain rate can prevent the localisation, explaining the influence of $\dot{\gamma}$. Because the microbands do not evolve into macroscopic localisations, it is deduced by Rauch and Schmitt [1989] that hardening within the microbands has to occur, which limits the amount of deformation within a microband. The microbands only play a role in the beginning of the substructural transition because at higher strains they get curved.

This type of localisation in microbands has only been reported in some grains of Al-Si and Al-Mn-Mg alloys [Lewandowska; 2003] and in highly deformed AA3004 samples [Gaspérini et al.; 1996]. A detailed mechanism controlling the substructure transition during a cross type SPC tests for fcc materials where only a gradual dissolution of the substructure is observed seems to be lacking in the literature up till now.

2.4 Existing models for strain path changes

Due to the demand for more accurate predictions of strength and failure during complex forming operations like e.g. deep drawing, a lot of research has in recent years been dedicated to plastic anisotropy and strain path changes. For the work hardening behaviour during strain path reversal, many modelling efforts stem from the experimental observations made during high strain cyclic loading tests.

One of the oldest models for cyclic deformation is the Masing model (reviewed by e.g. [Skelton et al.; 1997]). In this model the material is treated as a set of ideally plastic elements with different yield stress which receive the same total strain. At unloading and reverse loading, taking the peak load of the preloading as the new origin, the element with the lowest yield stress will start to deform plastically at a lower stress level as in the preloading, explaining the Bauschinger effect. This kind of approach is still present in some recent models [e.g. Gloaguen and François; 2006] to obtain kinematic hardening by describing the structure as consisting of two elements with different hardening behaviour (cell walls and cell interiors).

One of the best known models for cyclic deformation is that of Chaboche [1986]. This model consists of evolution equations describing both isotropic and kinematic hardening (cf. fig. 2-1). Its implementation into finite element codes can considerably improve predictions of spring back [e.g. Chun et al.; 2002b]. A recent extension of the Chaboche model [Chun et al.; 2002a], allowing for permanent softening to take place (cf. section 2.3.1.a) results in better predictions for all parameters analysed.

The above mentioned models predict the yield stress at strain reversal, but do not capture the subsequent transient regime in the work hardening behaviour as depicted in fig. 2-13. The often observed region of hardening stagnation has been modelled on a purely phenomenological basis by Yoshida and Uemori [2002] by introducing the concept of a bounding surface that limits the flow surface in the regime of non-monotonic hardening. A different evolution equation is presented for both the flow surface and the bounding surface, with the condition that the flow surface always remains inside of the bounding surface.

Hu et al. [1992] based their model for work hardening during strain reversal on the changes of the intragranular substructure observed by TEM (cf. section 2.3.2.a). In order to capture the state of the substructure, the model of Hu introduces three internal scalar variables related respectively to the back stress, the polarity of the substructure and the availability after strain reversal of remobilised dislocations that were stored during prestraining. The model specifies the evolution equations for these variables depending on the straining direction (either forward or reverse) and a flow criterium based on the three internal variables. The model has proven to predict accurately the work hardening behaviour of mild steel before and after strain reversal, even at large prestrains [Hu et al.; 1992] as well as work hardening during large strain cyclic shear tests [Hu; 1994].

A number of models have been proposed to predict the full anisotropy of the yield stress. Most of these models are formulated on the macro scale and describe the anisotropic hardening as a combination of isotropic, kinematic and rotational hardening [e.g. Wu; 2003, Suprun; 2006, Choi et al.; 2006]. The rotational hardening involves a rotation of the principal reference frame of the yield locus and aims mostly at capturing changes in the anisotropy due to changes in the crystallographic texture of the material. These models are however limited to the prediction of the yield locus at the point of the SPC and do not account for the subsequent characteristic transient hardening behaviour (cf. section 2.3.1.a).

The most successful approach in modelling the hardening anisotropy including the transient hardening effects after SPC has been by taking the substructural contribution explicitly into account while attributing special evolution equations to the internal variables that characterise the substructure. This approach has been initiated by the model of Teodosiu and Hu [1995]. In this section first this model will be discussed followed by the models of Peeters [Peeters et al.; 2001b] and Holmedal [Holmedal et al.; 2004, 2008]. The focus lies particularly on these models because they illustrate different methodologies of incorporating the substructure into the hardening equations.

2.4.1 Teodosiu-Hu model

The first comprehensive model for work hardening anisotropy and transient effects after strain path changes has been developped by Teodosiu and Hu [1995] for IF steel, but it has later also been applied to aluminium [Teodosiu et al.; 1997]. The model is loosely based on the phenomenological model for work hardening during strain reversal of Hu et al. [1992].

The model of Teodosiu-Hu generalises the scalar internal variables of the Hu model into tensorial quantities and formulates evolution equations for them. The possible directional differences of the internal variables with the current straining mode tensor $\mathbf{E}=\dot{\boldsymbol{\varepsilon}}/\|\dot{\boldsymbol{\varepsilon}}\|$ often play a crucial role within these equations. These directional differences are somewhat related to the Schmitt-parameter for strain path changes (equation (1.2)) in the sense that a directional difference indicates what kind of change in strain path has taken place. The evolution equations make that the internal variables will gradually readjust their direction towards the current straining mode, while the magnitudes of the internal variables and their evolution with strain determine the work hardening behaviour. The model (as the model of Hu) is formulated on the macro scale.

a) Model formulation

Since its first publication, the model has been slightly altered in order to become more quantitatively accurate. The formulation which is presented below, corresponds to the one which can be found in [Bouvier et al.; 2005] and [Haddadi et al.; 2006].

There are in principle five internal variables in the model of Teodosiu-Hu. There are two tensors of rank 4, $\mathbf{M}$ (dimensionless) and $\mathbf{S}$ (dimension of stress), where $\mathbf{M}$ characterises the average anisotropy due to texture and $\mathbf{S}$ the average anisotropy due to the dislocation substructure. Two other tensors are of rank 2. $\mathbf{X}$ represents the average back stress[16] (dimension of stress) and $\mathbf{P}$ characterises the state of polarity of the substructure (dimensionless). The final internal variable R is a scalar value (dimension of stress) which characterises the average isotropic hardening due to randomly stored dislocations. In the model formulation there is no evolution equation for $\mathbf{M}$ incorporated. $\mathbf{M}$ is kept constant and no influences on the anisotropy because of texture changes are modelled. The flow criterium based on these internal variables is expressed as:

$$\sigma_{eq} = \sqrt{(\boldsymbol{\sigma} - \mathbf{X}) : \mathbf{M} : (\boldsymbol{\sigma} - \mathbf{X})} = \sigma_0 + R + f \, \|\mathbf{S}\|, \tag{2.31}$$

where σ_0 is the initial flow stress and f is the volume fraction occupied by the organised substructure. Both σ_0 and f are considered to be constant material parameters. Equation (2.31) describes a yield locus of which the shape is solely determined by $\mathbf{M}$. $\mathbf{X}$ represents the kinematic hardening and $\sigma_0 + R + f\,\|\mathbf{S}\|$ the isotropic hardening (cf. fig. 2-1). Since $\mathbf{M}$ is fixed, the flow surface does not change its shape nor rotates. The focus of the model lies on how the kinematic and isotropic hardening evolves with ongoing strain as a function of the strain path.

---

[16] The back stress in this context describes the kinematic hardening (cf. fig. 2-1 (b)) and is not necessarily equal to the internal back stress as defined in section 2.2.3.a.

The evolution equations for the internal variables with strain all have the form of an exponentially decaying difference to a certain saturation value. Not all saturation values are however taken constant and many interdependences between the variables are enclosed in the equations for the saturation values. $\mathbf{S}$, $\mathbf{X}$, $\mathbf{P}$ and R have all the initial value of 0.

The evolution equation for the isotropic hardening contribution of randomly stored dislocation loops (i.e. not stored as a part of the organised dislocation substructure, which is represented by $\mathbf{S}$) is formulated as:

$$\dot{R} = c_R \left(R_{sat} - R \right) \dot{\varepsilon}_{eq} , \tag{2.32}$$

with R_{sat} the saturation value and c_R a material parameter controlling the saturation rate. $\dot{\varepsilon}_{eq}$ is the scalar strain rate equivalent corresponding to σ_{eq} of equation (2.31). Equation (2.32) is a classical Voce-type hardening law equivalent to equation (2.11). With increasing strain, R will asymptotically evolve towards R_{sat}, irrespective of the strain path.

The evolution equation of the back stress is expressed as

$$\overset{\circ}{\mathbf{X}} = c_X \left(X_{sat} \frac{\boldsymbol{\sigma} - \mathbf{X}}{\sigma_{eq}} - \mathbf{X} \right) \dot{\varepsilon}_{eq} , \tag{2.33}$$

which describes an asymptotic evolution of $\mathbf{X}$ towards the stress mode $\left(\boldsymbol{\sigma} - \mathbf{X} \right) / \sigma_{eq}$ multiplied with a scalar term X_{sat}. c_X is a material constant which determines the rate of saturation. The superimposed circle for the rate of $\mathbf{X}$, denotes a Jaumann type of derivative, implying a regular derivative in (and only in) the reference frame that is co-rotational with the material. The scalar saturation value X_{sat} is not constant, but depends on $\mathbf{S}$ and the strain mode $\mathbf{E}$. In the implementation of the model, $\mathbf{S}$ is decomposed into a scalar value $S_D = \mathbf{E} : \mathbf{S} : \mathbf{E}$, representing the part of the substructure which is associated with slip systems that are currently still active and a tensor $\mathbf{S}_L$ for the part of the substructure built up by slip activity which has become latent. The total substructural anisotropy tensor becomes:

$$\mathbf{S} = S_D \left(\mathbf{E} \otimes \mathbf{E} \right) + \mathbf{S}_L \tag{2.34}$$

The scalar saturation value of the back stress is expressed as

$$X_{sat} \left(\mathbf{S}, \mathbf{E} \right) = X_0 + \left(1 - f \right) \sqrt{r \left\| \mathbf{S}_L \right\|^2 + S_D^2} , \tag{2.35}$$

where X_0 and r are material parameters. In case of monotonic and reversal strain paths, $\mathbf{S}_L = 0$, making the magnitude of the back stress $\mathbf{X}$ directly related to S_D, while its direction is parallel to the stress mode (the sense will be initially opposite during strain reversal). In case of any other SPC the direction of the back stress will rotate towards the direction of the stress mode (equation (2.33)), while its saturation magnitude will be dominated by the value of $\left\|\mathbf{S}_L\right\|$, since $r > 1$. Because $\left\|\mathbf{S}_L\right\|$ will tend to 0 (see below), after sufficient straining the kinematic hardening will return to the monotonic behaviour of the second deformation mode.

Up till now the polarity tensor $\mathbf{P}$ has not been employed, it will however largely influence the evolution of the substructural anisotropy tensor $\mathbf{S}$. Therefore the evolution equation of $\mathbf{P}$ will be presented first:

$$\overset{\circ}{\mathbf{P}} = c_P \left(\mathbf{E} - \mathbf{P}\right) \dot{\varepsilon}_{eq}, \tag{2.36}$$

with c_P a material constant controlling the rate of polarisation. $\mathbf{P}$ is a tensor which tends towards the current straining mode. Whenever a difference occurs (due to an SPC) it will require a certain amount of straining to adapt the polarity of the substructure to the current straining mode.

The evolution of $\mathbf{S}$ is within the model described by the independent evolution of S_D and $\mathbf{S}_L$. The latter is described by an exponentially decaying function towards 0, where the rate of decay is a function of the magnitude of $\mathbf{S}_L$:

$$\overset{\circ}{\mathbf{S}}_L = -c_{SL} \left(\frac{\left\|\mathbf{S}_L\right\|}{S_{sat}} \right)^{n_L} \mathbf{S}_L \dot{\varepsilon}_{eq}, \tag{2.37}$$

with c_{SL} and n_L material constants. S_{sat} is the saturation value for S_D. In case of an abrupt change in the straining mode, $\mathbf{S}_L$ obtains non zero values, which will decay towards zero with further straining. The evolution equation of S_D consists of two terms, one driving the value of S_D towards a saturation value S_{sat} which is influenced by the polarity and the other one driving the value of S_D towards 0, controlled by the difference in direction between the back stress and the straining mode :

$$\dot{S}_D = c_{SD} \left(g \left(S_{sat} - S_D \right) - h S_D \right) \dot{\varepsilon}_{eq}, \tag{2.38}$$

with c_{SD} a material constant controlling the rate of saturation. g and h are values between 0 and 1, depending on the direction of the polarity $\mathbf{P}$ and the back stress $\mathbf{X}$ compared to the straining mode $\mathbf{E}$ respectively. The mathematical description of g depends on whether the polarity of the substructure is opposite to the straining mode or not:

$$g = 1 - \frac{c_P}{c_{SD} + c_P} \left| \frac{S_D}{S_{sat}} - \mathbf{P} : \mathbf{E} \right| \quad \text{if} \quad \mathbf{P} : \mathbf{E} \geq 0 \tag{2.39}$$

$$g = \left(1 + \mathbf{P} : \mathbf{E}\right)^{n_P} \left(1 - \frac{c_P}{c_{SD} + c_P} \frac{S_D}{S_{sat}}\right) \quad \text{if} \quad \mathbf{P} : \mathbf{E} < 0 \tag{2.40}$$

with n_P being the final material constant of the model. It should be pointed out that g is continuous at $\mathbf{P} : \mathbf{E} = 0$ and that $0 \leq g \leq 1$. g is initially equal to 1 and will slowly decrease during monotonic prestraining. At an SPC g abruptly takes a lower value (0 in case of strain reversal) but will, mainly controlled by the evolution of $\mathbf{P}$ towards $\mathbf{E}$, return to the monotonic straining case. The value of h in equation (2.38) is described by:

$$h = \frac{1}{2} \left(1 - \frac{\mathbf{X} : \mathbf{E}}{X_{sat}}\right). \tag{2.41}$$

Unfortunately it is nowhere explained why in this equation $\mathbf{X}$ is compared to the straining mode $\mathbf{E}$, instead of the stress mode to which it evolves according to equation (2.33). As for g the value of h also is limited between 0 and 1. The value of h is initially 0.5 and decreases with increasing back stress towards a very low value (depending on the directional difference between stress and straining mode). At an SPC, h abruptly takes a larger value and then decreases towards the low value of the monotonic case.

Just after an SPC a low value for g and a high one for h make that the value of S_D will temporarily decrease. This effect is most outspoken for strain reversal tests. The lowering of S_D corresponds to the partial dissolution of the substructure. For all possible strain path combinations, equation (2.38) becomes a differential equation where $\dot{S}_D$ is a quadratic function of S_D. The saturation value is however always S_{sat}.

b) Further developments

Due to the 13 modelling parameters needed to describe the substructural anisotropy and at least 6 parameters to describe the textural anisotropy, a large number of different mechanical tests is required to calibrate the model. In order to avoid the set of rather complex tests under many different deformation modes needed for the characterisation of the textural anisotropy, Hiwatashi et al. [1997] proposed to derive this anisotropy from an ODF obtained from measured texture data. This approach has been succesfully applied to predict forming limits for non monotonic straining modes [Hiwatashi et al.; 1998].

The incorporation of the Teodosiu-Hu model as the material model in finite element codes has proven to somewhat reduce the existing gap between experimental observations and model predictions of various process parameters and resulting shape discrepancies [Li et al.; 2003, Bouvier et al.; 2005, Haddag et al.; 2007, Wang et al.; 2008].

A further extension to the model has been proposed by Uenishi and Teodosiu [2004] by introducing evolution equations for σ_0 and R_{sat} (equations (2.31) and (2.32)) in order to let them depend on the strain rate. The other internal variables are left strain rate independent, although it is illustrated in a subsequent paper [Uenishi et al.; 2005] that the formation of the directional dislocation substructure is delayed at higher strain rates, which indicates a need to make at least $\mathbf{S}$ dependent of the strain rate as well.

2.4.2 Peeters model

The model of Peeters has been developed to capture the anisotropy and work hardening behaviour at SPC for IF steel (bcc). The model [Peeters et al.; 2001b, Peeters; 2002] does not separate the textural and substructural contributions to the anisotropy on the macro scale like the model of Teodosiu-Hu, but makes them interdependent on the meso scale. This is done by extending the FC Taylor texture model (cf. section 2.1.2.a) with a slip system dependent work hardening model. The critical resolved shear stresses of each slip system (the τ^{α} in equation (2.6)) are made dependent on the distribution of the overall slip $\dot{\Gamma}$ over the individual slip systems. To obtain the Bauschinger effect (which the kinematical hardening imposed by the back stress $\mathbf{X}$ accounts for in e.g. the Teodosiu-Hu model) the value of the critical resolved shear stress of all slip systems is decoupled based on the shear direction ($\dot{\gamma}^{\alpha}$>0 or $\dot{\gamma}^{\alpha}$<0), so that the resistance to slip can be different in the active and the opposing direction of the slip systems.

The internal variables for the substructure are specific for each orientation of which the reorientation is calculated within the Taylor model. The representative set of individual grains all have an orientation and a substructure which evolves independently from each other within a certain strain increment. The average of all mesoscopic anisotropy descriptions constitutes so to speak the overall macroscopic anisotropy. Compared to the model of Teodosiu-Hu, this approach results in many more internal variables and a larger number of equations to be solved for each increment, but enables to have an orientation dependent substructural anisotropy of which the existence is often suspected on the basis of TEM observations (section 2.2.1.b).

a) Model formulation

The model of Peeters considers a substructural scheme for each orientation as presented in fig. 2-22. The isotropic part of the work hardening is connected to the formation of cell walls. The dislocations stored in the cell walls are represented by the dislocation density ρ, which has a specific value for each grain. The anisotropy for other loading directions is caused by dense dislocation walls (cf. model of Winther discussed in section 2.2.3.c). In the model of Peeters the DDWs are assumed to be parallel to the two highest active {110} slip planes. The DDWs can only form on the six possible {110} planes. If one of the {110}

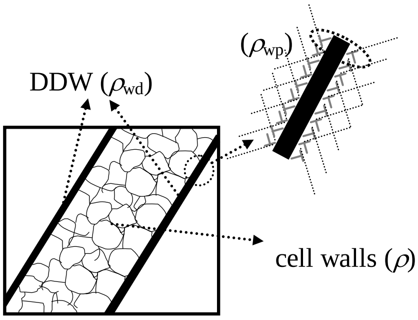

Fig. 2-22 : Substructural scheme as employed in the model of Peeters. Dislocations making up the cell walls are denoted by ρ, immobilised dislocations in the dense dislocation walls (DDW) are denoted by ρ_{wd} and dislocations which can be remobilised after an SPC sitting at the DDWs are denoted by ρ_{wp}. From [Peeters et al.; 2001b].

slip planes is dominantly active, a banded structure (cf. fig. 2-7 (b)) will be formed, otherwise the morphology is that of a checkerboard structure (cf. fig. 2-7 (a)). Within each orientation, each of the six {110} planes obtains two types of dislocation densities, making up the DDWs. The dislocations which are immobilised within the structure of the DDWs are represented by ρ_{wd}^{P} and dislocations which can be remobilised after an SPC by ρ_{wp}^{P}. The superscript P denotes the glide plane of the DDWs. The dislocations accommodating slip on the slip systems with the slip plane parallel to the DDWs will be assigned to ρ_{wd}^{P}, while dislocations on slip systems with one of the two $\langle 111 \rangle$ Burgers vectors intersecting the boundary plane will contribute to ρ_{wp}^{P}. Dislocations on intersecting glide planes with the Burgers vector within the boundary plane are considered not to contribute to either of both dislocation densities. Within the model the polarity of the substructure (cf. section 2.3.3.a) is completely assigned to the dislocations of ρ_{wp}^{P}. This density therefore receives a sign based on the slip direction of the contributing slip systems.

The contributions to the critical resolved shear stress of a certain slip system by the three types of dislocations are calculated as follows. The isotropic contribution from the dislocations in the cell walls is the same for all slip systems and is calculated by the classical Taylor equation for the flow stress (equation 2.8) :

$$\tau_I = \alpha G b \sqrt{\rho}\,. \tag{2.42}$$

The DDWs on a plane P contribute to the strength of a slip system α by both the immobilised dislocations and the polarised dislocations according to the formulas

$$\tau_{wd}^{P,\alpha} = \alpha G b \sqrt{\rho_{wd}^{P}} \left| \hat{\mathbf{b}}^{\alpha} \cdot \hat{\mathbf{n}}^{P} \right|, \tag{2.43}$$

$$\tau_{wp}^{P,\alpha} = \alpha G b \sqrt{\left|\rho_{wp}^{P}\right|} \left(\hat{\mathbf{b}}^{\alpha} \cdot \hat{\mathbf{n}}^{P} \right) \operatorname{sgn}\left(\rho_{wp}^{P}\right). \tag{2.44}$$

$\hat{\mathbf{b}}^{\alpha}$ is the unit vector parallel to the Burgers vector of the slip system α and $\hat{\mathbf{n}}^{P}$ is the unit vector normal to the plane of the DDWs P. The scalar product between both vectors makes that the slip systems with a Burgers vector parallel to the plane will not be hardened by the presence of the DDWs (although screw components of slip systems that have an intersecting glide plane might be blocked). The absolute value in equation (2.43) makes that this contribution for the immobilised dislocations is always positive, while it can either be positive or negative for the polarised dislocations (equation (2.44)) depending on whether the current polarisation state of the existing substructure (sign of ρ_{wp}^{P}) is according or opposite to the glide direction of the slip system (sign of $\hat{\mathbf{b}}^{\alpha}$).

The overall critical resolved shear stress of a slip system α becomes :

$$\tau^{\alpha} = \tau_0 + \left(1 - f\right)\tau_I + f\sum_{P}\left(\tau_{wd}^{P,\alpha} + \tau_{wp}^{P,\alpha}\right), \tag{2.45}$$

where τ_0 and f are the lattice resistance and the volume fraction of DDWs which are considered as material constants. The evolution of the τ^{α} is embedded in the energy criterium of the Taylor model (equation (2.6)) which results in an influence of the substructural anisotropy on the slip rates and therefore on the texture evolution (cf. section 2.1.2.a).

The evolution with strain of the different dislocation densities in the model depend on the slip activities of the available slip systems, characterised by the slip rates $\dot{\gamma}^{\alpha}$, which are obtained from the Taylor model. The sums of the slip rates of the coplanar $\{110\}\langle 111\rangle$ slip systems pairs are denoted as $\dot{\Gamma}^{P}$, being the slip rates of the six possible DDW sets. The two highest values among the $\dot{\Gamma}^{P}$ will accommodate the creation or strengthening of DDWs while the possible existing DDWs ($\rho_{wd}^{P} + \left|\rho_{wp}^{P}\right| > 0$) on the other four glide planes will be broken up. Consequently there are different evolution equations for the dislocation walls which are being built up and for the ones which are not.

The evolution of the dislocation density of dislocations stored in the cell walls contributing to isotropic hardening is modelled with a Kocks-Mecking type of hardening equation (cf. section 2.1.3.b) :

$$\dot{\rho} = \frac{1}{b}\left(I\sqrt{\rho} - R\rho\right)\dot{\Gamma} - \frac{1}{b}R_2\rho\frac{\rho_{rev}}{2\rho_{wp,sat}}\dot{\Gamma}\ , \tag{2.46}$$

where I and R are a dislocation storage and a dislocation annihilation proportionality constant respectively. $\dot{\Gamma}$ is the sum of all the slip rates $\dot{\gamma}^{\alpha}$. The last term of equation (2.46) models the annihilation of mobile dislocations with remobilised dislocations which were previously stored at the DDWs. R_2 is the dislocation annihilation proportionality constant for this process and $\rho_{rev}/2\rho_{wp,sat}$ is the fraction of polarised dislocations which gets remobilised. $\rho_{wp,sat}$ is the saturation value of the dislocation density of polarised dislocations at the DDWs and ρ_{rev} is the total dislocation density of polarised dislocations of which the dislocation flux (cf. supra) has been reversed :

$$\rho_{rev} = \sum_{P=rev} \left| \rho^{P}_{wp} \right| . \tag{2.47}$$

The last term in equation (2.46) is only different from zero whenever the strain path is at least partially reversed.

The evolution of the dislocation densities attributed to the two families of DDWs which are being built up, is modelled by Kocks-Mecking type of equations similar to equation (2.46), but with different proportionality constants :

$$\dot{\rho}^{P}_{wd} = \frac{1}{b}\left(I_{wd}\sqrt{\rho^{P}_{wd}} - R_{wd}\,\rho^{P}_{wd} \right)\dot{\Gamma}^{P}, \tag{2.48}$$

$$\dot{\rho}^{P}_{wp} = \left(\operatorname{sgn}\left(\Phi^{P}_{wp} \right) I_{wp}\sqrt{\rho^{P}_{wd} + \left| \rho^{P}_{wp} \right|} - R_{wp}\,\rho^{P}_{wp} \right)\Phi^{P}_{wp} . \tag{2.49}$$

with I_{wd} and I_{wp} the constants for dislocation storage and R_{wd} and R_{wp} the constants for dislocation annihilation, in both cases for immobilised and polarised dislocations respectively. $\dot{\Gamma}^{P}$ is the sum of the slip rates of the two coplanar slip systems contributing to the dislocation density ρ^{P}_{wd}. Φ^{P}_{wp} is the net dislocation flux through the family of DDWs P, which is calculated as :

$$\Phi^{P}_{wp} = \frac{1}{b}\sum_{\alpha} \dot{\gamma}^{\alpha}\left(\hat{\mathbf{b}}^{\alpha} \cdot \hat{\mathbf{n}}^{P} \right). \tag{2.50}$$

For families of DDWs which are not being built up ($\dot{\Gamma}^{P}$ is not among the two largest ones), the previously stored dislocations are being annihilated according to the following equations:

$$\dot{\rho}^{P}_{wd(hom)} = -\frac{1}{b} R_{ncg}\,\rho^{P}_{wd(hom)}\dot{\Gamma}^{new} \tag{2.51}$$

$$\rho^{P}_{wd(cut-through)} = -\sqrt{\beta_1 \Gamma^{new}}\,\beta_2 e^{-\beta_1 \Gamma^{new}}\,\rho^{P}_{wd(hom),0} \tag{2.52}$$

$$\rho^{P}_{wd} = \rho^{P}_{wd(hom)} + \rho^{P}_{wd(cut-through)} \tag{2.53}$$

$$\dot{\rho}^{P}_{wp} = -\frac{1}{b} R_{ncg}\,\rho^{P}_{wp}\dot{\Gamma}^{new} \tag{2.54}$$

R_{ncg} is the proportionality constant for the annihilation of non currently generating DDWs. $\dot{\Gamma}^{new}$ is the sum of the two largest $\dot{\Gamma}^{P}$, representing the slip activity that is instrumental in the breaking-up of the pre-existing DDWs. Γ^{new} is the integrated value of $\dot{\Gamma}^{new}$ since the SPC, $\rho^{P}_{wd(hom),0}$ is the value of ρ^{P}_{wd} at the SPC and β_1 and β_2 are material constants. Equations (2.51) and (2.54) describe an exponentially decaying dislocation density with ongoing strain, while equation (2.52) describes a negative dislocation density $\rho^{P}_{wd(cut\_through)}$ which in magnitude first increases almost parabolically from 0 to a peak value and then exponentially decreases to 0 again. This negative dislocation density is a correction factor on the dislocation density of the immobilised dislocations at the DDWs in order to model the cut-through process by the formation of microbands as discussed in section 2.3.2.b.

The final model equation describes the evolution of the polarised dislocations in case that the dislocation flux at a wall is reversed. This equation describes the annihilation of polarised dislocations by the net flux of dislocations with the opposite sign:

$$\dot{\rho}^{P}_{wp} = -R_{rev}\rho^{P}_{wp}\left|\Phi^{P}_{wp}\right| \tag{2.55}$$

with R_{rev} a proportionality constant for dislocation annihilation.

During monotonic (pre-)straining, the slip systems with a Burgers vector parallel to the DDWs of the highest active slip plane will have the lowest τ^{α}. After a cross type of SPC, the dislocation densities ρ^{P}_{wd} and ρ^{P}_{wp} of previously built-up DDWs, which are now contributing to the glide resistance of newly activated slip systems, will be gradually reduced to 0, according to equations (2.51-2.54). Simultaneously, two new families of DDWs will be built up following equations (2.48-2.49). During strain reversal, the density of the immobilised dislocations ρ^{P}_{wd} will continue to increase by equation (2.48), while the polarised dislocation densities ρ^{P}_{wp} will first decrease to zero according to equation (2.55) and subsequently will be built up again with the opposite sign following equation (2.49). The last term in equation (2.46) results in a permanent kinematic softening of the isotropic contribution. This combined with the strain interval necessary for diminishing and increasing ρ^{P}_{wp} leads to a value of $\gamma_0 > 0$ (cf. fig. 2-13 (a)).

b) Similar models

Mahesh et al. [2004] have embedded the work hardening equations of the Peeters model within a self-consistent crystal plasticity model (cf. section 2.1.2.b) with a visco plastic flow rule to relate stresses and strain rates. They applied the model to the work hardening behaviour after strain path changes of copper. No good agreement with experimental results has however been obtained because the Kocks-Mecking type equations could not sufficiently capture the monotonic hardening behaviour.

The model of Beyerlein and Tomé for SPC in copper [2007] is formulated along similar lines as the Peeters model, although the internal variables are not under the form of dislocation densities but are different types of contributions to the critical resolved shear stresses of the slip planes (in which aspect it resembles the model of Holmedal of section 2.4.3). An extended Voce law [Tomé et al.; 1984] is used to capture the monotonic work hardening behaviour. The strain rates on the slip systems are combined into shear rate vectors on the four {111} planes as the sum of the unit Burgers vectors weighted by the slip rates. The direction of these shear rate vectors compared to the direction of the accumulated shear vectors on the other planes determines what kind of hardening/softening mechanism is activated. The model employs a latent work hardening matrix (equation 2.14) but with interaction coefficients for intersection slip planes lower than those for coplanar and self hardening (cf. the work of Bassani and co-workers discussed in section 2.1.4). This lower latent hardening is compensated by a cut-through mechanism whenever an intersecting glide planes would be activated, considerably increasing the flow stress on the intersecting glide planes. For modelling strain reversal, a mechanism for the annihilation of polarised dislocations is employed, which is somewhat more advanced than in the Peeters model, but the monotonic work hardening is directly retaken at the end of the stress plateau, resulting in stress strain curves having a kink at the point where the transient behaviour ends and a corresponding discontinuity in the hardening rate curves.

Rauch et al. [2007] have formulated a model for strain path reversals by using an decoupled dislocation density which resembles the distinction between immobilised dislocations and polarity dislocations found in the Peeters-model. At the point of strain reversal the dislocation density of the Taylor equation for the flow stress (equation (2.8)) stored during prestraining is split-up into ρ_f and ρ_r, which encompass the dislocations associated with the forward and the reverse loading substructure respectively. The overall critical resolved shear stress is calculated as:

$$\tau = \tau_0 + \alpha G b \sqrt{\rho_f + \rho_r} \tag{2.56}$$

ρ_f evolves with further straining according to the same monotonic hardening law as applied during prestraining.[17] The initial value of ρ_f at the strain reversal $\rho_{f,0}$ represents the part of the substructure which cannot be broken down by straining in the reverse direction, similar to the ρ_{wd}^P in the model of Peeters. The evolution of ρ_r with further straining is associated with the dissolution of the pre-existing substructure, which is modelled by an exponentially decaying evolution towards 0:

$$\frac{d\rho_r}{d\gamma} = -\frac{1}{b\Lambda}\frac{\rho_r}{\rho_{f,0}}, \tag{2.57}$$

with Λ the mean free path for mobile dislocations. Equation (2.57) is clearly similar to equation (2.55), although an important difference between both models should be noted. In the model of Peeters the polarised dislocation density is first annihilated according to equation (2.55) and subsequently built up with the opposite sign following equation (2.49). This makes the polarised dislocation density during the transient regime after strain reversal first decay to 0, and only when the polarised dislocation density is sufficiently small, it is able to change its polarity and evolve further towards the saturation value with opposite sign. In the model of Rauch the inversion of the polarity by the annihilation of dislocations stored during prestraining and the storage of dislocations into the structure according to the new polarity is regarded as a parallel process where the evolutions of ρ_r and ρ_f capture these two aspects. The concept of polarity however still applies. Whenever $\rho_r > \rho_f$ the existing substructure can be said to have an opposite polarity to the current straining mode, and they will have the same polarity whenever $\rho_f > \rho_r$. A neutral polarity is obtained when $\rho_r = \rho_f$.

To model the fastly decaying hardening before the hardening stagnation just after the strain path change, Rauch et al. employ a back stress similar to the one in the model of Hu et al. [1992].

Although the model of Rauch is mathematically very simple compared to the other models discussed, it captures the transient work hardening behaviour after a strain path reversal rather accurately.

---

[17] Rauch et al. [2007] use the hardening model of Estrin and Mecking [1984].

2.4.3 Holmedal model

The model of Holmedal et al. [2004, 2008] is largely related to the Peeters model since it is also an extension of the FC Taylor model with evolution equations for the critical resolved shear stresses of the individual slip systems. Like in the Peeters model, the textural anisotropy and substructural anisotropy are treated separately at the macro and the meso scale level respectively. The hardening equations for the slip systems in the Holmedal model are however purely phenomenological.

An important aspect of the Holmedal model, which makes it inherently different from the model of Peeters, is that the substructural hardening anisotropy does not depend on the relative activity of the contributing slip systems, but only on which set of slip systems is active. The evolution of the critical resolved shear stress of a certain slip system only depends on whether it is active, whether its reverse slip direction is active or whether it is not active (latent).

The critical resolved shear stress of a slip system within the model is the sum of four internal variables:

$$\tau^{\alpha} = \tau_I + \tau_L^{\alpha} + \tau_R^{\alpha} + \tau_P^{\alpha}, \tag{2.58}$$

τ_I is the isotropic contribution and is common to all slip systems of a grain. Its evolution with the total amount of slip Γ is obtained from a monotonic hardening model.[18] τ_L^{α} represents the latent hardening contribution due to previous activity on other slip systems. τ_R^{α} is the softening contribution ($\tau_R^{\alpha} < 0$) due to previous activity in the reverse direction. τ_P^{α} represents the polarity of the slip system, which represents the part of the hardening contribution to a slip system during monotonic deformation that will gradually disappear when the slip system would stop to be active. τ_L^{α}, τ_R^{α} and τ_P^{α} are modelled by equations of the type:

$$\frac{d\tau_X^{\alpha}}{d\Gamma} = \frac{\tau_{X,sat}^{\alpha} - \tau_X^{\alpha}}{\Delta\gamma_X}, \tag{2.59}$$

---

[18] Holmedal has used the Alflow model [Holmedal et al.; 2004] and a phenomenological hardening equation [Holmedal et al.; 2008] for this.

Table 1 : Calculation of the saturation values of the anisotropic hardening contributions for the Holmedal model

	α is active slip sys.	α is latent slip sys.	α is reverse direction of active slip sys.
$\tau^{\alpha}_{L,sat}$	0	$q_L \tau_I$	$q_{LR} \tau_I$
$\tau^{\alpha}_{R,sat}$	0	0	$-q_R \tau_I$
$\tau^{\alpha}_{P,sat}$	$q_P \tau_I$	0	0

where X can be either L, R or P. Equation (2.59) models an exponentially decaying difference towards a certain saturation value. The $\Delta\gamma_X$-values are modelling constants which control the rate of decay. The saturation values $\tau^{\alpha}_{X,sat}$ are set to the values indicated in table 1 depending on the internal variable and the activity of the slip system.

During straining, the critical resolved shear stresses of the active slip systems will tend towards $(1+q_P)$ times the isotropic hardening value, where the modelling constant q_P determines the relative amount of polarised dislocations. The slip systems which are latent will tend towards $(1+q_L)\tau_I$. In order to have a latent hardening effect (cf. section 2.1.4), q_L has to be larger than q_P. If a previously latent slip system becomes active at an SPC, its positive latent hardening contribution τ^{α}_{L} will gradually be reduced to zero, while the then unpolarised slip system ($\tau^{\alpha}_{P} = 0$ MPa) will become more and more polarised (τ^{α}_{P} evolves towards $q_P \tau_I$). During e.g. a cross test a completely different set of slip systems will be activated, so that the combined effect of the softening of the latent hardening contribution and the hardening due to polarisation will be maximal in the overall work hardening behaviour.

The slip systems of which the reverse direction is active will tend towards $(1+q_{LR}-q_R)\tau_I$ during straining. If a slip system gets reversed, the softening contribution ($\tau_R^\alpha < 0$) of the newly active direction will be gradually reduced to zero, while a small latent hardening contribution will also diminish. The combination of these two processes results in the plateau like work hardening stagnation if $\Delta\gamma_L$ is considerably smaller than $\Delta\gamma_R$. The polarity of the newly active direction is built up while the polarity of the previously active direction is broken down.

The Holmedal model can qualitatively predict the main features of the work hardening transients after strain path changes, but a comparison to a set of experimental curves is unfortunately not yet available in the literature.

2.5 Summary

In the literature survey an overview is given on the different aspects that contribute to the anisotropy of the flow stress of single phase metallic materials. The main focus lies on the role that the dislocation substructure plays in the work hardening behaviour during strain path changes.

To account for the influence of texture on the anisotropy, crystal plasticity models (e.g. the FC Taylor model) have been developed and refined. Monotonic work hardening has been explained by the changing relative importance of dislocation storage and dislocation annihilation, through the interactions of mobile dislocations with stored forest dislocations. The anisotropy due to the interactions of individual dislocations has been derived as well. The straightforward combination of texture with this type of latent hardening does however not fully capture the experimentally observed anisotropy [Raphanel et al.; 1986, Juul Jensen and Hansen; 1990]. The dislocation substructure has been put forward as the most likely other contributor to the work hardening anisotropy. The importance of the substructure for work hardening is also illustrated by the transient effects observed after abruptly changing the strain path, which have been correlated to structural changes in the substructure.

It is however not yet well understood how exactly the dislocation substructure changes the overall anisotropy. Various models that aim at explaining the formation of the substructure come up with different reasons for the existence of certain internal stress fields and hardening mechanisms due to the presence of the substructure, but the nature and importance of these stress fields and mechanisms is still subject to a scientific debate. The evolution with further straining of the substructure after an abrupt SPC, is not well understood either. Vincze et al.

[2005] put forward the question whether the observed evolution of the substructural morphology is even at all responsible for the observed transient work hardening behaviour during strain path reversal. In the discussion of the microstructural mechanisms that operate during strain path reversals (section 2.3.3.a), the hypothesis has been put forward that the substructure is polarised regardless of its exact morphology.

The review of the experimental findings on work hardening behaviour after strain path changes shows that the influence of several processing and material parameters on the transient work hardening behaviour is well documented, but that a consistent set of data for different types of strain path changes of the same material under similar processing conditions is lacking in the literature. It is such a data set which is however necessary to calibrate and validate any model which aims at predicting work hardening anisotropy including transient effects after abrupt strain path changes. In order to provide the model that will be developped in chapter 4 with such a data set, experimental stress strain curves for different types of strain path changes will be presented in the next chapter.

Three models which account for the evolution of the substructure after an SPC are discussed in detail in the last section of the literature survey. The model of Teodosiu and Hu makes the isotropic and kinematic hardening equations of an anisotropic flow surface dependent on the directional difference between the current straining mode and some internal variable tensors that characterise the state of the substructure. This model is able to capture the transient work hardening behaviour after strain path changes, but cannot account for texture evolution. The model of Peeters is an extension of the FC Taylor model, including substructure based hardening laws for the individual slip systems. It makes texture and substructure evolution interdependent and uses several types of dislocation densities as internal variables. It has however only been successfully applied to IF steel at low to intermediate strains and would need significant modifications to be able to account for stage IV hardening. The model of Holmedal is also an extension of the FC Taylor texture model, but uses much simpler phenomenological equations to describe the hardening of individual slip systems and allows embedding stage IV work hardening models for monotonic straining. No slip system interdependence is however implemented, which might lead to an unrealistically low flow stress on slip systems which have had a low activity prior to the SPC.

The main objective for the new model is to improve the existing models for substructural anistropy by formulating slip system based hardening equations that can produce as closely as possible the anisotropy and the transient hardening behaviour after SPC as obtained and analysed in chapter 3. The possibility to including stage IV hardening models and the use of more recent texture models should be made available within the model.

The new multiscale model for work hardening anisotropy during strain path changes will be compared in chapter 5 to the three models which are reviewed in detail in this chapter. It will be tried to shed some light on the strong and the weak points of all the models involved in the comparison in order to come to suggestions for future research in chapter 6.

3

Experimental observations

In the literature overview presented in the previous chapter many aspects of the substructural anisotropy have been discussed as observed for a wide range of metals where results are obtained at different deformation conditions and for different research purposes. Apart from IF steel, almost no material has been consistently analysed for a wide range of SPC angles and different prestrains. In order to calibrate and validate a model which includes SPC effects, this kind of data set is however compulsory. The main purpose of this chapter is the presentation of such a dataset and of the way it is obtained.

Another pitfall in SPC research is that the methodology to compare stress and strains obtained by different deformation modes is not at all straightforward, unlike what the wide use of the von Mises equivalent stress and strain seem to suggest. This difficulty will be surpassed by obtaining data on the crystallographic texture and its evolution with strain and including this in the data processing. In this way the textural influence can be separated and a more accurate prediction of the prestrain can be obtained.

Within this chapter first the used aluminium alloy will be presented. As the hardening behaviour is characterised by simple shear tests, the developed equipment to perform such tests will be discussed in the second section. Finally, the mechanical behaviour during strain path changes and how it is obtained will be presented and analysed.

3.1 Material

The material investigated is an aluminium-manganese alloy (AA3103) in hot-rolled and annealed condition. Due to its good drawability and its high corrosion resistance the material is mainly used for roof-gutters, air-conditioning tubing and other fluid carrying tube lines [Daaland et al.; 2003]. The material is also used in the research on single point incremental forming (SPIF) [Eyckens et al.; 2007b], where multiple strain path changes are dominating the work hardening behaviour.

First the microstructure of the as received material will be discussed. In a second section the texture and the resulting anisotropy will be discussed.

3.1.1 Microstructure

The chemical composition of AA3103 is given in table 2. During the homogenization treatment after casting and during hot rolling $\alpha\text{–}Al_{12}FeSi_3$ and $\alpha\text{–}Al_{12}MnSi_3$ will precipitate into $\alpha\text{–}Al_{12}(Fe,Mn)Si_3$ dispersoids [Anselmino et al.; 2004, Verlinden et al.; 2007]. These precipitates are clearly visible in a light microscope (cf. fig. 3-1) and are randomly spread throughout the material. Processing of the images obtained with scanning electron microscopy (SEM) using the backscattered electron contrast (cf. fig. 3-2) enables the separation of the two phases (the dispersoids and the aluminium matrix) using standard image processing routines.

The volume fraction of particles obtained from the SEM images is 3%. The particle sizes were between 2 µm and 8 µm, with an average of 3.4 µm. The particles are predominantly elongated and aligned with the rolling direction (RD) of the hot rolling process. In the SEM image also smaller particles can be vaguely observed which most likely are phases containing manganese that precipitated at the grain boundaries during the annealing treatment after hot rolling [Daaland and Nes; 1996]. These particles have circular shapes and are smaller than 1 µm. The

Table 2: Chemical composition of the used Al-Mn alloy AA3103. Fe and Si are two other important components.

AA3103	Mn	Fe	Si	Cu	Zn	Al
Weight%	1.0	0.6	0.2	0.08	0.01	bal.

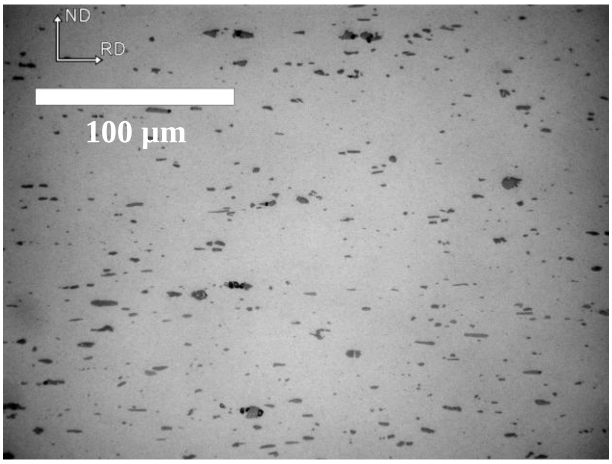

Fig. 3-1 : Micrograph obtained with light microscopy of a longitudinal section of the starting material. Particles randomly distributed in the matrix are clearly visible.

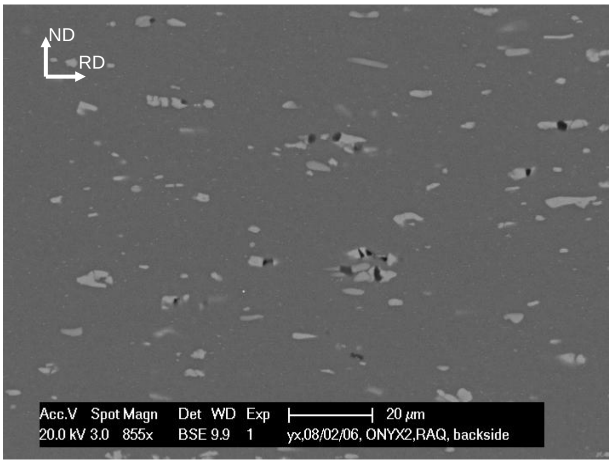

Fig. 3-2 : SEM backscattered electron image of a longitudinal section of the starting material. The white particles are α–$Al_{12}(Mn,Fe)Si_3$ dispersoids. The black spots are holes left by particles that were broken out of the matrix during grinding.

average grain size along RD is obtained with a line intercept method from EBSD data of the as received sample and equals 86 µm.

3.1.2 Texture and anisotropy

To determine the texture of the material, four incomplete pole figures, namely (111), (200), (220) and (311) are measured by means of X-ray diffraction using a Siemens D500 goniometer. All texture measurements are taken at half of the sheet thickness. The full texture is calculated by combining four incomplete pole figures using the MTM-FHM software [Van Houtte; 1995a]. Fig. 3-3 shows three φ_2-sections of the resulting orientation distribution function (ODF) containing all relevant texture components. The dominant one is the cube component $\{001\}\langle 100\rangle$ (intensity = 13.8) scattering towards the 18°-ND rotated cube component $\{001\}\langle 130\rangle$ (ND-RC). Two other prevalent components are Goss $\{011\}\langle 100\rangle$ (intensity = 3.2) and P $\{011\}\langle 455\rangle$ (intensity = 4.2). The moderate intensities of the β-fibre components (Copper $\{112\}\langle 111\rangle$, S $\{123\}\langle 634\rangle$ and Brass $\{011\}\langle 211\rangle$) indicate leftovers of the hot rolling process. Also the rotated copper orientation $\{112\}\langle 132\rangle$ (R-Cu) shown in fig. 3-3 is likely to remain from hot rolling.

The high occurrence of the P and ND-RC components can be possibly understood by a mechanism proposed by Daaland and Nes [1996] to explain the annealing texture of a AlMnMg-alloy similar to AA3103. During the annealing treatment the highly deformed β-fibre components resulting from hot rolling are consumed by growing nuclei originating from two possible sources. One source are the pre-existing nuclei from the hot rolling process that have a preferential 40° $\langle 111\rangle$

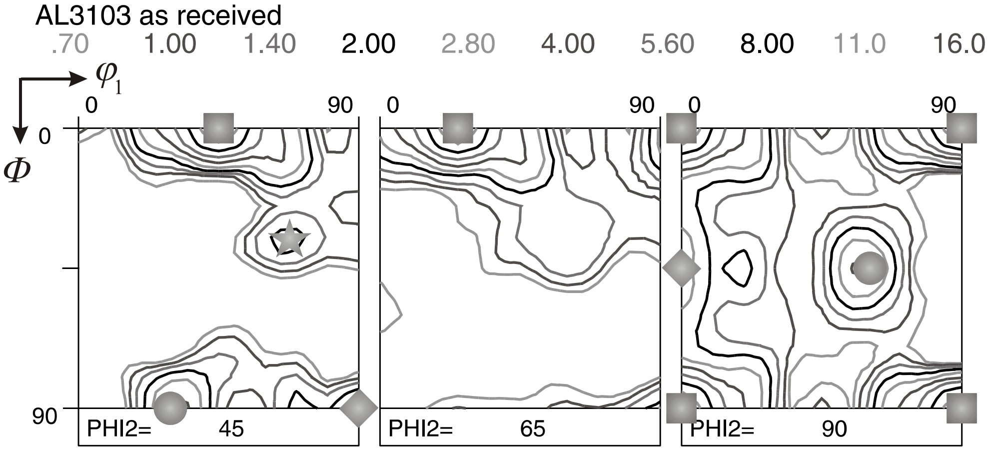

Fig. 3-3 : ODF of the texture of the starting material. Three φ_2-sections are chosen representing the important texture components. Indicated on the figure are Cube $\{001\}\langle 100\rangle$ (■), Goss $\{011\}\langle 100\rangle$ (◆), P $\{011\}\langle 455\rangle$ (●) and R-Cu $\{112\}\langle 132\rangle$ (★).

misorientation relationship with one of the β-fibre components (e.g. Cube, P and ND-RC). The other source are newly created nuclei with random orientation due to particle stimulated nucleation (PSN) at the α–$Al_{12}(Fe,Mn)Si_3$ dispersoids. At relatively low annealing temperatures the precipitation of Mn which is in solid solution happens simultaneously with the nucleation and will interfere with the nucleation process because of Zener-drag of the small precipitates. This especially hinders the smaller nuclei created by PSN compared to the pre-existing nuclei of hot rolling. This explains why the annealing texture has strong Cube, P and ND-RC components. Nevertheless this mechanism is still under discussion since recent in situ experiments have shown that growth of nuclei does not necessarily occur in the preferential 40° ⟨111⟩ directions [Anselmino et al.; 2004, Schmidt et al.; 2004].

The anisotropy due to the texture is analysed by calculating the initial *r*-values (longitudinal strain over thickness strain in a tensile test) in different in plane directions[19]. The results are compared to experimental *r*-values obtained from tensile tests in the rolling (0°), transverse (90°) and intermediate (45°) direction. The *r*-values calculated from the texture point to a low normal anisotropy (low $\bar{r}$ (20)) and a high planar anisotropy (large $abs(\Delta r)$)(21), while the experimental values indicate a fairly high normal anisotropy and a very low planar anisotropy. This difference might be partially attributed to the anisotropy of the dispersoids

Table 3 : r-values of three in plane direction of the as received AA3103, as calculated from the texture and as obtained from tensile tests.

	$r_{0°}$	$r_{45°}$	$r_{90°}$	$\bar{r}$	Δr
Texture	0.63	0.45	0.68	0.55	0.21
Experiment	0.68	0.65	0.59	0.64	-0.02

---

[19] The characterisation of the initial anisotropy and the analysis of the initial textures has been carried out by Philip Eyckens

[20] $\bar{r} = \frac{1}{4}\left(r_{0°} + 2r_{45°} + r_{90°}\right)$ is a good indicator of the normal anisotropy and the deep drawability.

[21] $\Delta r = \frac{1}{2}\left(r_{0°} - 2r_{45°} + r_{90°}\right)$ is a good indicator of the planar anisotropy.

and the grain shapes which are not covered by the calculations and are unfavourable for shears in the transverse direction.

3.2 Tests in simple shear

The planar simple shear test has some advantages above other conventional tests for the characterisation of work hardening behaviour [e.g. Rauch; 1998]. A homogeneous strain is achieved in the deformed zone, apart from a small edge effect at the free sides of the sample, up to relatively high strains (till about $\gamma = 1.7$ in one run for the material under investigation). Unlike tension and compression tests, no necking or barreling behaviour occurs and rectangular samples can be directly used without machining. The deformed zone remains planar and is visually accessible, so it can be characterised by a strain mapping system to obtain a high accuracy of the full strain field. Applying a reverse load to a sample can be done without unclamping the sample, by just changing the direction of the displacement. One disadvantage is that the ratio of the height versus the width of the deformed zone (respectively h and w in fig. 3-4, t is the thickness of the sample) has to be very small while the sample needs to remain firmly clamped along the full width during testing. This results in a severe limitation to the size of the deformed zone, so that cutting new samples out of the deformed zone for some specific strain path change tests are hardly feasible.

3.2.1 Dimensions of the test specimen

Fig. 3-4 indicates the dimensions of a shear test sample. The parts of the sample that are not sheared have to be firmly clamped, especially close to the deformed zone. The lateral displacement x is increased starting from 0 during the test. The shear strain γ is calculated as

$$\gamma = \frac{x}{h}. \tag{3.1}$$

In fig. 3-4 the upper clamped part is moved to the right, while the lower clamped part remains fixed. An external load F_S is required to increase x resulting in a constant shear stress

$$\tau = \frac{F_S}{wt} \tag{3.2}$$

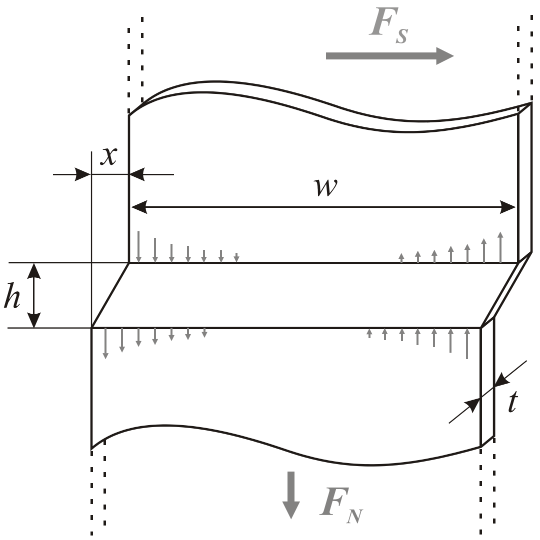

Fig. 3-4 : Dimensions of sample for simple shear tests. Only a part of the clamped zones is shown. Gray arrows illustrate forces by the machine on the sample and the normal forces at the edge zones during deformation.

on all horizontal planes in the deformed zone. A normal net force F_N has to be exerted on the sample by the lower grip in order to maintain simple shear conditions [G'Sell et al.; 1983]. The corresponding normal stress is expressed as

$$\sigma_N = \frac{F_N}{wt} \tag{3.3}$$

Some limitations on the dimensions of the deformed zone are derived by G'Sell et al. [1983] for the case of elastically isotropic materials. A first constraint comes from the requirement that no plastic buckling can be allowed. The ratio of the thickness t of the plate to the height h of the deformed zone has to be larger than

$$\frac{t}{h} > \sqrt{\frac{2\tau_{\max}(1-\nu)}{3\pi^2 G\eta}}, \tag{3.4}$$

with $\tau_{\max}$ the maximum attainable shear stress, ν Poisson's ratio, G the shear modulus and η a plastic softening factor approximately equal to $\sqrt{\theta/G}$ where θ is the hardening rate at $\tau_{\max}$. For values of $\tau_{\max} \approx 100$ MPa, $G \approx 29$ GPa, $\nu \approx 0.3$ and $\eta \approx 0.01$ the ratio thickness to height has to be larger than 0.13.

A second constraint minimizes the normal forces predominantly at the edges of the deformed zone exerted by the grips on the sample in order to counterbalance the rotational moment induced by the shear force F_S. If the normal forces are assumed to vary linearly along the width of the deformed zone w, then

$$F_S h = \frac{4}{3} |\bar{\sigma}_N| t w^2 , \tag{3.5}$$

with $|\bar{\sigma}_N|$ the mean average of the normal stresses within the sample. To keep this value below 10% of the applied shear stress the ratio between w and h should be larger than 7.5. According to G'Sell et al. [1983], the linear variation of the normal forces turns out to be a highly conservative approximation and a more realistic distribution of $|\sigma_N|$ would lead to a decrease of the minimum ratio between w and h.

A final limitation is set by the maximum loading capacity of the shear testing machine. Therefore the area of the shear plane should be lower than

$$wt < \frac{F_{S,\max}}{\tau_{\max}} . \tag{3.6}$$

Other limitations on the dimensions can arise depending on the technical implementation of the shear testing equipment, especially of the clamping system. For the shear tester presented in the next section an additional limitation on the thickness comes from the requirement to maintain through-thickness homogeneity and relates to the materials hardness, the applied clamping pressure and the clamped area. No mathematical relationship has been established for this, but the harder the material, the thinner the sample or the larger the clamping area and/or clamping pressure have to be.

The various sample dimensions used, are all within the constraints mentioned above with a width varying from 20 mm to 50 mm, a height of the deformation zone between 2.5 mm and 6.5 mm and sheet thicknesses of 1.2 mm and 1.5 mm. The total height of the sample including the clamped areas is about 100 mm.

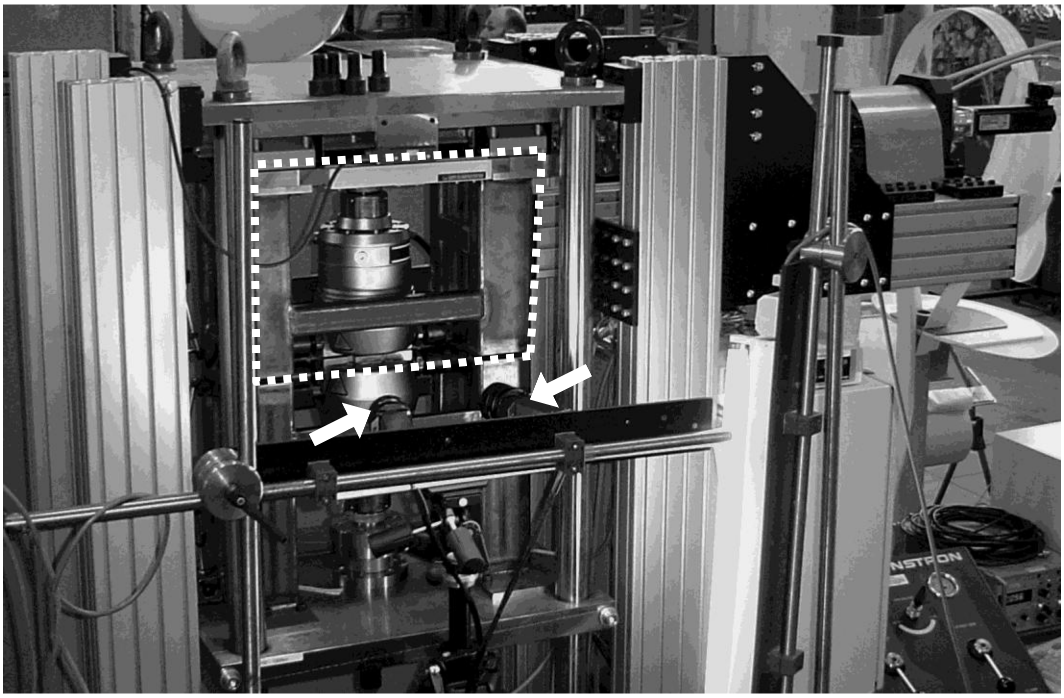

Fig. 3-5 : Picture of the shear tester constructed at the department MTM as a part of this Ph. D. project. The part demarcated with a white dotted rectangle can move left or right. The white arrows point to the cameras of the strain mapping system.

3.2.2 Shear tester

In order to perform tests in simple shear a shear tester has been built (fig. 3-5). The design is based on the biaxial shear tensile machine developed at the Université de Liège (ULg) by Flores and co-workers [Flores et al.; 2005; 2006]. The essential difficulty of rigidly fixing the sample into the machine is resolved by using hydraulic wedge grips commonly used for fatigue testing with clamp inserts specially adapted for shear tests. The wedge angle of the inserts is decreased by 1° in order to have the highest clamping pressure at area closest to the deformed zone. The surface in contact with the sample is entirely covered with teeth and not chamfered at the top. A pressure of 35-40 MPa is applied resulting in sufficient clamping throughout the test without material flow within the clamping zone and a low probability of fracture between the deformed zone and the clamped part of the sample.

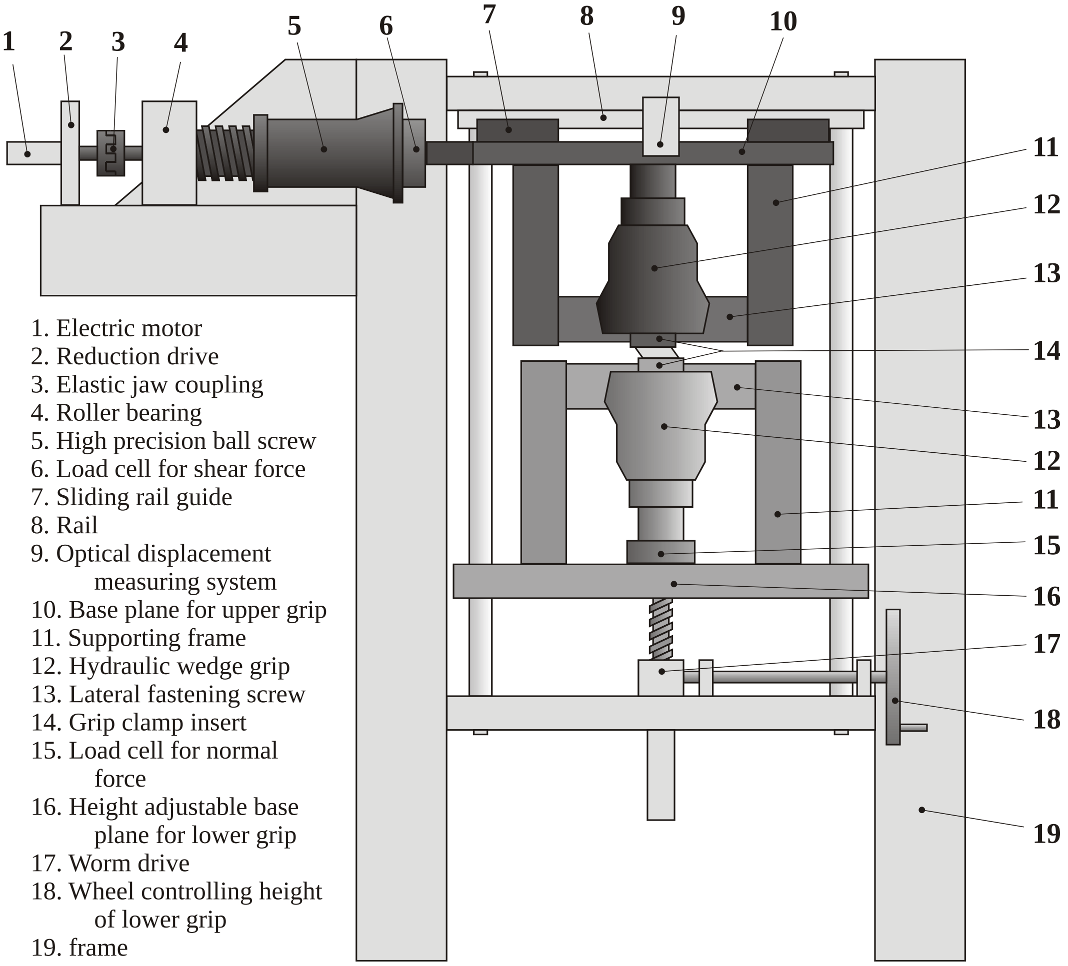

1. Electric motor
2. Reduction drive
3. Elastic jaw coupling
4. Roller bearing
5. High precision ball screw
6. Load cell for shear force
7. Sliding rail guide
8. Rail
9. Optical displacement measuring system
10. Base plane for upper grip
11. Supporting frame
12. Hydraulic wedge grip
13. Lateral fastening screw
14. Grip clamp insert
15. Load cell for normal force
16. Height adjustable base plane for lower grip
17. Worm drive
18. Wheel controlling height of lower grip
19. frame

Fig. 3-6 : Schematic drawing of the simple shear tester. Components operational in moving the upper grip right or left are indicated in dark gray, components operational in adjusting the height of the lower grip in medium gray and fixed components in light gray.

Fig. 3-6 shows a schematic drawing of the shear tester. The upper grip can be moved left or right in order to impose a simple shear deformation. Its base plane (10) is mounted on a rail (8) and is connected to a high precision ball screw (5) which translates the rotational motion of the electric motor (1) into a linear motion. The motor is displacement controlled by an optical displacement measuring system (9) fixed to the rail. This setup can generate a shear load up to 50 kN. The force is measured by a load cell (6) connecting the ball screw with the

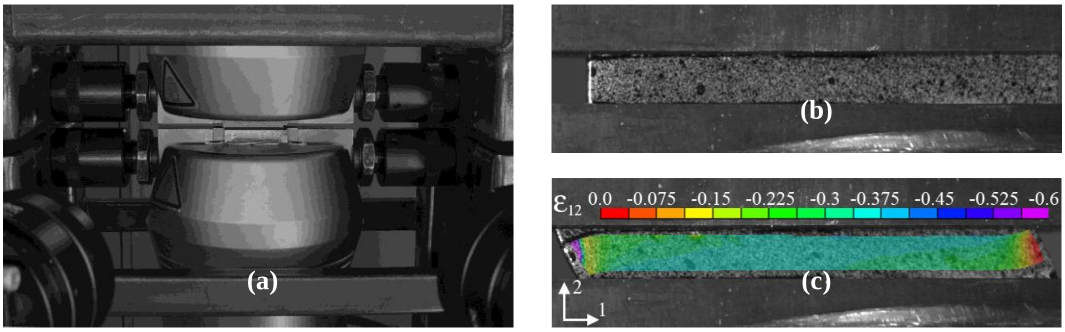

Fig. 3-7 : (a) A sample clamped in the shear tester. In the bottom corners two cameras of a strain mapping system are visible. The four lateral fastening screws (13) connecting clamp inserts (14) to the supporting frame (11) mentioned in fig. 3-6 are clearly visible. (b) Detail of the deformation zone of the sample prior to testing. The surface is covered with a speckle pattern for strain mapping. (c) The deformation zone at $\gamma = 0.65$. An overlay of the strain field calculated from strain mapping results shows the homogeneity of the deformation.

base plane. The accuracy of the force measurement is 0.01 kN. The high precision ball screw guarantees a positional accuracy of about 2 µm. The linear speed range of the set-up is between 0.01 mm/min to 5 mm/min. A supporting frame (11) is placed around the hydraulic grip and lateral fastening screws (13) are mounted directly on the clamp inserts to transfer the displacement of the base plane to the upper half of the sample (fig. 3-7 (a)). The components of the shear tester that move during the lateral displacement of the upper grip are indicated in dark gray in fig. 3-6.

The lower grip is mounted on a base plane (16) which can be adjusted in height by a wheel (18). This controls the height of the deformation zone. The base plane of the lower grip is fixed to the frame before testing by clamping it to the four shafts with screws. A load cell (15) between the grip and the base plane measures the normal force.

3.2.3 Strain mapping system

To characterise the strain field of the deformed zone a strain mapping system is used from Limess Gmbh. It reconstructs the evolution of the displacement field by correlating the images taken simultaneously from two CCD cameras in different positions and comparing the 3D positions of pixels on the sample surface with their initial position. To increase the reliability and resolution of the technique a random speckle pattern is painted on the area of the sample to be deformed (fig. 3-7 (b)). At the shear tester, the two cameras are placed symmetrically in front of the sample at a distance of about 40 cm at an angle of about 15° from the sample normal (fig. 3-7 (a)). Successive images are taken at a rate of 0.2 s^{-1} during elastic and early plastic deformation and 0.034 s^{-1} during further deformation when the stress increases at a much lower rate. The obtained displacement field is converted into a strain field after an eventual correction of the measurement system's reference frame by maximizing the displacement in the shear direction. The shear component ε_{12} of the strain field is shown in fig. 3-7 (c).

Apart from the edges the strain field is very homogeneous. The average of the ε_{12} component is calculated taking only the pixels into account that have the 11-component (normal component along the width of the deformation zone) of the deformation gradient tensor $\mathbf{F}$ within 0.5% of 1, this in order to filter out the edge zones. That the average is obtained from of a homogeneously deformed area is furthermore controlled by omitting all pixels that violated the previous requirement in earlier deformation steps. If the number of pixels included in the calculation of the average gets lower than 80% of the total number of pixels, the deformation field is regarded as inhomogeneous and no average is calculated. Only samples with a limited width to height ratio show a homogeneous area of less than 80% of the total deformed zone after a moderated deformation, indicating that the normal forces exerted by the grips on the sample (cf. section 3.2.2) are the main cause for the strain inhomogeneity at the edges.

The resolution of the strain mapping technique is mainly depending on the quality of the speckle pattern (spatial and size distribution of the speckles) and the contrast of the images. Adequate illumination to improve the contrast is indispensible. An estimate obtained from the elastic parts of the stress-strain curves indicates that a resolution of the strain of 0.1% is certainly feasible.

3.3 Mechanical work hardening behaviour

To characterise the work hardening behaviour of sheet materials, tests in simple shear will be used. To obtain SPC tests with highly different straining modes, prestrain deformation will be achieved by conventional cold rolling. Both types of deformation couple a homogeneous deformation with a known and stable straining mode with the possibility to achieve a high amount of strain.

3.3.1 Monotonic hardening behaviour

The work hardening behaviour of the AA3103 aluminium alloy under monotonic conditions has been characterised by tests in simple shear, using the equipment presented in the previous section.

a) Macroscopic stress-strain curve

Rectangular samples with dimensions as presented in section 3.2.1 are used with the longest side parallel to the rolling direction of the hot rolling process and the width parallel to the transverse direction. The shear that is imposed can be described in the macroscopic reference frame attached to the sample (rolling direction (RD) - transverse direction (TD) - normal direction (ND)) by the velocity gradient tensor:

$$\mathbf{L} = \begin{bmatrix} 0 & 0 & 0 \\ \dot{\gamma} & 0 & 0 \\ 0 & 0 & 0 \end{bmatrix}. \tag{3.7}$$

The shear direction is parallel to TD while the transverse plane TD-ND is the shear plane (cf. fig. 3-8). The shear imposed on the sample is obtained from the strain mapping system as described in section 3.2.3. The velocity of the electro-mechanical piston is set to obtain a constant strain rate of about $5.0 \cdot 10^{-4}\ \mathrm{s}^{-1}$. The measured shear force F_S is converted into the shear stress σ_{21} by using equation (3.2). The initial elastic part of the curve is used to obtain an estimate of the shear modulus G by linear regression. Values of G are in the range of 23 to 35 GPa, which compare to the literature value for aluminium of 26 GPa. The plastic shear strain γ_p is obtained by lowering the total shear strain with the elastic shear strain.

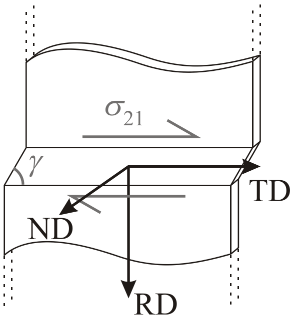

Fig. 3-8 : Diagram showing how samples are deformed in simple shear.

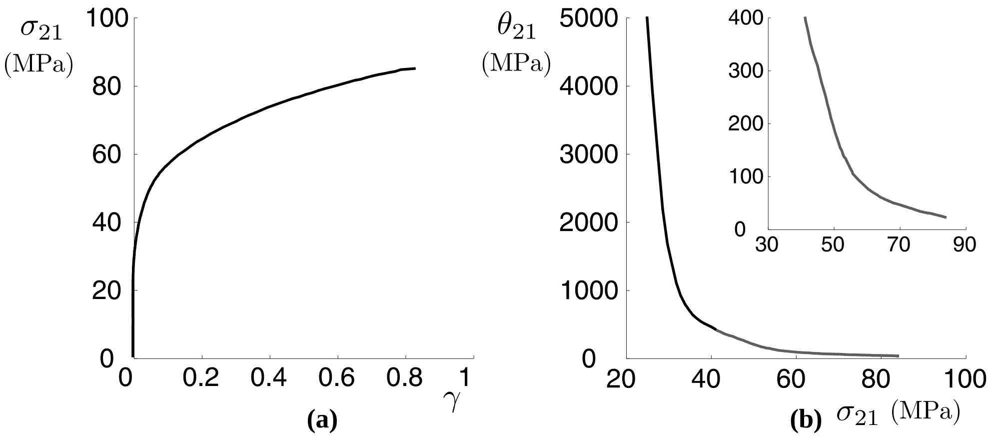

Fig. 3-9 : (a) Stress-strain curve of monotonic simple shear test (b) Corresponding hardening rate-stress curve. The inset shows the last part of the curve on another length scale.

For simplicity, from now on ‘strain’ will refer to ‘plastic strain’. All obtained stress-strain curves from different experiments (with different dimensions of the deformation zone) are within 3% of the averaged curve, showing a very good reproducibility. Tests performed on the biaxial testing machine of ULg made for comparison showed a similar result. The hardening rate

$$\theta_{21} = \frac{d\sigma_{21}}{d\gamma} \tag{3.8}$$

is obtained as the derivative of a locally fitted 3rd order polynomial taking 21 measurement points of the stress-strain curve into account, corresponding to a strain interval of minimum $\left[\gamma - 0.025 \quad \gamma + 0.025\right]$ and maximum $\left[\gamma - 0.15 \quad \gamma + 0.15\right]$, depending on the current sampling frequency of the strain mapping system. A smoothed stress-strain curve is calculated as the integral of the obtained hardening rate-strain curve. This final step is useful to maintain consistency between the values of hardening rate, stress and strain and to remove staircase like evolutions of the stress due to the limited accuracy of the load cell (0.01 kN) whenever the stress evolves slowly with increasing strain e.g. during strain path changes. It is checked that the measured and smoothed value of the stress are always within the accuracy of the load cell. Fig. 3-9 shows the stress-strain curve and the corresponding hardening rate-stress curve of a monotonic simple shear test up to a strain of 0.83.

b) Microscopic stress-strain curve

In order to get a better insight into the hardening mechanisms on the micro scale and to derive material parameters for a work hardening model, the stress-strain response, measured at the macro scale has to be related to the acting stresses and strains at the level of the slip systems in the individual grains. The macroscopic stress-strain curve $\sigma_{21}(\gamma)$ has to be converted into a microscopic stress-strain curve $\tau_{ref}(\Gamma)$ which represents the average hardening behaviour of the individual grains. τ_{ref} is a reference value for the critical resolved shear stresses on the active slip systems in a grain and the "total shear" Γ is the sum of slip on these slip systems. These microscopic values are related to their macroscopic counterparts by the Taylor factor M (cf. equation (A.1)):

$$M = \frac{d\Gamma}{d\varepsilon_{eq}} = \frac{\dot{\Gamma}}{\dot{\varepsilon}_{eq}}, \tag{3.9}$$

which is a geometric factor that links the sum of the slip rates $\dot{\Gamma}$ to a macroscopic equivalent strain rate $\dot{\varepsilon}_{eq}$ and which therefore can have a different value for each grain.

To calculate the Taylor factor some approximations have to be made. If it is assumed that a grain with a known crystallographic orientation deforms homogeneously, its Taylor factor for a certain straining mode can be calculated by the Taylor model. Because in a polycrystal, grains have different orientations, they also have different Taylor factors. If it is further assumed that every grain undergoes the same macroscopic strain (FC Taylor approximation), it would follow from the definition of the Taylor factor (equation 3.9) that every grain will accumulate a different amount of total shear strain Γ. Nevertheless, it is assumed that a good approximation of the average hardening behaviour of all grains (the functional dependence of τ_{ref} with Γ) can be obtained as $\tilde{\tau}_{ref}(\overline{\Gamma})$ [Tomé et al.; 1984] where $\tilde{\tau}_{ref}$ is the weighted average of τ_{ref} of all grains with their *M*-factor as weighting factor, so that

$$\overline{\sigma_{eq}} = \overline{M}\tilde{\tau}_{ref}. \tag{3.10}$$

$\overline{\Gamma}$ is the average amount of total microscopic shear or slip which can be obtained as

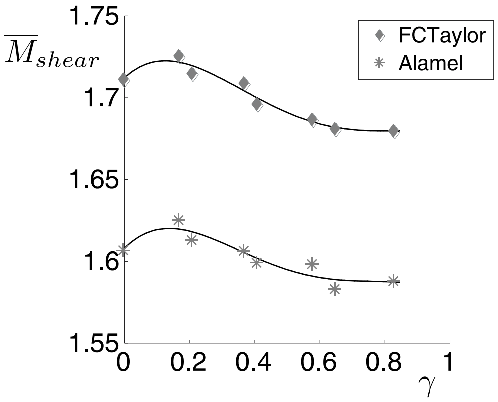

Fig. 3-10 : Evolution of the $\overline{M}$ -factor with strain in simple shear test as calculated with the FC Taylor model and the A-Lamel model. The black lines indicate the 4th order polynomial fit.

$$\overline{\Gamma} = \int \overline{M}\left(\varepsilon_{eq}\right) d\varepsilon_{eq} \,, \tag{3.11}$$

with $\overline{M}$ the average Taylor factor. The microscopic stress-strain curve $\tilde{\tau}_{ref}\left(\overline{\Gamma}\right)$ can be obtained from the macroscopic stress-strain curve by using equation (3.10) to obtain values for $\tilde{\tau}_{ref}$ and equation (3.11) to obtain the corresponding values for $\overline{\Gamma}$. More details on the Taylor factor and a discussion on equation (3.10) can be found in appendix A.

The functional dependence of the average *M*-factor on the strain is obtained from fitting a 4th order polynomial through $\overline{M}$ -values calculated from experimental textures measured at certain shear strains with the FC Taylor model (cf. section 2.1.2.a) and the A-Lamel model (cf. section 4.1.2.b) assuming equal critical resolved shear stresses on each slip system. 2000 discrete orientations are obtained for these models from the orientation distribution function (ODF) using a statistical model [Tóth and Van Houtte; 1992]. The A-Lamel model assumes that the initial grain shape is spherical. These grain shapes are made ellipsoidal according to the simple shear deformation. Fig. 3-10 shows the obtained values for both models. Due to the allowed relaxations in the A-Lamel model, the macroscopically implied deformation can be obtained by activating fewer slip systems per grain, so that the total amount of microscopic slip will be less than in the FC Taylor case, which results in a lower $\overline{M}$ -factor. The $\overline{M}$ -factor in both

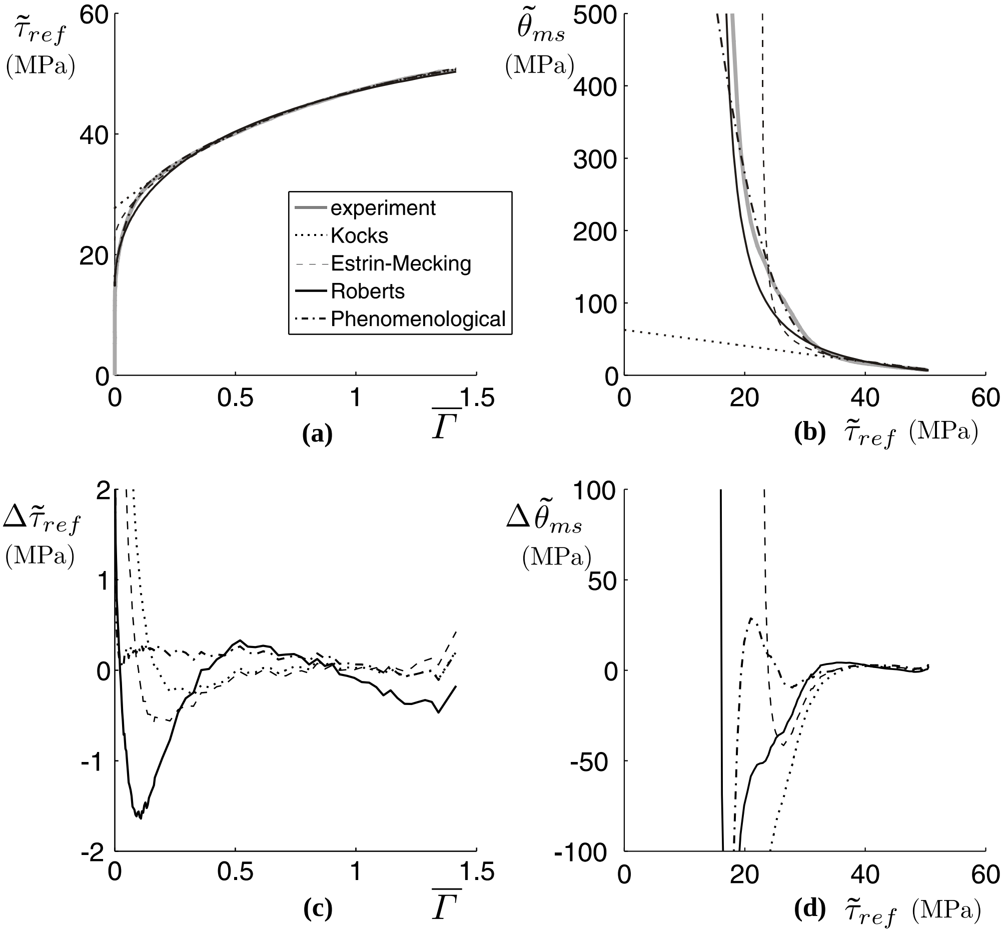

Fig. 3-11 : (a)+(b) Microscopic stress-strain curve and corresponding hardening rate-stress curve of fig. 3-9 calculated with the $\overline{M}$ -factor according to FC Taylor in fig. 3-10. Four fitted hardening models are displayed. In (c)+(d) difference values with the experimental curve for respectively the stress and the hardening rate are shown.

cases only varies slightly over the investigated strain range. Assuming a constant value would already result in a good approximation. Nevertheless the 4th order polynomial is used to obtain $\overline{\Gamma}$, as solving equation (3.11) is straightforward.

Fig. 3-11 (a) and (b) show the microscopic stress-strain and hardening rate-stress curve derived from the data of fig. 3-9 by using the $\overline{M}$ -factors obtained with the

FC Taylor model. The average hardening rate during monotonic straining $\tilde{\theta}_{ms}$ is defined as

$$\tilde{\theta}_{ms} = \frac{d\tilde{\tau}_{ref}}{d\overline{\Gamma}}. \tag{3.12}$$

Due to the only slight deviations in the $\overline{M}$-factor, both the $\tilde{\tau}_{ref}$ - $\overline{\Gamma}$ and the $\tilde{\theta}_{ms}$ - $\tilde{\tau}_{ref}$ curve have the same appearance as their macroscopic equivalents.

c) Selecting a work hardening model

Four different work hardening models are fitted to the microstructural stress-strain data. This is done by minimizing a weighted sum of squares of the difference of the experimental and calculated stress. The weights are made higher with increasing stress in order to obtain the best fit towards the highest strains. In appendix B the four models are derived and related to microscopic hardening mechanisms. Here only the correspondence to the experimental data and the obtained fitting parameters presented in table 4 will be discussed.

The Kocks work hardening model [Kocks; 1970, Kocks and Mecking; 2003] (cf. sections 2.1.3.b and B.1) is a three parameter model which fits the stress-strain curve very good from a strain of 0.2 onwards. This corresponds to a stress of 35 MPa and to the start of a linear decline in the hardening rate-stress curve. At lower strains the stresses are overestimated, while the hardening rate is much too low compared to the experimental one. This results in a lattice friction τ_0 that is highly overestimating the experimentally observed one.

The hardening mechanism modelled by Kocks is the interaction of mobile dislocations with the dislocation forest combined with a dynamic recovery mechanism proportional to the current dislocation density. Using equations (B.5) and (B.6) with $\alpha = 0.3$ and $G = 28\,\text{GPa}$, estimates are obtained for the average length of recovered dislocation line $L_R \approx 2.5b$ (22) and the proportionality constant $K \approx 120$. Compared to literature data for aluminium [Kocks and Mecking; 2003], L_R is an order of magnitude too low, while K is an order of magnitude too large. This would mean that dislocation segments can pass much easier forest obstacles but are much more slowly recovered, if these values would reflect physical reality.

---

[22] b is the length of the Burgers vector, which for aluminium is about 0.286 nm

Table 4 : Fitting parameters of four work hardening models shown in fig. 3-11. All values are in MPa, except the dimensionless values for κ.

	FC Taylor					A-Lamel				
	τ_0	τ_{sat}	θ_0	κ		τ_0	τ_{sat}	θ_0	κ	
Kocks	27.7	56.8	62.9			29.0	57.9	78.4		
Estrin-Mecking	22.4	60.0	39.1	0.8		24.7	65.7	39.1	0.8	
Roberts	14.8	59.8	24.4			16.3	69.4	20.7		
Phenomenological	τ_0	τ_A	θ_A	τ_B	θ_B	τ_0	τ_A	θ_A	τ_B	θ_B
	16.5	28.6	586.3	56.9	61.0	16.4	28.7	722.5	58.5	79.4

The model of Estrin and Mecking [1984] extends the Kocks model with hardening due to dislocation storage at precipitates. With this model a strong upward shift from the linear stage III behaviour in the low stress region of the hardening curve can be obtained. This lowers the value of τ_0 compared to the fit with the Kocks model, while the fit for the rest of the curve remains equally good. Estimated values for physical parameters are obtained from equations (B.11), (B.12) and (B.15). $L_R \approx 1.3b$ is even lower than the one from the Kocks model fit, while $K \approx 210$ is almost doubled. The inter particle distance derived from the fit $l_{part} \approx 50$ µm is in good agreement with the experimental data.

The third model of Roberts [1982] proposes a constant dislocation storage rate with a dynamic recovery mechanism which scales with the square root of the dislocation density. The constant storage rate indicates that the average length a mobile dislocation segment can shear through the material remains constant during the deformation, unlike in the model of Kocks where it decreases. The model achieves a reasonably good fit for the whole stress-strain curve, although it deviates somewhat more from the experimental values than the previous two models in the high strain range. The lattice friction τ_0 is in very good agreement with the experimental value. The parameters of the evolution equation of the dislocation density (B.24) can be obtained using equations (B.26) and (B.27) and correspond to $k_1 \approx 380\ \mathrm{m}^{-2}$ and $k_2 \approx 20\ \mathrm{m}^{-1}$. These values would be unrealistic for any known dislocation storage or recovery mechanism (cf. e.g. equation (B.8)). Although the model gives a good fit, it cannot be used to explain the hardening behaviour of the material.

Finally a phenomenological model is used which achieved the best possible fit of the experimental data. The stress is related to the strain according to

$$\tau = \tau_B - \left(\tau_B - \tau_A\right)\exp\left(-\frac{\theta_B}{\tau_B}\Gamma\right) - \left(\tau_A - \tau_0\right)\exp\left(-\frac{\theta_A}{\tau_A}\Gamma\right). \qquad (3.13)$$

τ_0, τ_A, τ_B, θ_A and θ_B are five fitting parameters. τ_0 corresponds to the lattice friction and τ_B to the saturation stress. No analytical dependence of the hardening rate to the stress can be derived from equation (3.13), so it cannot be used to gain insight in the storage and recovery mechanisms.

3.3.2 Cross tests

To achieve a strain path change that has orthogonal straining modes ($\theta = 90°$ in equation (1.2)) a combination of a cold rolling test followed by simple shear is carried out. The straining mode of cold rolling is in fact only orthogonal to the straining mode of simple shear if the shear plane normal (SPN) and shear direction (SD) are parallel to the principle directions of the rolling deformation. This is the case if, like in the monotonic tests before (cf. fig. 3-8), RD is taken parallel to SPN and TD parallel to SD. The Schmitt parameter (equation (1.2)) becomes:

$$\cos\theta = \frac{1}{\sqrt{2}}\begin{bmatrix}1 & 0 & 0\\ 0 & 0 & 0\\ 0 & 0 & -1\end{bmatrix} : \frac{1}{\sqrt{2}}\begin{bmatrix}0 & 1 & 0\\ 1 & 0 & 0\\ 0 & 0 & 0\end{bmatrix} = 0 = \cos\left(90°\right). \qquad (3.14)$$

On the microscopic scale this orthogonality guarantees the activation of different sets of crystallographic slip systems in both straining modes [Schmitt et al.; 1985]. The succession of two deformation experiments with orthogonal straining modes is often called a cross test.

In this section, first the details of the cold rolling operation are documented and discussed. Secondly the obtained stress-strain curves of the simple shear tests of samples that are prestrained in cold rolling are analysed.

a) Prestrain in cold rolling

All rolling operation have been performed on a Wellman cold rolling mill with a diameter of the rolls of 154.75 mm, and a rolling speed of 0.203 m/s. The rolling height is adjustable. The starting thickness of the as received plate is 1.50 mm and thickness reductions up to 0.90 mm or 40 % are performed in one rolling pass. These conditions result in a relatively high contact length compared to the thickness reduction, which might lead to some superficial transversal shear strains [Verlinden et al.; 2007]. The Δ-factor[23] defined by Hosford and Caddell [1983] remains for all tests below 1 (the highest Δ-factor 0.52 is obtained for the lowest thickness reduction of 6.7 %), which indicates a good through-thickness

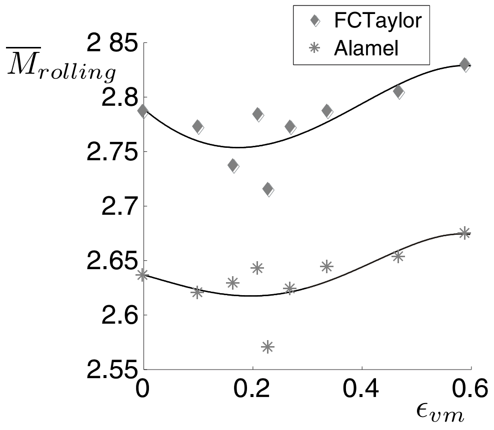

Fig. 3-12 : Evolution of the $\overline{M}$-factor with strain during cold rolling as calculated with the FC Taylor model and the A-Lamel model. The black lines indicate the 4th order polynomial fit.

---

[23] The Δ-factor is defined as the thickness divided by the contact length in the deformation zone, for sheet rolling, it is calculated as $\Delta = \frac{2-r}{r}\sqrt{\frac{h_0}{rR}}$ with r the thickness reduction, R the radius of the rolls and h_0 the initial sheet thickness.

homogeneity of the deformation. If strain inhomogeneities occur, they will be limited to the surface layer of the sample. For texture measurements the samples are ground and polished to the mid plane in order to obtain the orientation distribution of the homogeneously deformed bulk.

From texture measurements on samples deformed in cold rolling to different rolling reductions, $\overline{M}$-factors for the von Mises strain rate $\dot{\varepsilon}_{vm}$ are calculated with the FC Taylor model and the A-Lamel model (cf. section 3.3.1.b). In fig. 3-12 the evolution of the $\overline{M}$-factor with strain for both models is shown. As in the case of simple shear, the A-Lamel model predicts a somewhat lower value for the $\overline{M}$-factor because on average less slip systems are activated (cf. section 3.3.1.b). Compared to simple shear, the $\overline{M}$-factor values are more scattered and have a more varying course.

An equivalent amount of microscopic slip $\overline{\Gamma}$ can be derived using equation (3.11). An estimate of the amount of macroscopic prestrain γ for the successive simple shear test can be obtained from the microscopic slip $\overline{\Gamma}$, using the inverse of the relationship between the macroscopic shear γ and $\overline{\Gamma}$ obtained in section 3.3.1.b. The differences between the values of the equivalent amount of simple shear obtained with either FC Taylor or A-Lamel are limited to 1%. For reasons of simplicity the ones obtained with the FC Taylor model will be used further on.

b) Stress versus strain after the strain path change

In fig. 3-13 (a) the microscopic stress-strain curves of several cross tests with different amounts of prestrain are shown. The microscopic stress-strain curves are derived from the measured macroscopic stress-strain curves in exactly the same way as for the monotonic deformation tests (cf. section 3.3.1.b), using a linear interpolation of the $\overline{M}$-factor for evaluating equations (3.10) and (3.11), between the values calculated from two textures, one measured after rolling and the other after the second straining in simple shear. The prestrain is calculated as explained in the previous section. As a reference, the monotonic hardening curve of simple shear (fig. 3-11) is indicated as a dashed line.

After the SPC the reyielding occurs at a higher level than the flow stress of the monotonic curve at the same amount of microscopic strain (fig. 3-13 (a)). Since the anisotropy due to texture differences is cancelled out by the transition from the macroscopic to the microscopic stress-strain curves, this higher flow stress is

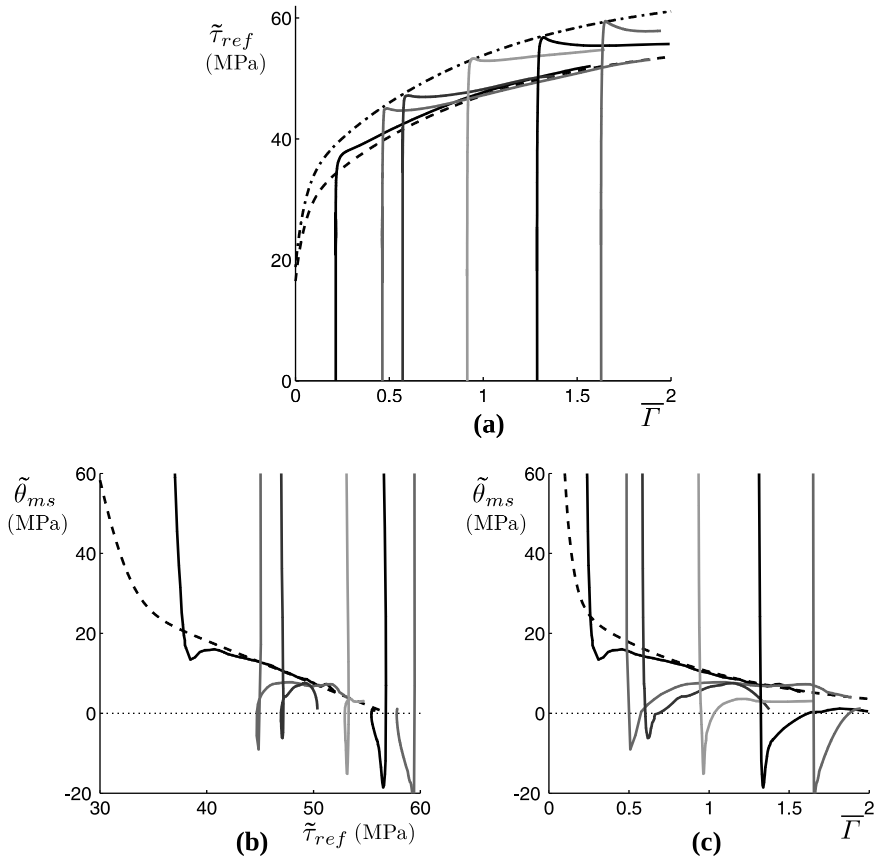

Fig. 3-13 : (a) Microscopic stress-strain curve of samples deformed in simple shear after a certain amount of prestraining in cold rolling. The curves are shifted with the equivalent amount of microscopic strain accumulated in the cold rolling deformation which is obtained from the evolution of the $\overline{M}$ -factor as displayed in fig. 3-12. (b) and (c) hardening rate-stress and hardening rate-strain curves corresponding to the curves of (a).

caused by the anisotropy of the substructure built up during prestraining as explained in paragraph 2.3. The average critical resolved shear stress τ_{ref} just after the strain path change is about 15 % higher (dash-dotted line in fig. 3-13 (a)) than the monotonic reference curve (dashed line).

The work hardening rate just after the SPC quickly drops below the work hardening curve of the monotonic case (fig. 3-13 (b)). At higher prestrains, in this case for a microscopic prestrain above 0.5, work softening occurs. With further straining the work hardening rate tends to evolve back towards the monotonic hardening rate-stress curve. Once the hardening rate-stress curve coincides with the monotonic curve, the monotonic curve is in most cases very closely followed.

This is difficult to see for the samples with a higher prestrain, since the stress does not change too much at low hardening rates, but the corresponding hardening rate-strain curves (fig. 3-13 (c)) indicate that the deformation continues for a considerable amount of strain. At lower prestrains the stress-strain curves and the hardening rate-strain curves return to the monotonic reference curves as well. This certainly is not valid for larger prestrains.

c) Contributions to the macroscopic work hardening

For one of the cross tests (corresponding to the second lowest amount of prestrain in fig. 3-13) the macroscopic stress-strain and the corresponding work hardening curve are shown in fig. 3-14. For this amount of prestrain, after the transient regime both the microscopic stress-strain and hardening rate-stress curves coincide with the monotonic curves (cf. fig. 3-13). This is clearly not the case for their macroscopic counterparts.

The macroscopic hardening rate can be decomposed into a contribution due to substructural hardening and a contribution due to texture changes. Equation (3.10) derived with respect to the macroscopic strain results in

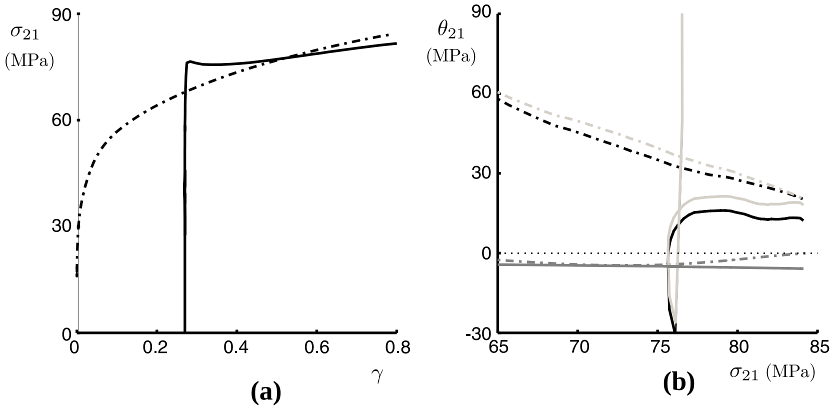

Fig. 3-14 : The macroscopic stress-strain (a) and hardening rate-stress curve (b) for the cross test with (microscopic) prestrain $\overline{\Gamma}_{pre}$ = 0.46. In (b) the substructural and textural hardening contributions are plotted in light and dark grey respectively. As a reference the same curves are shown for monotonic simple shear in dash-dotted lines.

$$\frac{d\bar{\sigma}}{d\varepsilon_{eq}} = \overline{M}^2 \frac{d\tilde{\tau}_{ref}}{d\bar{\Gamma}} + \tilde{\tau}_{ref} \frac{d\overline{M}}{d\varepsilon_{eq}} \tag{3.15}$$

The first term of equation (3.15) gives an estimate of the substructural contribution, and the second term of the textural contribution (cf. appendix A). Both contributions are shown in fig. 3-14 (b) in light and dark grey respectively. The textural contribution is small for both cases. For the monotonic straining it is almost of no importance compared to the substructural one. For the cross test it does influence the overall hardening, since the substructural contribution is relatively low due to the transient behaviour.

3.3.3 Strain Reversal tests

The reversal of the straining mode can be easily performed in a simple shear test. After a prestrain in simple shear, the shear direction just needs to be reversed, which can be done with the shear tester presented in section 3.2.2 in a single test, without unclamping the specimen. The Schmitt parameter (equation (1.2)) becomes:

$$\cos\theta = \frac{1}{\sqrt{2}}\begin{bmatrix} 0 & -1 & 0 \\ -1 & 0 & 0 \\ 0 & 0 & 0 \end{bmatrix} : \frac{1}{\sqrt{2}}\begin{bmatrix} 0 & 1 & 0 \\ 1 & 0 & 0 \\ 0 & 0 & 0 \end{bmatrix} = -1 = \cos(180°) \tag{3.16}$$

It is most likely that on the microscopic scale the same slip systems will remain active, but in the opposite slip direction as before the SPC [Schmitt et al.; 1985].

Although equation (3.16) applies regardless of how the sample is loaded in simple shear, the same orientation of the sample with respect to the shear plane normal and shear direction as in the monotonic case (cf. fig. 3-8) is used for the strain reversal tests discussed below. The deformation behaviour before the SPC is therefore the same as in the monotonic tests described in section 3.3.1. The dependence of the $\overline{M}$-factor on the macroscopic shear γ as represented in fig. 3-10 can be used to obtain the microscopic prestrain $\bar{\Gamma}$ using equation (3.11).

In fig. 3-15 (a) the microscopic stress-strain curves after strain reversal for four different amounts of prestrain are shown. The stress-strain curve of the monotonic loading is depicted as a dashed line. In order to obtain the microscopic stress-strain curves from the measured macroscopic stress-strain curves, a linear dependence of the $\overline{M}$-factor with the macroscopic strain is assumed, between the

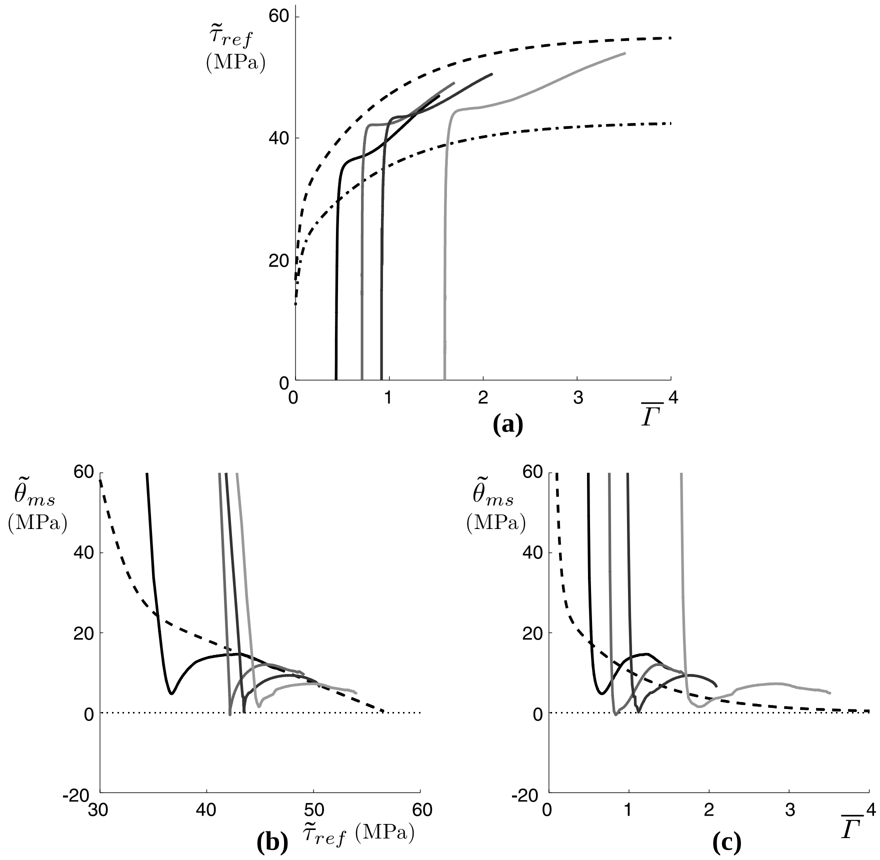

Fig. 3-15 : (a) Microscopic stress-strain curve of samples deformed in simple shear after a certain amount of prestraining in simple shear in the opposite direction. The curves are shifted with the equivalent amount of microscopic strain accumulated in the prestrain which is obtained from the evolution of the $\overline{M}$ -factor as displayed in fig. 3-10. (b) and (c) hardening rate-stress and hardening rate-strain curves corresponding to the curves of (a).

$\overline{M}$ -factor obtained from fig. 3-10 at the prestrain and the one calculated from the measured texture of the sample at the end of the test.

After the SPC a clear Bauschinger effect (cf. section 2.3.1.a) is visible. Reyielding occurs at a much lower stress than the flow stress of the monotonic curve at the same amount of microscopic strain. The average critical resolved shear stress τ_{ref} at strain reversal is about 25% lower (dash-dotted line in fig. 3-15 (a)) compared to its value just before the SPC (dashed line). The work hardening rate decreases in a short strain interval after yielding to a value below the monotonic work hardening curve (fig. 3-15 (b)). With further straining the workhardening rate reaches a minimum and after an increase, it returns to the work hardening curve of the monotonic deformation. This resembles very much the transient work hardening behaviour observed during cross tests (cf. section 3.3.1.b), although in the case of strain path reversal only very limited strain softening is observed at higher prestrains. The corresponding stress-strain curves (fig. 3-15 (a)) clearly show this stagnation of the work hardening as a plateau at a certain stress-level after which hardening resumes. Due to the relatively large difference between the stress of the reversal deformation compared to the monotonic case, it is more clear than for cross tests that the work hardening rate-stress curve after a transient regime coincides again with the monotonic work hardening curve (fig. 3-15 (b)) and that this is not the case for the hardening rate-strain curve (fig. 3-15 (c)).

3.3.4 Other strain path changes

In this section the results of the work hardening behaviour after intermediate changes in the strain path are discussed. Two strain path changes which are intermediate to the continuation of the monotonic deformation and the orthogonal SPC with Schmitt parameters (equation (1.2)) of $\theta = 30°$ and $\theta = 60°$ and one intermediate to the orthogonal SPC and complete strain reversal with $\theta = 120°$ are characterised. In all cases the microscopic work hardening curve is obtained from the measured microscopic one in an equivalent manner as discussed for the cross and the reversal tests (sections 3.3.2 and 3.3.3), by assuming a linear dependence of the $\overline{M}$ -factor during the second straining mode.

a) Strain path change with $\theta = 30°$

An SPC with Schmitt parameter (equation (1.2)) $\theta = 30°$ is achieved by cutting a smaller test specimen out of a 60 mm wide sample deformed in simple shear with a height of the deformed zone as large as 4 mm (cf. section 3.2.1). An angle of 15° around ND between the shear direction for the second strain mode and TD is imposed. It is paid attention to that the deformation zone of the cut out sample is contained within the homogeneously deformed zone of the prestrain. The obtained samples for the second deformation in simple shear have a width of 20 mm and a height of the deformation zone of 2 mm. Fig. 3-16 depicts how the

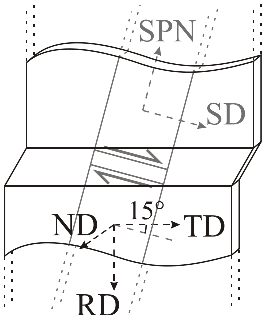

Fig. 3-16 : Diagram showing how a sample is obtained from a deformed sample in simple shear to achieve a strain path change with Schmitt parameter cosθ = cos(30°).

macroscopic reference frames of the two deformations relate to each other. The Schmitt parameter (equation (1.2)) is obtained as

$$\cos\theta = \frac{1}{\sqrt{2}}\begin{bmatrix} 0 & 1 & 0 \\ 1 & 0 & 0 \\ 0 & 0 & 0 \end{bmatrix} : \frac{1}{\sqrt{2}}\begin{bmatrix} -0.5 & \cos(30°) & 0 \\ \cos(30°) & 0.5 & 0 \\ 0 & 0 & 0 \end{bmatrix} = \cos(30°) \qquad (3.17)$$

Fig. 3-17 shows the stress-strain, work hardening rate-stress and work hardening-strain curves for SPC tests with cosθ = 30° for two different amounts of prestrain. The work hardening behaviour of the monotonic test is indicated as a dashed line. It is noted from fig. 3-17 (a) that the yield stress just after the strain path change is noticeably larger than the flow stress of the monotonic curve at the same amount of microscopic shear. The work hardening rate initially decreases rapidly with strain but starts to return towards the monotonic behaviour already when the work hardening rate it still larger than that of the monotonic case at the same stress. The work hardening curve after the SPC eventually falls below the monotonic work hardening curve, and for the higher prestrain a work hardening stagnation is observed. Also for this SPC the work hardening-stress curve will after the transient behaviour coincide with the monotonic work hardening curve.

As can be clearly seen in fig. 3-17 (c) the transient part in the work hardening curve (from the prestrain value to the point where the curve becomes parallel to the monotonic case) covers a large strain interval which does not depend on the amount of prestrain. The stress-strain curve (fig. 3-17 (a)) of the sample with the larger prestrain offers a distinct example of permanent hardening. In order to make the monotonic stress-strain curve to coincide with the part of the curve after

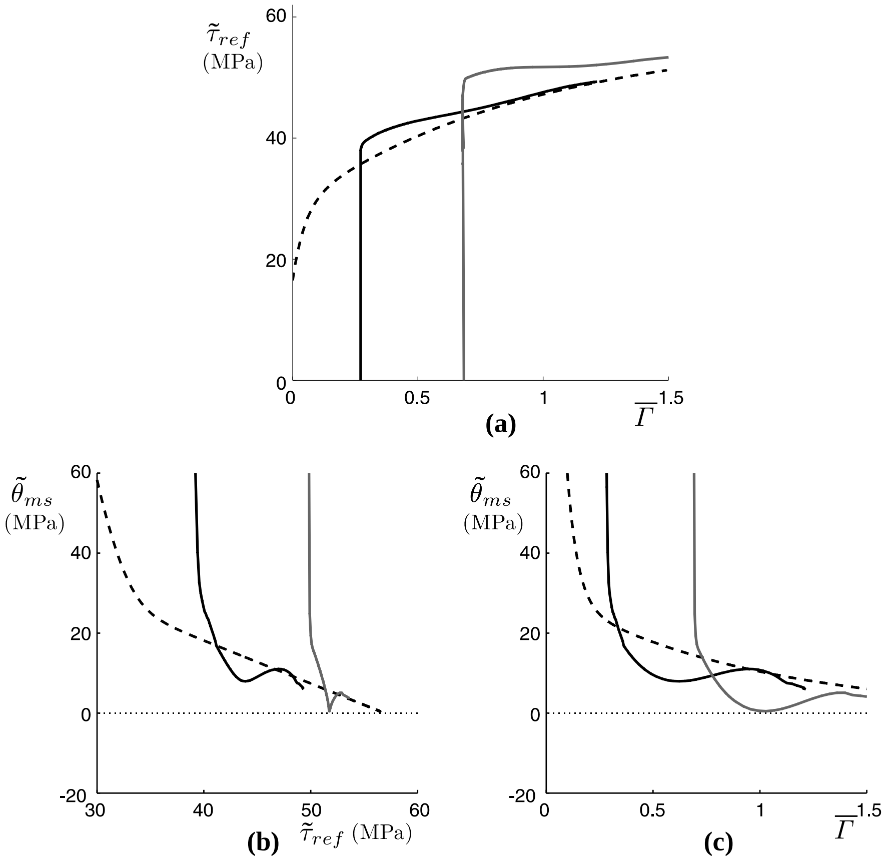

(a)

(b)

(c)

Fig. 3-17 : (a) Microscopic stress-strain curve of samples deformed in simple shear after a certain amount of prestraining in simple shear on another shear plane. The shear plane normals - as well as the shear directions - of the two straining modes are 15° inclined to each another, resulting in a Schmitt parameter θ = 30°. The curves are shifted with the equivalent amount of microscopic strain accumulated in the prestrain which is obtained from the evolution of the $\overline{M}$ -factor as displayed in fig. 3-10. (b) and (c) hardening rate-stress and hardening rate-strain curves corresponding to the curves of (a).

the transient behaviour (from about $\overline{\Gamma}$ = 1.4 onwards), the monotonic curve needs to be shifted with a negative amount of strain of γ_0 = -0.43 (cf. fig. 2-13 (a)).

b) Strain path change with $\theta = 60°$

To obtain strain path changes with Schmitt parameter $\theta = 60°$, a sample for simple shear is cut out of a cold rolled plate deformed to a specific prestrain, with the shear plane normal (SPN) and shear direction (SD) at +45° from RD and TD respectively. This combination of straining modes results in a Schmitt parameter (equation (1.2)) equal to

$$\cos\theta = \frac{1}{\sqrt{2}}\begin{bmatrix} 1 & 0 & 0 \\ 0 & 0 & 0 \\ 0 & 0 & -1 \end{bmatrix} : \frac{1}{\sqrt{2}}\begin{bmatrix} 1 & 0 & 0 \\ 0 & -1 & 0 \\ 0 & 0 & 0 \end{bmatrix} = \cos\left(60°\right). \tag{3.18}$$

The obtained microscopic stress-strain and work hardening curves for the deformation after the SPC (fig. 3-18), show the same features as the curves for the cross tests (fig. 3-13), with a higher yield stress after the SPC, a drop in the work hardening rate, resulting in strain softening for the higher prestrains, and a return to the monotonic work hardening-stress curve.

The somewhat different behaviour of the sample with the lowest prestrain is believed to be a measurement artefact which might be due to a small amount of slip of the sample in the clamps. It is unfortunately the only sample obtained for relatively low prestrains.

c) Strain path change with $\theta = 120°$

If a sample which is cut out of a cold rolled sample at an angle of 45° after a prestain as described in the previous section, is sheared in the opposite direction, the Schmitt parameter (equation (1.2)) becomes:

$$\cos\theta = \frac{1}{\sqrt{2}}\begin{bmatrix} 1 & 0 & 0 \\ 0 & 0 & 0 \\ 0 & 0 & -1 \end{bmatrix} : \frac{1}{\sqrt{2}}\begin{bmatrix} -1 & 0 & 0 \\ 0 & 1 & 0 \\ 0 & 0 & 0 \end{bmatrix} = \cos\left(120°\right) \tag{3.19}$$

This is an SPC which is intermediate to the cross test and the reversal test. The microscopic stress-strain curves and work hardening curves of the tests in simple shear for four different amounts of prestrain are shown in fig. 3-19. Also for this SPC the resemblance with the curves of the cross tests (cf. fig. 3-13) is high. Compared with the data for an SPC with $\theta = 90°$ and $\theta = 60°$, the yield stress after the SPC is only slightly higher than the monotonic flow stress at the same amount of microscopic strain. The stress and strain intervals over which the transient

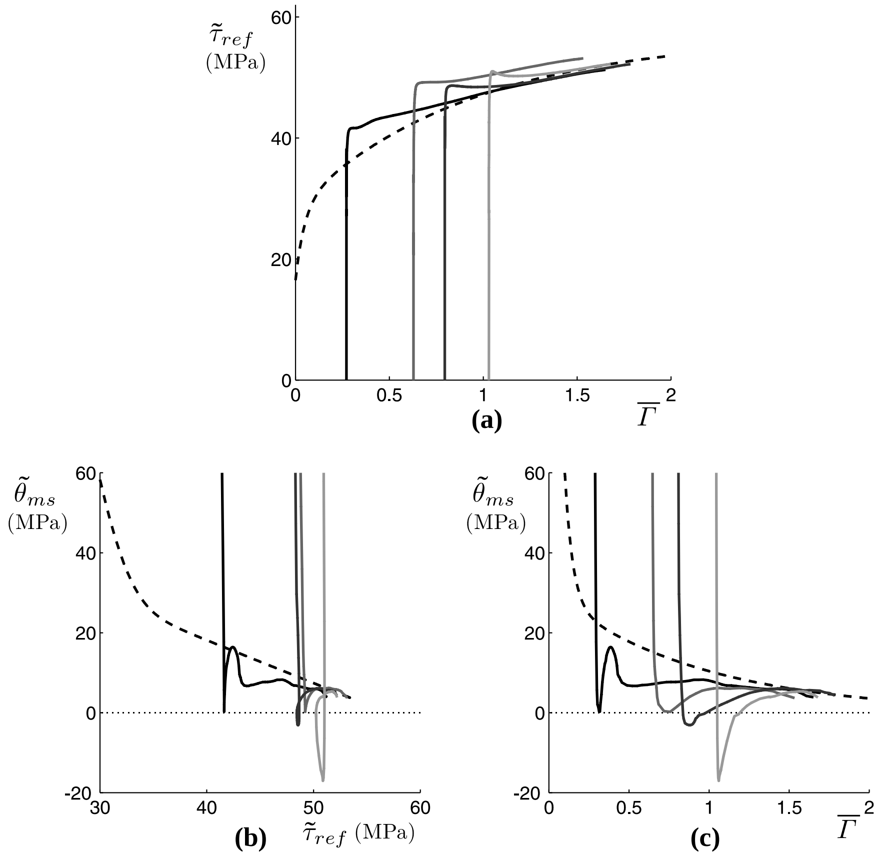

Fig. 3-18 : (a) Microscopic stress-strain curve of samples deformed in simple shear after a certain amount of prestraining in cold rolling. The sample is cut out of the rolling plate in such a manner that the Schmitt parameter θ = 60°. The curves are shifted with the equivalent amount of microscopic strain accumulated in the cold rolling deformation which is obtained from the evolution of the $\overline{M}$ -factor as displayed in fig. 3-12. (b) and (c) hardening rate-stress and hardening rate-strain curves corresponding to the curves of (a).

behaviour occurs are larger than for θ = 90° and θ = 60°, with a closer match to the intervals obtained for the reversal tests (cf. fig. 3-15 and fig. 3-20).

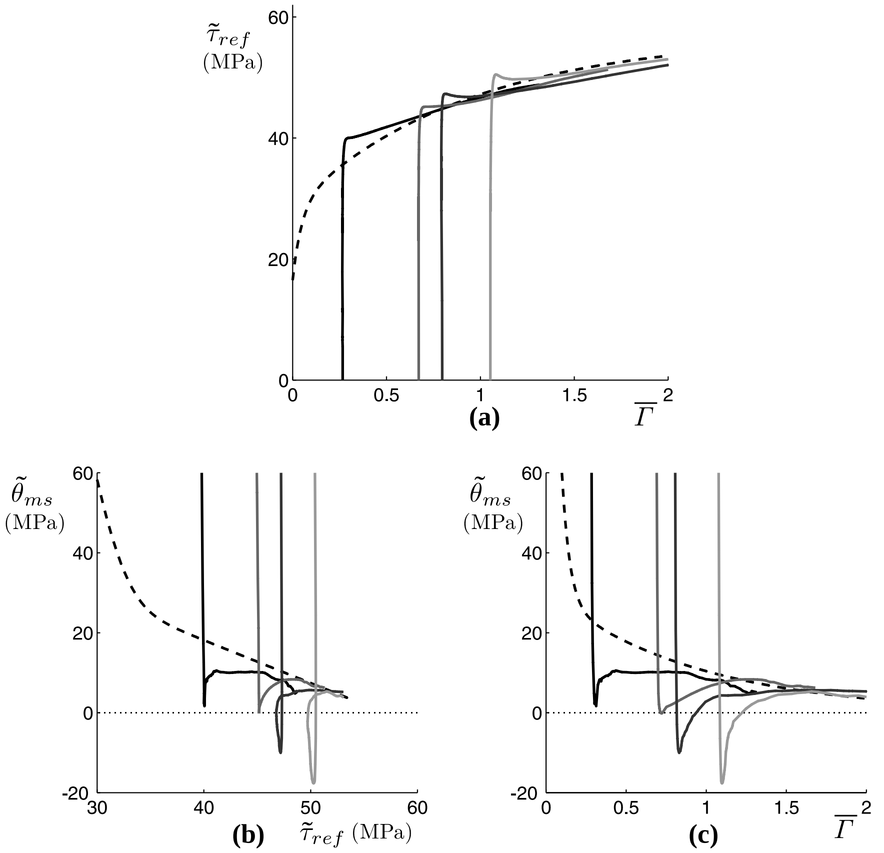

Fig. 3-19 : (a) Microscopic stress-strain curve of samples deformed in simple shear after a certain amount of prestraining in cold rolling. The sample is cut out of the rolling plate in such a manner that the Schmitt parameter $\theta = 120°$. The curves are shifted with the equivalent amount of microscopic strain accumulated in the cold rolling deformation which is obtained from the evolution of the $\overline{M}$ -factor as displayed in fig. 3-12. (b) and (c) hardening rate-stress and hardening rate-strain curves corresponding to the curves of (a).

3.3.5 Comparison of the different strain path changes

In order to quantitatively compare the different strain path changes, some of the parameters introduced in section 2.3.1.a, are obtained from the experimental results shown in figs. 3-13 to 3-19. It should be noted that only possible trends can be deduced due to the limited amount of data sets, which is mainly because of the technical complexity of obtaining strain data with the strain mapping technique.

First the calculated parameters are compared to one another in some dedicated figures from which certain possible trends are deduced. The second subsection discusses these trends and how they relate to both the substructural mechanisms and the upcoming model for predicting work hardening transients.

a) Strain path change parameters

To compare the lengths of the strain intervals in which the work hardening transient occurs, the value of γ_3 is plotted against the prestrain Γ_{pre} in fig. 3-20. For most types of SPC, a rather wide spread of γ_3 can be observed from which no obvious trends with prestrain can be derived. For the case of $\theta = 30°$, two very similar values of about 0.7 are obtained for the length of the transient, but of

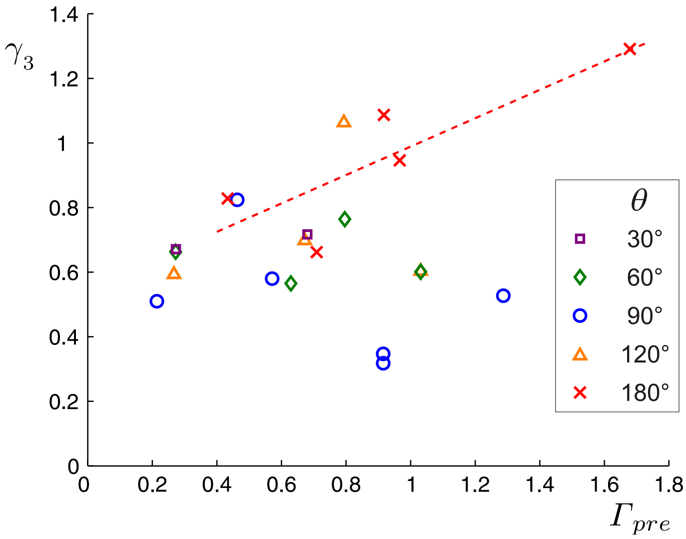

Fig. 3-20 : Length of the transient work hardening interval as a function of prestrain for the different series of experiments presented in figs. 3-13 to 3-19. The different symbols indicate the different types of strain path changes.

course more measurements at different levels of prestrain are necessary to find out whether this is a general feature for this type of SPC. For θ = 60° a somewhat larger spread is obtained, but the value of the strain interval also here seems to remain stable at about 0.6 with increasing prestrain. Most cross-type tests (θ = 90°) have a little bit shorter strain interval in which the hardening rate goes through its transient behaviour, but also here no systematic variation with increasing prestrain can be observed. Apart from one possible outlier at $\Gamma_{pre} = 0.8$ the γ_3 values of tests with θ = 120° are very close to those of θ = 60° (at $\Gamma_{pre} = 1.0$ they have exactly the same value).

Only for the strain path reversal tests (θ = 180°) an increasing trend of the length of the transient work hardening regime with prestrain can be observed. This is consistent with the observations reported in the literature on strain path reversal tests (cf. section 2.3.1.b), where in all reports addressing this issue the length of the transient (defined in many different ways) increases with Γ_{pre}. For other types of strain path changes this specific characteristic seems not to have been analysed up till now.

To evaluate the reduction of the hardening rate during the strain path reversal, the hardening rate θ_1 at the first inflection point in the stress strain curve (γ_1, τ_1 in fig.

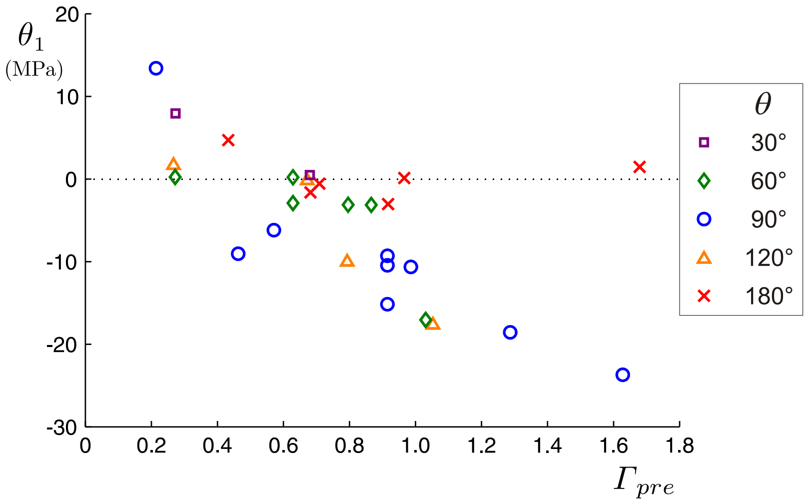

Fig. 3-21 : The minimum of the hardening rate during the transient work hardening behaviour after a strain path change with respect to the prestrain for the mechanical tests shown in figs. 3-13 to 3-19. The symbols indicate the different types of strain path changes.

2-13 (a)) is plotted as a function of the prestrain Γ_{pre} in fig. 3-21. θ_1 corresponds to the minimum in the hardening curve but is not equal to the local minimum in the stress-strain curves (at that point the hardening rate is 0).

Fig. 3-21 shows that in general the minimum hardening rate becomes lower at higher prestrains. This apparent rule does not apply to the reversal tests results ($\theta = 180°$) where the hardening rates do not get much lower than 0. The trend is very well followed by the results of the cross tests ($\theta = 90°$). For the intermediate SPC angles, only the results of the higher prestrains get a negative hardening rate comparable to those of the cross tests. For prestrains $\Gamma_{pre} < 0.8$ the hardening rate only becomes slightly negative similar to strain reversal tests.

To further analyse this reduction of the hardening rate which occurs during all SPC transients, the value of θ_1 is plotted against the stress τ_1 at which this low hardening rate is obtained in fig. 3-22. In the whole transient behaviour this is the point which is usually the furthest away in the θ_1-τ_1 curve from the regular monotonic hardening curve. This monotonic curve is indicated as well in fig. 3-22 as a dashed black line.

In this graph all experimental results are situated in a broad band approximately parallel to the monotonic curve. The results of the SPC tests with $\theta = 30°$ are

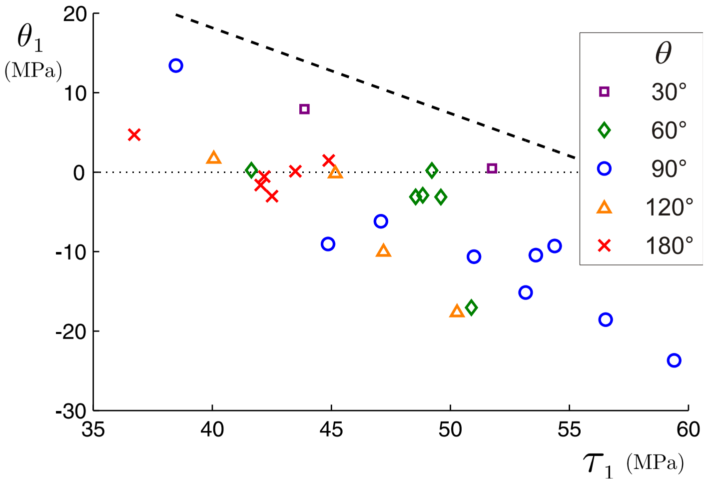

Fig. 3-22 : The minimum of the hardening rate during the transient work hardening behaviour after a strain path change versus the flow stress at that point for the mechanical tests shown in figs. 3-13 to 3-19. The work hardening curve of the monotonic deformation is plotted in a dashed black line. The symbols indicate the different types of strain path changes.

situated at the top of this band closest to the monotonic curve. The limited shift away from the monotonic behaviour seems to correspond with the fact that the straining mode during these tests is reasonably close to the straining mode of the prestrain. The large deviation from monotonic behaviour observed for cross tests ($\theta = 90°$) is consistent with this interpretation, since the orthogonality of the involved straining modes before and after the SPC guarantees the activation of a different set of slip systems. What is more surprising is that the shift hardly increases with increasing level of stress. A largely increasing difference with the monotonic work hardening curve can only be observed when the stress level results in stage IV hardening behaviour for the monotonic curve ($\tau > 55$ MPa).

An intermediate shift away from the monotonic behaviour is maintained by most of the work hardening curves for the case of $\theta = 60°$, with the exception of the lowest and the highest amount of prestrain. These latter two data points seem to be more in correspondence with the trend followed by the orthogonal SPC. For the strain path reversal tests ($\theta = 180°$), the rather limited range in which the transient plateau stresses (represented by τ_1) are situated, makes that most of the curves seem to obey the overall trend of the cross tests. The large range of prestrains (cf. fig. 3-21) and the general observation from literature data that pronounced softening rarely occurs during strain reversal tests however indicate that the reversal of the slip directions do not lead to an overall substructural work softening. The SPC tests in between the cross and strain reversal tests ($\theta = 120°$) obey essentially the trend of the cross tests, although the two tests with the lowest prestrains do not show softening and could as well be in line with the strain reversal tests.

The clearest trends which can be obtained from the gathered data appear when the extra or deficient amount of strain γ_0 which is necessary to obtain the same hardness after the transient regime compared to the monotonic hardening behaviour, is plotted against the prestrain as is done in fig. 3-23. γ_0 has been defined in figs. 2-13 and 2-14 in section 2.3.1.a.

With increasing prestrain γ_0 becomes more negative for the cross tests and more positive for the reversal tests. The relation appears in both cases to be linear. The two curves for the tests with $\theta = 30°$ as well as the two curves with the lowest prestrains for the tests with $\theta = 60°$ follow the same trend as the cross tests, while the higher prestrains for $\theta = 60°$ do not have any shift at all. The tests with $\theta = 120°$ all need an extra amount of strain to obtain the same hardening behaviour as the monotonic case, but not as much as the full reversal tests. It

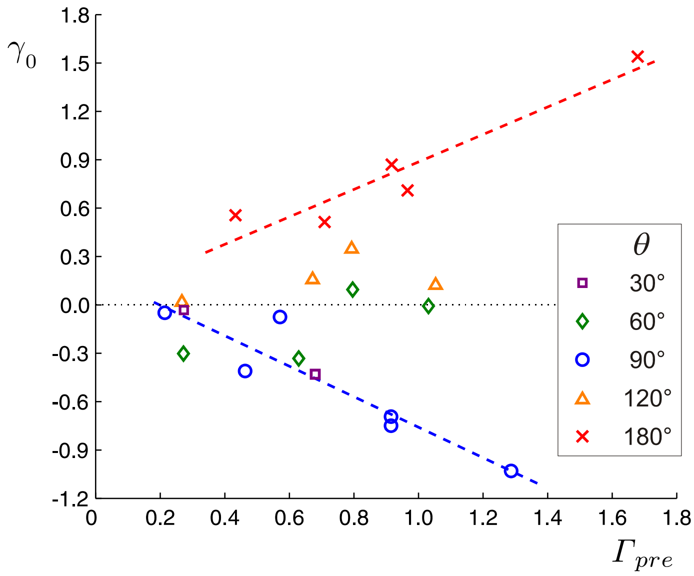

Fig. 3-23 : The amount of strain shift γ_0 between the monotonic work hardening behaviour and the one after an SPC against the prestrain Γ_{pre} for the different types of SPC as obtained from the mechanical tests shown in figs. 3-13 to 3-19.

might be that a linear trend is followed as well for $\theta = 120°$, but this is difficult to establish with only four points available.

b) Discussion

Due to the limited amount of data only a tentative discussion can be formulated about the apparent trends as described in the previous paragraphs. Moreover, it might be that the observed trends only apply to the used material with its specific starting texture and/or for the used combinations of straining modes, since this analysis is so far only performed on this particular set of work hardening curves. Nevertheless the possible explanations for the observed trends as given below will be valuable in deducing appropriate assumptions to model the transient work hardening behaviour after strain path changes.

An important aspect of all work hardening curves, which is already strongly established in the literature, is that - after the removal of the texture influence - all work hardening curves eventually return to the monotonic hardening behaviour. Since the ongoing work hardening is supposedly controlled by the current applied stress (cf. work hardening models based on dislocation densities), this implies that the θ-τ curve after a certain amount of strain should coincide with the curve of the monotonic case. This indeed is the case in all work hardening curves shown in figs. 3-13 to 3-19. Consequently, the substructure has to be stable with respect to the imposed straining mode from the point of return onwards and all transitional work hardening mechanisms caused by the SPC will have lost their importance.

From the consistently different trends found in figs. 3-20 to 3-23 for orthogonal SPC on the one hand and reversal SPC on the other hand, it can be concluded that two different mechanisms are at the basis of both transient regimes.

The increase of the length of the transient regime (γ_3) during strain path reversal tests can be attributed to the increasing amount of stored dislocations with a sign opposite to the one of the dislocations that accommodate the strain of the reversed straining mode. This results in enhanced mutual annihilation and a higher amount of strain to restore and surpass the previously reached dislocation density. This has been earlier described as the polarity of the substructure by Hasegawa and Yakou [1980] or the different nature of the dislocations of the prestrain and the reverse strain by Rauch and coworkers [2007].

The absence of a systematic trend for the length of the transient γ_3 with prestrain for the other SPC tests indicates that the average critical resolved shear stress of the substructure is not relevant in the process of replacing it. This would be the case for a break through mechanism, like e.g. the one found for bcc materials [Rauch; 1997]. Since no evidence is found for such a mechanism in TEM data of fcc materials after low and moderate prestrains, this will probably have to take place on a very fine scale. Also the fast drop of the hardening rate to negative values suggests the localisation of strain on the microscopic level. Self hardening processes have already been proposed by Rauch [1997] to explain why these microscale localisations do not evolve into strain localisations at the macro scale. A large number of localisations with a limited livespan due to selfhardening are not in contradiction with the observed apparent dissolution and superposition of the substructure during cross tests [Barlat et al.; 2003].

A cut-through mechanism most likely results in a different dislocation storage mechanism and corresponding governing equation, while the equal amount of drop of the hardening rate for all amounts of prestrain in stage III (cf. fig. 3-22) suggests that the annihilation mechanism remains similarly active as during the prestrain at least in the initial stages after the SPC. A different storage but a similar annihilation mechanism might also explain why the minima of the work hardening curves follow a consistent downward trend, even when the monotonic case has gone into stage IV.

The negative shift in strain ($\gamma_0 < 0$) of the work hardening curve after the transient proves that a part of the pre-existing substructure formed during prestraining maintains an influence on the flow stress even when the hardening transient is over. The larger amount of γ_0 with increasing prestrain indicates that the portion of this remaining substructure increases with prestrain. A cut through mechanism does not only break down the resistance of the substructural elements but also allows incorporating the finer scale remainings of the previous substructure with their contribution to the overall anisotropy stemming from the dislocation nature within the newly formed substructure.

The positive shift in strain ($\gamma_0 > 0$) observed for strain reversal tests means that a part of the straining going on during the transient in the end has been neutral to the overall substructural development. This implies that an amount of strain γ_0 does not result in an increase of the substructure strength. Whatever active dislocations have been stored during this amount of strain has been compensated by annihilation of other dislocations. This is explained by the polarity of the substructure which during the transient regime changes its sign. The average ratio of γ_0/γ_3 is about 75 %.

The observed intermediate γ_0 values for θ=120° can be explained by a mixture of both trends of the orthogonal and reversal SPC tests, while the low values of γ_0 for θ=60° at higher prestrains remain very unclear.

3.4 Summary

In order to obtain a homogeneous and stable deformation up to high strains, a mechanical device has been built that deforms samples in simple shear. In combination with prestraining tests using cold rolling or simple shear, the full range of strain path changes as characterised by the Schmitt parameter (equation 1.2) can be characterised.

By taking the texture evolution obtained by XRD measurements into account, the macroscopic stress-strain curves of all measurements are transposed to their microscopic counterparts in order to characterise the work hardening behaviour as resulting from the substructural mechanisms. The textural contribution to the anisotropy is substracted in this way.

The resulting microscopical work hardening rate-stress curves for different SPC tests demonstrate clearly that the hardening behaviour of the substructure returns to the monotonic case after a transient regime. Because of the occurrence of negative values for the strain shift γ_0 for cross type SPC tests, it is concluded that the existing substructure formed during prestraining partly maintains its contribution to the anisotropy even after the transient regime. Because of the different trends observed for many parameters describing the transient hardening regime, it is concluded that different mechanisms controll the work hardening behaviour during Bauschinger tests and cross tests. For strain path reversals the change of the polarity of the substructure can explain the observed trends, while for orthogonal strain path changes the mechanical data suggest the existence of a break-up mechanism.

4

Multiscale model for cold deformation

As reviewed in chapter 1, different mechanisms working at different length scales will contribute to the overall material behaviour. One approach to model material behaviour during complex processes is by separating these different mechanisms based on the length scale at which they operate and model them separately in length scale specific submodels. These submodels can be interlinked into a multiscale model that combines the different mechanisms. An important requirement however is that each submodel has to be able to influence the others by an appropriate scale linking (otherwise the submodel would be redundant). As explained in chapter 1 this scale linking can be either done by a homogenisation step (hierarchic scale transition) or by embedding one submodel into another. The model for work hardening behaviour during strain path changes, which is presented in this chapter, follows a multiscale approach.

In the first section the overall framework with the different length scales will be introduced, with the focus on how the different length scales are interlinked. The FC Taylor and advanced Lamel (A-Lamel) models that predict texture evolution during cold deformation are shortly reviewed, since these models are used as the macro- to meso scale transition part of the multiscale model.

In the second section the meso scale model for work hardening anisotropy during monotonic strain paths is discussed in detail. The above mentioned plasticity models need to be extended in order to predict the anisotropy resulting from the substructure. As discussed in chapters 2 and 3, this substructural anisotropy is essential to explain the observed reyielding behaviour at strain path changes.

The meso scale model is further elaborated in the third section to include the different transient work hardening behaviours that can occur after a strain path change.

In chapter 5 the multiscale model will be validated with the data presented in chapter 3. Also the capabilities of the model will be discussed and compared to those of other SPC models.

4.1 Modelling framework

The multiscale modelling framework serves as the backbone of the model presented in this chapter. In order to understand how the substructural anisotropy might affect the overall work hardening behaviour within the model, first the general framework and how its constituent submodels are interlinked will be presented, before the used submodels are discussed in more detail.

4.1.1 Overview

a) General scheme

The presented multiscale model fits into the framework of which a general scheme is depicted in fig. 4-1. This framework is shared with many other multiscale models predicting mechanical properties of materials [e.g. Kalidindi et al.; 2004, Ma et al.; 2008]. This modelling framework encompasses 4 of the 6 length scales that are presented in section 1.1.

At the application scale where the loading configuration of the material is modelled, the dimensions and the shape of the workpiece and certain boundary conditions to which the workpiece is subjected (e.g. applied forces and imposed displacements) are specified. As a result of the application scale model, the displacement field and the associated stress field are obtained. The constitutive material response which interrelates both fields is acquired by invoking the macro scale model. The knowledge of the stress and displacement fields can be useful for assessing e.g. tool design, required forces for shaping, weak spots in the material after deformation, obtained shape, ...

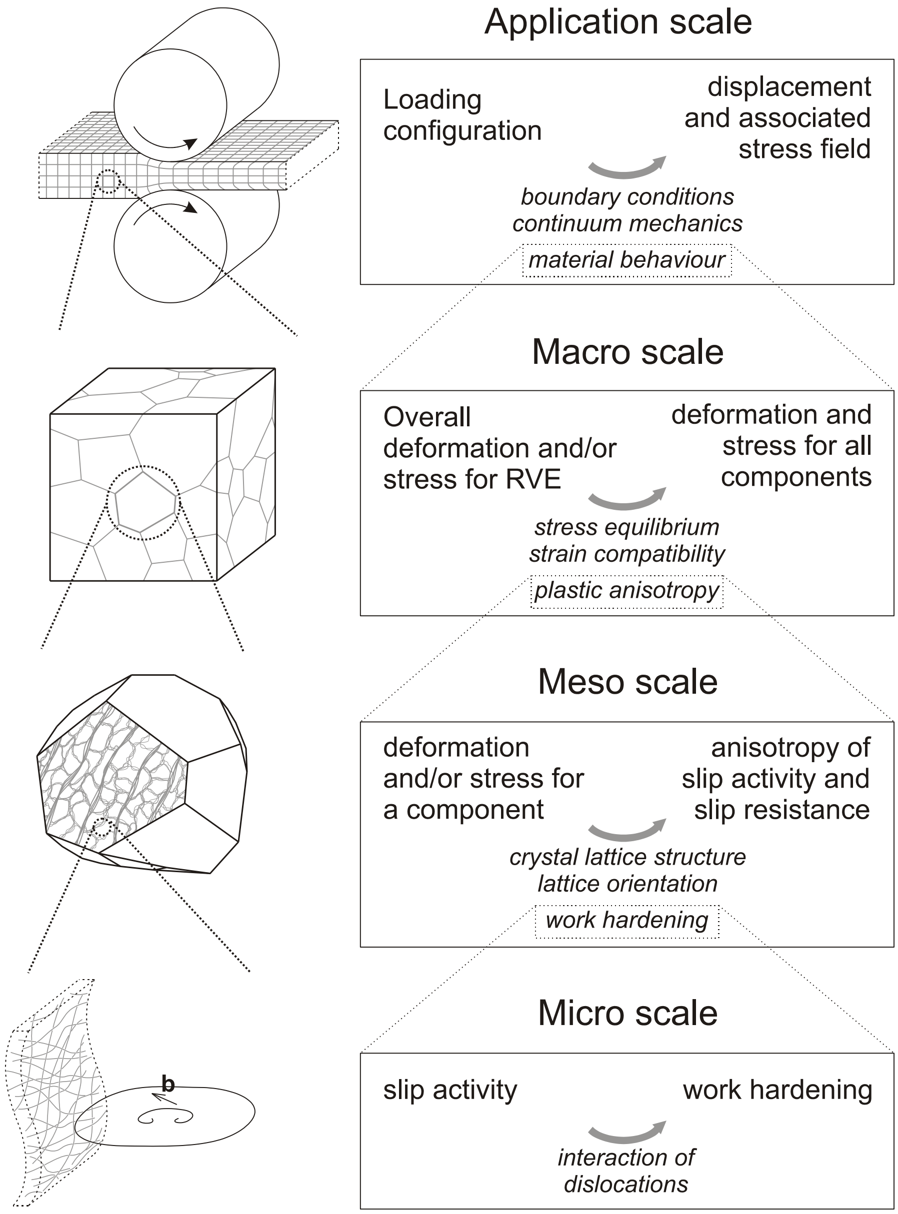

Fig. 4-1 : Schematic representation of the multiscale model framework, indicating the governing concepts at the individual length scales.

At the macro scale the material is treated as a homogeneous part of a continuum, by averaging the individual responses of a set of discrete components within a representative volume element (RVE). Such components can be individual grains, grain boundary regions or parts of a grain. The depiction of a grain in fig. 4-1 is only meant as an illustrative example. To be representative for the whole material, the set of discrete components needs to encompass the statistical distributions of all relevant quantities regarding the mechanical behaviour of the material. To the discrete components various quantities can be attributed, like e.g. a lattice orientation, a strength tensor, several dislocation densities, a size or a volume, a shape, a topological position in the set of components, ... Statistics on the boundary structure and the relative grain to grain misorientation can be imposed as well [Van Houtte et al.; 2005]. Because the orientations of the discrete components are distributed according to the crystallographic texture of the material, the influence of the texture on the mechanical material behaviour is incorporated into the model at this scale. In order to solve the constitutive relation between stress and deformation, the macro scale model has to consider the requirements of stress equilibrium and strain compatibility inside a RVE as well as the plastic anisotropy of each individual component arising from both orientation and substructure. The relation between stress and deformation homogenised over the RVE is passed on to the application scale model.

The plastic anisotropy and how it evolves with ongoing deformation for every component is modelled at the meso scale. The stress and strain of an individual component are here directly related to each other while accounting for the anisotropy caused by the crystal lattice orientation and possibly the substructure. Depending on the crystal lattice structure and its orientation relative to the imposed stress and/or deformation conditions, a set of slip systems is activated which accommodates the deformation under a certain stress. The anisotropy stemming from the arising substructure is reflected in different values of the critical resolved shear stresses for the individual slip systems. The critical resolved shear stresses are adapted according to the results of the micro scale model. In this way work hardening is introduced into the modelling framework. The evolution of the work hardening anisotropy and the specific work hardening behaviour after an SPC can be modelled at the meso scale level (as e.g. in the present model) or be incorporated in evolution equations at the micro scale [e.g. Peeters et al.; 2001b, Rauch et al.; 2007][24]. From the active set of slip systems, the possible reorientation of the crystal lattice can be calculated (cf. section 2.1.2.a). This enables the multiscale model to predict crystallographic texture changes.

---

[24] The model of Teodosiu and Hu [1995] which models the substructural anisotropy at the macro scale does not fit into the multiscale framework as depicted in fig. 4-1.

At the micro scale the work hardening rates of all slip systems or a homogenised value of them are related to the activities of the individual slip systems or a homogenised slip activity off all slip systems. Usually the critical resolved shear stresses of the slip systems are related to dislocation density values representing immobile dislocations stored in the substructure. These are updated by the micro scale model through the slip rates coming from the mesoscopic level which describe the glide of mobile dislocations on the slip systems. The interaction of mobile with immobile and other mobile dislocations will lead to dislocation storage and annihilation. The increase or decrease of the dislocation density values will affect the critical resolved shear stresses of all slip systems which will lead to hardening or softening. The specifics of the substructural morphology can be taken into account by the chosen formulation of the evolution equations at this length scale. This is however not necessary. The evolution equations can also be formulated in a more generic way to be applicable for various forms of substructural morphology. The depicted substructure in fig. 4-1 should therefore also be considered as an example in order to illustrate the modelling approach.

b) Linking of the length scales

Fig. 4-2 pictures the implementation of the multiscale model for cold deformation within the framework presented in fig. 4-1. The scheme focuses on the quantities that link the different scales to one another. The exact functional dependences within the submodels will be treated in the following sections of this chapter.

The model only ranges from the macro to the micro scale and does not include a submodel for the application scale. The main reason for this is that the evaluation of the material behaviour is solely addressed at the three lower scales. For this reason simple shear and cold rolling (cf. section 3.3) are selected as mechanical tests to calibrate and validate the model. The stress and deformation field of the deformation zone can be approximated by homogeneous values for these tests if the processing parameters are selected with care. The homogeneous fields enable to directly give a good approximation of the material response to the imposed boundary conditions without the need to use a tedious reverse engineering approach due to the extra modelling shell on the application scale.

There are two versions of the model implemented. Both differ in the macro to meso transitional model which is used. For the first version this is FC Taylor, while in the second A-Lamel is used. The equations in fig. 4-2 denoted in blue are related to these two models. The quantities that are only used by A-Lamel are printed in light blue and gray. The functional dependence that is printed in red,

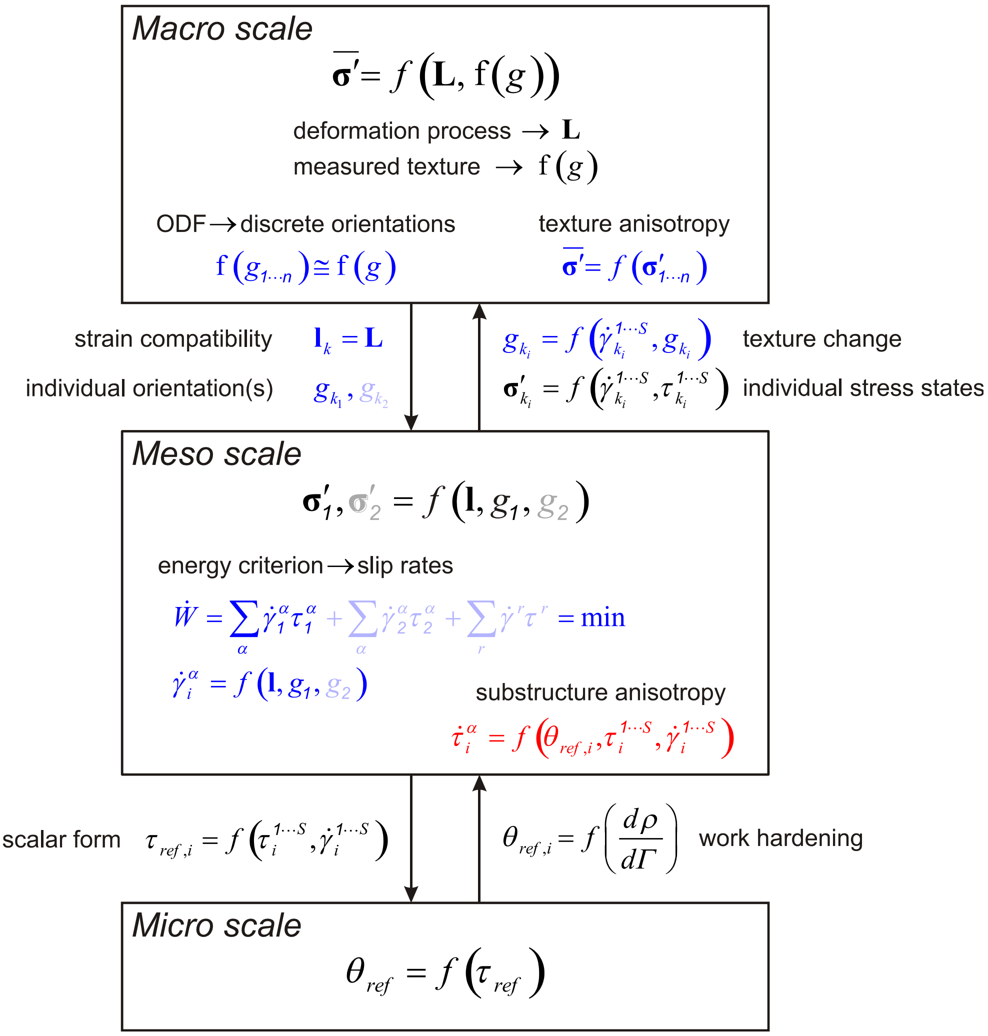

Fig. 4-2 : Scheme of the multiscale model specifying which quantities are evaluated at the three involved length scales.

models the substructural anisotropy and the work hardening behaviour after strain path changes and is the keystone of the present modelling work.

The input of the macro scale model consists of the velocity gradient $\mathbf{L}$ which characterises the applied deformation and the ODF $\mathrm{f}(g)$ which characterises the initial crystallographic texture of the material and is obtained experimentally.

The output is the homogenised deviatoric stress $\overline{\boldsymbol{\sigma}'}$. Inside the macro scale model the mathematical description of the ODF $\mathrm{f}(g)$ gets replaced by a set of n discrete orientations $g_{1\cdots n}$. The components which are passed on to the meso scale model are individual grains, each represented by a particular orientation g_k, for the FC Taylor model and boundary regions that are determined by two orientations g_{k_1} and g_{k_2} as well as the direction of the normal to the boundary plane $\hat{\mathbf{n}}_k$ for A-Lamel. For each component the velocity gradient $\mathbf{l}_k$[25] is made equal to the overall imposed velocity gradient $\mathbf{L}$, guaranteeing strain compatibility between the individual components. The deviatoric stress states of the individual orientations obtained from the meso scale model are simply averaged to obtain the homogenised deviatoric stress $\overline{\boldsymbol{\sigma}'}$, which means that stress equilibrium between the components is not imposed by the model.

At the meso scale, the stress states of the individual components is obtained. This requires that a set of slip rates $\dot{\gamma}_i^{1\cdots S}$ for the involved orientation(s) is found that complies with the imposed velocity gradient $\mathbf{l}$ and minimises the dissipated work $\dot{W}$. S denotes the number of slip systems per orientation and equals 12 in case of fcc materials. In this calculation the deviatoric stress(es) $\boldsymbol{\sigma}_i'$ for the orientation(s) and the reorientation of the crystal lattice(s) g_i are obtained as well. From the updated orientations, a new ODF can be obtained at the macro scale. The model as described up till here can therefore be used to predict texture evolution. Both the FC Taylor and A-Lamel model are in essence texture models, which are in the present model applied to account for textural anisotropy.

Important parameters in the calculation of $\dot{W}$ are the critical resolved shear stresses $\tau_i^{1\cdots S}$ of the individual slip systems. As explained in the previous section they can account for the substructural anisotropy and one task of the meso scale model is to update these values with further straining. This is represented in fig. 4-2 by the functional dependence in red. This part of the model will be further elaborated in sections 4.2 and 4.3.

For every orientation the current τ^{α} are homogenised into single scalar value τ_{ref}. At the micro scale model an average work hardening rate θ_{ref} is obtained which at the meso scale model is divided over the individual slip systems. Due to

---

[25] For the A-Lamel model $\mathbf{l}_k$ is the velocity gradient of the whole boundary region which is the sum of the velocity gradients of the two orientations $\mathbf{l}_{k_1}$ and $\mathbf{l}_{k_2}$.

the homogenisation of the critical resolved shear stresses for the individual slip systems, any scalar work hardening model (like all the models presented in appendix B) can be used as the micro scale model. Most of these models use the stored dislocation density ρ as an internal variable. The conversion of τ_{ref} into ρ can be achieved by the Taylor equation for the flow stress (equation (2.8)). The evolution equations for dislocation storage and annihilation give a rate of change of the stored dislocation density from which the work hardening rate can be obtained by equation (2.9). Usually the functional dependence between θ_{ref} and τ_{ref} can be reformulated in a direct analytical form so that the conversion to ρ is not done explicitly within the implementation of the model.

Now that the individual parameters that link the different submodels are identified, it will be shortly discussed for each scale transition whether it is hierarchical or embedded.

Since the macro scale model calls the meso scale model for every individual component to obtain values for the deviatoric stress(es) of the orientation(s), the meso scale model is embedded into the macro scale model.

For the FC Taylor version of the model, the micro scale model is hierarchical in respect to the meso scale model, due to the homogenisation of the critical resolved shear stresses. Since the meso scale model is however embedded into the macro scale model every grain has its own hardening rate which depends on the M -factor of the grain.

For the A-Lamel version, the micro scale is in principle embedded into the meso scale model, since every call of the meso scale model needs (at least) two calls of the micro scale model, namely one for every orientation. One can however also argue that the meso scale of A-Lamel exists of two sublevels. The level of the grain boundary region (the component, meso-1) and the level of the two individual orientations (subcomponents, meso-2). Since for both orientations the same homogenisation is applied as in the FC Taylor version, a hierarchical relation holds between the micro and meso-2 (orientations). Meso-2 is embedded into the meso-1. Every orientation has its own hardening rate which means that the work hardening of the two grains in a boundary region can be different.

4.1.2 Texture models

FC Taylor and A-Lamel, which are the texture models used in the present framework, can be regarded as macro to meso scale transition models. The macro scale part of these models handles the selection of the discrete values to describe the components and the homogenisation of the deviatoric stress values resulting from the meso scale model applied on each of the components. As the input of the texture model, a description of the current texture of the material and the imposed deformation are required.

For the texture description, the ODF - a probability density function in orientation space - is used, represented in terms of c-coefficients [Bunge; 1982]. For the FC Taylor model a reduced set of c-coefficients can be used to take advantage of the sample symmetry imposed by the applied deformation. If the deformation is however not constant due to an SPC, only the lowest degree of sample symmetry in the deformation process can be applied. The discrete orientations for the components are selected by random sampling of the ODF, so that the set of discrete orientations is distributed according to the statistical distribution of the ODF [Tóth and Van Houtte; 1992]. This approach makes the model a Monte Carlo type of simulation.

The overall deformation is characterised by the deformation gradient **F** (cf. section 2.1.2.a). Since the meso scale model uses the small strain approximation (cf. supra), the overall deformation needs to be split up in small deformation increments described by a velocity gradient **L** (cf. equation (2.1)), which is constant during the increments. To obtain the overall deformation, the model has to be integrated over the deformation path, where each increment implies a calculation cycle by the macro scale model. Because of the incremental formulation of the model, it is possible to change the deformation by applying a different velocity gradient from a certain increment onwards. Through the abrupt change of this boundary condition, strain path changes can be achieved in the model. In principle it is possible to model very complex deformation paths with many successive SPC.

The output of the macro scale model is a homogenised deviatoric stress which in the present model is obtained as the arithmetic average $\overline{\boldsymbol{\sigma}'}$ of the deviatoric stresses of the individual orientations.

The implementation of the macro scale part of the texture models is straightforward and to a large extent equal for both FC Taylor and A-Lamel. The difference is situated in the approach towards the strain compatibility and stress equilibrium requirements and the implications this has on the meso scale model calculations.

a) FC Taylor

The FC Taylor model has already been introduced in section 2.1.2.a of the literature review. The main assumption of the model is to impose the same plastic deformation (velocity gradient) to all individual grains, guaranteeing a compatible straining of all grains (neglecting elastic deformation). The necessary stress equilibrium at the grain boundaries is disregarded based on the reasoning that due to the high value of the elastic modulus, it requires very large differences in the stress field to obtain significant changes in the strain field [Kocks; 1970]. The internal stress field that brings the grain boundaries into stress equilibrium does only make the deformation field deviate very little from the macroscopic imposed deformation.

The main modelling equations at the meso scale relate the imposed deformation for a single orientation to dislocation glide on equally distributed glide planes in a number of slip systems (equation (2.4) - (2.5)) :

$$\dot{\boldsymbol{\varepsilon}} = \sum_{\alpha} \mathbf{M}^{\alpha} \dot{\gamma}^{\alpha} \text{ with } \mathbf{M}^{\alpha} = \frac{1}{2}\left(\hat{\mathbf{b}}^{\alpha} \otimes \hat{\mathbf{n}}^{\alpha} + \hat{\mathbf{n}}^{\alpha} \otimes \hat{\mathbf{b}}^{\alpha}\right) \tag{4.1}$$

$$\dot{\boldsymbol{\Omega}} = \sum_{\alpha} \frac{1}{2}\left(\hat{\mathbf{b}}^{\alpha} \otimes \hat{\mathbf{n}}^{\alpha} - \hat{\mathbf{n}}^{\alpha} \otimes \hat{\mathbf{b}}^{\alpha}\right) \dot{\gamma}^{\alpha} + \dot{\boldsymbol{\omega}}_{l} \tag{4.2}$$

where $\dot{\gamma}^{\alpha}$ is the slip rate of a slip system α, which can be linked to the density and velocity of mobile dislocations active on that slip system. $\hat{\mathbf{b}}^{\alpha}$ and $\hat{\mathbf{n}}^{\alpha}$ are the unit directions parallel to respectively the Burgers vector and the glide plane normal of the slip system α. The strain rate $\dot{\boldsymbol{\varepsilon}}$ and the rate of rotation $\dot{\boldsymbol{\Omega}}$ are the symmetric and the anti-symmetric part of the imposed velocity gradient $\mathbf{l}$. $\dot{\boldsymbol{\omega}}_{l}$ is the lattice spin which describes the reorientation of the crystal lattice which is the needed variable to calculate the texture evolution. The deviatoric stress required to have the slip systems activated can be found by solving the set of equations

$$\tau^{\alpha} = \mathbf{M}^{\alpha} : \boldsymbol{\sigma}' \tag{4.3}$$

for all active slip systems. Although the tensorial equations (4.1) – (4.3) are valid regardless of the reference system in which they are expressed, it is advantageous to implement them in the crystal lattice frame, since the components of all $\hat{\mathbf{b}}^{\alpha}$ and $\hat{\mathbf{n}}^{\alpha}$ are then constant values depending on the crystal lattice structure. If the small strain approximation is applied, the orientation of the lattice frame as well as the slip rates $\dot{\gamma}^{\alpha}$ can be assumed to be constant during one deformation increment.

The model uses in other words an explicit integration scheme to solve its equations, which leads to good approximations if the increments are sufficiently small. Both the slip rates $\dot{\gamma}^{\alpha}$ and the lattice spin $\dot{\boldsymbol{\omega}}_l$ are obtained by this explicit integration scheme.

Equation (4.1) represents a set of 5 independent linear equations. Since there are more unknowns (in case of fcc materials there are 12 slip systems) an energy criterion is used to select the solution that minimises the rate of dissipated work :

$$\dot{W} = \sum_{\alpha} \tau^{\alpha} \left|\dot{\gamma}^{\alpha}\right| = \min \tag{4.4}$$

If the positive and negative slip rates are decoupled within the modelling equations (leading to an artificial doubling of the available slip systems as well as twice the amount of unknown slip rates which can only obtain positive values), solving equation (4.1) becomes a linear programming problem, with equation (4.4) as the cost-function [Van Houtte and Aernoudt; 1975]. The simultaneous activation of a slip system in both directions is impossible because this would imply an increase of $\dot{W}$ compared to the solution where only one of both directions is active. The decoupling of the positive and negative slip rates also enables to attribute a different critical resolved shear stress to the two slip directions of a slip system. This possibility will be taken advantage of in the part of the work hardening model that simulates the Bauschinger effect and the subsequent work hardening evolution. In the remainder of the text all slip rates will be considered to be decoupled, which means that all slip rates $\dot{\gamma}^{\alpha}$ will be positive by definition and the superscript α will have twice as many possible values. To indicate the slip rate and critical resolved shear stress of the opposite slip direction of a certain slip system α, the designations $\dot{\gamma}^{-\alpha}$ and $\tau^{-\alpha}$ will be used.

If the τ^{α} of all slip systems are equal, due to the high degree of symmetry of the crystal lattice, the linear program does not always result in a unique solution of the shear rates $\dot{\gamma}^{\alpha}$. Multiple combinations of slip systems can then accommodate the deformation, while having the same minimal value of the dissipated work. Every linear combination of individual solutions (where the sum of the non-negative weighting factors must be equal to 1) is a solution as well, leading to maximum 8 different slip systems that can be active with their $\dot{\gamma}$ within a certain range. All different solutions will moreover result in different values of $\dot{\boldsymbol{\omega}}_l$. For the deviatoric stress $\boldsymbol{\sigma}'$ and the *M*-factor, unique solutions are however obtained. This is known as the Taylor ambiguity problem. To obtain a unique solution for

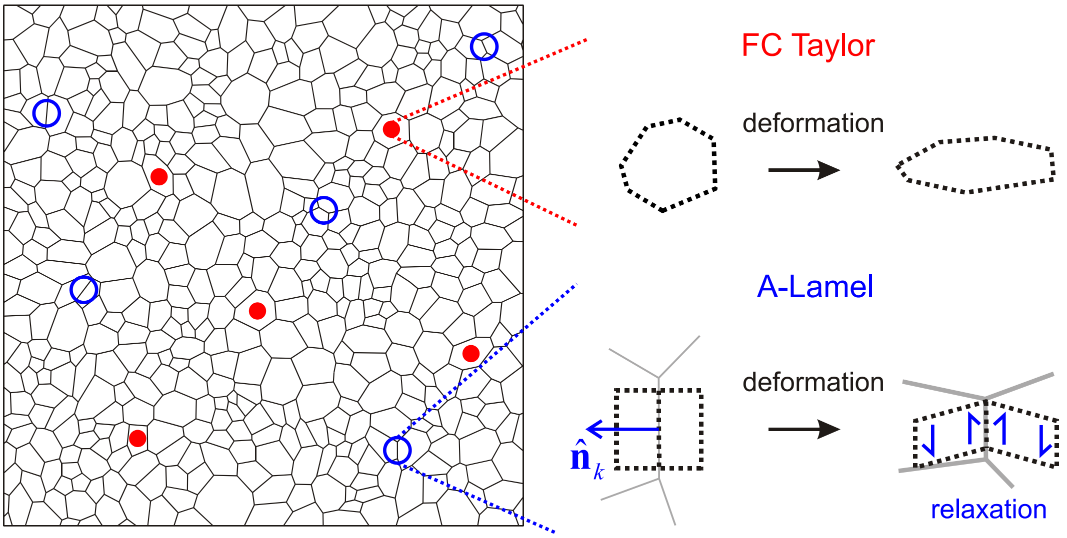

Fig. 4-3 : Schematic representation of the difference in the selection of meso scale components between the FC Taylor and A-Lamel model.

the $\dot{\gamma}^{\alpha}$, a secondary minimisation criterion is applied in the implementation of the model :

$$\sum_{\alpha}\left(\dot{\gamma}^{\alpha}\right)^{2}=\min \tag{4.5}$$

This criterion distributes the unique solution of the sum of slip rates $\dot{\Gamma}$ as equally as possible over all available active slip systems. Whenever there is a difference in the τ^{α} of the slip systems, the Taylor ambiguity does not occur [Gil Sevillano et al.; 1980, Peeters et al.; 2001a]. The secondary criterion is however needed to obtain a solution at the first increment if a simulation is performed for a recrystallised material, where there is no reason why the τ^{α} would differ between the different slip systems. The onset of substructure formation will make the τ^{α} evolve in a different manner based on the slip rates of the first increment.

b) A-Lamel

The difference between the selection of the meso scale components at the macro scale in the FC Taylor model and the A-Lamel model is schematically illustrated in fig. 4-3. The FC Taylor model randomly selects a number of grains from the microstructure (indicated with red dots in fig. 4-3), which are each characterised by the orientation of the respective grain. The A-Lamel model randomly selects a number of boundary regions (indicated with blue circles in fig. 4-3), which are each characterised by the two orientations of the grains at either side of the grain boundary segment and the normal $\hat{\mathbf{n}}_k$ to the boundary segment plane. To make such a selection from a statistical description of the microstructure, three distributions and their correlation functions should in principle be obtained, namely the ODF to represent the crystallographic texture, the misorientation distribution function (MODF) to represent the probability for a neighbour relation between to orientations and the grain boundary segment orientation distribution function (GBSODF) to represent the distribution of the normals to the grain boundary segment planes [Van Houtte et al.; 2005]. For recrystallised materials it can be assumed that these distribution functions are not correlated and that the MODF has a uniform probability for all grain orientation pairs within the ODF. Since the microstructure of the undeformed material shows grains with nearly equiaxed shape (cf. section 3.4.1), the initial GBSODF is taken to be uniform as well. The directions of the selected $\hat{\mathbf{n}}_k$ are however updated according to the change of the grain shape imposed by the velocity gradient $\mathbf{L}$. The modelling assumption of the A-Lamel model is that each component k in total deforms according to the macroscopically imposed deformation, meaning that $\mathbf{l}_k = \mathbf{L}$, while stress equilibrium is achieved at the grain boundary segment.

To achieve the stress equilibrium at the boundary segment, the shear deformation components in the boundary plane of both grains are relaxed. For each component at the meso scale, both orientations deform homogeneously, but with somewhat different imposed deformations :

$$\mathbf{l}_{k_1} = \mathbf{l}_k - \sum_r \mathbf{K}^r \dot{\gamma}^r \tag{4.6}$$

$$\mathbf{l}_{k_2} = \mathbf{l}_k + \sum_r \mathbf{K}^r \dot{\gamma}^r \tag{4.7}$$

where $\mathbf{K}^r$ indicates the velocity gradient of a simple shear relaxation with the boundary plane as the shear plane and $\dot{\gamma}^r$ the corresponding slip rate[26]. Since such a shear relaxation can be decomposed into two orthogonal shear components r will run from 1 to 2. The exact values of the two relaxation slip rates $\dot{\gamma}^r$ are initially unknown and will be free variables to be solved in the linear

---

[26] The slip rates $\dot{\gamma}^r$ of the relaxations are bound to the grain boundary plane and are therefore not necessarily crystallographic, unlike the slip rates $\dot{\gamma}^\alpha$ of the slip systems.

programming algorithm. In a reference system with the 3rd axis parallel to $\hat{\mathbf{n}}_k$, the relaxation tensors are described as :

$$\mathbf{K}^1 = \begin{bmatrix} 0 & 0 & 1 \\ 0 & 0 & 0 \\ 0 & 0 & 0 \end{bmatrix} \text{ and } \mathbf{K}^2 = \begin{bmatrix} 0 & 0 & 0 \\ 0 & 0 & 1 \\ 0 & 0 & 0 \end{bmatrix} \tag{4.8}$$

The modelling equations to relate the imposed deformation to the slip system activity for the both orientations and to obtain the deviatoric stress are equal to the ones used in the FC Taylor model (cf. equations (4.1) - (4.3)), although here the set of five 5 equations with 24 unknowns is extended to a set of 10 equations with 50 unknowns (for both grains 12 available slip systems with two slip directions plus the two slip rates of the relaxation which are common for both orientations). The energy cost function for the whole meso scale component becomes :

$$\dot{W} = \sum_{\alpha} \tau_1^{\alpha} \dot{\gamma}_1^{\alpha} + \sum_{\alpha} \tau_2^{\alpha} \dot{\gamma}_2^{\alpha} + \sum_{r} \tau^r \dot{\gamma}^r = \min \tag{4.9}$$

where α now ranges from 1 to 24, due to the decoupling of the slip directions and τ^r is a penalty factor for the relaxation. In the model the values of the τ^r are set to 0.

The A-Lamel model uses like FC Taylor an explicit integration scheme to solve its model equations.

4.1.3 Micro scale model

In order to find an average measure of the hardening rate θ_{ref} from the average critical resolved shear stress τ_{ref} at the micro scale, the phenomenological model presented in section 3.3.1.c will be used. The hardening rate is described by :

$$\theta = \frac{d\tau}{d\gamma} = \frac{\theta_B}{\tau_B}(\tau_B - \tau_A)\exp\left(-\frac{\theta_B}{\tau_B}\gamma\right) + \frac{\theta_A}{\tau_A}(\tau_A - \tau_0)\exp\left(-\frac{\theta_A}{\tau_A}\gamma\right) \tag{4.10}$$

Since in this model, the hardening rate is expressed as a function of strain and not as a function of stress, an iterative procedure is implemented in the model to obtain the hardening rate at the imposed stress level.

4.2 Meso scale model for work hardening anisotropy

In the framework presented in the previous section, the contribution of the substructure to the overall anisotropy is reflected in the different values τ_i^α for the slipsystems α of the individual orientations i. To model the substructural anisotropy, a set of equations will be formulated to describe the evolution of the τ_i^α of the individual slip systems. For a certain orientation i, the evolution of the τ_i^α during a deformation increment in the calculation cycle of the overall model will depend on the slip rates $\dot{\gamma}_i^{1\cdots S}$ coming from the texture model and the average work hardening rate $\theta_{ref,i}$ obtained from the work hardening model. The current state of substructural anisotropy, represented by the current values $\tau_i^{1\cdots S}$ of all slip systems also influences the further evolution of the individual τ_i^α. Since a different τ_i^α will be attributed to the positive and negative slip direction, each physical slip system will be decoupled into two modelling slip systems. Each modelling slip system will have by definition a slip rate $\dot{\gamma}_i^\alpha \geq 0$. For fcc materials the number of modelling slip systems S hence becomes 24.

In this section the functional dependence for the substructural anisotropy which is printed in red in fig. 4-2 will be elaborated :

$$\dot{\tau}_i^\alpha = f\left(\theta_{ref,i}, \tau_i^{1\cdots S}, \dot{\gamma}_i^{1\cdots S}\right) \tag{4.11}$$

Since this functional dependence only relates to an particular crystal orientation, there is no difference in how it is implemented in either the FC Taylor or A-Lamel version of the overall model. For sake of simplicity the index for the orientation will be omitted. It however needs to be stressed that every orientation within the model can and most likely will have a different set of $\tau^{1\cdots S}$.

In this section, only the aspects of the meso scale model that relate to the substructural anisotropy during monotonic loading conditions will be discussed. A further elaboration of the model to include the work hardening transients after a strain path change (cf. sections 2.3.1 and 3.3) will be presented in section 4.3. The model as presented in this section can therefore only predict the reyielding stress at an SPC, but neither the subsequent work hardening behaviour nor the evolution of the substructural anisotropy after an SPC.

First the mathematical elaboration of equation (4.11) will be introduced. In a second subsection the influence of the phenomenological modelling parameters will be evaluated. Finally the model formulation will be discussed in the light of the experimental observations discussed in chapters 2 and 3.

4.2.1 Mathematical formulation

Unlike the slip rates $\dot{\gamma}^{\alpha}$, the critical resolved shear stresses τ^{α} will not be treated as constant values by the model during the evaluation of a single deformation increment. Their mutual influence during a deformation increment (having fixed values of $\dot{\gamma}^{\alpha}$) will be obtained by an implicit integration over the model equations. This is necessary because the different τ^{α} can change very rapidly, especially immediately after strain path changes.

Within a deformation increment the evolution of the τ^{α} will be obtained by solving a set of coupled first order differential equations numerically. Within the deformation increment the sum of shear strains on the slip systems Γ will be taken as the independent variable to characterise the increasing strain :

$$\Gamma = \int_t \dot{\Gamma} dt \qquad (4.12)$$

with

$$\dot{\Gamma} = \sum_{\alpha} \dot{\gamma}^{\alpha} . \qquad (4.13)$$

The hardening rates of the individual slip systems are expressed as

$$\theta^{\alpha} = \frac{d\tau^{\alpha}}{d\Gamma} = \theta_{ref} \frac{h^{\alpha}}{h_{ref}} \qquad (4.14)$$

where

$$\theta_{ref} = \frac{d\tau_{ref}}{d\Gamma} \qquad (4.15)$$

is the hardening rate obtained from the micro scale model and h^{α}/h_{ref} is the rate of anisotropy change which will be detailed below. Regardless of the exact definition of h^{α}, the normalisation factor h_{ref} can be derived as follows.

Throughout the increment, the definition of τ_{ref} (cf. section 2.1.2.a and equation (A.4)) should be maintained, meaning that

$$\tau_{ref} = \frac{\sum_{\alpha} \tau^{\alpha} \dot{\gamma}^{\alpha}}{\dot{\Gamma}}. \tag{4.16}$$

Because the slip rates $\dot{\gamma}^{\alpha}$ are constant during a deformation increment, θ_{ref} (equation (4.15)) becomes:

$$\theta_{ref} = \frac{\sum_{\alpha} \theta^{\alpha} \dot{\gamma}^{\alpha}}{\dot{\Gamma}}. \tag{4.17}$$

Combining equation (4.14) with equation (4.17) results into

$$h_{ref} = \frac{\sum_{\alpha} h^{\alpha} \dot{\gamma}^{\alpha}}{\dot{\Gamma}}. \tag{4.18}$$

This definition of h_{ref} keeps the average work hardening of the substructure, which is characterised by the change of τ_{ref} with increasing deformation conform to the work hardening prescribed by the micro scale model during monotonic deformation, regardless of the degree of anisotropy that is imposed by having different values of h^{α} for the different slip systems.

For the equation for h^{α}, which governs the anisotropy, a phenomenological expression is used :

$$h^{\alpha} = \sum_{\beta} \frac{\tau^{\beta}}{\tau^{\alpha}} H^{\alpha\beta} \left(\frac{\dot{\gamma}^{\beta}}{\dot{\Gamma}} \right)^{n} \tag{4.19}$$

This equation is inspired on the modelling equation of Kocks et al. [1991] for latent hardening of slip systems which has been discussed in section 2.1.4 (cf. equation (2.20)). $H^{\alpha\beta}$ are the values of a hardening matrix H and n is a modelling parameter. The values of H and n will be constant throughout the deformation. The combination of equations (4.14), (4.10), (4.18) and (4.19) results in a set of S coupled differential equations. These are solved numerically for each orientation at each deformation increment by using the 4th order Runge-Kutta method.

Equation (4.19), unlike equation (2.20), does not intend to model the latent hardening at low strains due to the specific nature of the slip system interactions, but aims at capturing the effect that the build-up of a substructure due to the slip activity on slip systems β will have on the hardening of a slip system α at a relatively large strain.

In the present model, it will be assumed that the relative hardening contribution will predominantly depend on the slip rate and on the angle between the glide planes of the slip systems involved. For fcc materials, this angle can be either 0° for coplanar or 70.5° for non-coplanar slip systems. In order to model the Bauschinger effect, the hardening contribution to the slip system with the opposite glide direction will be very low. These considerations result in three different values within the hardening matrix H:

- $H_{//}$, which will be used for self hardening and all coplanar slip systems,
- H_X, which will be used for all intersecting slip systems,
- $H_{\leftrightarrow}$, which will be used for opposing glide directions.

Since within the model, only the ratios between these values are of importance, the value of $H_{//}$ is set to unity. As will be demonstrated in the next section, the value of n will influence the relative importance of the slip rates.

The presence of the ratios $\tau^{\beta}/\tau^{\alpha}$ makes that for constant slip rates, these ratios will evolve to saturation values.

4.2.2 Influence of H_X, $H_{\leftrightarrow}$ and n

The anisotropy resulting from the build-up of a substructure at the meso scale is in the model achieved by the influence of three anisotropy modelling parameters : H_X, $H_{\leftrightarrow}$ and n, which are all present in equation (4.19). To demonstrate their effect, the resulting τ^{α} - Γ curves of a single orientation which has three slip systems that are activated with constant slip rates $\dot{\gamma}^{\alpha}$, is shown in fig. 4-4 (a). The corresponding evolution of the anisotropy ratios τ^{α}/τ_{ref} with Γ is shown in fig. 4-4 (b). It should be noted that in this specific example the three active slip systems have three different values for their slip rates and that the two slip systems with the lower slip rates are coplanar. All τ^{α} are initiated with the same

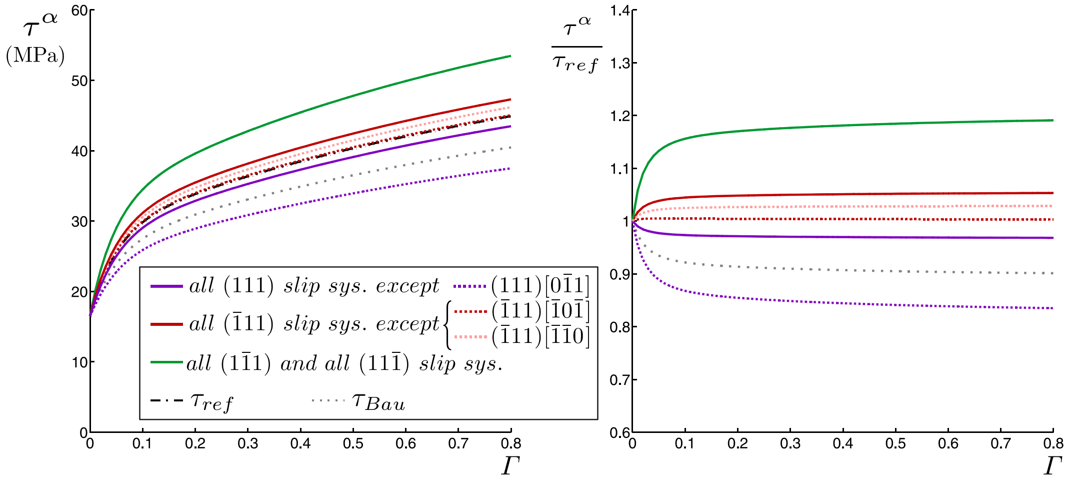

(a) $H_X = 2.6$ $H_\leftrightarrow = 0.2$ $n = 1.0$ **(b)**

Fig. 4-4 : The evolution of the critical resolved shear stresses τ^α (a) and the anisotropy ratios to τ_{ref} (b) with the total amount of slip Γ in a single orientation that deforms with 3 active slip systems, having a constant slip rate throughout the deformation : $\dot{\gamma}$ on (111)[01$\bar{1}$] is 0.625$\dot{\Gamma}$, $\dot{\gamma}$ on ($\bar{1}$11)[101] is 0.25$\dot{\Gamma}$ and $\dot{\gamma}$ on ($\bar{1}$11)[110] is 0.125$\dot{\Gamma}$.

value, assuming no pre-existing substructure to be present at the beginning of the deformation.

It is clear from equation (4.19) that if all anisotropy modelling parameters would be unity, all τ^α would harden the same way as τ_{ref} and all anisotropy ratios would be 1, resulting in an isotropic hardening of all slip systems. Values different from unity for H_X and $H_\leftrightarrow$ will introduce anisotropic hardening as demonstrated in fig. 4-4. Due to the scaling with $\left(\dot{\gamma}^\beta/\dot{\Gamma}\right)^n$ of the hardening contributions to other slip systems in equation (4.19), only the active slip systems will contribute to the hardening of the slip systems. If $n \geq 1$, the relative contribution to the overall hardening of the highest active slip system $(111)\left[01\bar{1}\right]$ is larger than in the case where the slip rates are taken as the weighting factors (this is if $n = 1$). Since the contribution to the work hardening of intersecting slip systems in the example is $H_X = 2.6$ times higher than to the self hardening (and the hardening of coplanar slip systems), the slip systems with the $\left(1\bar{1}1\right)$ and the

$(11\bar{1})$ glide planes, that have no slip activity on them, will harden the most (green curves in fig. 4-4). The glide plane with the highest activity (111) will harden the least (purple curves in fig. 4-4).

Initially, when all τ^β / τ^α ratios in equation (4.19) are 1, the rate of anisotropy change h^α / h_{ref} of the slip systems on non active glide planes (green curve) will be at its maximum. Due to the resulting more rapid increase of τ^α of these slip systems compared to the increase of the τ^β of the active slip systems, the presence of the ratios τ^β / τ^α in equation (4.19) makes that h^α / h_{ref} will asymptotically decrease towards a steady state. This causes the increase of τ^α / τ_{ref} of slip systems on non active glide planes to gradually level off, as can be seen in fig. 4-4 (b).

The active slip systems will receive hardening contributions of the other active slip systems (depending on their slip rates and whether they are intersecting or not) and a self hardening contribution equal to $\theta_{ref} \left(\dot{\gamma}^\alpha / \dot{\Gamma}\right)^n / h_{ref}$, with $\dot{\gamma}^\alpha$ the slip rate of the slip system. Since in the example of fig. 4-4 $H_X > 1$, the hardening rate of active slip systems will be lower than the hardening rate of slip systems on non active glide planes. Due to the presence of the ratio τ^β / τ^α in equation (4.19), the increase or decrease of τ^α / τ_{ref} will gradually level off.

For non-active slip systems on glide planes that have other activated slip systems, the hardening will be identical to that of the active slip systems on the same glide plane, since these slip systems will receive exactly the same hardening contributions. Only the slip systems that have opposite glide directions as active slip systems will undergo a different hardening. The hardening of such a slip system will be equal to

$$\theta^\alpha = \theta_{ref} \frac{\tau^{-\alpha} H_{\leftrightarrow} \left(\dot{\gamma}^{-\alpha} / \dot{\Gamma}\right)^n + \tau^\beta \left(\dot{\gamma}^\beta / \dot{\Gamma}\right)^n + \sum_\delta \tau^\delta H_X \left(\dot{\gamma}^\delta / \dot{\Gamma}\right)^n}{\tau^\alpha h_{ref}} \tag{4.20}$$

with $\dot{\gamma}^{-\alpha}$ the slip rate of the opposite active slip system, β indicating another possibly active slip system on the same glide plane and δ indicating all active intersecting slip systems. If $H_{\leftrightarrow} < 1$, then the hardening rate will be lower than the hardening rate of the opposite slip system. This enables the model to predict the Bauschinger effect (cf. section 2.3.1.a). To illustrate this, the value of the

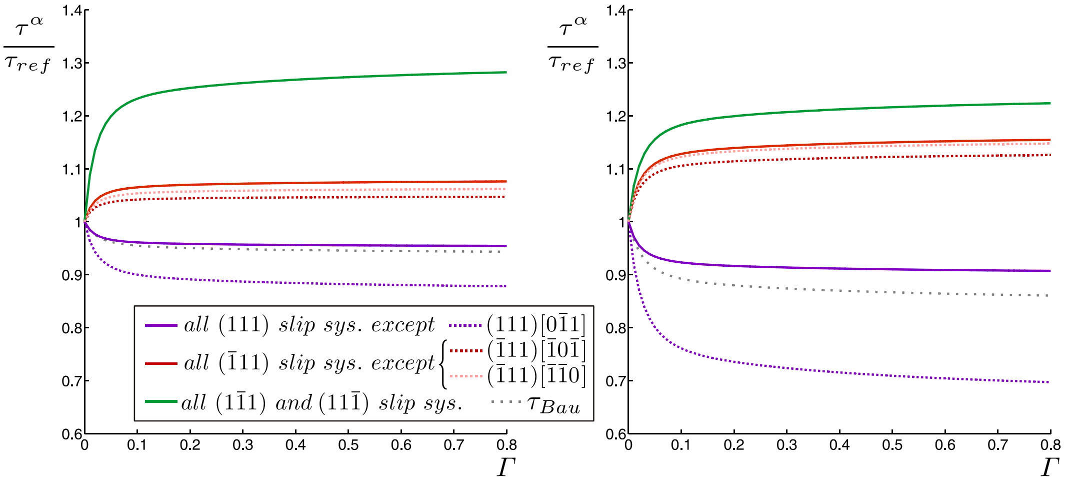

$H_X = 5.2 \quad H_{\leftrightarrow} = 0.2 \quad n = 1.0$

(a)

$H_X = 2.6 \quad H_{\leftrightarrow} = 0.2 \quad n = 2.0$

(b)

Fig. 4-5 : Evolution of the anisotropy ratios for the same imposed deformation as in fig. 4-4 but with different values for the modelling constants : (a) a twice as large value for H_X and (b) a twice as large value for n.

microscopic reference stress at a complete stress reversal τ_{Bau} is plotted in fig. 4-4 (a) and its ratio to τ_{ref} in fig. 4-4 (b).

If the value for H_X is increased (fig. 4-5 (a)), the non-active and lesser active slip systems will be hardened more by the most active slip systems, while the most active slip systems, due to the normalisation of h^{α} with h_{ref} in equation (4.14), will receive a lower hardening. Since $n=1$ in fig. 4-5 (a), the level of anisotropy will be increased conform the distribution of the overall slip rate $\dot{\Gamma}$ over the different slip rates $\dot{\gamma}^{\alpha}$. As can be seen from equation (4.20) and fig. 4-5 (a), this will also influence the hardening rate of the slip systems with an opposite direction to an active slip system (if these slip systems at least intersect with another active slip system). In the example of figs. 4-4 and 4-5 increasing H_X will decrease the initial softening just after a complete strain reversal.

The value of n influences the build-up of anisotropy in a different way. It determines the relative importance of the contributions of the active slip systems. If n is much higher than 1, the slip system with the highest slip rate will contribute the greater part of the overall hardening. If n is lower than 1, slip systems with a low slip rate will as well contribute considerably to the hardening of other slip systems. If n is set to 0, all active slip systems will contribute equally to the hardening regardless of the slip rates.

According to the FC Taylor model, 5 slip systems on at least three different glide planes need to be active to accommodate an arbitrary deformation of a single orientation of an fcc material. After an SPC, again three out of four glide planes will most likely be activated. In the A-Lamel version of the model on average 4 slip systems will be activated on at least two glide planes. The fewer the slip systems that contribute considerably to the overall hardening, the higher the degree of substructural anisotropy inside the model. Where the value of H_X controls predominantly the anisotropy ratios between the most active and non active glide planes, n governs how different the hardening of the most active and the lesser active slip systems will be. This effect of n is illustrated in fig. 4-5 (b) with the larger than average hardening of the slip systems on the $\left(\bar{1}11\right)$ glide plane.

n also has a large effect on the hardening of the opposite directions of active slip systems (equation (4.20) and fig. 4-5 (b)). The opposite direction of the most active slip system obtains a much lower hardening rate, while the opposite directions of the other active slip systems harden considerably faster. These opposing tendencies do not completely compensate each other in the critical resolved shear stress of a complete strain path reversal τ_{Bau}. Depending however on how exactly $\dot{\Gamma}$ is distributed over the slip systems, in general τ_{Bau} will decrease with increasing n.

4.2.3 Relation to experimental observations

The model, as elaborated up to this point, should be able to predict the yielding stress at reloading after an SPC of any type. To get an insight on how the phenomenological submodel for substructural anisotropy attributes to the overall work hardening anisotropy, this section provides an intermediate assessment of how this model relates to the mechanical and substructural observations discussed in the previous chapters. Placing the modelling mechanisms in this context should provide a better understanding of the next section on the work hardening transient as well.

First the model is related to the relevant experimental observations, discussed in section 2.3.1.b and the last three sections of 3.3. Then the possible substructural mechanisms as given in section 2.3.3 are discussed within the context of the model. Finally some consequences inherent to the model formulation, but not apparent from experimental observations, will be discussed.

a) Mechanical observations

It is obvious from the example of fig. 4-4 that the model can lead to a reyielding stress at an SPC that is different from the flow stress reached at the end of prestraining and that this anisotropy cannot only be attributed to the texture. In a different straining mode, when a different set of slip systems is activated, the value of τ_{ref} (cf. equation (4.16)), calculated from the same set of τ^{α}, but with different values for the $\dot{\gamma}^{\alpha}$, can be considerably higher (if most new active slip systems were inactive before) or lower (if many active slip systems get reversed) than the value of τ_{ref} prior to the SPC. The model also incorporates the textural contribution, since a different straining mode applied to the same orientation will need a different value of $\dot{\Gamma}$ to accommodate the imposed strain rate, and will therefore have a different *M*-factor (equation (A.1)). For a textured material, this will result in a different $\overline{M}$ and consequently a textural contribution to the anisotropy (equation (2.30)).

The observation that for a certain combination of straining modes the difference between the reyielding stress and the flow stress at the end of prestraining increases with increasing prestrain, is also captured by the model. Although the anisotropy ratios after some amount of prestraining are almost constant (fig. 4-4 (b)), the difference between the τ^{α} steadily increases due to the ongoing work hardening (increase of τ_{ref}). The constant anisotropy ratios correspond well to the observed scaling with the overall work hardening of the microscopic reyielding stress as illustrated in figs. 3-13 (a) and 3-15 (a) in section 3.3.

The influence of the Schmitt parameter $\cos\theta$, quantifying the abruptness of the SPC, on the reyielding stress is a natural result of the model as well. For small changes in the strain path, with a Schmitt parameter close but different from 1, the same set of slip systems will be activated for most orientations, however with a somewhat different distribution of the overall slip rate on the individual slip systems, resulting in a slight increase of the value of τ_{ref}. With a decreasing value of $\cos\theta$, more and more grains will have slip systems activated on slip planes that were inactive before, resulting in a stronger influence of H_X on the reyielding stress. Whenever $\cos\theta$ gets sufficiently negative, some previously active slip systems will get activated in the opposite direction and $H_{\leftrightarrow}$ will influence the reyielding stress. For a full strain reversal, all previously active slip systems will be reversed and the contribution of $H_{\leftrightarrow}$ to the reyielding stress will be at its maximum.

How abrupt an SPC has to be to result in a certain difference of the flow stress is in the model largely controlled by the value of n. A large value of n combined with $H_X > 1$ makes any decrease of the slip rate on the glide plane of the largest active slip system result in a considerable increase of τ_{ref}, due to the higher amount of hardening that all other glide planes did receive during prestraining. The effect that a large value of n makes the slip systems on the glide plane of the most active slip system more energetically favourable for selection in the texture model does not prevent that for most SPC the slip rate on this glide plane will decrease. This has been confirmed by several model calculation experiments.

b) Substructural mechanisms

In section 4.2.1 on the mathematical formulation of the substructural anisotropy model, it is argued that the effect of hardening of slip systems due to the build-up of a substructure by the dislocation activity on other slip systems might differ from the hardening due to the nature of the direct interactions of the involved dislocations which has been studied in latent hardening experiments (cf. section 2.1.4). In fact, little is known about whether the hardening contribution of a well-developed substructure to a certain slip system at large strains might still very much depend on the nature of the specific dislocation-dislocation interactions. If the substructure has taken the form of dislocation cells with DDWs and microbands (cf. section 2.2.1), other hardening contributions might come from the probably low penetrableness of the formed dislocation entanglements at the walls and the internal stress fields due to misorientation across the walls (cf. section 2.2.3.b).

Dislocation walls and intragranular misorientations are no explicit entities in the model, but the anisotropy induced by these structures can be mimicked by appropriate values of H_X and n. These walls namely tend to align themselves with the most active glide plane or the plane with the highest shear stress (cf. section 2.2.1.b). To obtain a sufficient degree of anisotropy, a relatively high value of H_X is needed. If the value for n is high, the highest active slip system will largely contribute to the hardening of the intersecting glide planes, making the activation of slip systems intersecting the most active glide plane more difficult, which resembles the effect that DDWs or microbands parallel to the glide plane of the highest active slip system will have on intersecting slip systems. For a lower value of n, activity on other slip systems will contribute as well to the hardening of intersecting glide planes. In the language of substructural elements this translates to DDWs or microbands somewhat rotated away from the highest active slip system. In a similar way two intersecting slip systems that are simultaneously active with comparable high slip rates can be seen as representing a double set of intersecting DDWs.

In the model there is no distinction whether the hardening of intersecting glide planes is due to misorientation or penetration difficulties of mobile dislocations through the walls. From an EBSD study it is clear that the aluminium alloy used in this work has a high degree of misorientation anisotropy (results not included in the text), which will certainly contribute to the substructural anisotropy.

For materials or deformation conditions where this type of substructure does not form (cf. section 2.3.3), it is not clear from experimental observations how the stored dislocation density might affect the hardening on intersecting slip systems. In any case it is clear that the latent hardening due to the specific nature of dislocation interactions will be a lower limit for the substructural anisotropy. This can also be captured by the model by assigning a relatively low value to H_X and setting n to 1, thereby reducing equation (4.19) to the latent hardening equation of Kocks et al. [1991]. The proposed model is therefore not limited to materials with a certain substructural morphology. The main underlying assumption is that the anisotropy is directly related to the relative activity of the individual slip systems.

The difference between the critical resolved shear stresses of the forward and reverse direction of an active slip system $\tau^{\alpha} - \tau^{-\alpha}$ corresponds to the back stress which arises during the build-up of the substructure as discussed in sections 2.2.3 and 2.3.3. As illustrated by the examples of figs. 4-4 and 4-5, this back stress inside the model is specific for each slip system and is not a common value for the slip systems on a certain glide plane. This corresponds to the notion of the back stress being a highly directed internal stress state caused by e.g. the local inhomogeneity of the deformation field, lattice misorientations or dislocation pile-ups at substructural obstacles. The influence of this back stress on other slip systems is however neglected in the model.

c) Further discussion

Equation (4.19) has a certain rate sensitive effect incorporated into it, although in a different way than what is usually understood under this term. Rate sensitivity is commonly used in visco-plastic formulations of crystal plasticity [e.g. Asaro and Needleman; 1985, Tóth et al.; 1988]. In these models the slip rate and the resolved shear stress on a slip system are directly linked by a power law :

$$\tau^{\alpha} = \tau_0 \cdot \mathrm{sign}\left(\dot{\gamma}^{\alpha}\right)\left(\frac{\left|\dot{\gamma}^{\alpha}\right|}{\dot{\gamma}_0}\right)^{\mu} \tag{4.21}$$

in which μ is the strain rate sensitivity exponent and τ_0 and $\dot{\gamma}_0$ are certain reference values. The use of this power law enables to solve the problem of linking a macroscopic strain rate to corresponding slip rates and an overall stress state for an individual orientation without the use of an energy criterion like equation (4.4). A result of this approach is that all slip systems will be simultaneously active (although some slip systems only with a very small strain rate). The main difference between the visco-plastic approach and the one used in the present model lies in the fact that equation (4.21) makes that the resolved shear stress directly relates to the slip rate of the slip system, while through equation (4.19) the evolution with strain of the critical resolved shear stress τ^{α} is scaled with the slip rates of the different systems. Where the value of μ directly influences the size and shape of the yield locus [Van Houtte; 1994], the value of n will not have any effect on the initial yield locus. That the hardening is dependent on the distribution of the shear rates is a feature of almost all latent hardening models. The rate sensitivity of the hardening does not change the fact that the present model is rate insensitive in the classical meaning of the terminology.

As a consequence of equation (4.19) the cross- and Bauschinger effect will be more pronounced if fewer slip systems are considerably active during prestraining. Within the model this might be somewhat counteracted by setting a large value for n, providing the larger active slip systems an increased weight in the overall hardening contribution. Since it is known that for a certain texture different straining modes can result in differences in the number of considerably active slip systems [Kocks et al.; 1998], it would however be interesting to find out whether this model prediction would be confirmed by SPC tests on samples with particularly chosen textures of the same material.

4.3 Work hardening during strain path changes

In section 2.3.2 it has been documented that after an abrupt change in the strain path the existing substructure gets gradually replaced by a new one which is stable to the current straining mode. This transition can happen via several mechanisms, depending on the material, the substructure morphology and the type of SPC. Because a part of the anisotropy is caused by the substructure (cf.sections 2.2 and 2.3), its replacement will consequently also change the anisotropy. Certain substructural elements are dissolved or broken up and their contribution to the material strength and its anisotropy is therefore removed. Simultaneously with this process, a new substructure is built up which is compatible with the current straining mode. This will alter the anisotropy correspondingly.

For the model this implies that after an SPC previous hardening contributions of slip systems which become much less active have to be gradually removed and that further hardening will depend on the current slip activities. Some slip systems will therefore experience work softening, while others, due to slip activity on a new set of slip systems, will get an increased work hardening rate.

To determine whether a slip system is less active than before, some memory of the values of the slip rates before the SPC is required. The transient hardening effects after an SPC manifest themselves over many deformation increments of the macro scale model, so a comparison with the slip rate values of the previous increment is not sufficient. The notion of memory of the previous amounts of slip, which in the physical material is provided by the detailed configuration of the substructural elements, is not present in the current work hardening equations and has to be explicitly modelled. How this is done will be explained in the first section.

The hardening transients after an SPC are discussed in the subsequent sections. Here it is detailed how abrupt changes in slip rates affect the work hardening of all slip systems. First this is done for slip systems that become much less active and then for slip systems of which the slip direction gets reversed.

4.3.1 Extra state variables for each slip system

The fundamental differences between the mechanical material response during a cross test and a Bauschinger test (cf. section 3.3.5), suggest that it is important whether the hardening contributions of a certain slip system before the SPC are reversed by either the activity on other slip systems or the activity on the same slip system in the opposite direction.

From the micromechanical point of view this difference can be understood if one considers that the dominant type of dislocation interaction after a strain path reversal is dislocation annihilation, while when other slip systems are active more complex interactions take place which lead to the partial disintegration of the substructure (cf. section 2.3.3).

After a strain path reversal, a high amount of stored dislocations is present which have an opposite sign as the dislocations that need to be mobilised to accommodate the current straining mode. This indeed leads to a high probability for annihilation events to occur. It is a direct consequence of what Kocks and co-workers [1980] have termed the polarity of the substructure. Polarity is an important concept in this context which has been briefly introduced in section 2.2.3.a and further discussed in section 2.3.3. It has been argued there that dislocation storage during deformation, regardless whether this storage is temporary or definite, requires the separation of dislocations of opposite sign to prevent dislocation annihilation. This separation requires some sort of obstacles which can be either large and complex like DDWs or precipitates or small like dislocation interaction products and dislocation entanglements. The polarity of the substructure merely designates this separation between the locations where (a few or many) dislocations of a particular sign are stored and the locations where the dislocations of opposite sign are stored. The polarity is therefore not related to the exact morphology of the substructure. The polarity depends on the stored dislocation density and the relative activity of the slip systems which have contributed to this storage. The importance of the polarity for the work hardening transient after strain path reversal however is material dependent and might also depend on the morphology of the substructure.

The mechanisms that lead to the partial disintegration of the substructure when a different set of slip systems is activated are only understood for bcc materials which form cellular structures with DDWs and microbands (cfr. section 2.3.3.b). In this case the deformation is localised in narrow microbands in which the pre-existing substructure is broken up. Self hardening inside the microbands limits the amount of deformation which can be accommodated before new microbands have to be created, ultimately resulting in the renewal of the substructure. Although this mechanism is only rarely reported for fcc materials, a similar mechanism should also be active to accommodate the observed dissolution of the substructure, since the mechanical response is very much alike. It is however clear that the contribution to the anisotropy of a particular slip system which has been active in prestraining but is inactive after the SPC, will gradually be decreased by the new slip activity, whatever the micromechanical mechanism might be. It seems to be necessary for a slip system to remain active to maintain its previous anisotropy contributions.

The polarity of a slip system and whether its previous anisotropy contributions can be maintained will be accounted for by introducing two different internal state variables for each slip system[27] into the model to simulate the memory of the slip activity.

a) Slip rate to maintain anisotropy

The variable λ^{α} represents the necessary slip rate to maintain the previous contributions to the anisotropy during further deformation for a slip system α. The λ^{α} value is always positive and the same for the forward and the backward direction of the slip system, since it is assumed that whenever a slip system gets reversed that its contribution to the anisotropy by previous hardening contributions to other slip systems will be maintained. λ^{α} is initiated as the (positive) value of the first slip rate $\left|\dot{\gamma}^{\alpha}\right|$ at the beginning of the (pre)deformation. The evolution equation of λ^{α} is:

$$\frac{d\lambda^{\alpha}}{d\Gamma}=b_1\left(\left|\dot{\gamma}^{\alpha}\right|-\lambda^{\alpha}\right). \tag{4.22}$$

This describes a exponentially decaying difference between λ^{α} and $\left|\dot{\gamma}^{\alpha}\right|$ with ongoing microscopic strain Γ. b_1 is a dimensionless modelling constant which controls the decay rate. Whenever λ^{α} gets smaller than $\left|\dot{\gamma}^{\alpha}\right|$ it is corrected to equal $\left|\dot{\gamma}^{\alpha}\right|$. This is done because the difference between λ^{α} and $\left|\dot{\gamma}^{\alpha}\right|$ will be used later on to model softening events because of the substructure dissolution. A value of λ^{α} smaller than $\left|\dot{\gamma}^{\alpha}\right|$ does not make sense in this context.

Fig. 4-6 shows an illustrative example of a single orientation that first deforms with two slip systems active, and after an SPC with three slip systems. The

---

[27] this means two variables (λ^{α} and π^{α}) are introduced for each physical slip system having both a positive and negative slip direction and not for the decoupled ones that only have one positive slip direction.

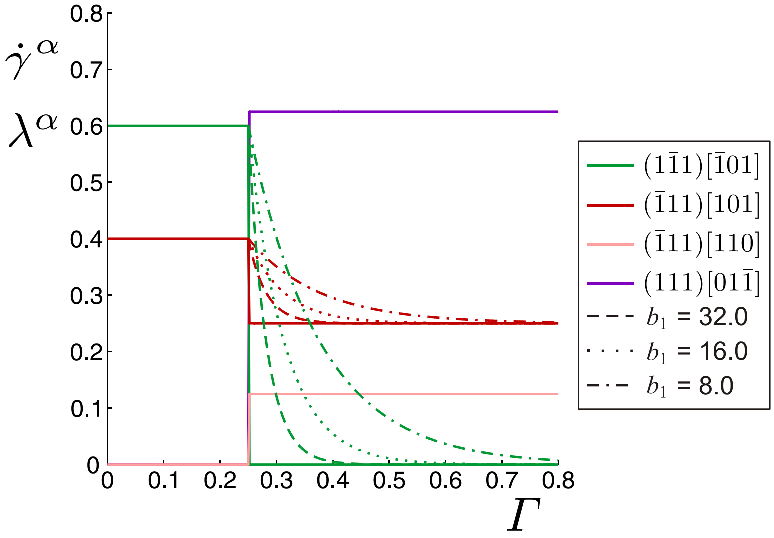

Fig. 4-6 : The evolution of the slip rates $\dot{\gamma}^{\alpha}$ (solid lines) and λ^{α} (dashed-dotted lines) with the total amount of slip Γ in a single orientation that deforms first with 2 slip systems and than with 3 active slip systems, having constant slip rates throughout both the deformation paths. The evolution of λ^{α} is shown for three different values of the modelling constant b_1.

$(1\bar{1}1)[\bar{1}01]$ slip system indicated in green gets completely inactive after the SPC. The value for its λ asymptotically decreases to 0 corresponding to equation (4.22). The higher the value of b_1, the faster the decay. The $(\bar{1}11)[101]$ slip system indicated in red, has a diminished activity after the SPC. Here the value of λ decays to the new value of $\dot{\gamma}$. The $(111)[01\bar{1}]$ and $(\bar{1}11)[110]$ slip systems are inactive before and active after the SPC. Their values for λ are equal to the corresponding values of $\dot{\gamma}$ for the whole deformation. In section 4.3.2 it will be explained how the difference between λ and $\dot{\gamma}$ will be used to model the softening due to the partial dissolution of the substructure.

b) Polarity of slip

The variable π^{α} describes the current polarity of a certain slip system. It can be both positive and negative, depending on whether the positive or the negative slip direction has been active. It is initialised as the signed slip rate $\dot{\gamma}^{\alpha}$ of its corresponding slip system. The polarity variable is like λ simultaneously associated to both slip directions of a physical slip system. Its evolution equation is:

$$\frac{d\pi^{\alpha}}{d\Gamma}=\frac{c_1}{\tau_{ref}-\tau_0}\left(\dot{\gamma}^{\alpha}-\pi^{\alpha}\right). \tag{4.23}$$

This, like equation (4.22), also describes an exponentially decaying difference between π^{α} and $\dot{\gamma}^{\alpha}$ (but not its absolute value) with ongoing microscopic strain Γ. c_1 is in this case a modelling constant with the dimension of a stress which controls the decay rate. τ_{ref} is the current value of the average critical resolved shear stress (equation (4.16)) and τ_0 equals the lattice friction that is also used in the micro scale model (equation (4.10)). The term in the denominator assures that it will take longer to undo the polarity of a structure that has hardened more as well as to subsequently rebuild it again in the opposite sense.

Whenever a new slip system[28] is activated during an SPC, the value of π^{α} is corrected to its current $\dot{\gamma}^{\alpha}$. Slip systems which become less or completely inactive after an SPC (like $\left(1\bar{1}1\right)\left[\bar{1}01\right]$ and $\left(\bar{1}11\right)\left[101\right]$ in fig. 4-6) will have a course for their π^{α} as described by equation (4.23), since it can be expected that the polarity of the slip system will gradually adapt itself with ongoing deformation to the polarity prescribed by the new straining mode.

In fig. 4-7 an example is given of how π^{α} evolves during a complete strain reversal. At the SPC the values of the π^{α} are opposite to the new slip rates $\dot{\gamma}^{\alpha}$. The difference gradually decreases with c_1 as the controlling variable for the decay rate. At a strain reversal the slip rate $\dot{\gamma}^{\alpha}$ will oppose the polarity of the slip system. This polarity gets gradually reduced with onging deformation until it is switched into a polarity of the same sign as the actual slip rate, from where it is again gradually built up according to the new sign.

However, the polarity is in the implementation of the model not regarded as a quality simply belonging to a singular slip system, where each slip system would have its own independent polarity value. It is regarded as the state of the whole

---

[28] meaning a new physical (not a decoupled) slip system. This can be checked within a strain increment by e.g. checking whether $\lambda^{\alpha}=0$ at the start of the increment (before its value is updated so that it reflects the slip rate of the previous increment).

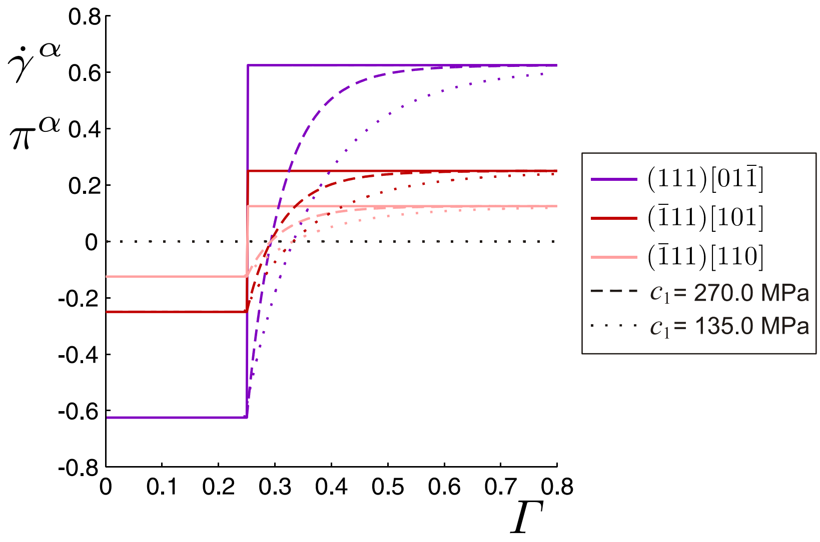

Fig. 4-7 : The evolution of the slip rates $\dot{\gamma}^{\alpha}$ (solid lines) and polarity variables π^{α} (dashed-dotted lines) with the total amount of slip Γ in a single orientation that deforms with 3 active slip systems that are reversed at an SPC. The evolution of π^{α} is shown for three different values of the modelling constant c_1.

substructure (irrespective of its morphology). Therefore it is also chosen to have the sum of all slips Γ as the independent variable in equation (4.23), instead of γ^{α} as well as including τ_{ref} in this equation rather than τ^{α}. The change of polarity is a result of the combined slip in the new straining mode, instead of only the slip on the particular slip system α. For constant slip rates and full strain reversal this means that the polarity switches at a singular point in the strain history (cf. fig. 4-7). For non constant slip rates, there can be differences in the points where the polarity variables of the individual slip systems switch sign. The difference between the polarity variable and the current slip rate will be used to model the transient effects that occur during a strain path reversal in section 4.3.3.

c) Memory of prestraining

The values of the λ^{α} and π^{α} are only related to the slip rates $\dot{\gamma}^{\alpha}$ obtained for the strain increment just before an abrupt SPC. They do not contain any information about the evolution of the slip rates during prestraining (the strain history). This strain history is however reflected in the current anisotropy of the substructure which is represented by the values of τ^{α}. In the model both the differences of the variables λ^α and π^α with the current values of the slip rates $\dot{\gamma}^\alpha$ (memory of the slip rates just before the SPC) and the values of τ^α (memory of the strain history) will have an influence on the additional hardening and softening terms which will be introduced in the following sections for cases where slip systems abruptly change their activities.

4.3.2 Softening if slip system becomes much less active

As has been discussed in the literature survey, the dissolution of the pre-existing substructure during cross type SPC is typically accompanied by a transient work softening regime after which the work hardening curve returns to the monotonic hardening curve of the new straining mode (cf. section 2.3). The anisotropy because of the substructure will be altered during this process.

In section 4.2 it is explained that the influence of the pre-existing substructure on the flow behaviour within the model is represented by the anisotropy due to differences in hardening contributions by the individual slip systems. In the previous section, it has been proposed to use the drop of the slip rate of a certain slip system as predicted by the texture model to initiate the reduction of this slip system’s previous contribution to the work hardening anisotropy. If this reduction is substantial, work softening will occur. This extra softening will gradually diminish with further deformation, since the influence of the pre-existing substructure on the anisotropy has to disappear with its dissolution. Meanwhile the anisotropy due to the development of a substructure characteristic to the new straining mode has to be built up, which results in the work hardening behaviour as would be observed during monotonic deformation.

First a mathematical description for the work hardening equations will be formulated in correspondence with the above mentioned principles. Then the influence of the fitting parameters will be demonstrated with an example for a single orientation. Finally the introduced variables and fitting parameters will be discussed in relation to the experimental observations.

a) Mathematical formulation

To account for the softening because of a drop in the slip rate of certain slip systems, the hardening equation for a single slip system of equation (4.14) will be altered into:

$$\theta^{\alpha}=\frac{d\tau^{\alpha}}{d\Gamma}=\theta_{ref}\frac{h^{\alpha}}{h_{ref}}-b_2\frac{l^{\alpha}}{h_{ref}}, \tag{4.24}$$

where l^{α} is related to the previous hardening contributions which the slip system α received due to slip activity on a number of slip systems β of which the slip rate has dropped to a lower value after an SPC. b_2 is a fitting parameter with the dimension of a work hardening rate (MPa) which corresponds to the intial softening rate because of the dissolution process. l^{α} is like h^{α} a factor which describes the anisotropy. The normalisation with h_{ref} is done in order to keep this ratio between 0 and 1, irrespective of the value of n. While h^{α} describes the anisotropy contribution of the new substructure which is being built up, l^{α} describes the anisotropy contribution of the old substructure which is dissolved because of the SPC. The softening because of the break-up of the pre-existing substructure is therefore modelled by the second term in equation (4.24). l^{α} is calculated as:

$$l^{\alpha}=\sum_{\beta}\frac{\tau^{\beta}}{\tau^{\alpha}}H^{\alpha\beta}\left(\frac{\lambda^{\beta}-\left|\dot{\gamma}^{\beta}\right|}{\dot{\Gamma}}\right)^{n}, \tag{4.25}$$

which is analogue to the equation for h^{α} (equation (4.19)). The slip rates $\dot{\gamma}^{\beta}$ of the contributing slip systems β from equation (4.19) are replaced here by the difference between λ^{β} and $\left|\dot{\gamma}^{\beta}\right|$. λ^{β} represents the slip rate necessary for a slip system β to maintain its previous hardening contributions as introduced in section 4.3.1.a. At an SPC it is initially equal to the absolute value of the slip rate prior to the SPC. With further deformation it exponentially decays to the magnitude of the current slip rate $\left|\dot{\gamma}^{\beta}\right|$, which can e.g. be 0, if the slip system has become inactive (cf. fig. 4-6). As long as the current slip rate is lower than λ^{β}, this slip system will have a softening contribution to all slip systems via their l^{α}, which will be non-zero. The extent of the transient regime is therefore a function of the decay rate of λ^{β}, which is controlled by the fitting parameter b_1. The softening contribution eventually becomes negligible for all slip systems and the hardening rates of the slip systems will obey the anisotropy contributions according to the new substructure, represented by h^{α}. The true derivative of τ_{ref}, which is called θ_{sub}, deviated from the value of θ_{ref} (prescribed by the micro scale model) when the values for the for the l^{α} were non-zero . It will now become equal to θ_{ref} again. This results in the return to the monotonic work hardening curve.

The back stress $\tau^{\beta}-\tau^{-\beta}$ on the slip systems that had a drop of their slip rate at an SPC (so $\lambda^{\beta}>\left|\dot{\gamma}^{\beta}\right|$), will also be altered due to the dissolution of the pre-existing substructure. The hardening rate of the critical resolved shear stress $\tau^{-\beta}$ of the opposite direction as the slip rate prior to the SPC, $\theta^{-\beta}$ will get an additional hardening term:

$$\theta^{-\beta}=\frac{d\tau^{-\beta}}{d\Gamma}=\theta_{ref}\frac{h^{-\beta}}{h_{ref}}-b_2\frac{l^{-\beta}}{h_{ref}}+b_2\frac{\tau^{\beta}-\tau^{-\beta}}{\tau_n}\frac{l^{\beta}}{h_{ref}}\,. \tag{4.26}$$

This hardening term scales with the back stress $\tau^{\beta}-\tau^{-\beta}$, which will lower with ongoing deformation and the value of the softening term $b_2\, l^{\beta}/h_{ref}$ that the other (previously active) slip direction receives. τ_n is a normalisation factor with a similar order of magnitude as the back stress. In the current model τ_n is set to 1.0 MPa.

b) Influence of b_1 and b_2

To show the influence of the two fitting parameters, the model is applied to a single orientation with slip rates as described by fig. 4-6, using different values of both parameters. Other modelling constants have been taken equal to the ones in fig. 4-4. The evolution of τ_{ref} with the sum of slips Γ and the corresponding hardening curve are shown in fig. 4-8.

It is clear that b_1 has an influence on the length of the strain interval in which softening occurs. For higher values of b_1 this interval tends to be shorter. It is however more appropriate, following equations (4.22) and (4.25), to link b_1 to the length of the strain interval over which the work hardening shows a transient behaviour. This is the amount of strain until the stress strain curve becomes parallel to the monotonic one (defined as γ_3 in fig. 2-13). Whether there is softening and the length of the corresponding strain interval is also influenced by the value of b_2. This explains why the curve with the lowest $b_1=8.0$ does not

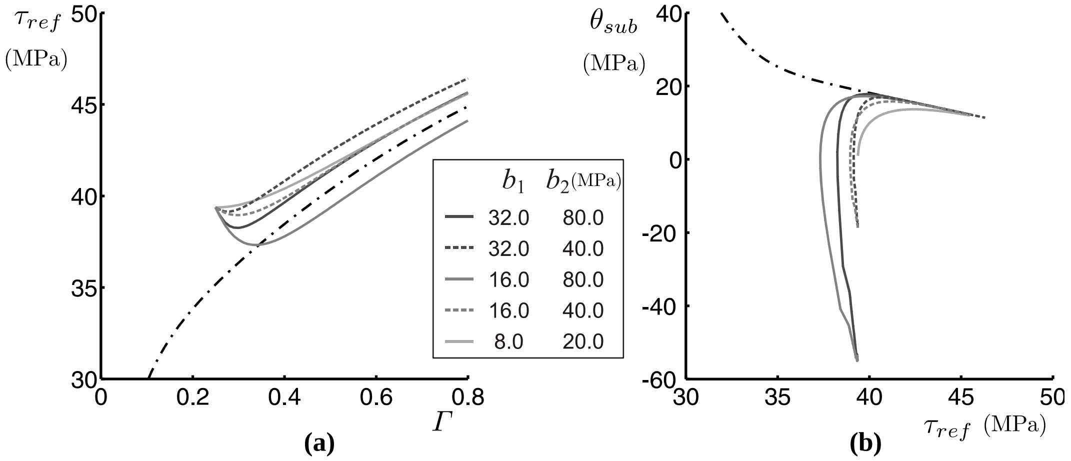

(a) **(b)**

Fig. 4-8 : The evolution of τ_{ref} with Γ (a) and the corresponding work hardening curve θ_{sub} vs τ_{ref} (b) according to the meso scale model for a single orientation which deforms with slip rates as shown in fig. 4-6 and anisotropy constants as in fig. 4-4. The different curves have been obtained with different values of the parameters b_1 and b_2 as indicated. The black dash-dotted lines represent the monotonic stress-strain and the corresponding work hardening curve.

show softening. The influence of b_2 is most obvious in the starting points of the work hardening curves. The higher the value of b_2, the lower the initial work hardening rate becomes. This scaling is linear with the monotonic hardening curve corresponding to $b_2 = 0.0$ MPa, which follows from equation (4.24). Of course the value of b_2 is also reflected in fig. 4-8 by the initial slope of the stress-strain curves.

Curves with the same ratio of b_1/b_2 eventually return to exactly the same monotonic stress-strain curve (which means that they, according to definitions in fig. 2-13 have the same values for θ_3, τ_3 and γ_3). Consequently this ratio is related to the value of the strain offset (defined as γ_0 in fig. 2-13) which determines whether there is an additional or deficient strain to obtain the same strength via a monotonic deformation path (cf. section 2.3.1.a).

The stress-strain curves and the anisotropy ratios of the individual slip systems for two of the examples of fig. 4-8 are shown in fig. 4-9. Both examples have the same value of b_1/b_2. The stress-strain curves of the individual slip systems are all

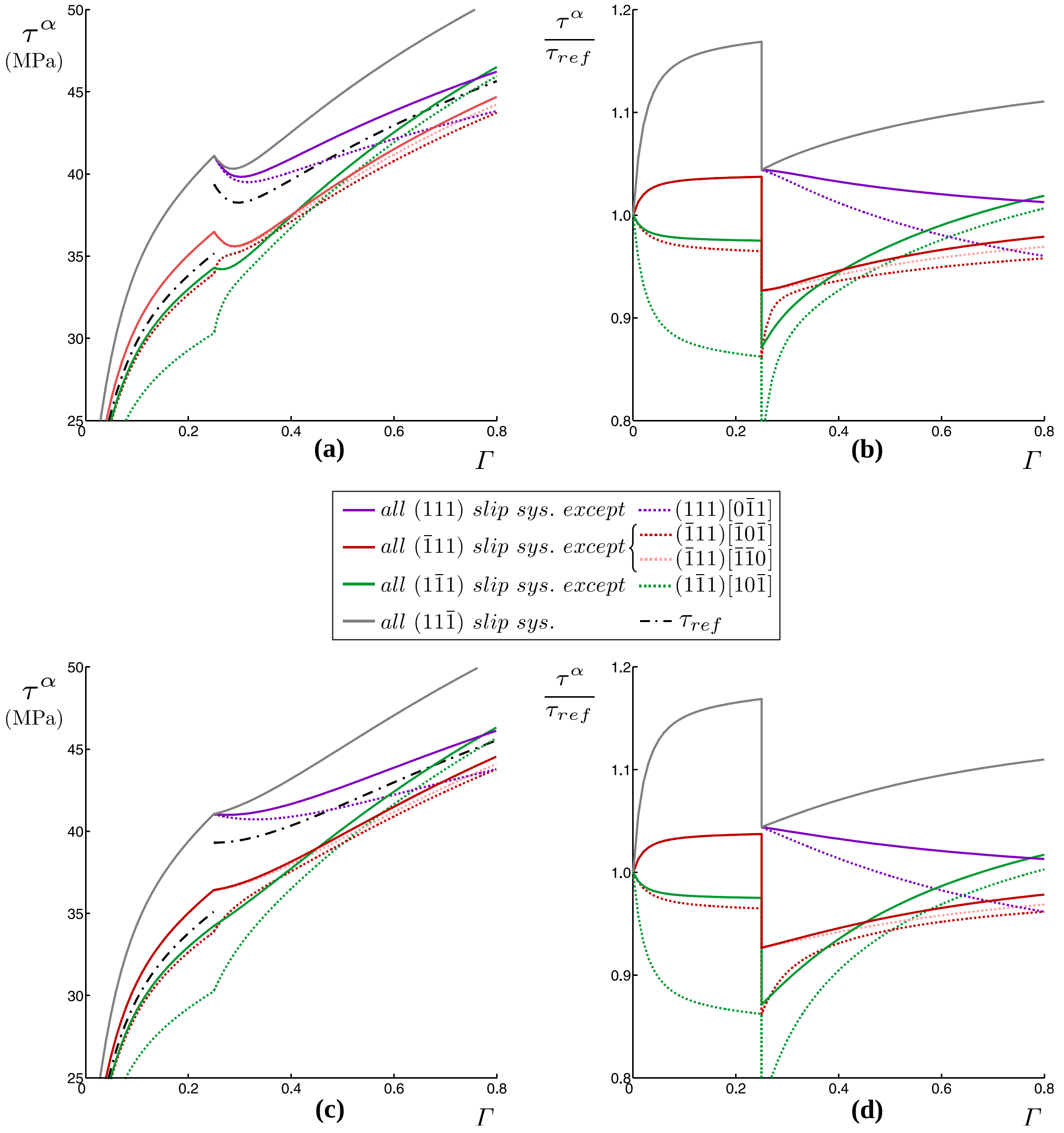

Fig. 4-9 : Stress-strain curves of the individual slip systems and the corresponding anisotropy ratios for two of the examples shown in fig. 4-8. (a)-(b) : b_1=32.0**,** b_2=80.0 MPa**; (c)-(d) :** b_1=8.0**,** b_2=20.0 MPa**.**

continuous curves, but the completely different slip rates after the SPC (shown in fig. 4-6) result in a large step of τ_{ref} at the SPC. This makes all anisotropy ratios discontinuous functions. This is in fact an illustration of the anisotropy of the strength of the substructure towards the straining mode.

First the tendencies for the individual slip systems will be explained relating to fig. 4-9 (a) and (b). The $(111)\left[01\bar{1}\right]$ slip system, displayed in purple, is inactive during prestraining and becomes highly active after the SPC. It has a high critical resolved shear stress, which after the SPC is initially lowered due to the dominating softening processes. The value of $b_2\, l^{\alpha}/h_{ref}$ in equation (4.24) is larger than $\theta_{ref}\, h^{\alpha}/h_{ref}$. The softening term however decreases with the lowering of the λ-values of the previous active slip systems. The hardening term due to the build-up of the new substructure gradually takes over and makes the slip system harden according to the principles for a monotonic straining path. Since the $(111)\left[01\bar{1}\right]$ system is active after the SPC, it has a lower value of h^{α}/h_{ref} compared to the $\left(11\bar{1}\right)$-systems displayed in gray. Its reverse direction $(111)\left[0\bar{1}1\right]$, indicated in the purple dotted line, has a lower hardening rate because of the build-up of the back stress.

The $\left(1\bar{1}1\right)\left[\bar{1}01\right]$ slip system, displayed in green, is active during prestraining and becomes inactive after the SPC. Its low critical resolved shear stress undergoes much less softening after the SPC, because of its relatively low value of l^{α}, which is due to the presence of the H-matrix in equation (4.25). The softening of a previously highly active slip system has a high relative contribution of the self ‘hardening’ coefficient $H_{//}$, which results in lower softening rates than for inactive slip systems which are softened faster under the dominance of H_X in their equation for l^{α}. When the softening becomes negligible, the $\left(1\bar{1}1\right)\left[\bar{1}01\right]$ hardens rather fast because of its high relative value of h^{α} which is effected by its inactivity. The hardening of the opposite direction $\left(1\bar{1}1\right)\left[10\bar{1}\right]$, indicated in the green dotted line, is prescribed by equation (4.26). Apart from some softening contribution which also applies to the forward direction, it is predominantly hardened by the lowering of the back stress described by the final term in equation (4.26). The lowering of the back stress happens much faster than the ongoing softening processes, due to the multiplication with the value of the current back stress in equation (4.26), but it is however controlled by the softening process which explains the presence of $b_2\, l^{\beta}/h_{ref}$ in the final term of equation (4.26).

Because the extra hardening is scaled with the actual value of the back stress and the remaining hardening and softening terms are equal to the hardening equation of the opposite direction, it is guaranteed that the extra hardening only decreases the back stress and cannot lead to a back stress of opposite sign.

The slip systems on the $(\bar{1}11)$ glide plane, indicated in red and pink, display a mixture of the behaviours of the two described slip systems above, since $(\bar{1}11)[101]$ is active before and after the SPC and $(\bar{1}11)[110]$ is activated by the second straining mode.

The tendencies are similar for all slip systems in case of the lower values of b_1 and b_2 (fig. 4-9 (c) and (d)). Because of the lower value of b_2, the initial softening rate is much lower and only counterbalances the hardening due to the build-up of the new substructure. The softening however remains a significant process for a longer strain interval due to the lower value of b_1. Although this results in a very different transient regime for τ_{ref}, an almost equal evolution of the anisotropy ratios can be observed. *The value of the ratio b_1/b_2 largely controls how the substructural anisotropy evolves after a cross type SPC.* Different values of b_1/b_2 would evidently lead to different evolutions of the anisotropy ratios. An exception to this applies to the reverse direction of previously active slip systems like $(1\bar{1}1)[10\bar{1}]$ and $(\bar{1}11)[\bar{1}0\bar{1}]$, indicated in dotted green and dotted red. Their initial anisotropy ratio is very much affected by the value of b_2, the eventual anisotropy ratio after the transient regime is however very similar.

Compared to the anisotropy ratios of the same straining mode for monotonic straining (cf. fig. 4-4 (b)), the ratios are still very different even long after the transient regime. They however still evolve and will tend to the ratios of the monotonic case because of the ratio $\tau^{\beta}/\tau^{\alpha}$ in the equation for h^{α} (equation (4.19)). This indicates that with the used values of b_1 and b_2 in the example, the original substructure still maintains an important contribution in the overall substructural anisotropy. Only a very large value of b_2, combined with a rather low b_1 could, with these modelling equations, achieve the total disappearance of this contribution during the transient, but this would result in a high amount of additional strain to obtain the same strength as via a monotonic deformation path (a high positive value for γ_0).

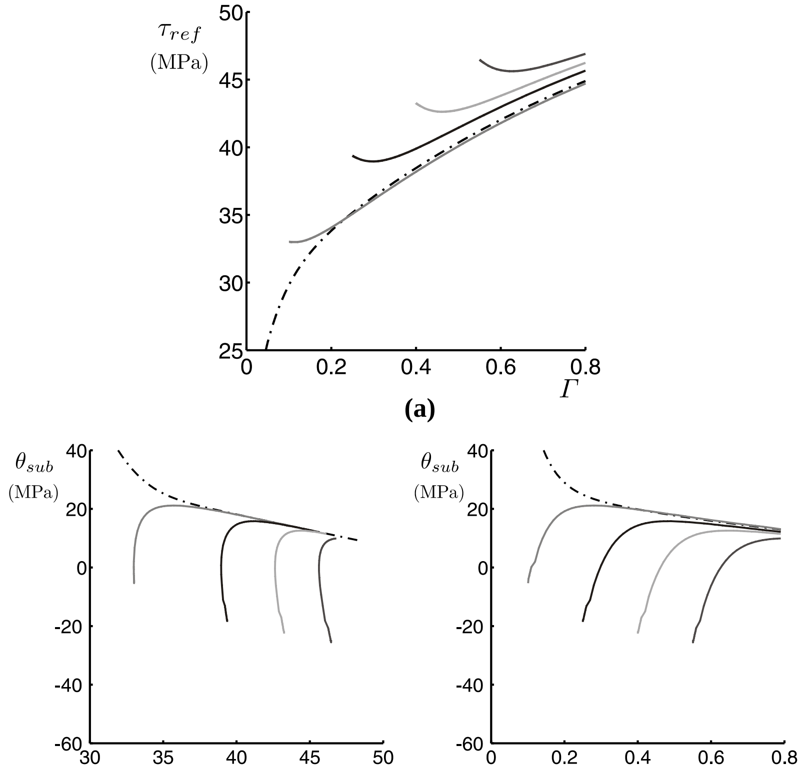

(a)

(b)

(c)

Fig. 4-10 : Work hardening according to the meso scale model for a single orientation which deforms with slip rates as shown in fig. 4-6 but with the SPC occurring at different amounts of prestrain. The modelling constants are b_1=32.0, b_2=80.0 MPa, **with the anisotropy constants as in fig. 4-4. (a) Stress vs. strain, (b) hardening rate vs. stress, (c) hardening rate vs. strain.**

In fig. 4-10 the work hardening behaviour is shown for the same example but with the SPC occurring at different amounts of prestrain. For all curves the same values for the modelling constants have been used. Here it can be seen how the amount of prestrain affects the transient regime. At lower prestrains the initial averaged critical resolved shear stress τ_{ref} after the SPC is of course lower, which means that the value of θ_{ref} will be higher. This results in a higher value of the initial work hardening rate θ_{sub}. For the lowest prestrain now almost overall softening occurs, while the largest prestrain results in a large drop of τ_{ref} just after the SPC. The difference between the initial hardening rate after the SPC and the monotonic hardening rate at the same stress value (which in the model is θ_{ref} as obtained from the microscopic work hardening model), is constant. The remainder of the work hardening transient is rather similar for all curves, with an exponentially decaying difference between the work hardening curve of the examples and the work hardening curve of the monotonic case. The amount of strain until the stress-strain and the hardening rate-strain curves become exactly parallel to the monotonic case γ_3 is almost equal for all prestrains and about 0.2, because it only depends on b_1 and the anisotropy ratios which have been obtained during prestraining (they behave similarly to the ones shown in fig. 4-4 (b)). Because of the permanent hardening (defined as $\Delta\tau$ in fig. 2-13), the visual interpretation of especially the hardening rate vs. strain curve to resolve this, is misleading since only at larger strains the curves seem to coincide.

Qualitatively, these modelling curves resemble the experimentally obtained ones of hardening behaviour during cross tests as shown in fig. 3-13. It should be noted that this modelling curve only represents the behaviour of one single orientation, while the experimental curves contain the averaged behaviour of thousands of grains, which all could have somewhat different responses. It is already discussed in section 3.3.5, that for the experimental curves, it appears that the drop in hardening rate and the length of the transient regime are fairly constant and are not related to the amount of prestrain.

c) Relation to experimental observations

Most effects of the modelling equations related to the substructural transition during cross type of SPC (equations (4.22, 4.24-4.26)) on the mechanical work hardening behaviour, have been discussed in the previous section. In this section the physical meaning of the modelling parameters and their relation to the observed substructural transitions will be discussed.

In section 4.3.1.a, the λ^{α} parameter has been defined as the slip rate for a slip system α to maintain its previous anisotropy contributions. Because of its gradual decrease with further strain if the slip rate $\left|\dot{\gamma}^{\alpha}\right|$ is lowered or becomes 0, it is applied through equation (4.25) to delay the adaptation of the critical resolved shear stress τ^{α} to the hardening behaviour prescribed by the new straining mode. λ^{α} has the quality of a damped equivalent of the new value of $\left|\dot{\gamma}^{\alpha}\right|$. This damping is related to the microstructural observation that the pre-existing substructure is not instantly replaced by something different, but by processes of dissolution, gradual replacing or breaking up which are currently not well understood (sections 2.3.2.b and 2.3.3.b). The λ parameters constitute the gradual transition of the old substructure, which dissolves, to a new substructure which replaces it, under the change of the loading conditions. The modelling equations describing this transition are phenomenological and do not distinguish between the mentioned physical mechanism that could take place.

The mechanical effect of this damping, which consists of the decaying of the softening contribution to the slip systems, is controlled by the value of b_1. This can be e.g. observed in the difference between the stress strain curves of fig. 4-9 (a) and (c). For a high value of b_1 the damping only occurs in a short strain interval and the different τ^α as well as τ_{ref} show a rather fast convergence towards new stress-strain curves according to the hardening rates of the new straining mode. For the low value of b_1 the stress-strain curves will converge to the same set of stress-strain curves, but this transition is much more damped. Hypothetically this would mean that the pre-existing substructure in the case of fig. 4-9 (a) would much quicker vanish with further strain than in the case of fig. 4-9 (c). It is not necessarilly true that the mechanical importance completely corresponds to the visual perception of the substructure via e.g. TEM.

As mentioned in the discussion on fig. 4-9, the anisotropy ratios in the model after a cross type SPC do not correspond to the ratios of the same monotonic deformation. This is because the τ^α in their actual value also contain a memory of the deformation history, which is only partially erased by the softening process. This might as well be true for real substructures which under the form of unannihilated debris, dislocation structures at the core of substructural elements or at particles could result in a contribution to the substructural anisotropy which is very difficult to undo. The scaling in the hardening equation (4.19) with the ratio of the current critical resolved shear stresses of the interacting slip systems, however results in a slow decay of the difference between the momentary anisotropy ratios and the monotonic ones.

Because b_1 controls the length of the strain interval in which the substructural transition occurs, it can be regarded as a parameter describing the *sustainability* of the substructure when subjected to a different straining mode.

b_2 would accordingly give a measure for the *stability* of an existing substructure under the condition of a new straining mode. For a larger value of b_2, the substructure tends to dissolve initially faster. Consequently a larger amount of its previous contributions to the anisotropy becomes undone.

The ratio b_1/b_2 quantifies the *strength* of the substructure under a cross type SPC. The larger this ratio, the more the substructure will contribute to the remaining strength of the material after the work hardening transient, which correlates to a higher value of $\Delta\tau$ and correspondingly a more negative γ_0. More of the pre-existing substructure will remain that persists with further deformation.

4.3.3 Hardening if slip system is reversed

The work hardening after a strain path reversal has been extensively studied. The mechanisms on the micro scale that cause the characteristic transient behaviour are however not yet well understood. For cell forming materials, TEM studies show that the pre-existing dislocation substructure first gradually dissolves and that after some more strain a new substructure very similar to the previous one is built up (cf. section 2.3.2.a). From these observations, the percolation model by Kocks et al. [1980] has emanated. It is a theoretical framework describing the mechanisms for cell formation (cf. section 2.2.2.a) that both can explain the Bauschinger effect and the subsequent transient work hardening by the existence of a back stress facilitating dislocation flow in the reverse direction and the polarity of the substructure leading to remobilisation and fast annihilation of dislocations stored during prestraining respectively (cf. sections 2.2.3.a and 2.3.3.a). However, the occurrence at room temperature of a very similar transient behaviour in IF steel prestrained at -120 °C and therefore not having a cellular substructure [Rauch; 1997], challenges the necessity of a cellular substructure or other specific substructural elements implied by the percolation model explanations (cf. section 2.3.3.a).

It is nevertheless clear that the dislocations stored during prestraining play an important role for the work hardening during reverse straining. This has been the motivation for introducing a polarity variable for each slip system in section 4.3.1.b. The difference in polarity of the existing substructure and the newly formed one will have consequences for the hardening of the individual slip systems.

The Bauschinger effect, which refers to the lower reyielding stress at a strain path reversal, has already been modelled in the anisotropy equations for monotonic strain paths (equation (4.19)) by introducing a low value for $H_{\leftrightarrow}$. It has been discussed in section 4.2.3.b that the resulting value of $\tau^{\alpha} - \tau^{-\alpha}$ represents the back stress on a slip system α. This back stress will have an influence as well on the hardening behaviour after a strain path reversal.

How the polarity and the back stress are influencing the work hardening after a strain path reversal, will be described first by adapting the involved mathematical equations. Then these equations will be applied to an example of a single orientation to show the influence of the fitting parameters. Finally the most important variables and fitting parameters for strain path reversal will be discussed in the light of the experimental observations.

a) Mathematical formulation

According to the percolation model, the work hardening after a strain path reversal will mainly depend on whether the polarity of the pre-existing substructure has already been reversed or not. This aspect is transferred to the present model by formulating two sets of equations for the hardening of individual slip systems. One set will be used whenever the polarity parameter of a slip system is of opposite sign as the current slip rate, the other whenever the slip rate and polarity parameter have equal signs.

Initially after a strain path reversal, the polarity of each slip system is opposite to its current slip rate. Within the model this condition corresponds to $\pi^{\alpha}\dot{\gamma}^{\alpha} < 0$. Due to the Bauschinger effect, the critical resolved shear stress in the now active slip direction τ^{α} is smaller than the one of the opposite slip direction $\tau^{-\alpha}$ (in this section the currently active slip direction will be indicated α, its reverse which used to be active during prestraining by $-\alpha$). The back stress $\tau^{-\alpha} - \tau^{\alpha}$ that assists the dislocation motion in the new straining mode, will however decrease relatively fast. For slip systems that are reversed (which have $\pi^{\alpha} < \dot{\gamma}^{\alpha}$ if $\dot{\gamma}^{\alpha} > 0$ or $\pi^{\alpha} > \dot{\gamma}^{\alpha}$ if $\dot{\gamma}^{\alpha} < 0$), the hardening of the two slip directions will in the initial stage of the strain reversal ($\pi^{\alpha}\dot{\gamma}^{\alpha} < 0$) be described by

$$\theta^{\alpha} = c_2\left(\tau^{-\alpha} - \tau^{\alpha}\right)\frac{\left|\pi^{\alpha}\right|}{\left|\dot{\gamma}^{\alpha}\right|}\frac{h'^{\alpha}}{h'_{ref}} - b_2\frac{l^{\alpha}}{h_{ref}} \tag{4.27}$$

for the newly active direction and

$$\theta^{-\alpha} = -c_2\left(\tau^{-\alpha} - \tau^{\alpha}\right)\frac{\left|\pi^{\alpha}\right|}{\left|\dot{\gamma}^{\alpha}\right|}\frac{h'^{\alpha}}{h'_{ref}} - b_2\frac{l^{\alpha}}{h_{ref}} \tag{4.28}$$

for the reverse direction. These two equations result in an exponential decrease of the back stress. c_2 is a fitting constant with as dimension the inverse of strain, that controls the initial decay rate of the back stress. The h'^{α}/h'_{ref} ratio describes a somewhat altered anisotropic hardening ratio, which will be detailed below. Compared to the regular hardening equation for an individual slip system (cf. equation (4.24)) some changes have been introduced. The hardening term of the active direction does not scale with the average hardening rate θ_{ref} of the micro scale model, but with the back stress $\tau^{-\alpha} - \tau^{\alpha}$ and the degree of remaining polarity $|\pi^{\alpha}|/|\dot{\gamma}^{\alpha}|$. The presence of the latter incorporates the modelling assumption that the initial high degree of polarity facilitates the reduction of the back stress. This assumption will be further commented in section 4.3.3.c. The presence of the current value of the back stress value results in an exponential decrease of this value towards 0. This implies that the initial hardening after reyielding at a strain path reversal, which for single phase materials usually levels off relatively fast, in this model is attributed to the disappearing back stress which initially eases the dislocation flow.

During the strain interval that the substructural polarity value associated to a given slip system is of opposite sign as its current slip rate, all hardening contributions of such a slip system to other slip systems will be put on hold. This because the dislocations with the sign of the actual slip rate (irrespective whether they are newly created or remobilised out of the pre-existing substructure) will not be able to make a long lasting hardening contribution, since they are destined to annihilate because of the abundance of dislocations of opposite sign in the substructure due to its opposite polarisation. This will result in the different anisotropic hardening ratios h'^{α}/h'_{ref} which already has been used in equations (4.27) and (4.28). For all slip systems which were not reversed the hardening equation becomes :

$$\theta^{\beta} = \theta_{ref} \frac{h'^{\beta}}{h'_{ref}} - b_2 \frac{l^{\beta}}{h_{ref}} . \tag{4.29}$$

h'^{α} is defined by

$$h'^{\alpha} = \sum_{\beta \neq \delta} \frac{\tau^{\beta}}{\tau^{\alpha}} H^{\alpha\beta} \left(\frac{|\dot{\gamma}^{\beta}|}{\dot{\Gamma}} \right)^{n} \tag{4.30}$$

where the summation does not include the slip systems δ. These are the slip systems which are reversed except for the slip system α itself and its coplanar slip systems. The self hardening is maintained, because this will attribute to the reduction of the back stress in equations (4.27) and (4.28). The normalisation factor h'_{ref} is the weighted average of the h'^{α} and is calculated equivalently to h_{ref} (equation (4.18)). Within the model, the foregoing equations (4.27-4.30) govern the first part of the transient behaviour after the reversal of a slip system, which is as long as the polarity parameter π^{α} has the opposite sign of $\dot{\gamma}^{\alpha}$.

Whenever the polarity parameter π^{α} has become zero and evolves further towards $\dot{\gamma}^{\alpha}$ (e.g. at about $\Gamma = 0.3$ for $c_1 = 16.0$ in fig. 4-7), the polarity of the overall substructure becomes equal to the polarity of the straining mode. This means that the influence on the work hardening of the remaining elements of the pre-existing substructure is compensated and subsequently dominated by the influence of the newly built-up substructure according to the polarity of the current straining mode. Because the polarity is still being built up, the slip system hardens to a much lower extent. This is related to the higher probability for annihilation of dislocations that accommodate the slip compared to the situation at the same level of the critical resolved shear stress during monotonic deformation. This higher probability is because dislocations of opposite sign stored during prestraining still exist. As the polarity value π^{α} becomes equal to the value of $\dot{\gamma}^{\alpha}$, the probability for annihilation will become similar to that during monotonic straining.

The hardening equation for slip systems that have a polarity value π^{α} lower but of equal sign as $\dot{\gamma}^{\alpha}$ becomes:

$$\theta^{\alpha} = \theta_{ref} \frac{|\pi^{\alpha}|}{|\dot{\gamma}^{\alpha}|} \frac{h''^{\alpha}}{h''_{ref}} - b_2 \frac{l^{\alpha}}{h_{ref}} . \tag{4.31}$$

The hardening of its opposite slip direction becomes :

$$\theta^{-\alpha} = \theta_{ref} \frac{|\pi^{\alpha}|}{|\dot{\gamma}^{\alpha}|} \frac{h''^{-\alpha}}{h''_{ref}} - b_2 \frac{l^{\alpha}}{h_{ref}} . \tag{4.32}$$

For other slip systems the hardening is described by :

$$\theta^{\beta} = \theta_{ref} \frac{h''^{\beta}}{h''_{ref}} - b_2 \frac{l^{\beta}}{h_{ref}} \tag{4.33}$$

In these equations again a somewhat altered formulation of the anisotropic hardening ratio h''^{α}/h''_{ref} is used. The reason for this is that the hardening contribution of the slip systems δ of which the polarity value is not yet equal to their slip rate, do not harden the other slip systems as much, due to the higher annihilation probability as described above. The hardening contributions of these slip systems, will therefore be scaled with $\left(\left|\pi^{\delta}\right|/\dot{\Gamma}\right)^{n}$ instead of $\left(\left|\dot{\gamma}^{\delta}\right|/\dot{\Gamma}\right)^{n}$, which results in

$$h''^{\alpha}=\sum_{\beta\neq\delta}\frac{\tau^{\beta}}{\tau^{\alpha}}H^{\alpha\beta}\left(\frac{\left|\dot{\gamma}^{\beta}\right|}{\dot{\Gamma}}\right)^{n}+\sum_{\delta}\frac{\tau^{\delta}}{\tau^{\alpha}}H^{\alpha\delta}\left(\frac{\left|\pi^{\delta}\right|}{\dot{\Gamma}}\right)^{n} \tag{4.34}$$

The back stress of a reversed slip system will also increase again, whenever the polarity value of the slip system is of the same sign as the slip rate. The hardening equation in the opposite direction therefore receives an extra softening term which scales with the difference between the slip rate and the polarity value :

$$h''^{-\alpha}=\sum_{\beta\neq\delta}\frac{\tau^{\beta}}{\tau^{-\alpha}}H^{-\alpha\beta}\left(\frac{\left|\dot{\gamma}^{\beta}\right|}{\dot{\Gamma}}\right)^{n}+\sum_{\delta}\frac{\tau^{\delta}}{\tau^{-\alpha}}H^{-\alpha\delta}\left(\frac{\left|\pi^{\delta}\right|}{\dot{\Gamma}}\right)^{n}-\frac{\tau^{\alpha}}{\tau^{-\alpha}}\left(\frac{\left|\dot{\gamma}^{\alpha}-\pi^{\alpha}\right|}{\dot{\Gamma}}\right)^{n} \tag{4.35}$$

It is clear that if all polarity values equal their corresponding slip rates, all equations become equivalent to their counterparts in section 4.3.2.a.

b) Influence of c_1, c_2 and $H_{\leftrightarrow}$

In fig. 4-11 results are shown of the model applied to a single orientation which is subjected to a complete strain path reversal. The slip rates for this example are constant with straining mode and only change in sign at the SPC. They can be found in fig. 4-7. The different curves are obtained with different values of the three most relevant modelling constants for a strain path reversal, being c_1, c_2 and $H_{\leftrightarrow}$. The resulting curves clearly feature the main characteristics of the experimental stress-strain and work hardening curves as described in section 2.3.1.a (cf. fig. 2-13). It should be noted that for all curves the hardening rate becomes 0 at a specific point. It will be explained further on that this is a feature inherent to the model formulation, whenever constant slip rates are applied.

The value of c_1 controls the length of the strain interval of the transient work hardening regime after the SPC (γ_3 in fig. 2-13). It also determines the strain at which the hardening rate increases again after being zero. These two specific points are respectively related to the moment that all polarity values are only negligibly different from their slip rates and the point where the polarity values change sign. This is not surprising since the evolution of the polarity values with strain in the model is solely controlled by the value of c_1 (equation (4.23)).

The initial hardening rate right after the SPC and how it decreases with further strain is largely affected by c_2. This can be most clearly seen in the hardening rate-stress curve. The hardening rates decrease (almost) linearly starting at 32.0 MPa for the curves with $H_{\leftrightarrow} = 0.2$ and at 33.5 MPa for $H_{\leftrightarrow} = 0.6$. The slope of the decrease also depends on the value of c_1 which follows from equations (4.27) and (4.28) and is illustrated by the difference between the two median gray curves with $c_2 = 50.0$ and $H_{\leftrightarrow} = 0.2$.

The ratio c_1/c_2 for the same value of $H_{\leftrightarrow}$ determines the stress level of the

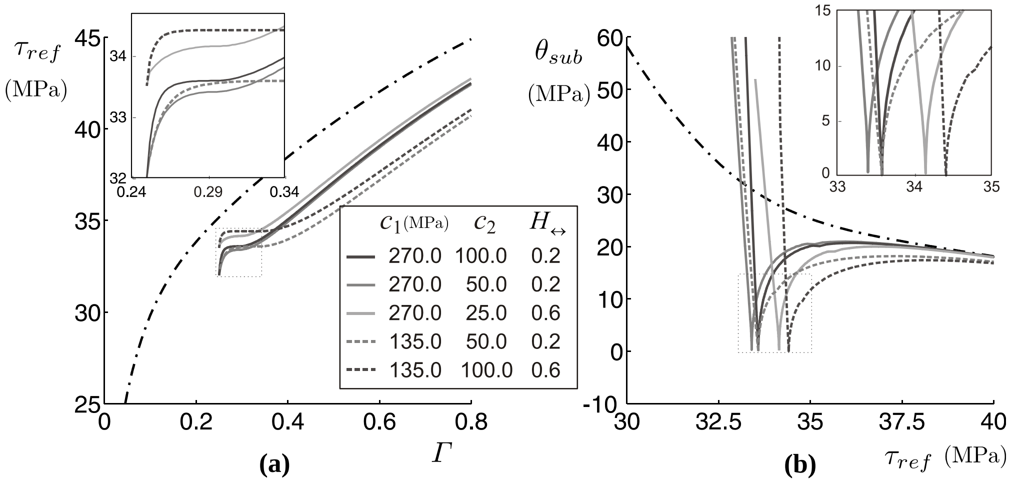

Fig. 4-11 : The evolution of τ_{ref} with Γ (a) and the corresponding work hardening curve θ_{sub} vs. τ_{ref} (b) according to the meso scale model for a single orientation which is subjected to a strain path reversal with the slip rates as shown in fig. 4-7 and anisotropy constants as in fig. 4-4. The different curves have been obtained with different values of the parameters c_1, c_2 and $H_{\leftrightarrow}$ as indicated. The black dash-dotted lines represent the monotonic work hardening behaviour.

plateau-like regime where the hardening rate is zero. Since all π^α values change sign at the same point, due to the constant slip rates, the overal hardening rate should, according to the equations (4.27) and (4.28), be zero for at least a single point in the curve. In some cases the work hardening remains 0 for a longer interval of strain, resulting in a plateau in the stress-strain curve. For these cases (e.g. $c_1 = 270$ MPa, $c_2 = 100.0$ and $H_{\leftrightarrow} = 0.2$) the back stress has become negligibly small after only a small amount of strain, while the polarity values are still of opposite sign to the slip rates. Because of the presence of the back stress in equation (4.27) this results in a hardening rate of (almost) zero for a certain amount of strain. Since equation (4.34) only allows for an increasing hardening rate, it is within the model impossible for a single orientation to soften its value of τ_{ref} during a complete strain path reversal.

Fig. 4-12 shows the stress-strain and the anisotropy ratio-strain curves for all individual slip systems for the example with $c_1 = 135.0$ MPa, $c_2 = 50.0$ and $H_{\leftrightarrow} = 0.2$. This will help to analyse the effects that a strain path reversal has on the individual slip systems and on the overall substructural anisotropy. The slip rates are again the same as shown in fig. 4-7.

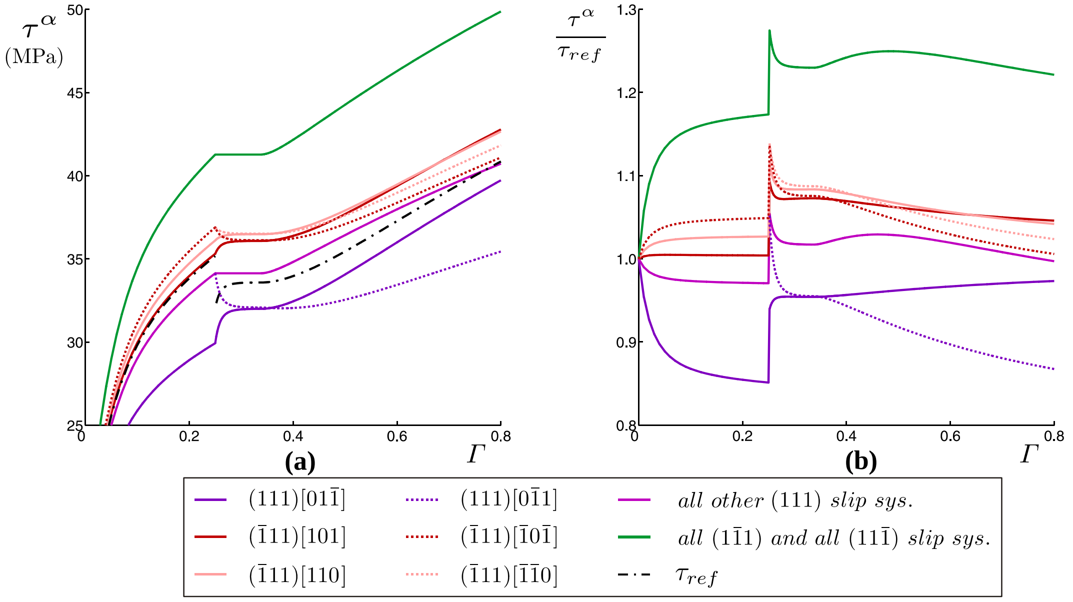

Fig. 4-12 : Stress-strain curves of the individual slip systems and the corresponding anisotropy ratios for the example shown in fig. 4-11 with c_1=135.0 MPa, c_2=50.0 and $H_{\leftrightarrow}$=0.2.

The $(111)\left[0\bar{1}1\right]$ slip system, indicated with a purple dotted line, is the most active slip system during prestraining, so its reverse direction $(111)\left[01\bar{1}\right]$ has the lowest τ^{α} at the SPC. The difference with its $\tau^{-\alpha}$ (which is the τ^{α} of the $(111)\left[0\bar{1}1\right]$ slip system) defines the back stress for the slip system α. This back stress is lowered with ongoing strain by the simultaneous hardening and softening of the forward and the reverse slip direction (equations (4.27) and (4.28)). Because there are no extra softening contributions as all slip systems are fully reversed and obtain the exact opposite slip rate (meaning that all $\lambda^{\alpha} - \left|\dot{\gamma}^{\alpha}\right| = 0$ and so all $l^{\alpha} = 0$), the hardening and softening rate are exactly opposite to each other until the polarity value π^{α} changes sign. From that point on both directions gradually regain their hardening contributions as in a monotonic strain path because of the scaling with the polarity ratio in equations (4.31) and (4.32). The reverse direction has a much lower hardening ratio due to the last term in equation (4.35), resulting in the build-up of the back stress.

The anisotropy ratios of both systems make a jump at the SPC due to the discontinuous value of τ_{ref}. They almost become equal (no back stress) just before the hardening sets in again. With the increase of the back stress the both curves separate increasingly. Even when the polarity variable π^{α} becomes negligibly different from $\dot{\gamma}^{\alpha}$, the anisotropy ratios will evolve further towards the ratios of their counterpart just before the SPC. This is due to the presence of the ratio $\tau^{\beta}/\tau^{\alpha}$ in equation (4.34).

The evolution of the two other active slip systems, which are both on the $(\bar{1}11)$ slip plane, is equivalent to the previous discussed one. The only difference is that their back stresses are considerably smaller due to the large latent hardening contribution of the $(111)\left[0\bar{1}1\right]$ system during prestrain and its opposite direction after the SPC.

The non active slip systems have a constant τ^{α} just after the strain path reversal until the polarity values of the active slip systems change sign. This is due to the exclusion of the reversed slip systems in the calculation of the hardening ratios (equation (4.30)). Whenever the polarity values have the same signs of the current slip rates, the hardening contributions are gradually increased with increasing π^{α} (equation (4.34)). The corresponding anisotropy ratios are lowered during the decrease of the back stresses on the active slip systems because of the increasing value of τ_{ref}. When the latent hardening resumes, the anisotropy ratios initially increase (as a result of $H_X > H_{//}$) but will eventually start to decrease as the difference between the actual average hardening rate θ_{sub} and the monotonic hardening rate θ_{ref} becomes smaller. Also these anisotropy ratios will tend towards the values of the monotonic case.

The influence of the prestrain on the transient regime is illustrated in fig. 4-13. The same set of modelling parameters has been used as for one of the examples in fig. 4-11, but the strain reversal is imposed at different amounts of prestrain. For all prestrains, the hardening rate initially drops to zero, which is not the case in the experimental results, especially at low prestrains. This modelling example however has constant slip rates throughout the applied deformation modes which will only occur in perfectly stable orientations to the specific deformation mode. For most orientations, the slip rates will vary with strain, leading to a somewhat larger strain region in which the polarity values of the individual active slip systems will change their signs. For these cases the hardening rate will become very low, but not completely zero. This low hardening rate however does not depend on the amount of prestrain. The model will therefore most likely not perform very well at low prestrains, where no plateau in the stress-strain curve is observed. On the other hand, strain softening during complete strain reversal is impossible within the model, which corresponds to what has been observed experimentally (cf. fig. 3-15).

The transient regimes for the different prestrains are very similar. The length of the plateau of constant stress however increases with increasing prestrain. This can be attributed to including τ_{ref} in the evolution equation of π^{α} (equation (4.23)). The higher τ_{ref}, the more strain it takes to reduce π^{α} to zero, resulting in a longer stress plateau. It will also take more strain to build up the polarity of the newly formed substructure. This can most clearly be seen in the shapes of the hardening rate-strain curves (cf. fig. 4-13 (c)), where the cases of higher prestrain after zero hardening show a larger amount of strain in order to become parallel to the monotonic hardening curve.

Qualitatively, the curves of fig. 4-13 show the same tendencies as the experimental curves of fig. 3-15 which are discussed in section 3.3.5, apart from the zero work hardening rate at low prestrain.

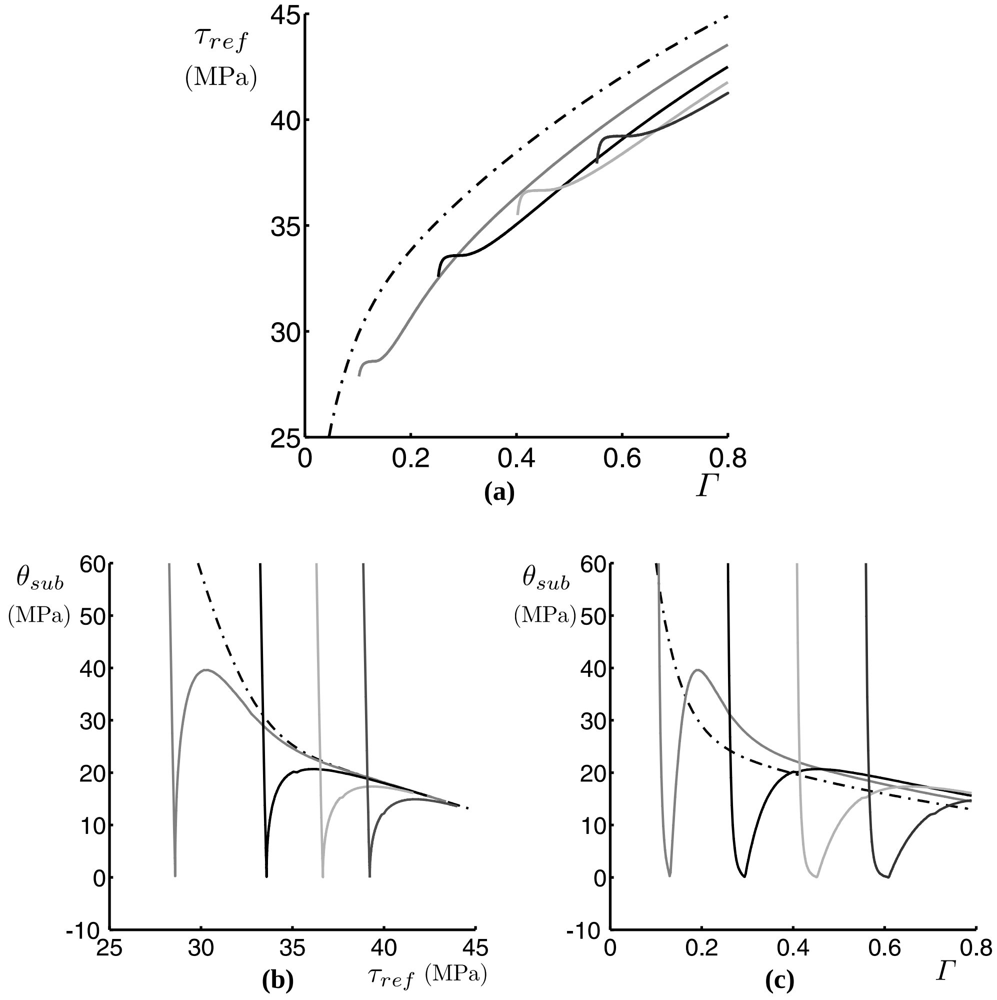

Fig. 4-13 : Work hardening according to the meso scale model for a single orientation which is subjected to a strain path reversal with slip rates as shown in fig. 4-7 but with the SPC occurring at different amounts of prestrain. The modelling constants are $c_1 = 270.0$ MPa, $c_2 = 100.0$ **and** $H_{\leftrightarrow} = 0.2$ **with the anisotropy constants as in fig. 4-4. (a) Stress vs. strain, (b) hardening rate vs. stress, (c) hardening rate vs. strain.**

c) Relation to experimental observations

In the discussion of the work hardening curves as predicted by the model for a single orientation subjected to strain reversal, the implications of the modelling assumptions on the mechanical behaviour have been pointed out. In this section, the meaning of these assumptions regarding the physics of the strain reversal process as well as the nature of the fitting constants will be commented.

One of the most important aspects during strain reversal is the polarity of the substructure which is related to the dominant sign of the stored dislocations in front of substructural obstacles. The governing model equations are completely different whether the overall polarity is of opposite sign or of like sign as the dislocations activated by the reverse straining mode.

Initially when the pre-existing substructure is still the dominant structure that will interact with dislocations that are mobilised by the deformation, the hardening rate is according to the model predominantly controlled by the back stress. In equation (4.27) the hardening rate θ_{ref} at a similar strength during monotonic deformation is absent. The value of θ_{ref} would according to the classical work hardening models be the outcome of the dislocation storage versus annihilation contributions to the overall dislocation density. Because the overall polarity of the existing substructural elements is opposite, the two most likely microstructural mechanisms to accommodate the imposed strain are on the one hand the remobilisation and shrinking of pre-existing dislocation loops of opposite sign and on the other hand the annihilation of dislocations with like sign to the current slip rate by interaction with the dislocations stored during prestraining. Because of completely different annihilation possibilities, the comparison with hardening behaviour at the same level of stress during monotonic deformation becomes pointless.

The remobilisation of pre-existing dislocation has been put forward due to the observed untangling of cell walls (cf. fig. 2-19 (c)). It is, however, not clear how much strain can be accommodated by this process. If it would be relatively easy for these dislocations to retrace their steps to the original sources, it probably would happen already during unloading where only a small anelastic effect is observed (cf. fig. 2-15). These dislocations seem to be mostly constrained in their current positions. They are however perfect annihilation partners for newly generated dislocation of the opposite sign (which are maybe even coming from the same original sources activated in the reverse direction).

The back stress which is according to the ideas of the percolation model highest in between the local obstacles at which the dislocation of the prestrain are contained, helps the motions of dislocation with the like sign of the slip rate. If these dislocations are however not immediately annihilated and would form an opposing substructure on top of the pre-existing one, the back stress would be lowered by a stress shielding process. This would as well result in a decrease of the flow stress in the opposite slip direction. This is a hypothesis which results in an opposite hardening and softening rate for the active and previously active slip direction as formulated in equations (4.27) and (4.28).

Since annihilation is a thermally activated process, this hypothesis can also explain why the amount of strain until the end of the stress plateau (which is the point where according to this model the polarity of the overall substructure changes sign) becomes smaller with increasing deformation temperature as indicated by the results of Hasegawa and co-workers [1975]. This implies a temperature dependence of c_1.

Because the reduction of the back stress is supposedly related to dislocation storage creating a counteracting stress field, the hardening of the slip system is linked to the portion of the overall hardening which the slip system would contribute to itself, hence the inclusion of the self hardening coefficients in equation (4.30). The current degree of polarity scales the reduction rate of the back stress (equations (4.27) and (4.28)) because the higher the polarity still remains, the easier mobile dislocations which contribute to the reduction of the back stress can be mobilised and stored.

The reduction of the back stress will end when the storage rate of dislocations with like sign of the slip rate equals the annihilation rate of these dislocations with dislocations of the pre-existing structure, resulting in a plateau like regime in the stress-strain curve. This can only last until the dislocations of opposite sign to the slip rate are the majority (opposite sign of polarity value and slip rate). If not the rate of this extra annihilation will gradually slow down and the work hardening will return to the monotonic behaviour. In this process π^α plays a similar role as λ^α in case of a drop in the slip rate, namely the damping of the transition towards the new substructure in case of a strain reversal. This can be very clearly seen in equation (4.34) where the values of π^α have taken the place of $\dot{\gamma}^\alpha$ for all slip systems that are reversed. The slow return of the back stress as visible in fig. 4-12, can explain why the Bauschinger effect gradually disappears during large strain cyclic testing.

It should be stressed that all above mentioned hypotheses stem from theoretical considerations and are only included to make the particular form of the evolution equations plausible. They do not alter the premise that the work hardening model at this scale is purely phenomenological or that these explanations would be valid if the model would describe the true material behaviour well.

As in the case of the slip systems that become much less active, the value of c_1 relates to the *sustainability* of the substructural polarity under strain reversal. c_2 can quantify the *sustainability* of the back stress under strain reversal.

4.4 Summary

A new multiscale model for anisotropic work hardening behaviour of aluminium alloys, including transient work hardening effects after strain path changes is presented in this chapter. It is formulated within a general multiscale framework that enables to treat the different aspects of plastic deformation of polycrystals at the appropriate length scales.

For the macro to meso scale transition, well established deformation texture models are used like FC Taylor and A-Lamel. The isotropic component of the substructural hardening is modelled by a phenomenological equation at the micro scale. It is selected in order to accurately capture the average microstructural hardening behaviour during a monotonic strain path for the studied aluminium alloy of chapter 3.

To model the substructural contribution to the anisotropy, the hardening of the individual slip systems within a grain are evolving differently with increasing strain. The hardening of a particular slip system is made dependent on the way the total amount of slip is distributed on the active slip systems of the grain by using an adapted latent hardening model. In order to capture the Bauschinger effect, the hardening of slip directions opposite to active slip systems is also evolving differently compared to the active forward directions. It is however ensured within the model that the average hardening rate during monotonic straining equals the hardening rate obtained from the microstructural model. This is an essential aspect of the model, since it guarantees that the work hardening behaviour returns to the monotonic case after an SPC when the transient hardening mechanisms have lost their importance.

The transient hardening behaviour after changes of the strain path is modelled by the gradual reduction of previous hardening contributions accommodated by the slip activity on a different set of active slip systems. Two internal variables are introduced for each physical slip system to establish a memory effect of the slip rates prior to the strain path change. The hardening evolutions of the individual slip systems are made dependent on the type of SPC by comparing the current slip rates with the values of the internal variables. A different type of transient behaviour is imposed depending on whether slip systems have become inactive at the SPC or active in the opposite direction.

The followed approach is supported by theoretical considerations regarding the possible micro scale mechanisms active during strain path changes and the observations made in the experimental work of chapter 3. It is demonstrated with model calculations on an individual grain deforming with constant slip rates that the characteristics of the macroscopic hardening behaviour during the transient after an SPC can be reproduced on the meso scale for an individual grain.

5

Assessment of the model

As already mentioned in chapter 1, multiscale models can be excellent tools to get a better understanding of how different mechanisms on their specific length scales cooperate to establish the overall material response. So far, two important causes of anisotropy, namely texture and substructural work hardening, have been treated separately. It is however clear that both effects take place simultaneously. Therefore, their joint contribution to the overall anisotropy as well as their mutual influence within the presented model will be discussed in this chapter.

The multiscale model for work hardening anisotropy presented in the previous chapter will be thoroughly evaluated in order to determine its successes and shortcomings. In the first section, the work hardening predictions of the different versions of the model will be compared to the experimental results discussed in chapter 3. Predictions for different prestrains and different strain path combinations will be discussed with respect to the current understanding of the physical mechanisms responsible for the distinct work hardening behaviour after strain path changes.

Secondly the overall achievements of the model will be summarised and compared to some of the other models presented in chapter 2 that incorporate work hardening effects during strain path changes. Some possible lines of thought to improve the current model as well as the overall insight in the physical processes governing substructural hardening and its anisotropy will conclude this chapter.

5.1 Work hardening predictions for different strain paths

In this section it will be examined how succesfull the model can predict the experimental work hardening curves reported in chapter 3. As will be shown in the first section, the texture evolution is unfortunately not accurately predicted. In order to assess the performance of the model in capturing the work hardening stemming from the substructure, the textural contribution to the overall work hardening will be substracted. This is achieved by using the microscopic stress-strain and hardening curves to compare the experimental results with the model predictions.

First certain aspects regarding the separation of the textural and substructural contribution to the overall work hardening will be discussed. In the first two sections the influence of the substructural anisotropy within the individual orientations on the calculation of the experimental microscopic stress-strain curves will be discussed. In the third section the effect of hardening differences between the individual orientations will be analysed.

In the fourth and the fifth section, the results of the FC Taylor version of the model will be compared to the experimentally observed work hardening behaviour for different types of strain path changes. The implementation into the A-Lamel model will be discussed after that.

The last section will give a summary of the achievements and shortcomings of the model in predicting work hardening behaviour for SPC tests.

5.1.1 Considerations regarding texture and the presence of second phase dispersoids

As explained in section 3.3.1, the average Taylor factor $\overline{M}$ incorporates the influence of the texture on the overall work hardening. Within the model framework it is assured that the work hardening contribution of the substructure for all individual orientations during monotonic strain paths only depends on the used micro scale model. This means that the value of τ_{ref} for each orientation is only a function of the total amount of slip Γ that it has received. Each orientation obeys the same functional dependence $\tau_{ref} = f\left(\Gamma\right)$ during monotonic strain paths. Γ can however differ for every orientation. Its value depends through equation (A.9) on the evolution of the Taylor factor M of the individual orientation. A sufficiently accurate prediction of at least the evolution of the average Taylor factor is therefore necessary to obtain meaningful macroscopic work hardening predictions using multiscale models that separate the influence of texture and substructure on two different scales as e.g. the model presented in this work.

If the evolution of $\overline{M}$ is not well predicted, it might still be possible to obtain a close fit to experimental curves on the macro scale, because the discrepancy in the textural contribution could be compensated by an opposite discrepancy in the substructural contribution. This however makes the use of a multiscale model that incorporates texture evolution rather pointless, since it would be computationally less costly, if the texture prediction would be left out of the model (like e.g. in the Teodosiu-Hu model (cf. section 2.4.1)).

In appendix A it is argued that the current Taylor factor M of an individual grain *throughout a monotonic deformation* only depends on its current orientation and the imposed straining mode. The possible anisotropy of the critical resolved shear stresses τ^{α} of the different slip systems does not affect the *current value of M*. The change of the orientation of the crystal lattice with further straining and consequently the evolution of M does however depend on the particular combination of slip rates which is selected to accommodate the deformation. This selection is dependent of the current substructural anisotropy.

Consequently, it is possible to calculate the current value of $\overline{M}$ of a deformed sample from an experimentally obtained texture by using the FC Taylor model with equal τ^{α} for a single increment. This disregards the substructural anisotropy that is present in the individual grains of the sample, but that is not a problem as explained in appendix A. Anyhow, it is presently not possible to quantify this anisotropy experimentally, because it would require measuring the individual τ^{α} of all slip systems for all the orientations in a sample.

The values of $\overline{M}$ as calculated from the experimental textures shown in figs. 3-10 and 3-12 are therefore indisputable within the modelling assumptions regarding strain compatibility and stress equilibrium which are used to calculate them (hence the difference between the FC Taylor and A-Lamel values).

Fig. 5-1 recapitulates the evolution of $\overline{M}$ obtained with FC Taylor from experimental textures by applying a single strain increment for both simple shear and cold rolling (diamond markers, cf. figs. 3-10 and 3-12). Since FC Taylor predicts the texture evolution with ongoing strain starting from a measured texture and since for each strain increment the value of $\overline{M}$ can be easily obtained from

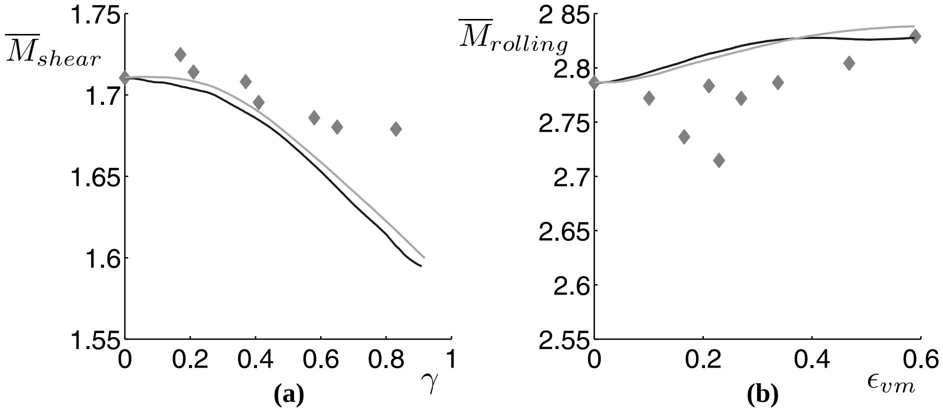

(a) **(b)**

Fig. 5-1 : Comparison between the average Taylor factor $\overline{M}$, calculated with the FC Taylor model from experimental textures (diamonds), with the evolution of $\overline{M}$ based on the texture evolution as predicted by the FC Taylor model (black line) and the FC Taylor model with anisotropic slip system hardening implemented (grey line) for (a) simple shear and (b) cold rolling.

the model calculations, it is possible to plot the evolution of $\overline{M}$ with strain, based solely on the starting texture. The values of $\overline{M}$ in these curves (solid lines in fig. 5-1) correspond to the texture evolution as predicted by the model. Both the texture evolutions are included in fig. 5-1 that are predicted by either the FC Taylor model without (black line) or with (grey line) the substructural work hardening equations of chapter 4 activated. The calculations are performed on a set of 2000 orientations which are distributed according to the ODF of the starting material (cf. fig. 3-3).

For both monotonic simple shear and cold rolling somewhat different values of $\overline{M}$ are predicted by the models compared to the experimentally obtained data. The inclusion of the anisotropic hardening equations does hardly influence the predictions of the average Taylor factor (as also observed by Peeters [2002]). For simple shear the predictions are in reasonable agreement up to a shear strain of $\gamma = 0.5$ but after that the models predict a persistent decrease of the average Taylor factor while the experimental results show a more stable value after a slight decline. For cold rolling the predicted values are higher than the experimental values.

The existing discrepancies between the $\overline{M}$-values obtained from the experimental textures and the ones predicted by FC Taylor models show that the textural contribution to the overall anisotropy due to the changing $\overline{M}$-factor is not completely captured. The most likely reason for this different texture evolution is the influence that the hard α–$Al_{12}(Fe,Mn)Si_3$ dispersoids (cf. section 3.1.1) have on the distribution of the plastic strain throughout the material. Due to the presence of incoherent particles, the local deformation field around the undeformable particles deviates from the macroscopically imposed one [Van Houtte; 1995b], which can result in considerable crystal lattice rotations [Humphreys; 1979]. The FC Taylor model (as well as all other current statistical deformation texture models) is not suited to capture that effect. As a result the predicted texture will deviate from the experimental textures.

The possible influence of the particles on the substructural contribution to the hardening behaviour is accounted for in the model. The initial strengthening is negligibly small due to the small volume fraction of the second phase[29]. Any additional contribution to the overall isotropic hardening is taken into account by the used work hardening equation on the micro scale (equation (4.10)), while a possible contribution to the substructural anisotropy is captured by equation (4.19). These equations are however of phenomenological nature and do not separate between substructural contributions stemming from the zones affected by the particles and the rest of the material. They model the average behaviour.

The differences between modelled and experimental Taylor factors will evidently have an influence on the macroscopic work hardening curves that would be obtained by the model. In order to have a more direct assessment of the substructural contributions to the work hardening anisotropy, the model will be fitted and validated to the microscopic work hardening curves $\tilde{\tau}_{ref} = f\left(\overline{\Gamma}\right)$ instead of the usual macroscopic ones $\overline{\sigma_{eq}} = f\left(\varepsilon_{eq}\right)$. In this way the discrepancies due to differences in texture are cancelled out, if it is assumed that the influence of the difference in the texture evolution (predicted by the model compared to the experimentally observed one) on the development of the overall anisotropy due to the substructure can be neglected.

---

[29] The additional strength due to the presence of undeformable spherical particles via the mechanism of the formation of Orowan loops can be calculated as $\Delta\tau = Gb/\left(L-2r\right)$ where $L = r\sqrt{\pi/f}$ is the average interparticle spacing, r is the average radius of the particles and f the volume fraction of the second phase [Verlinden et al.; 2007]. Using G = 26 GPa, b = 0.286 nm, r = 1.7 µm and f = 0.03, this results in $\Delta\tau$ = 0.53 MPa.

5.1.2 Consideration regarding hardening differences between slip systems of individual orientations

The transformation of experimentally obtained macroscopic stress-strain curves to their microscopic counterparts using the evolution $\overline{M}$ calculated from experimental textures is in principle only possible for *monotonic strain paths*. If abrupt strain path changes occur, the value of $\overline{M}$ *cannot be correctly calculated from experimental textures*.

Applying the FC Taylor model for a single increment using equal τ^{α} will give the lower limit of $\overline{M}$, since the values of M for the individual orientations obtained by assuming equal τ^{α} are lower or equal to the ones which would be obtained if the true substructural anisotropy would be known (cf. Appendix A). The microscopic curves obtained from experimental data will consequently have somewhat too high values for the stress and hardening rate and somewhat too low values for the total slip. Because it is experimentally observed that the substructural morphology after the transient regime becomes similar again to that obtained after monotonic straining (cf. section 2.3.2) and that the microscopic hardening rate-stress curves (derived as explained in this section) after SPC eventually return to the monotonic ones (cf. section 3.3), it can be concluded that after the transient regime, the $\overline{M}$-factors calculated from experimental textures using equal τ^{α} reflect the correct textural contribution to the work hardening.

Since the texture evolution is not correctly predicted by the model, it will not be attempted to correct for this discrepancy in the calculation of the experimental microscopic stress-strain curves after strain path changes. Because the model uses phenomenological equations for the transient hardening behaviour with fitting parameters that cannot be directly related to any physical quantity, the main interest lies in whether the model can capture certain experimentally observed trends.

5.1.3 Considerations regarding hardening differences between orientations

Although the influence of the texture on the macroscopic stress-strain evolution $\overline{\sigma_{eq}} = f\left(\varepsilon_{eq}\right)$ can be filtered out by calculating an average microscopic stress-strain curve $\tilde{\tau}_{ref} = f\left(\overline{\Gamma}\right)$, using the evolution of $\overline{M}$ based on experimental textures, there remains one specific problem in order to directly compare the experimental and modelling data.

If the set of parameters that describe the microscopic curve $\tilde{\tau}_{ref} = f\left(\overline{\Gamma}\right)$, which is obtained by fitting to the experimental data (cf. table 4), is used inside the model to prescribe $\tau_{ref} = f\left(\Gamma\right)$ for all the individual orientations, an average microscopic stress-strain curve is obtained by the model that is somewhat different from the prescribed one.

This means that it is not guaranteed that when all individual orientations follow a certain functional dependence $\tau_{ref} = f\left(\Gamma\right)$, this also implies that the average amount of slip $\overline{\Gamma}$ has the average critical resolved shear stress $\tilde{\tau}_{ref}$ as the result of the same functional dependence[30].

Since within the model all orientations based on their Taylor factor receive a different amount of slip, the average critical resolved shear stress over the slip systems τ_{ref} will be somewhat different for each orientation. As explained in appendix A, the deviations from $\overline{\tau}_{ref}$ will induce a difference between the true average substructural hardening contribution $\overline{M^2\, d\tau_{ref} / d\Gamma}$ and the supposed substructural hardening contribution $\left(\overline{M}\right)^2 d\tilde{\tau}_{ref} / d\overline{\Gamma}$ (cf. equation (A.16)). This implies that even if the texture evolution is taken into account ($\overline{M}\left(\varepsilon_{eq}\right)$ for the experimental data and $M\left(\varepsilon_{eq}, g, \dot{\boldsymbol{\varepsilon}}\right)$ for all orientations in the model), there is a somewhat different functional dependence $\tilde{\tau}_{ref} = f'\left(\overline{\Gamma}\right)$, even if all orientations obey the same hardening relation $\tau_{ref} = f\left(\Gamma\right)$.

Since the spreads on τ_{ref} and M cannot be easily measured experimentally, it is only possible to obtain the true substructural hardening contribution $\overline{M^2\, d\tau_{ref} / d\Gamma}$ by inverse modelling (which is bounded by the ability of the model to sufficiently capture the real material behaviour). A macroscopic stress-strain curve does not provide sufficient information for this, even if it can be assumed that the average Taylor factor does not vary much.

---

[30] Jensen's inequality theorem proves that $f\left(\overline{x}\right) \neq \overline{f\left(x\right)}$ for every non-linear function $f\left(x\right)$.

Table 5 : Adapted values of the hardening parameters of the micro scale model in order to fit the microscopic work hardening curves using the extended FC Taylor model.

	τ_0	τ_A	θ_A	τ_B	θ_B
Hardening parameters (MPa)	16.5	29.3	542.0	56.9	54.0

The fitting parameters deduced from the microscopic stress-strain curve obtained from the experimental macroscopic simple shear test, using the experimental $\overline{M}$ -values (as presented in section 3.3.1), can therefore only be used as first approximations of the parameters for the embedded micro scale model that describes $\tau_{ref} = f\left(\Gamma\right)$ for the individual orientations.

Fitting the microscopic stress-strain curve produced by the model to the experimentally obtained curve of fig. 3-11(a) results in a new set of fitting parameters for the phenomenological work hardening model of equation (4.10), which are presented in table 5. The use of these new values enables to make a direct comparison between the modelled and experimental microscopic stress-strain curves $\tilde{\tau}_{ref}$ vs. $\overline{\Gamma}$.

5.1.4 Model predictions of strain path changes at different prestrains

The remaining unknown parameters of the multiscale hardening model H_X , $H_{\leftrightarrow}$, n, b_1, b_2, c_1 and c_2 (equations (4.19, 4.22-4.24 and 4.27)) are simultaneously fitted to the microscopic stress-strain curves of a cross test and a Bauschinger test. This is necessary because the values responsible for the substructural anisotropy H_X, $H_{\leftrightarrow}$ and n will not only influence the reyielding stress after the SPC but also the subsequent hardening transients. The results obtained after such a fitting procedure with an SPC occurring at $\overline{\Gamma}_{pre}$ = 0.5 for both the reversal and the cross test are displayed in fig. 5-2, and the obtained fitting parameters are presented in table 6. The monotonic work hardening curve is included as well for reference.

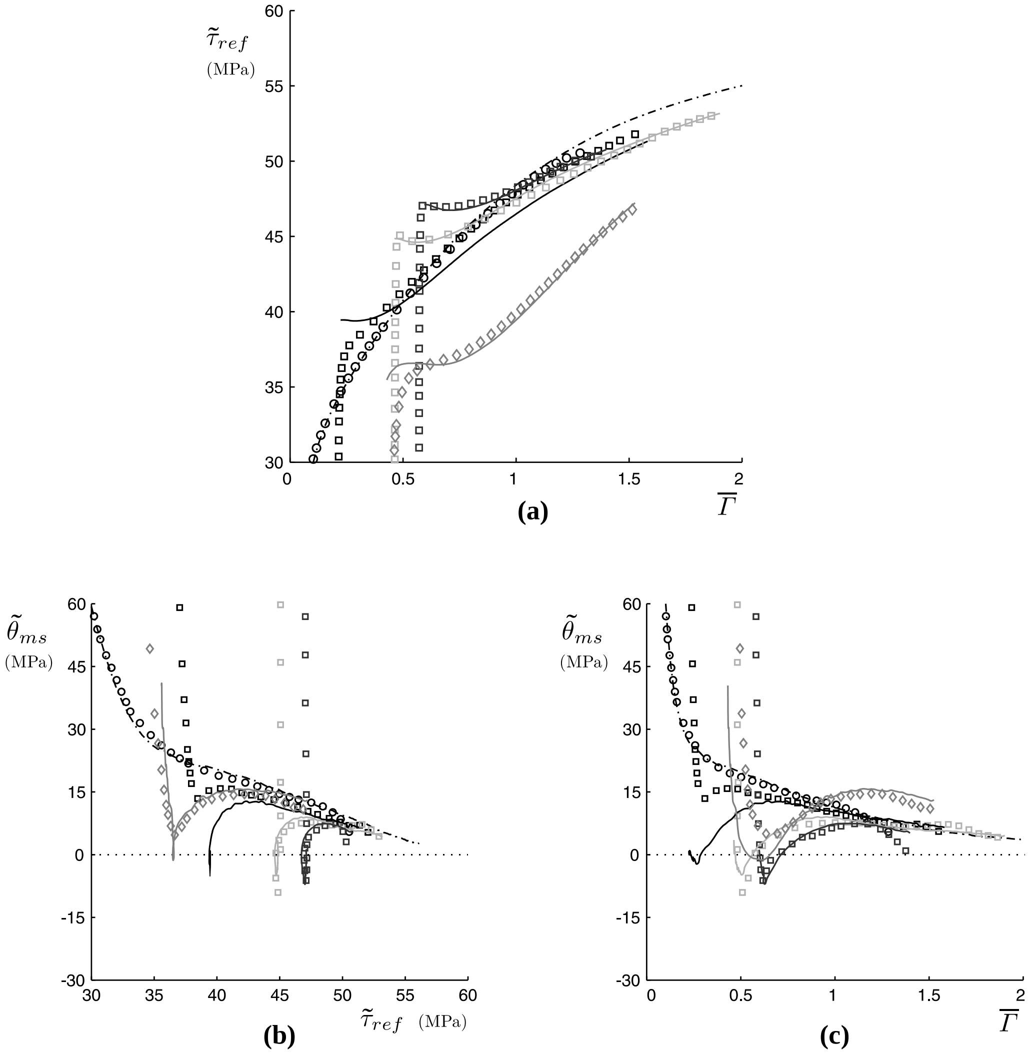

Fig. 5-2 : Model predictions (full lines) and experimental results (symbols) for the work hardening behaviour of cross tests at lower amounts of prestrain ($\overline{\Gamma}_{pre}$ =0.2, 0.5 or 0.6). The model is fitted to the experimental results with $\overline{\Gamma}_{pre}$ =0.5 (cf. table 6). The light grey curves show the cross (squares) and Bauschinger (diamonds) tests which are used to fit the model parameters. The monotonic work hardening curve is indicated in a dash-dotted line (model) and circles (experiment). (a) Microscopic stress-strain curves, (b) and (c) corresponding hardening rate-stress and hardening rate-strain curves.

The experimental counterparts of all displayed modelling curves are shown by chains of open symbols.

The model obtains an excellent fit to the experimental curves of the monotonic deformation and both the cross test and strain reversal tests at $\overline{\Gamma}_{pre} = 0.5$. The fact that the model is not capable of generating a steadily increasing stress-strain curve during strain reversal has already been addressed during the discussion of the modelling equations in section 4.3.3.b. This explains why the initial part of the reversal test does not have a closer fit to the experimental curve.

The values obtained for the anisotropy parameters suggest a high degree of substructural anisotropy. The value of 6.2 for H_X results in a high hardening of the inactive slip systems while $n = 3.4$ very much enhances the relative share of the highest active slip system within the overall hardening contributions. The negative value of -0.6 for $H_{\leftrightarrow}$ combined with the high value of n implies that the opposite direction of the highest active slip system softens with ongoing strain.

The fact that the overall average critical resolved shear stress at strain reversal as predicted by the model ($\tilde{\tau}_{ref} \approx 35\text{ MPa}$) is still more than the double of the initial slip resistance ($\tau_0 = 16.5\text{ MPa}$) indicates that the relative importance of the slip rates dramatically changes due to the lattice rotation in respect to the straining mode. If the relative importance of the slip systems would have been unchanged throughout the prestraining, the value of $\tilde{\tau}_{ref}$ would have become smaller than τ_0, due to the negative value for $H_{\leftrightarrow}$.

The anisotropy within the model, which is incorporated in the differences between the τ^{α} of the individual slip systems, is co-rotational with the crystal lattice frame and will therefore continuously adapt itself to the straining mode that might rotate in a completely different way (or not at all like in case of plain strain compression and rolling to a first approximation).

The values for b_1 and c_1, which influence the length of the transient work hardening regime, are rather low compared to the illustrative values in the examples with constant shear rates in chapter 4. Especially in the case of strain reversal, evolving slip rates can of course increase or shorten this transient as well. A slip system which has an increasing slip rate after the strain reversal will increase the overall length of the transient. If the highest active slip systems however have predominantly decreasing slip rates, the transient will become shorter compared to what the same value of c_1 would produce for an example with constant slip rates. For a certain value of b_1, the length of the transient regime will also shorten compared to the case of constant slip rates, if the slip

Table 6 : Values for the modelling constants of the meso scale model for anisotropic work hardening and transient work hardening after SPC, obtained by fitting to the experimentally obtained stress strain curve of a cross and a Bauschinger test at two levels of prestrain.

Parameters for anisotropy and transient hardening	H_X	$H_{\leftrightarrow}$	n	b_1	b_2 (MPa)	c_1 (MPa)	c_2
Low prestrain : $\overline{\Gamma}_{pre} = 0.5$	6.2	-0.6	3.4	2.5	30.0	80.0	35.0
High prestrain : $\overline{\Gamma}_{pre} = 1.0$	*8.2*	-0.6	*4.8*	2.5	30.0	*120.0*	35.0

systems inactivated at an orthogonal SPC are, after some amount of further strain, reactivated with increasing slip rates.

Apart from the curves to which the model is fitted, two other modelling and experimental results for cross tests are shown in fig. 5-2. For the test with a somewhat higher prestrain of $\overline{\Gamma}_{pre} = 0.6$, excellent agreement is found between model and results. For the lower prestrain however no good correspondence is found between the model and the experimental result. The reyielding stress is overestimated and the subsequent hardening is too low. Only towards the end of the transient regime, a relatively close match between both is achieved, especially for the hardening rate.

Also for prestrains $\overline{\Gamma}_{pre} > 1.0$ no good correspondence is found between the experimental curves and the model predictions for both cross and reversal tests if the fitting parameters for $\overline{\Gamma}_{pre} = 0.5$ are used. It turns out to be impossible to find a combination of fitting parameters that predicts the correct evolution of the anisotropy for a wide range of prestrains.

The modelling results for the multiscale work hardening model fitted to a cross test and a reversal test at a prestrain of $\overline{\Gamma}_{pre} = 1.0$ compared to all available experimental curves are shown in figs. 5-3 and 5-4 for cross tests and reversal tests respectively. As can be seen in table 6, only three fitting parameters need to be adapted for this. The degree of substructural anisotropy has even been further

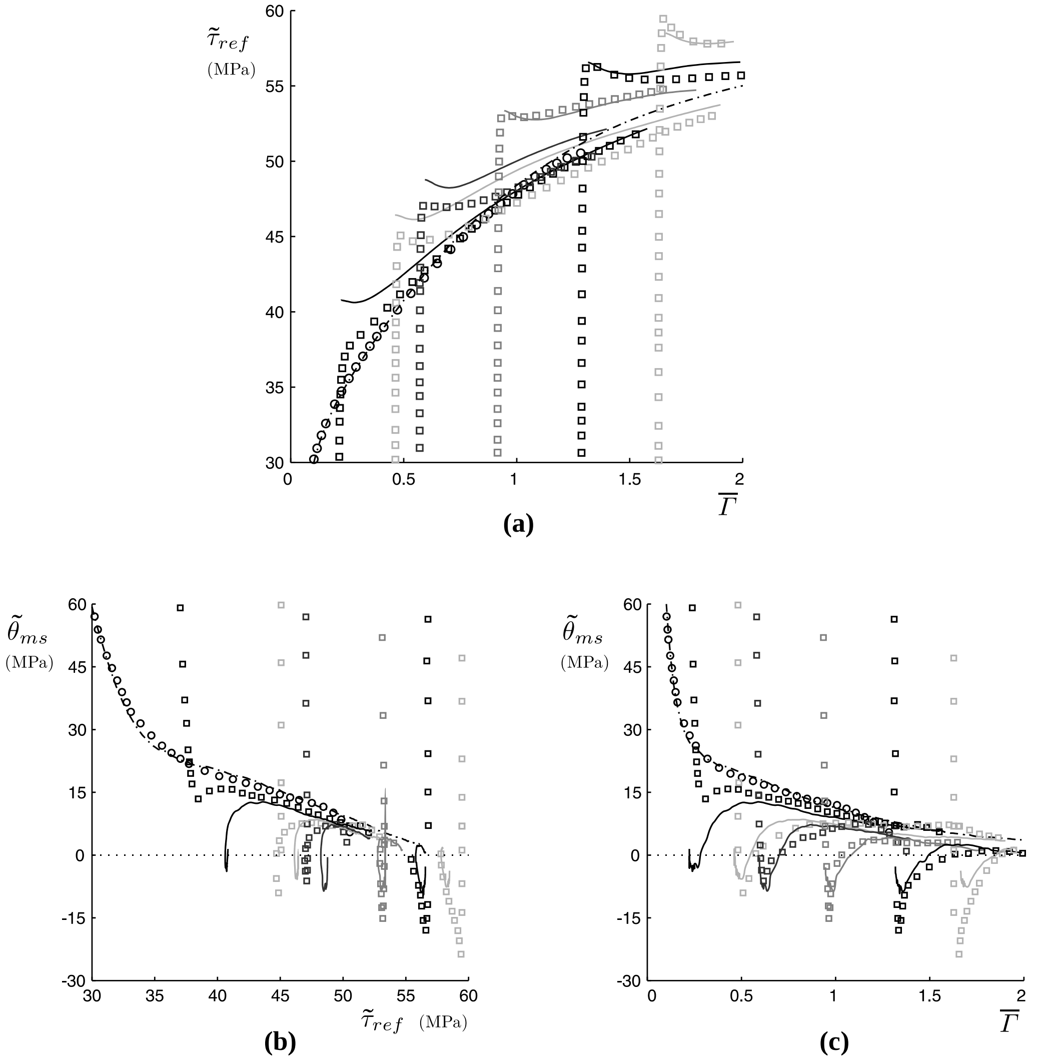

Fig. 5-3 : Model predictions (full lines) and experimental results (symbols) for the work hardening behaviour of cross tests at different amounts of prestrain using the modelling parameters fitted for $\overline{\Gamma}_{pre} = 1.0$ (cf. table 6). The monotonic work hardening curve is indicated in a dash-dotted line (model) and circles (experiment). (a) Microscopic stress-strain curves, (b) and (c) corresponding hardening rate-stress and hardening rate-strain curves.

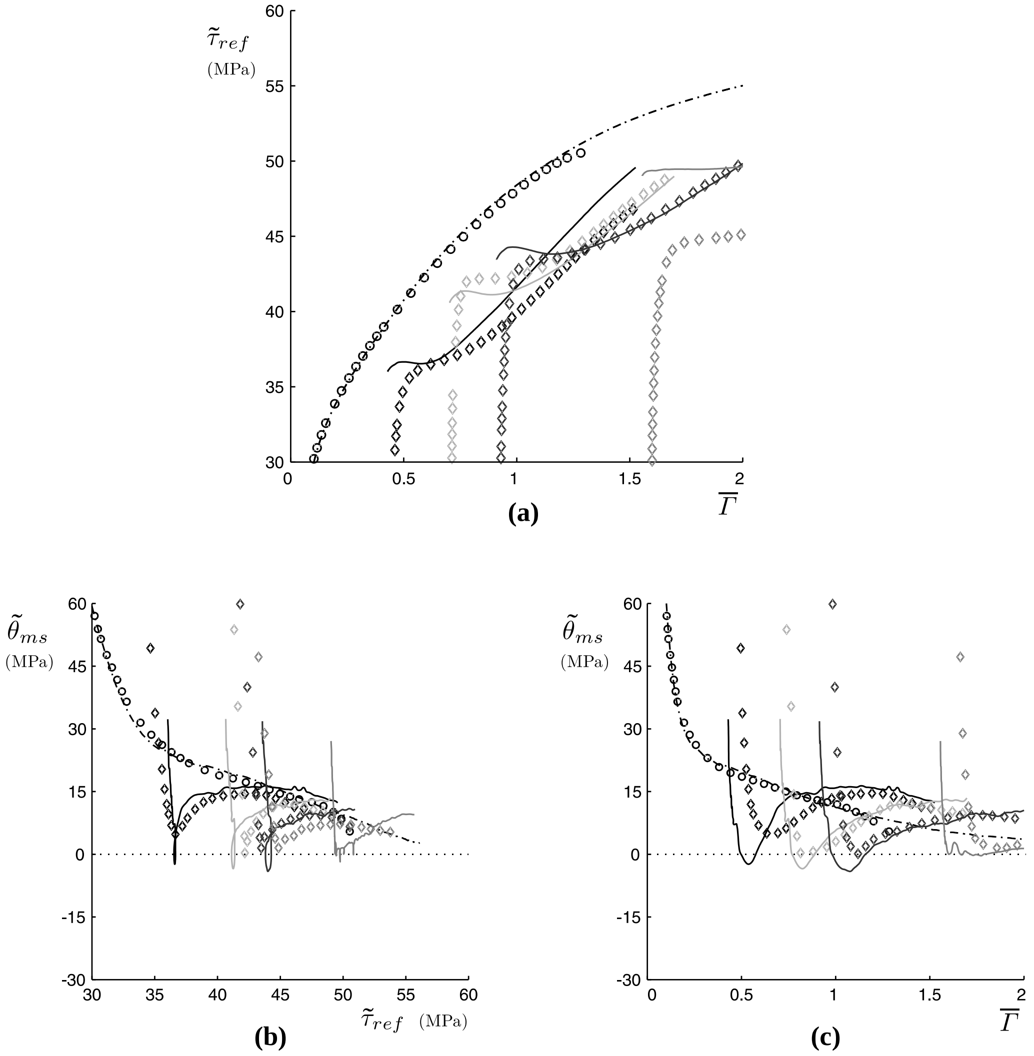

(a)

(b)

(c)

Fig. 5-4 : Model predictions (full lines) and experimental results (symbols) for the work hardening behaviour of Bauschinger tests at different amounts of prestrain using the modelling parameters fitted for $\overline{\Gamma}_{pre}$ = 1.0 (cf. table 6). The monotonic work hardening curve is indicated in a dash-dotted line (model) and circles (experiment). (a) Microscopic stress-strain curves, (b) and (c) corresponding hardening rate-stress and hardening rate-strain curves.

increased by larger values of H_X and n, while the length of the transient regime after strain reversal has been shortened by a larger value of c_1.

Fig. 5-3 shows that with the alternative parameters (cf. second line of table 6), the stress-strain and work hardening curves for the larger prestrains of the cross tests are reasonably well predicted, but that agreement for the lower prestrains is lacking. The shape of the stress-strain curves for the SPC at 0.5 and 0.6 is however rather well approached which can be seen at the corresponding hardening rate-strain curves which are in good agreement with the experimental ones. This is largely due to the fact that the most important parameters controlling the evolution of the hardening rate after a cross SPC, b_1 and b_2, are not changed in the new fitting procedure.

The details of the hardening rate curves for the cross tests are somewhat surprising. First a decrease of the hardening rate occurs before it starts to increase again. This initial decrease is not observed for individual orientations with constant slip rates (cf. fig. 4-8). For the polycrystal simulations it however occurs at all prestrains. The evolution of the hardening rates for the individual orientations would need to be studied in detail to trace back the reason of this phenomenon.

The work hardening behaviour of the reversal tests as depicted in fig. 5-4, shows that the later part of the transient is accurately reproduced by the model for $\overline{\Gamma}_{pre}$=1.0, but that the initial hardening is always followed by some softening before the hardening rate is increased again. This is most likely due to the fact that the effects of increasing and decreasing slip rates become more prominent. The reversal test at a prestrain of $\overline{\Gamma}_{pre}$=0.7 is still reasonably predicted, while the simulation result of the test with prestrain $\overline{\Gamma}_{pre}$=0.5 gives a too short transient regime. The evolution of the average hardening rate $\overline{\theta}_{ms}$ as a function of the average stress $\tilde{\tau}_{ref}$ is captured reasonably well for $\overline{\Gamma}_{pre}$=0.5 (cf. fig. 5-4 (b)). The higher value of c_1 which is used here explains this shorter transient interval. It can be concluded that the proposed governing equation of the polarity variable (equation (4.23)), which determines the length of transient during strain reversal, is too simple to predict this length in the case of polycrystalline materials with changing values for the slip rates. The yield stress as predicted by the model for the strain reversal test at $\overline{\Gamma}_{pre}$=1.6 is much higher than the experimentally observed value. A long strain interval of work hardening stagnation is however predicted by the model. This is most likely due to the high amount of prestrain,

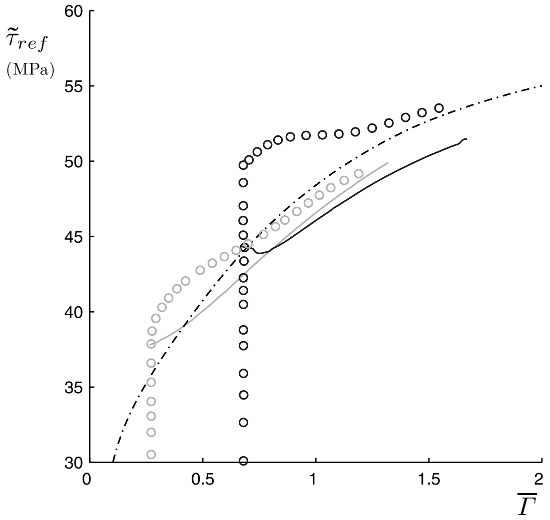

Fig. 5-5 : Microscopic stress-strain curves of model predictions (full lines) and experimental results (open symbols) for the work hardening behaviour of simple shear tests after an SPC with θ = 30° using the model parameters fitted for $\overline{\Gamma}_{pre}$ = 0.5 (cf. table 6). The monotonic curve is indicated in a dash dotted line.

which results in orientations which are much more stable to the deformation mode and therefore slip rates which do not change as fast.

5.1.5 Model predictions for intermediate Schmitt parameters

The results of model simulations of strain path change tests with intermediate Schmitt parameters are shown in figs. 5-5 to 5-7.

For θ=30° (fig. 5-5), neither the substructural anisotropy at the SPC, nor the evolution of the hardening rate during the transient work hardening regime resembles to the experimentally observed trend. The flow stress obtained by the model is close to the value of the monotonic deformation, while a considerably higher value is observed experimentally for both prestrains. This difference indicates that the substructural contribution to the anisotropy is quite pronounced, even for moderate changes of the strain path. Because the anisotropy is correctly predicted in case of a cross test (cf. fig. 5-2), where for most orientations a completely new set of slip systems is activated, this indicates that the model predicts too many slip systems to remain active after the SPC which should have been replaced by a combination of other previously inactive slip systems. It is hard to tell how much the incorrectly predicted texture evolution contributes to

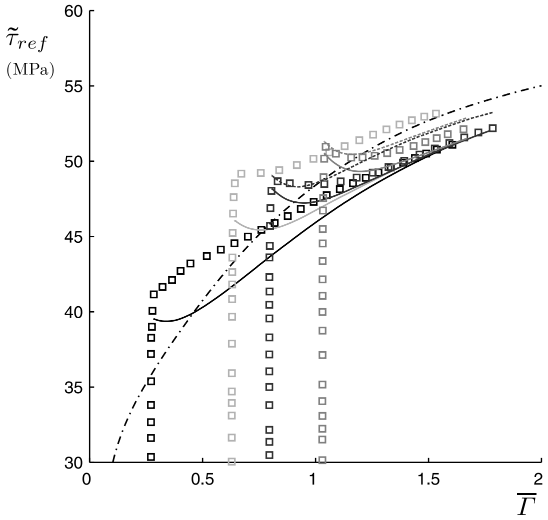

Fig. 5-6 : Microscopic stress-strain curves of model predictions (lines) and experimental results (open symbols) for the work hardening behaviour of simple shear tests after an SPC with θ = 60° using the model parameters fitted for $\overline{\Gamma}_{pre}$ = 0.5 (full lines) and for the higher prestrains also for $\overline{\Gamma}_{pre}$ = 1.0 (dashed lines). The monotonic curve is indicated in a dash dotted line.

this effect. The lower flow stress combined with the occurrence of a transient work hardening regime also makes that the model predicts a positive strain shift γ_0 (cf. section 3.3.5.a), which is not present in the experimental curves.

The transient regime as predicted by the model occurs in a limited strain interval, while this interval is rather wide for the experimental curves. The relatively short intervals obtained by the model are due to fast changing slip rates shortening the transient. For the experimental data a similar length of the transient is observed for SPC tests with θ either 30° or 90° (cf. fig. 3-20). The same value of b_1, which controls the length of the transient, does however result in different predictions of the lengths of these strain intervals by the model for the two different types of SPC.

The model predictions for the SPC with θ=60° are shown in fig. 5-6. For the different amounts of prestrain, the set of model parameters is used which has been fitted to a cross test and a Bauschinger test at $\overline{\Gamma}_{pre}$=0.5 (cf. top row of table 6). To simulate the two SPC tests with a high amount of prestrain, also the model parameters fitted at $\overline{\Gamma}_{pre}$=1.0 (cf. bottom row of table 6) are applied (dashed

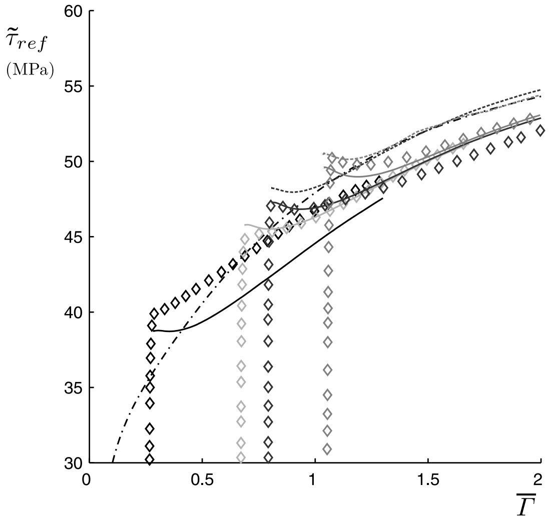

Fig. 5-7 : Microscopic stress-strain curves of model predictions (lines) and experimental results (open symbols) for the work hardening behaviour of simple shear tests after an SPC with θ = 120° using the model parameters fitted for $\overline{\Gamma}_{pre}$ = 0.5 (full lines) and for the higher prestrains also for $\overline{\Gamma}_{pre}$ = 1.0 (dashed lines). The monotonic curve is indicated in a dash dotted line.

lines). The stress strain curves for the SPC test with the lowest prestrain is not well predicted during the work hardening transient, but the subsequent return to the monotonic behaviour is well captured. The curve for the test with $\overline{\Gamma}_{pre}$=0.6 has a too low initial flow stress and remains below the experimental curve with ongoing strain. It should however be noted that the experimental result at this prestrain stands out compared to the other experimental results for this type of SPC, having a high flow stress and a pronounced positive strain shift γ_0. For the two highest amounts of prestrain, the model predictions obtained with the set of fitting parameters obtained for $\overline{\Gamma}_{pre}$=1.0 give the best correspondence to the experiment for the initial part of the transient regime, while the later part is well predicted by the model with the parameters for $\overline{\Gamma}_{pre}$=0.5.

In fig. 5-7 the model predictions are compared to the experimental results for SPC tests with θ=120°. Also in this case the two sets of fitting parameters of table 6 are used to predict the SPC tests with high prestrains. The best correspondence to the experimental curves is generally achieved by the model using the fitting parameters obtained for $\overline{\Gamma}_{pre}$=0.5. Only for the lowest prestrain, there is a considerable difference between the model prediction and the experimental result. For the experimental curve at $\overline{\Gamma}_{pre}$=1.0 the best correspondence to the initial part of the stress strain curve is however obtained by using the model parameters for $\overline{\Gamma}_{pre}$=1.0. The higher value of c_1 in this second set of parameters reduces the length of the transient so that the return to the monotonic behaviour starts too early after the SPC.

From figs. 5-5 to 5-7 it can be concluded that the SPC tests with intermediate values for $\cos\theta$ are reasonably well predicted by the model for strain path changes that have a large change of the straining mode (θ=60° and θ=120°). In these two cases most grains have a number of slip systems that get replaced by others. For the case that the SPC is not that large (θ=30°), the model fails to predict the observed increase in the flow stress and the positive hardening rate just after the SPC that only slowly decreases with further straining. Instead, a too low initial flow stress and a negative hardening rate are obtained by the model. The former seems to indicate that, on average, the new sets of slip systems which are activated in the individual grains after the SPC are too similar to the previously active ones, while the latter points to the opposite conclusion. It appears that the transient work hardening behaviour after an SPC with a low value for θ, is not caused by the same type of mechanism that is active after an SPC with θ=90°. A new set of evolution equations for this type of SPC needs to be developed and incorporated into the model in order to improve the model predictions.

5.1.6 Implementation of substructural anisotropy in the A-Lamel model

It has been attempted to embed the model for substructural anisotropy into the A-Lamel model (cf. section 4.1.2.b). The resulting work hardening curves are however generally not smooth and often contain discontinuities, strain softening during monotonic prestraining and limited anisotropy at SPC. The influence of the model parameters on the anisotropy and the transient behaviour is not as expected.

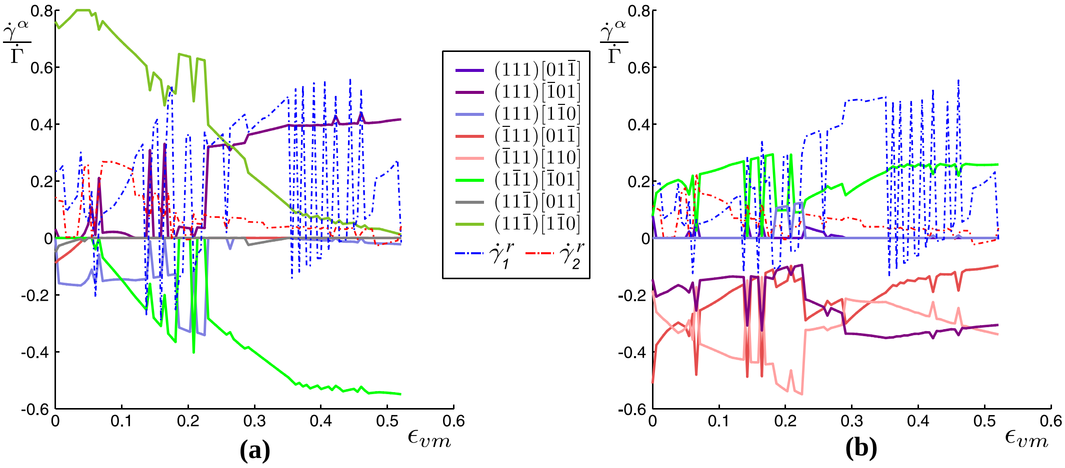

Fig. 5-8 :The evolution of the slip rates with ongoing strain of two orientations as obtained by the A-Lamel model with equal τ^α within each orientation. The imposed deformation is simple shear with the TD as the shear direction and TD-ND as the shear plane. The deformation is relaxed on a common boundary plane between the two orientation with initial boundary plane normal [0.821 -0.018 0.571]. (a) orientation φ_1 = 172.5°, Φ = 47.5°, φ_2 = 52.5° (b) orientation φ_1 = 120.0°, Φ = 42.5°, φ_2 = 85.0°.

The cause of these irregularities has been found to be that a considerable number of grain boundary regions show a substructural work hardening in the individual orientations which is far from the average behaviour, displaying all the artefacts as described above to a much larger extent. The slip rates of these grain boundary regions turn out to be always very unstable during certain strain intervals. At subsequent increments a different set of slip rates is obtained, making the evolution of the slip rates discontinuous, even if there is no abrupt change in the strain path. Very often an oscillating behaviour between 2 or 3 different solutions to the set of equations is observed.

This phenomenon also occurs for these grain boundary regions if no substructural anisotropy is allowed, but only isotropic work hardening is implemented for the two orientations. Fig. 5-8 gives an example of such a grain boundary region. The slip rates of the active slip systems oscillate between two solutions during certain strain intervals. The relaxation shears ($\dot\gamma_1^r$ is the shear component parallel to the resolved shear on the boundary plane as imposed by the external straining mode, while $\dot\gamma_2^r$ is the shear in the direction perpendicular to it) also oscillate corresponding to the slip rates. This indicates that for this combination of orientations and boundary plane, there are several equally valid solutions (cf. Taylor ambiguity problem in FC Taylor) and the model chooses one of these based on small numerical differences. This ambiguity problem does however not disappear if different τ^{α} for the various slip systems are used.

The oscillating slip rates explain why the work hardening behaviour predicted by the substructure model becomes so peculiar. The model regards every switch to an alternative solution as an abrupt change of the strain path, where the transient behaviour has to become active. This results in discontinuous jumps in the flow stress, due to previous latent hardening and subsequent softening, which gets prolonged by the oscillating behaviour of the slip rates.

The model of substructural anisotropy as presented in chapter 4 requires a gradual evolution of the slip rates during monotonic straining, which is unfortunately not guaranteed for all possible boundary regions in the A-Lamel model. It can be expected that other statistical models where there are certain relaxations of the straining mode allowed, will also show a similar behaviour for some of the obtained slip rates, which would as well have an effect on embedded work hardening anisotropy models.

5.1.7 Conclusions

Because the evolution of the texture is not well captured by the model, the work hardening predictions have been compared to microscopic stress-strain data. This data has been obtained from combining directly measured macroscopic stress-strain data with info on the texture evolution measured at intermediate steps.

The likely cause of the discrepancies in the texture evolution predictions compared to the experimental results is the presence of hard intermetallic particles. The comparison of modelling and experimental results based on microscopic stress-strain data is however possible, bearing in mind that here as well differences can arise because of the substructural anisotropy within the individual orientations after an SPC, and the spread on τ_{ref} for the different orientations.

This explains why no perfect return to the monotonic hardening behaviour is observed in the curves of figs. 5-2 to 5-4, although that is ensured for all individual orientations by the model equations. As can be seen for the larger prestrains in fig. 5-3, it is possible for the model to predict negative values of the strain shift γ_0. These two features can be seen as the major achievements of the model, as they are clearly present in the experimental data (cf. section 3.3) but cannot be predicted by any of the other models for SPC as will be discussed in the next section.

With the current model it is only possible to get a good correspondence with the same set of fitting parameters for a limited range of prestrain. The parameters that need to be altered to obtain close fits at other prestrains, are mainly the ones which relate to the evolution of the substructural anisotropy during monotonic straining. The parameters which control the transient regime after an SPC can mostly be left unchanged. This indicates that the evolution of the anisotropy due to changes in the substructure is not well captured by equation (4.19).

For SPC tests with intermediate values of $\cos\theta$, no good predictions are obtained, especially not for SPC combinations that have a high degree of strain path continuation (e.g. θ=30°). The straightforward combination of the transient effects at orthogonal SPC with no transient effects at all for strain path continuation, which is obtained by the model, does not result in the experimentally observed behaviour.

The A-Lamel version of the model is not able to produce the experimentally observed anisotropy and transients, since for certain grain boundary zones, no stable slip rates are obtained.

5.2 Comparison with other SPC models

In this section, the different modelling approaches to capture work hardening anisotropy and transient effects after strain path changes which are presented in section 2.4, will be compared to the multiscale model presented in chapter 4.

5.2.1 Comparison with the model of Teodosiu-Hu

The most apparent difference with the model of Teodosiu and Hu (cf. section 2.4.1) is the length scale at which the substructural contribution to the anisotropy is modelled. The Teodosiu-Hu model is formulated at a single length scale, which corresponds to the macro scale as defined in fig. 4-1. The parameters which describe the state of the substructure ($\mathbf{X}$, $\mathbf{P}$ and $\mathbf{S}$) capture some average influence of the substructure on the overall anisotropy. The model presented in chapter 4 describes the substructure for each grain individually at the mesolevel and the contribution to the overall anisotropy is obtained through the average of the stress states of the individual grains. The fact that Teodosiu and Hu do not account for changes in the anisotropy due to the texture evolution with strain is an important difference with the multiscale model.

In the formulation of both models some similarities can be found in the function which certain variables have in describing the work hardening transients after strain path changes. The role of the $\mathbf{S}$ tensor in the Teodosiu-Hu model is played by the differences in the values of the τ^{α} in the multiscale model. The latent part of $\mathbf{S}$, $\mathbf{S}_L$, controls how the substructure softens if it is subjected to a different straining mode, which is similarly done by the differences between the λ^{α} and $\dot{\gamma}^{\alpha}$. The polarity of the substructure is characterised by either $\mathbf{P}$ or the π^{α} which both have equivalent evolution equations. How the polarity affects the substructural anisotropy is however modelled in a very different way (equations (2.38)-(2.40) for the Teodosiu-Hu model compared to equations (4.27)-(4.35) for the multiscale model). The influence of the back stress $\mathbf{X}$ during strain reversal is accounted for by the differences between τ^{α} and $\tau^{-\alpha}$. The role of $\mathbf{X}$ in the Teodosiu-Hu model during other types of SPC (gradually shifting the center of the flow surface to a position in correspondence with the new straining mode) is performed by the simultaneous evolution of the τ^{α} and the $\tau^{-\alpha}$ of the newly and previously active slip systems.

The two models differ in their capability of predicting certain features of the work hardening behaviour after SPC tests. The flow surface of the material in the model of Teodosiu and Hu is described by (cf. equation (2.31)) :

$$\sigma_{eq} = \sqrt{(\boldsymbol{\sigma}-\mathbf{X}):\mathbf{M}:(\boldsymbol{\sigma}-\mathbf{X})} = \sigma_0 + R + f\,\|\mathbf{S}\| \tag{5.1}$$

Since the anisotropy tensor $\mathbf{M}$ is constant, the shape of the flow surface does not change with strain. As a consequence of this, it is impossible for the model to obtain a negative value for the strain shift γ_0 (cf. fig. 2-14). At the end of the transient work hardening regime, $\mathbf{X}$ and $\mathbf{S}$ will become equal to the corresponding tensors which would be obtained by a monotonic deformation with the same straining mode as after the SPC. This however requires additional strain during the transient as illustrated for $\mathbf{S}$ during a cross type of SPC in fig. 5-9 (a). The value of R is however a function of the accumulated strain (cf. equation (2.32)). The right hand side of equation (5.1) can therefore never obtain a higher value after an SPC than for the monotonic deformation at the same amount of accumulated strain, which is necessary to obtain a negative strain shift.

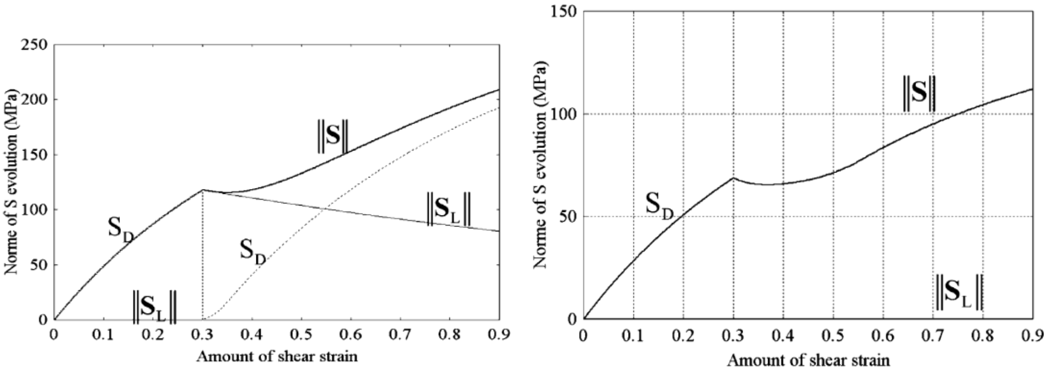

(a) **(b)**

Fig. 5-9 : Evolution of the parameters $\|\mathbf{S}\|$, S_D and $\|\mathbf{S}_L\|$ of the Teodosiu-Hu model during a cross (a) and a Bauschinger (b) type of SPC. From [Bouvier et al.; 2005]

Moreover, the work hardening behaviour after an SPC does not exactly return to the monotonic hardening behaviour as described by the hardening rate vs. stress curve. Due to the fact that R depends on the amount of accumulated strain, it is only possible for the work hardening curve to return after the transient to the monotonic behaviour, if the value for the strain shift γ_0 would be 0. Any other value for γ_0 results in different rates $\dot{R}$ and $\dot{S}_D$ than during monotonic straining at the same stress level and therefore a somewhat different overall hardening rate. In the Teodosiu-Hu model the value of γ_0 is always positive for both cross tests and Bauschinger tests, as can be deduced from the evolution of $\|\mathbf{S}\|$ in fig. 5-9. It should however be mentioned that this return to the work hardening behaviour of the monotonic straining mode is only observed for the microscopic stress-strain curves (cf. section 3.3) and is not necessarily true for macroscopic stress-strain curves, which are obtained by the Teodosiu-Hu model. It is possible that a deformation with an SPC and a monotonic deformation according to the second straining mode would result in textures with the same average Taylor factor, leading to return of the macroscopic work hardening curve to the monotonic curve as well. This behaviour cannot be predicted by the Teodosiu-Hu model.

In the multiscale model presented in chapter 4, it is however imposed that the work hardening curves of the individual grains return to the monotonic behaviour by equation (4.14). As illustrated by fig. 4-10, the model is also capable of obtaining a negative value for γ_0.

The lack of texture prediction in the Teodosiu-Hu model, makes it also impossible to have an interdependent substructure and texture evolution. By using Jaumann rates in the evolution equations of the tensorial parameters, the substructural anisotropy is made corotational with the material in the Teodosiu-Hu model, while in the multiscale model the substructural anisotropy is for the individual grain corotational with the crystal lattice orientation.

5.2.2 Comparison with the models of Peeters and Rauch

A more direct comparison is possible with the model of Peeters since both models are multiscale models based on the FC Taylor texture model where the substructural anisotropy is modelled at the level of the individual slip systems.

The model of Peeters has been developed for IF steel (bcc), while the research presented in this text is dedicated to aluminium alloys (fcc). In this section both approaches will however be compared, disregarding as much as possible the difference of the lattice structure. Moreover, the model of Peeters has also been applied to copper (fcc) by Mahesh et al. [2004].

The differences between the critical resolved shear stresses τ^{α} within a grain are for both models dependent on the distribution of the total slip rate $\dot{\Gamma}$ over the individual slip systems. In the model of Peeters this is accomplished through the combination of slip rates in total slip on {110} glide planes ($\dot{\Gamma}^{P}$) and dislocation fluxes through these planes (Φ_{wp}^{P}, cf. equation (2.50)). In the model of chapter 4, the slip rates lead to differences between τ^{α} through a latent hardening model (equation (4.19)), using coefficients for the hardening matrix $\mathbf{H}$ based on the types of the slip system interactions.

In both models the strain history determines the hardening behaviour during the transient regime after an SPC. It is however differently accounted for by the two models. In the Peeters model the strain history is reflected by the values of the two types of dislocation densities which are connected to the {110} planes, while in the present model the strain history is contained within the values of τ^{α}, λ^{α} and π^{α} for each individual slip system. The decision to activate the mechanism that reverses the polarity of the substructure if the straining mode is partially reversed (cf. equation (2.55) and section 4.3.3) depends on the change of the direction of the flux Φ_{wp}^{P} for the Peeters model, compared to the change of the slip direction of an individual slip system for the present model. Since Φ_{wp}^{P} can obtain also an opposite direction after an SPC by the activation of a completely different set of slip systems, the softening mechanism ascribed to the polarity of the substructure will be activated in more strain path change cases in the Peeters model. This means that especially for strain path changes where there is a partial reversal of the straining mode ($\cos\theta < 0$), a different transient behaviour will be obtained by the two models.

Another difference between the models is how slip activity on a certain slip system leads to the latent hardening of other slip systems. In the model of Peeters the latent hardening contribution is a function of the angle between the Burgers vector of the latent slip system and the normal to the glide plane of the active slip system (through equations (2.43) and (2.48)), while in the current model the latent contribution depends on whether the glide planes of the slip systems are intersecting or not, thus on the angle between the two glide plane normals ($H_X > H_{//}$ for the values of the hardening matrix $\mathbf{H}$ in equation (4.19)). This makes the hardening anisotropy during prestraining evolve differently between the two models.

In the model of Peeters, the critical resolved shear stress of a slip system is given by (cf. equation 2.45) :

$$\tau^{\alpha} = \tau_0 + (1 - f)\tau_I + f\sum_P \left(\tau_{wd}^{P,\alpha} + \tau_{wp}^{P,\alpha}\right). \tag{5.2}$$

Since all hardening contributions from not currently being building-up DDWs will gradually disappear during the transient work hardening regime (ρ_{wd}^P and ρ_{wp}^P decreasing to 0, cf. equations (2.51) and (2.54)), it is also not possible to obtain a negative strain shift γ_0 with the Peeters model for cross tests. As discussed in section 3.3.5.b a remaining part of the substructural anisotropy of the prestrain is necessary to obtain negative value for γ_0.

An exact return to the monotonic hardening behaviour after the work hardening transient can also not be predicted by the Peeters model. If there is no partial reversal of the strain path, the evolution of τ_I in equation (5.2) continues with further accumulated strain, while the evolution of the $\tau_{wd}^{P,\alpha}$ and $\tau_{wp}^{P,\alpha}$ are influenced by the SPC. When a partial reversal of the strain path occurs, the evolution of τ_I is not a function of only the accumulated strain anymore (cf. equation (2.46)), but a return to the monotonic work hardening behaviour is not guaranteed by the model equations.

The part of the model described in section 4.3.3, that is of importance to model a complete reversal of the strain path can also be compared to the model of Rauch (cf. section 2.4.2.b). The evolution of the back stress just after the strain reversal is in both models employed to obtain a quickly decaying hardening rate towards stagnation. The build-up of the dislocation density ρ_f associated with forward straining, starting from a low value $\rho_{f,0}$ at the SPC, with the simultaneous decrease of ρ_r (associated to straining before SPC) towards 0, ensures that the work hardening behaviour returns to the microscopic hardening rate – stress curve after the transient. A low value of $\rho_{f,0}$, implies that a positive strain shift γ_0 will be predicted which is somewhat smaller than the prestrain. It has been argued in section 2.4.2.b that the polarity of the substructure evolves differently in the model of Rauch as in the model of Peeters (1 step exponential decay compared to a 2 step exponential decay). In the model presented in chapter 4, the polarity of the substructure evolves according to a single step exponential decay function and is therefore more similar to the model of Rauch than to the model of Peeters in predicting strain reversal tests.

5.2.3 Comparison with the model of Holmedal

The critical resolved shear stress of a slip system in the model of Holmedal (cf. section 2.4.3) is the sum of four contributions (cf. equation (2.58)):

$$\tau^{\alpha} = \tau_I + \tau_L^{\alpha} + \tau_R^{\alpha} + \tau_P^{\alpha} . \tag{5.3}$$

The three slip system specific contributions gradually evolve to saturation values which are dependent on whether the slip system is active, the opposite slip direction is active or the slip system is not active at all. The value of τ_L^{α} is similar to the difference between the τ^{α} of an active and a non-active slip system in the model of chapter 4. The value of τ_R^{α} has the same role as the back stress $\tau^{\alpha} - \tau^{-\alpha}$, while no straightforward equivalent can be found for τ_P^{α}. The fact that the evolution of the contributions in equation (5.3) are not related to the slip rates of the different slip systems, but only to whether the slip system is active or not, leads to considerable differences for the substructural anisotropy for individual grains as predicted by the two models.

The obtained transient work hardening behaviour during cross tests is qualitatively very similar, due to the exponentially decaying previous latent hardening contributions in both models. Also the length of the transient for such types of SPC is in both models independent of the prestrain. For the reversal of the strain path, a qualitatively different behaviour will be predicted by the two models. In the model of Holmedal also the length of the transient for strain reveral is independent of the prestrain, while this is not the case for the model and the experimental results presented in this text.

Since τ_I is a function of the accumulated total slip Γ and the values of τ_P^α will, after sufficient straining, become a fixed fraction of τ_I, the microscopic work hardening curve returns to the monotonic case after an SPC if the τ_L^α and τ_R^α become negligible. Due to the functional dependence of τ_I on Γ, it is however impossible for the model of Holmedal to predict a strain shift γ_0.

5.3 Discussion

The comparison between the experimental data and the model simulations results in a number of interesting observations. The high degree of anisotropy needed in the model and the discrepancies between model predictions and experimental results for intermediate SPC tests will be discussed in more detail.

The degree of substructural anisotropy which has to be introduced into the model (through the values of H_X, $H_\leftrightarrow$ and n) in order to obtain the experimentally observed anisotropy is surprisingly large. To fit the model to the experimental data of the larger prestrains, the anisotropy values have to increase even more. In the analysis of the experimental data for cross tests, a 15% higher flow stress compared to the monotonic value at the same amount of accumulated strain has been observed (cf. fig. 3-13 (a)). Large changes of the relative importance of the slip systems during prestraining, which has been discussed in section 5.1.4, can partially explain the need for these high values. If several different slip systems subsequently become the highest active one, the induced anisotropy will be more equally spread out over the available slip planes, resulting in a more isotropic distribution of the τ^α compared to the situation where one slip system consistently remains the highest active one during prestraining. To obtain a reasonable agreement with experimental values for a whole range of SPC angles for low carbon steels, Raphanel et al. [1986] needed to increase the τ^α of the non-active slip systems during prestraining with only 10%. Since in their approach this is only done at the moment of the SPC, only the predicted slip activity at the end of the prestraining is taken into account, whereas in the model of chapter 4 the whole prestraining history determines the substructural anisotropy at the moment of the SPC.

A too rapidly evolving texture, which is commonly observed in FC Taylor model predictions, most likely enhances changes in the relative importance of the slip systems. Within the model, this leads to an influence of the texture evolution on the substructural hardening which cannot be substracted by the calculation of the $\overline{M}$-factor. It remains unanswered whether a more accurate texture prediction would also result in an improved simulation of the substructural anisotropy. As discussed in section 2.2.1.b, it has been suggested that different parts of an individual grain deform by the activation of different and fewer slip systems in order to avoid energetically costly dislocation cutting processes. This leads to the subdivision of grains into cell blocks which all deform somewhat differently but as a whole manage to comply with the imposed deformation. In the present model the slip system activity is however homogenised over the whole volume of the grain, leading to mutual hardening contributions which might not take place in the real material. A model that could account for grain subdivision by obtaining a more realistic distribution of slip throughout the grain, might quite naturaly lead to a more accurate prediction of the substructural anisotropy. Such a model is however currently unavailable. The model of Sedláček et al. [2001] might turn out to be a first step towards such an advanced microstructural model.

The discrepancies between modelling predictions and experimental observations for intermediate types of SPC, reveal that the true material behaviour in these cases is more complex than what is obtained by mixing the dominant mechanisms of the extreme SPC cases (θ=0°, θ=90° and θ=180°) as is done by the present model. The fact that the predicted reyielding stress for SPC with θ=60° and especially θ=30° are too low, indicates that the existing substructure contributes to an increased flow stress even if the the imposed strain path change has a rather low value of θ. The fact that the model predicts activity on certain slip systems homogenised over the whole volume of the grain, which most likely differs from the true local distribution of slip activity on the slip systems in cell blocks, might also be a possible explanation for this observation. The cooperation of the individual cell blocks having locally fewer slip systems active and therefore deforming according to somewhat different local deformation modes, yet as an ensemble still complying with the imposed deformation, remains most likely only stable for small changes of the strain path. If the strain path is changed to a sufficient extent, most of the grains might need to subdivide themself into cell blocks with a different orientation of their morphology, which would result localy in the activation of different slip systems as before the SPC and therefore a higher yield stress, whereas the present model for these grains would find a solution with a rather similar set of slip systems to be active.

Another important aspect of the model is that the substructural anisotropy is corotational with the crystal lattice. Although this might be true for specific orientations [Hansen and Huang; 1998, Liu et al.; 1998], it has been reported [Bay et al.; 1992, Christoffersen and Leffers; 1998] that DDW structures in general keep their directionality constant relative to the macroscopic reference system (in which for the mentioned reports also the imposed deformation gradient is kept constant) and therefore do not follow either the orientation change expected from the imposed geometrical shape change, nor the reorientation of the crystallographic lattice. This might therefore also apply to the substructural contribution to the anisotropy for materials which form these types of intragranular substructures. One possible explanation is that the dislocation substructure during deformation continuously renews itself (analogous to what has been recently observed for dislocation cell structures [Jakobsen et al.; 2006]) or that the DDW structures rotate in an opposite sense to the geometrically imposed rotation [Christoffersen and Leffers; 1998]. For this latter mechanism a model has been proposed by Pantleon and Hansen [1998]. In order to improve the current predictions, it could be tried out to extend the present model with a similar mechanism to take this effect into account.

Because of the fact that the intermediate types of SPC cannot be obtained by a straightforward interpolation of the extreme cases as applied in the present model, it could be very informative if more experimental and modelling studies would be focussed on these types of SPC tests.

6

Conclusions

In this work a number of steps are taken to get a better understanding of the development of substructural anisotropy during cold deformation of aluminium.

From a broad literature survey emerges that many aspects of the formation of the substructure remain unclear and that the anisotropy stemming from substructural elements is difficult to assess. The mechanical behaviour after abrupt strain path changes (SPC) most clearly reveals the effects of this substructural anisotropy. Apart from the initial flow resistance also the subsequent transient regime in the evolution of the work hardening rate is related to the not yet fully understood mechanisms that cause the anisotropy of the substructure.

In order to perform mechanical tests on the lab scale involving abrupt changes of strain path, an apparatus has been designed and built to load specimens in simple shear. Simple shear tests in combination with conventional cold rolling tests have enabled to perform a wide range of strain path change combinations.

The work hardening during monotonic deformation and after abrupt strain path changes has been evaluated and analysed in detail in order to find sensible assumptions to base a work hardening model on which can predict flow stress anisotropy and work hardening transients.

A multiscale work hardening model has been formulated, incorporating existing models for isotropic work hardening at the micro scale and crystal plasticity models at the transition from the macro to the meso scale, to account for texture evolution. At the meso scale new evolution equations have been formulated, evoking the substructural anisotropy and the hardening transients after SPC.

Finally the model has been evaluated to the available mechanical test results and compared to similar models for anisotropic work hardening behaviour.

Because tests in simple shear provide the advantage of having a homogeneous, constant and stable (no necking) deformation mode, it turns out to be the ideal tool for SPC tests. The work hardening behaviour can be monitored up to high amounts of strain and all possible directions of in plane shear can be examined. The most difficult aspect of simple shear testing is to monitor the ongoing strain. In this work a strain mapping system has been successfully applied for that purpose. For SPC angles in between 60° and 120° prestraining has been performed by cold rolling, which can be performed homogeneously as well.

In the data analysis, the obtained macroscopic stress strain curves have been complemented with texture data in order to derive the micro scale hardening law and to obtain work hardening curves without anisotropy contributions stemming from texture changes. From the resulting microscopic hardening curves for SPC tests following aspects have been highlighted in the work:

- the exact return after an SPC to the monotonic hardening behaviour as a function of stress. The transient work hardening mechanisms are therefore, similar to monotonic work hardening, controlled by stress.
- an increasing length with increasing prestrain of the strain interval of the transient for strain reversal tests. This has been connected to the increasing degree of polarisation of the substructure.
- the absence of a systematic trend in the evolution of this strain interval with prestrain for all other SPC combinations, which is most likely related to the nature of the mechanism on the micro scale that carries out the transition of the pre-existing substructure to a substructure corresponding to the new straining mode.
- the constant drop in hardening rate for cross type of SPC. It has been suggested that this might be due to the continuation of the annihilation mechanisms of the prestrain combined with a different mechanism of dislocation storage.
- an increasing amount of deficient strain with prestrain for cross type SPC and extra strain for reversal tests to obtain the same work hardening behaviour as in a monotonic test. This has been attributed to the remaining influence of the anisotropy of the prestrain substructure during cross tests and the transformation to a similar substructure of opposite polarisation for strain reversal tests.

The substructural anisotropy at the meso scale of the work hardening model has been implemented by assigning different critical resolved shear stresses for the different slip systems of the individual orientations.

To obtain a description of the current anisotropy of the flow stress, an adapted version of the latent hardening model of Kocks et al. [1991] has been employed which allows for a higher degree of anisotropy due to the substructural elements.

Within the model a notion of memory of previous slip activity has been introduced for each slip system by introducing two internal variables λ and π which correspond respectively to the slip rate in order to maintain the current hardening contributions and the polarity state of the slip system.

When a slip system becomes less or inactive, its previous hardening contributions to itself and other slip systems are softened during a transient regime described by a gradual adaptation of the λ value to the new slip rate. When a slip system gets reversed, a fast reduction of the back stress is followed by a gradual increase of the hardening from 0 towards the monotonic behaviour during the restoring of the polarity in the opposite slip direction.

The model captures the transient work hardening behaviour after an abrupt change of the straining mode, except for test combinations in between strain continuation and cross type SPC. The retaking of slip activity seems to delay the softening contributions by inactive systems.

The model for substructural anisotropy can unfortunately not accurately predict the evolution of the flow stress in different directions with increasing prestrain. The model can however be fitted to a certain amount of prestrain, resulting in reasonable predictions of the flow stress.

Cross type of SPC are generally very well described by the model, while the initial hardening behaviour after the SPC of strain reversal tests is not captured. SPC tests intermediate to these both types are not convincingly predicted, while SPC tests with a large amount of strain continuation are far from the experimentally observed behaviour.

The discrepancies between experimental results and model simulations indicate that understanding the local distribution of slip system activity might be an important factor in advancing the microstructural modelling. It has been discussed that the intermediate types of strain path changes do not show an intermediate behaviour in between the extreme SPC cases as predicted by the model.

From the whole analysis follows that a better texture prediction is indispensible to model the overall work hardening of the used aluminium alloy (AA3103).

For further research in the subject of this work, a couple of possible directions can be proposed.

From the experimental side, there is a need for a further complementation of the existing data for SPC which can be found in the current literature. A wide range of SPC combinations and materials has not been characterised yet. Also for those materials and SPC that have been reported, a more detailed analysis of the transient regime after the SPC using e.g. the methodology applied in this work would contribute to the understanding of substructural hardening and anisotropy. Only for strain reversals a more or less clear image is available, while for orthogonal and intermediate strain path changes a systematic analysis for almost all materials is still lacking.

From the modelling side, further efforts could be directed to separating the textural and substructural contributions in model predictions, in order to find out how both evolutions are mutually influenced. For a material that has already a reasonable texture prediction using a certain texture model, it can be tested wether imcorporating substructural hardening either improves or deteriorates the texture predictions.

Grain Interaction models could be applied to reduce the spread on the average critical resolved shear stresses between the orientations, but these models need to have stable solutions for the slip rates. It should be further analysed what causes this instability in e.g. the A-Lamel model.

On the physical level, a proper modelling of active slip systems in different cell blocks of the grains, resulting also in a prediction of the misorientation distribution, might lead to a more straightforward incorporation of substructural work hardening. For this the causes of such a division, should be better understood. The works of Hähner and Zaiser [1999], Sedláček [2001] and Pantleon [2004] could give some inspiration for the possible grounds of this phenomenon. It however would be a very ambitious objective to formulate such a model.

References

Aernoudt, E., Gil Sevillano, J. and Van Houtte, P. (1987) *Structural background of yield and flow.* In: Proceedings of the 8th Risø International Symposium on Metallurgy and Materials Science: Constitutive relations and their physical basis, Ed: Andersen, S.I., Bilde-Sørensen, J.B., Hansen, N., Leffers, T., Lilholt, H., Pedersen, O.B. and Ralph, B., Risø National Laboratory, Roskilde, Denmark, 1-38.

Aernoudt, E., Van Houtte, P. and Leffers, T. (1993) *Deformation and textures of metals at large strain*. In: Materials Science and Technology, Vol. 6 Plastic deformation, Ed: Cahn, R.W., Haasen, P. and Kramer E.J., Wiley-VCH, Weinheim, 89-136.

An, Y.G. (2001) *Effect of strain path changes on strain hardening of 6082 aluminium alloy*. Mater. Sci. Tech. **17**, 249-257.

Anselmino, E., Miroux, A., van der Zwaag, S., Seward, G.G.E., Seaton, N.C.A. and Prior, D.J. (2004) *In-situ observation of recrystallisation in AA3103 using FEG-SEM and EBSD.* Proc. 9th International Conference on Aluminium Alloys, Brisbane, Australia, Materials Forum **28**, 811-817.

Argon, A.S. and Haasen, P. (1993) *A new mechanism of work hardening in the late stages of large strain plastic flow in FCC and diamond cubic crystals.* Acta Metall. **41**, 3289-3306.

Argon, A.S. (2002) *Patterning in crystal plasticity of FCC metals.* Scripta Mater. **47**, 683-687.

Arminjon, M. and Bacroix, B. (1991) *On plastic potentials for anisotropic metals and their derivation from the texture function.* Acta Mech. **88**, 219-243.

Asaro, R.J. (1983) *Micromechanics of crystals and polycrystals*. Adv. Appl. Mech. **23**, 1-115.

Asaro, R.J. and Needleman, A. (1985) *Texture development and strain hardening in rate dependent polycrystals*. Acta Metall. **33**, 923-953.

Asaro, R.J. and Lubarda, V.A. (2006) *Mechanics of solids and materials.* Cambridge University Press, New York, ISBN 2-521-85979-4.

Banabic, D., Bunge, H.-J., Pöhlandt, K. and Tekkaya, A.E. (2000) *Formability of metallic materials.* Springer-Verlag, Berlin, ISBN 3-540-67906-5.

Barlat, F., Ferreira Duarte, J.M., Grácio, J.J., Lopes, A.B. and Rauch, E.F. (2003) *Plastic flow for non-monotonic loading conditions of an aluminum alloy sheet sample*. Int. J. Plasticity **19**, 1215-1244.

Basinski, Z.S. and Jackson, P.J. (1965a) *The effect of extraneous deformation on strain hardening in Cu single crystals*. Appl. Phys. Lett. **6**, 148-150.

Basinski, Z.S. and Jackson, P.J. (1965b) *The instability of the work hardened state. I. Slip in extraneously deformed crystals*. Phys. Status Solidi **9**, 805-823.

Basinski, Z.S. and Jackson, P.J. (1965c) *The instability of the work hardened state. II. Slip in alien dislocation distributions*. Phys. Status Solidi **10**, 45-56.

Bassani, J.L. (1991) *Hardening of FCC crystals undergoing multiple slip.* In: proc. ICOTOM 9, Ed. Bunge, H.J. (Textures and Microstructures **14-18**), 1097-1102.

Bate, P.S., Roberts, W.T. and Wilson, D.V. (1982) *The plastic anisotropy of two-phase aluminium alloys – II anisotropic behaviour in load-reversal tests*. Acta Metall. **30**, 725-737.

Bate, P.S. and Wilson, D.V. (1986) *Analysis of the Bauschinger effect*. Acta Metall. **34**, 1097-1105.

Bay, B., Hansen, N. and Kuhlmann-Wilsdorf, D. (1989) *Deformation structures in lightly rolled pure aluminium.* Mater. Sci. Eng. A **113**, 358-397.

Bay. B., Hansen, N., Hughes, D.A. and Kuhlmann-Wilsdorf, D. (1992) *Evolution of FCC deformation structures in polyslip.* Acta Metall. Mater. **40**, 205-219.

Benzerga, A.A., Bréchet, Y., Needleman, A. and Van der Giessen, E. (2004) *Incorporating three-dimensional mechanisms into two-dimensional dislocation dynamics.* Modelling Simul. Mater. Sci. Eng. **12**, 159-196.

Beyerlein, I.J. and Tomé, C.N. (2007) *Modeling transients in the mechanical response of copper due to strain path changes*. Int. J. Plasticity **23**, 640-664.

Bourelier, F. and Le Héricy, J. (1963) *Ecrouissage, Restauration, Récristallisation.* Presses Univ. De France, Paris, 33.

Bouvier, S. and Haddadi, H. (2001) *Modelling the behaviour of a bake-hardening steel using a dislocation structure based model*. In: Proc. of the 4th International ESAFORM Conference on Material Forming, Ed.: Habraken, A.M., University of Liège, Liège, Belgium, 429-432.

Bouvier, S., Alves, J.L., Oliveira, M.C. and Menezes, L.F. (2005) *Modelling of anisotropic work-hardening behaviour of metallic materials subjected to strain –path changes*. Comp. Mater. Sci. **32**, 301-315.

Bunge, H.J. (1982) *Texture analysis in materials science*. Cuvillier Verlag, Göttingen, ISBN 3-928815-81-4.

Chaboche, J.L. (1986) *Time independent constitutive theories for cyclic plasticity*. Int. J. Plasticity **2**, 149-188.

Charpentier, P.L. and Piehler, H.R. (1984) *Yielding anisotropy from the Bauschinger effect and crystallographic texture in drawn HSLA steel sheet*. Metall. Trans. A **15**, 1699-1710.

Choi, Y., Han, C.S., Lee, J.K. and Wagoner, R.H. (2006) *Modeling multi-axial deformation of planar anisotropic elasto-plastic materials, part I: Theory*. Int. J. Plasticity **22**, 1745-1764.

Christodoulou, N., Woo, O.T. and MacEwen, S.R. (1986) *Effect of stress reversals on the work hardening behaviour of polycrystalline copper*. Acta Metall. **34**, 1553-1562.

Christoffersen, H. and Leffers, T. (1998) *The orientation of dislocation walls in rolled copper relative to the sample coordinate system*. Acta Mater. **46**, 4093-4102.

Chun, B.K., Jinn, J.T. and Lee, J.K. (2002a) *Modeling the Bauschinger effect for sheet metals, part I: theory*. Int. J. Plasticity **18**, 571-595.

Chun, B.K., Jinn, J.T. and Lee, J.K. (2002b) *Modeling the Bauschinger effect for sheet metals, part II: applications*. Int. J. Plasticity **18**, 597-616.

Daaland, O. and Nes, E. (1996) *Recrystalliszation texture development in commercial Al-Mn-Mg alloys*. Acta Mater. **44**, 1413-1435.

Daaland, O., Auran, L. and Furu, T. (2003) *Extrudable and drawable, high corrosion resistant aluminium alloy*. European Patent EP20000907618.

Delannay, L, Mishin, O.V., Juul Jensen, D. and Van Houtte, P. (2001) *Quantitative analysis of grain subdivision in cold rolled aluminium.* Acta Mater. **49**, 2441-2451.

Delannay, L (2001) *Observation and modelling of grain interactions and grain subdivision in rolled cubic polycrystals.* PhD. Thesis, Departement MTM, KULeuven

Delannay, L., Jacques, P.J. and Kalidindi, S.R. (2006) *Finite element modeling of crystal plasticity with grains shaped as truncated octahedrons.* Int. J. Plasticity **22**, 1879-1898.

Dirras, G.F. (1997) *Cyclic shear tests on aluminium 3004 and 5182 alloys: macroscopic behaviour and substructural development*. Mater. Sci. Eng. A **234-236**, 966-969.

Dirras, G.F., Duval, J.L. and Swiatnicki, W. (1999) *Macroscopic behaviour versus dislocation substructures development under cyclic shear tests on the aluminium-3004 alloy*. Mater. Sci. Eng. A **263**, 85-95.

Duggan, B.J. and Lee, C.S. (1996) *The development of the deformed state in cold rolling*. In: Proceedings of the 11th International Conference on textures of materials (ICOTOM 11) in Xian, China, Ed: Liang, Z., Zuo, L. and Chu, Y., International Academic Publishers, Beijing, ISBN 7-80003-376-7/TG.26, 225-235.

Engler, O., Crumbach, M. and Li, S. (2005) *Alloy-dependent rolling texture simulation of aluminium alloys with a grain-interaction model.* Acta Mater. **53**, 2241-2257.

Estrin, Y. and Mecking, H. (1984) *A unified phenomenological description of work hardening and creep based on one-parameter models.* Acta Metall. **32**, 57-70.

Estrin, Y., Tóth, L.S., Molinari A. and Bréchet, Y. (1998) *A dislocation-based model for all hardening stages in large strain deformation.* Acta Mater. **46**, 5509-5522.

Estrin, Y., Tóth, L.S., Brechet, Y. and Kim, H.S. (2006) *Modelling of the evolution of dislocation cell misorientation under severe plastic deformation.* In: Proc. Nanomaterials by Severe Plastic Deformation, ed. ??? (Mater. Sci. Forum **503-504**), 675-680.

Eyckens, P., He, S., Van Bael, A., Van Houtte, P. and Deflou, J. (2007a) *Forming limit predictions for the serrated strain paths in single point incremental sheet forming.* In: Proc. Numiform '07, Materials processing and design: modeling simulation and applications, Ed.: César de Sá, J.M.A. and Santos, A.D., American institute of physics, New York, United States, 141-146.

Eyckens, P., He, S., Van Bael, A., Duflou, J. and Van Houtte, P. (2007b) *Finite element based formability predictions of sheets subjected to the incremental forming process.* In: ComPlas 2007: Proc. of the Ninth International Conference on Computational Plasticity, Ed.: Oñate, E., Owen, D.R.J., CIMNE, Barcelona, Spain, 529–532.

Feaugas, X. (1999) *On the origin of the tensile flow stress in the stainless steel AISI 316L at 300 K: back stress and effective stress*. Acta Mater. **47**, 3617-3632.

Feaugas, X. and Haddou, H. (2007) *Effects of grain size on dislocation organiszation and internal stresses developed under tensile loading in FCC metals.* Philos. Mag. **87**, 989-1018.

Feltner, C.E. and Laird, C. (1967a) *Cyclic stress-strain response of FCC metals and alloys-I phenomenological experiments.* Acta Metall. **15**, 1621-1632.

Feltner, C.E. and Laird, C. (1967b) *Cyclic stress-strain response of FCC metals and alloys-II dislocation structures and mechanisms.* Acta Metall. **15**, 1633-1653.

Flores, P. (2006) *Development of experimental equipment and identification procedures for sheet metal constitutive laws*. Ph.D. thesis, département ArGEnCo, ULg, Liège.

Flores, P., Rondia, E. and Habraken, A.M. (2005) *Development of an experimental equipment for the identification of constitutive laws*. International Journal of Forming Processes, 117–137.

Franciosi, P., Berveiller, M. and Zaoui, A. (1979) *Latent hardening in FCC crystals.* In: Proceedings of the 5th international conference on strength of metals and alloys (ICSMA), Aachen, Ed: Haasen, P., Gerold, V. and Kostorz, G., Pergamon press, Oxford, 23-28.

Franciosi, P. and Zaoui, A. (1982) *Multislip in FCC crystals, a theoretical approach compard with experimental data.* Acta Metall. **30**, 1627-1637.

Franciosi, P. (1985) *The concepts of latent hardening and strain hardening in metallic single crystals.* Acta Metall. **33**, 1601-1612.

Gaspérini, M., Pinna, C. and Swiatnicki, W. (1996) *Microstructure evolution and strain localization during schear deformation of an aluminium alloy*. Acta Mater. **44**, 4195-4208.

Gaspérini, M., Dirras, G.F. and Richard, V. (2001) *Microstructural evolution during monotonic and reverse shearing of AA5182 aluminium alloy*. Mater. Sci. Eng. A **319-321**, 457-460.

Gil Sevillano, J., Van Houtte, P. and Aernoudt, E. (1980) *Large strain work hardening and textures.* Prog. Mater. Sci. **25**, 69-412.

Gil Sevillano, J. (1993) *Flow stress and work hardening*. In: Materials Science and Technology, Vol. 6 Plastic deformation ed. Cahn, R.W., Haasen, P. and Kramer E.J., Wiley-VCH, Weinheim, 19-88.

Gloaguen, D. and François, M. (2006) *Prediction of intragranular strains in metallic polycrystals with a two-level homogenisation approach: Influence of dislocation microstructure on the mechanical behaviour*. Phys. Status Solidi A **203**, 1940-1953.

Gómez García, D., Devincre, B. and Kubin, L.P. (2006) *Dislocation patterns and the similitude principle: 2.5D mesoscale simulations.* Phys. Rev. Lett. **96**, 125503,1-4.

G'Sell, C., Boni, S. and Shrivastava, S. (1983) *Application of the plane simple shear test for determination of the plastic behaviour of solid polymers at large strains*. J. Mater. Sci. **18**, 903-918.

Gurtin, M.E. (1981) *An introduction to continuum mechanics,* Academic Press, New York, ISBN 0-12-309750-9.

Haddadi, H., Bouvier, S., Banu, M., Maier, C. and Teodosiu, C. (2006) *Towards an accurate description of the anisotropic behaviour of sheet metals under large plastic deformations: Modelling, numerical analysis and identification*. Int. J. Plasticity **22**, 2226-2271.

Haddag, B., Balan, T. and Abed-Meraim, F. (2007) *Investigation of advanced strain-path dependent material models for sheet metals forming simulations*. Int. J. Plasticity **23**, 951-979.

Hähner, P. and Zaiser, M. (1999) *Dislocation dynamics and work hardening of fractal dislocation cell structures.* Mater. Sci. Eng. A **272**, 443-454.

Hähner, P. (2002) *Statistical mechanics approach to dislocation cell patterning.* Scripta Mater. **47**, 415-421.

Hansen, N. and Huang, X. (1998) *Microstructure and flow stress of polycrystals and single crystals.* Acta Mater. **46**, 1827-1836.

Hansen, N. and Juul Jensen, D. (1999) *Development of microstructure in FCC metals during cold work.* Philos. T. Roy. Soc. A **357**, 1447-1469.

Hansen, N., Huang, X., Pantleon, W. and Winther, G. (2006) *Grain orientation and dislocation patterns.* Philos. Mag. **86**, 3981-3994.

Hasebe, T., Kumai, S. and Imaida, Y. (1999) *Impact compression behavior of FCC metals with pre-torsion strains*. J. Mater. Process. Tech. **85**, 184-187.

Hasebe, T. (2003) *Cross hardening effect of IF steels*. In: Proceedings of the international forum for the properties and application of IF steels, Ed.:

Takechi, H., The Iron and Steel Institute of Japan (ISIJ), Tokyo, Japan, 128-137.

Hasegawa, T. and Yakou, T. (1974) *"Region of constant flow stress" during compression of aluminium polycrystals prestrained by tension*. Scripta Mater. **8**, 951-954.

Hasegawa, T., Yakou, T. and Karashima, S. (1975) *Deformation behaviour and dislocation structures upon stress reversal in polycrystalline aluminium*. Mater. Sci. Eng. **20**, 267-276.

Hasegawa, T. and Yakou, T. (1980) *Effects of stress reversal and thermal recovery on stress vs strain behavior in aluminum*. Scripta Mater. **14**, 1083-1087.

Hasegawa, T., Yakou, T. and Kocks, U.F. (1982) *Length changes and stress effects during recovery of deformed aluminum.* Acta Mater. **30**, 235-243.

Hasegawa, T., Yakou, T. and Kocks, U.F. (1986) *Forward and reverse rearrangements of dislocations in tangled walls*. Mater. Sci. Eng. **81**, 189-199.

Hill, R. (1950) *The mathematical theory of plasticity.* Oxford University Press, London, ISBN 0-19-850367-9.

Hirth, J.P. (1961) *On dislocation interactions in the FCC lattice.* J. Appl. Phys. **32**, 700-706.

Hiwatashi, S., Van Bael, A., Van Houtte, P. and Teodosiu, C. (1997) *Modelling of plastic anisotropy based on texture and dislocation structure*. Comp. Mater. Sci. **9**, 274-284.

Hiwatashi, S., Van Bael, A., Van Houtte, P. and Teodosiu, C. (1998) *Prediction of forming limit strains under strain-path changes: application of an anisotropic model based on texture and dislocation structure*. Int. J. Plasticity **14**, 647-669.

Holmedal, B., Van Houtte, P., An., Y., Pedeseren, K., Furu, T., Court, S., Daniel, D. and Nes, E. (2004) *Strain path changes in Aluminium alloys.* In: proc. VIR[*]Conference 2004, (Aluminium **80**).

Holmedal, B., Van Houtte, P. and An, Y. (2008) *A crystal plasticity model for strain-path changes in metals*. Int. J. Plasticity **24**, 1360-1379.

Holt, D.L. (1970) *Dislocation cell formation in metals.* J. Appl. Phys. **41**, 3197-3201.

Hosford, W.F. and Caddell, R.M. (1983) *Metal forming, mechanics and metallurgy*. Cambridge University Press, Cambridge, ISBN 0521881218.

Hu, H. (1963) in Recovery and recrystallization of metals. ed. Himmel, L., Interscience, New York, 311-362.

Hu, Z., Rauch, E.F. and Teodosiu, C. (1992) *Work-hardening behavior of mild steel under stress reversal at large strains*. Int. J. Plasticity **8**, 839-856.

Hu, Z. (1994) *Work-hardening behavior of mild steel under cyclic deformation at finite strains*. Acta Metall. Mater. **42**, 3481-3491.

Huang, X. and Hansen, N. (2004) *Flow stress and microstructures of fine grained copper.* Mater. Sci. Eng. A **387-389**, 186-190.

Hughes, D.A. (1993) *Microstrucural evolution in a non cell-forming metal: Al-Mg*. Acta Metall. Mater. **41**, 1421-1430.

Hughes, D.A., Liu, Q., Chrzan, D.C. and Hansen, N. (1997) *Scaling of microstructural parameters: misorientations of deformation induced boundaries.* Acta. Mater. **45**, 105-112.

Hughes, D.A. (2001) *Microstructure evolution, slip patterns and flow stress.* Mater. Sci. Eng. A **319-321**, 46-54.

Humphreys, F.J. (1979) *Local Lattice rotations at second phase particles in deformed metals*. Acta Metall. **27**, 1801-1814.

Humphreys, F.J. and Bate, P.S. (2006) *Measuring the alignment of low-angle boundaries formed during deformation.* Acta Mater. **54**, 817-829.

Jackson, P.J. and Basinski, Z.S. (1967) *Latent hardening in copper.* Can. J. Phys. **45**, 707-735.

Jackson, P.J. (1985) *Dislocation modelling of shear in FCC crystals.* Prog. Mater. Sci. **29**, 139-175.

Jakobsen, B., Poulsen, H.F., Lienert, U., Almer, J., Shastri., S.D., Sørensen, H.O., Gundlach, C. and Pantleon, W. (2006) *Formation and subdivision of deformation structures during plastic deformation*. Science **312**, 889-892.

Juul Jensen, D. and Hansen, N. (1990) *Flow stress anisotropy in aluminium*. Acta Metall. Mater. **38**, 1369-1380.

Kalidindi, S.R., Bronkhorst, C.A. and Anand, L. (1992) *Crystallographic texture evolution in bulk deformation processing of FCC metals.* J. Mech. Phys. Solids **40**, 537-569.

Kalidindi, S.R., Bhattacharyya, A. and Doherty, R.D. (2004) Detailed analyses of grain-scale plastic deformation in columnar polycrystalline aluminium using orientation image mapping and crystal plasticity models. P. Roy. Soc. Lon. A Mat. **460**, 1935-1956.

Kocks, U.F. (1964) *Latent hardening and secondary slip in aluminium and silver*. T. Metall. Soc. AIME **230**, 1160-1167.

Kocks, U.F. (1970) *The relation between polycrystal deformation and single-crystal deformation.* Metall. Trans. **1**, 1121-1143.

Kocks, U.F. (1976) *Laws for work-hardening and low-temperature creep.* J. Eng. Mater. Technol. **98**, 76-85.

Kocks, U.F., Hasegawa, T. and Scattergood, R.O. (1980) *On the origin of cell walls and of lattice misorientations during deformation.* Scripta Mater. **14**, 449-454.

Kocks, U.F., Franciosi, P. and Kawai, M. (1991) *A forest model of latent hardening and its application to polycrystal deformation.* In: proc. ICOTOM 9, Ed. Bunge, H.J. (Textures Microstruct. **14-18**), 1103-1114.

Kocks, U.F., Tomé, C.N. and Wenk, H.R (1998) *Texture and anisotropy: preferred orientations in polycrystals and their effect on material properties*. Cambridge University Press, New York, ISBN 0521465168

Kocks, U.F. and Mecking, H. (2003) *Physics and phenomenology of strain hardening: the FCC case.* Prog. Mater. Sci. **48**, 171-273.

Kratochvíl, J., Kružík, M. and Sedláček, R. (2007) *Statistically based continuum model of misoriented dislocation cell structure formation.* Phys. Rev. B **75**, 064104,1-14.

Kubin, L.P. (1993) *Dislocation patterning.* In: Materials Science and Technology, Vol. 6 Plastic deformation ed. Cahn, R.W., Haasen, P. and Kramer E.J., Wiley-VCH, Weinheim, 137-190.

Kuhlmann-Wilsdorf, D. and Comins, N.R. (1983) *Dislocation cell formation and workhardening in the unidirectional glide of FCC metals. I: Basic theoretical analysis of cell walls parallel to the primary glide plane in early stage II.* Mater. Sci. Eng. **60**, 7-24.

Kuhlmann-Wilsdorf, D. (1992) *Fundamentals of cell and subgrain structures in historical perspective.* Scripta Metall. Mater. **27**, 951-956.

Kuwabara, T. (2003) *Mechanical properties of IF steels: yield locus, differential hardening, and Bauschinger and strength differential effects*. In: Proceedings of the international forum for the properties and application of IF steels, Ed.: Takechi, H., The Iron and Steel Institute of Japan (ISIJ), Tokyo, Japan, 92-101.

Laukonis, J.V. and Ghosh, A.K. (1978) *Effects of strain path changes on the formability of sheet metals*. Metall. Trans. A **9**, 1849-1856.

Lebensohn, R.A. and Tomé, C.N. (1993) *A self-consistent anisotropic approach for the simulation of plastic deformation and texture development of polycrystals: application to zirconium alloys.* Acta Metall. Mater. **41**, 2611-2624.

Lewandowska, M. (2003) *Dependence of the deformation microstructure of aluminium alloys on the strain path*. Mater. Chem. Phys. **81**, 555-557.

Li, F. and Bate, P.S. (1991) *Strain path change effects in cube textured aluminium sheet.* Acta Metall. Mater. **39**, 2639-2650.

Li, S., Hoferlin, E., Van Bael, A., Van Houtte, P. and Teodosiu, C. (2003) *Finite element modeling of anisotropy induced by texture and strain-path change*. Int. J. Plasticity **19**, 647-674.

Liu, Q., Juul Jensen, D. and Hansen, N. (1998) *Effect of grain orientation on deformation structure in cold-rolled polycrystalline aluminium.* Acta Mater. **46**, 5819-5838.

Lopes, A.B., Rauch, E.F. and Gracio, J.J. (1999) *Textural vs structural plastic instabilities in sheet metal forming*. Acta Mater. **47**, 589-866.

Lopes, A.B., Barlat, F., Gracio, J.J., Ferreira Duarte, J.F. and Rauch, E.F. (2003) *Effect of texture and microstructure on strain hardening anisotropy for aluminum deformed in uniaxial tension and simple shear*. Int. J. Plasticity **19**, 1-22.

Lloyd, D.J. and Sang, H. (1979) *The influence of strain path on subsequent mechanical properties – orthogonal tensile paths*. Metall. Trans. A **10**, 1767-1772.

Ma, D., Friák, M., Neugebauer, J., Raabe, D. and Roters, F. (2008) *Multiscale simulation of polycrystals mechanics of textured b-Ti alloys using ab initio and crystal-based finite elements methods*. Phys. Stat. Sol. (b) **245**, 2642-2648.

Madec, R., Devincre, B. and Kubin, L.P. (2002a) *Simulation of dislocation patterns in multislip.* Scripta Mater. **47**, 689-695.

Madec, R., Devincre, B. and Kubin, L.P. (2002b) *From dislocation junctions to forest hardening.* Phys. Rev. Lett. **89**, 255508, 1-4.

Madec, R., Devincre, B., Kubin, L.P., Hoc, T. and Rodney, D. (2003) *The role of collinear interaction in dislocation-induced hardening.* Science **301**, 1879-1882.

Mahesh, S., Tomé, C.N., McCabe, R.J., Kaschner, G.C., Beyerlein, I.J. and Misra, A. (2004) *Application of a substructure-based hardening model to copper under loading path changes*. Metall. Mater. Trans. A **35**, 3763-3774.

Maudlin, P.J., Wright, S.I., Kocks, U.F. and Sahota, M.S. (1996) *An application of multisurface plasticity theory: yield surfaces of textured materials.* Acta Mater. **44**, 4027-4032.

Molinari, A., Canova, G.R. and Ahzi, S. (1987) *A self-consistent approach of the large deformation viscoplasticity.* Acta Metall. **35**, 2983-2994.

Mughrabi, H. (1983) *Dislocation wall and cell structures and long-range internal stresses in deformed metal crystals.* Acta Metall. **31**, 1367-1379.

Mughrabi, H. (1987) *A two-parameter description of heterogeneous dislocation distributions in deformed metal crystals.* Mater. Sci. Eng. A **85**, 15-31.

Nabarro, F.R.N. (1989) *Work hardening and dynamical recovery of FCC metals in multiple glide.* Acta Metall. **37**, 1521-1546.

Nabarro, F.R.N. (2001) *Sequences of dislocation patterns.* Mater. Sci. Eng. A **317**, 12-16.

Nes, E. (1998) *Modelling of work hardening and stress saturation in FCC metals.* Prog. Mater. Sci. **41**, 129-193.

Nesterova, E.V., Bacroix, B. and Teodosiu, C. (2001) *Microstructure and texture evolution under strain-path changes in low-carbon interstitial-free steel.* Metall. Mater. Trans. A **32**, 2527-2538.

Pantleon, W. (1998) *On the statistical origin of disorientations in dislocation structures.* Acta Mater. **46**, 451-456.

Pantleon, W. and Hansen, N. (1998) *On the behaviour of low-energy dislocation boundaries during plastic deformation*. In: Proceedings of the 19th Risø International Symposium on Materials Science: Modelling of structure and mechanics of materials from microscale to product, Ed: Carstensen, J.V., Leffers, T., Lorentzen, T., Pedersen, O.B., Sørensen, B.F. and Winther, G., Risø National Laboratory, Roskilde, Denmark, 405-410.

Pantleon, W. (2001) *The evolution of disorientations for several types of boundaries.* Mater. Sci. Eng. A **319-321**, 211-215.

Pantleon, W. and Hansen, N. (2001) *Dislocation boundaries – the distribution function of disorientation angles.* Acta Mater. **49**, 1479-1493.

Pantleon, W. (2004) *Stage IV work-hardening related to disorientations in dislocation structures.* Mater. Sci. Eng. A **387-389**, 257-261.

Pantleon, W. (2005) *On the apparent saturation of the average disorientation angle with plastic deformation.* Scripta Mater. **53**, 757-762.

Peeters, B., Seefeldt, M., Van Houtte, P. and Aernoudt, E. (2001a) *Taylor ambiguity in BCC polycrystals: a non-problem if substructural anisotropy is considered.* Scripta Mater. **45**, 1349-1356.

Peeters, B., Seefeldt, M., Teodosiu, C., Kalidindi, S.R., Van Houtte, P. and Aernoudt, E. (2001b) *Work-hardening/softening behaviour of bcc polycrystals during changing strain paths: I. an integrated model based on substructure and texture evolution, and its prediction of the stress-strain behavior of an IF steel during two-stage strain paths*. Acta Mater. **49**, 1607-1619.

Peeters, B. (2002) *Multiscale modelling of the induces plastic anisotropy in IF steel during sheet forming.* PhD. Thesis, Department MTM, KULeuven.

Raphanel, J.L., Schmitt, J.H. and Baudelet, B. (1986) *Effect of prestrain on the subsequent yielding of low carbon steels sheets: experiments and simulations*. Int. J. Plasticity **2**, 371-378.

Raphanel, J.L., Rauch, E.F., Shen, E.L. and Schmitt, J.H. (1987a) *Shear of prestrained steel specimens*. Scripta Metall. **21**, 1087-1090.

Raphanel, J.L., Schmitt, J.H. and Baudelet, B. (1987b) *Plastic behavior of prestrained materials: experiments and analysis through a simple model*. In: Proceedings of the 8th Risø International Symposium on Metallurgy and Materials Science: Constitutive relations and their physical basis, Ed: Andersen, S.I., Bilde-Sørensen,J.B., Hansen, N., Leffers, T., Lilholt, H., Pedersen, O.B. and Ralph, B., Risø National Laboratory, Roskilde, Denmark, 491-496.

Rauch, E.F. and G'Sell, C. (1989) *Flow localization induced by a change in strain path in mild steel*. Mater. Sci. Eng. A **111**, 71-80.

Rauch, E.F. and Schmitt, J.H. (1989) *Dislocation substructures in mild steel deformed in simple shear*. Mater. Sci. Eng. A **113**, 441-448.

Rauch, E.F. and Thuillier, S. (1993) *Rheological behaviour of mild steel under monotonic loading conditions and cross-loading*. Mater. Sci. Eng. A **164**, 255-259.

Rauch, E.F. (1997) *The stresses and work hardening rates of mild steel with different dislocation patterns*. Mater. Sci. Eng. A **234-236**, 653-656.

Rauch, E.F. (1998) *Plastic anisotropy of sheet metals determined by simple shear tests*. Mater. Sci. Eng. A **241**, 179-183.

Rauch, E.F., Lopes, A.B. and Gracio, J.J. (1999) *The origin of softening in predeformed metals*. Arch. Metall. **44**, 139-155.

Rauch, E.F., Gracio, J.J., Barlat, F., Lopes, A.B. and Ferreira Duarte, J. (2002) *Hardening behavior and structural evolution upon strain reversal of aluminum alloys*. Scripta Mater. **46**, 881-886.

Rauch, E.F. (2005) *Dislocation substructure and mechanical behaviour of metals*. In: Proceedings of the 8th ESAFORM conference on material forming, Ed: Banabic, D., Romanian Academy, Bucharest, Romania, 185-188.

Rauch, E.F., Gracio, J.J. and Barlat, F. (2007) *Work-hardening model for polycrystalline metals under strain reversal at large strains*. Acta Mater. **55**, 2939-2948.

Ricks, R.A. (1999) *The deformation models needed by the aluminium industry*. Philos. T. Roy. Soc. A **357**, 1513-1529.

Roberts, W. (1982) *Dynamic changes that occur during hot working and their significance regarding microstructural development and hot workability*. In: Deformation, Processing and Structure, ed. G. Krauss, ASM, St.Louis, 109-180.

Rollett, A.D., Kocks, U.F. and Doherty, R.D. (1987) *Stage IV work hardening in cubic metals.* In: Formability and metallurgical structure. Ed.: Sachdev, A.K. and Embury, J.D., TMS-AIME, Warrendale, 211-225.

Roters, F., Raabe, D. and Gottstein G. (2000) *Work hardening in heterogeneous alloys – a microstructural approach based on three internal state variables.* Acta Mater. **48**, 4181-4189.

Schmidt, S., Nielsen, S.F., Gundlach, C., Margulies, L., Huang, X. and Juul Jensen, D. (2004) *Watching the growth of bulk grains during recrystallization of deformed metals*. Science **305**, 229-232.

Schmitt, J.H., Aernoudt, E. and Baudelet, B. (1985) *Yield loci for polycrystalline metals without texture.* Mater. Sci. Eng. **75**, 13-20.

Schmitt, J.H., Shen, E.L. and Raphanel, J.L. (1994) *A parameter for measuring the magnitude of a change of strain path: validation and comparison with experiments on low carbon steel*. Int. J. Plasticity **10**, 535-551.

Schuh, F. and von Heimendahl, M. (1974) *Die Ausbildung der Versetzungsstruktur in Aluminium und deren Beziehungen zum Verformungsverhalten (Teil I).* Z. Metallkde. **65**, 346-352.

Sedláček, R., Kratochvíl, J. and Blum. W. (2001) *Deformation induced misorientations: initial stage of subgrain formation as a plastic instability.* Phys. Stat. Sol. (a) **186**, 1-16.

Shenoy, V.B., Kukta, R.V. and Phillips, R. (2000) *Mesoscopic analysis of structure and strength of dislocation junctions in FCC metals.* Phys. Rev. Lett. **84**, 1491-1494.

Skelton, R.P., Maier, H.J. and Christ, H.J. (1997) *The Bauschinger effect, Masing model and the Ramberg-Osgood relation for cyclic deformation in metals.* Mater. Sci. Eng. A **238**, 377-390.

Strauven, Y. and Aernoudt, E. (1987) *Directional strain softening in ferritic steel*. Acta Metall. **35**, 1029-1036.

Suprun, A.N. (2006) *A constitutive model with three plastic constants: the description of anisotropic workhardening*. Int. J. Plasticity **22**, 1217-1233.

Taylor, G.I. (1938) *Plastic strain in metals.* J. Inst. Metals **62**, 307-324.

Teodosiu, C. (1992) *Materials science input to engineering models*. In: Proceedings of the 13th Risø symposium on materials science : modeling of plastic deformation and its engineering applications, Ed: Andersen, S.I., Bilde-Sørensen, J.B., Hansen, N., Juul Jensen, D., Leffers, T., Lilholt, H., Pedersen, O.B. and Ralph, B., Risø National Laboratory, Roskilde, Denmark, 125-146.

Teodosiu, C. and Hu, Z. (1995) *Evolution of the intragranular microstructure at moderate and large strains: modelling and computational significance*. In: Proc. Numiform ’95, Ed: Shen, S.F. and Dawson, P.R., Balkema, Rotterdam, the Netherlands, 173-182.

Teodosiu, C., Duval, J.L. and Haddadi, H. (1997) *Modelling the microstructural evolution during large plastic deformations*. In: Proc. Of the IUTAM Symposium on Macrostructural Aspects of Thermoplasticity, Kluwer Academic, Dordrecht, 479-488.

Tomé, C., Canova, G.R., Kocks, U.F., Christodoulou, N. and Jonas, J.J. (1984) *The relation between macroscopic and microscopic strain hardening in FCC polycrystals*. Acta Metall. **32**, 1637-1653.

Tóth, L.S., Gilormini, P. and Jonas, J.J. (1988) *Effects of rate sensitivity on the stability of torsion textures*. Acta Metall. **36**, 3077-3091.

Tóth, L.S. and Van Houtte, P. (1992) *Discretization techniques for orientation distribution functions.* Textures Microstruct. **19**, 229-244.

Uenishi, A. and Teodosiu, C. (2004) *Constitutive modelling of the high strain rate behaviour of interstitial-free steel*. Int. J. Plasticity **20**, 915-936.

Uenishi, A., Teodosiu, C. and Nesterova, E.V. (2005) *Dislocation-based intragranular hardening model takint into account strain path and strain rate changes for steels*. In: Proceedings of the 8th ESAFORM conference on material forming, Ed: Banabic, D., Romanian Academy, Bucharest, Romania, 213-216.

Van Boxel, S., Seefeldt, M., Pantleon, W., Verlinden, B. and Van Houtte, P. (2004) *Study of grain subdivision in aluminium using electron back-scattering diffraction.* In: Proceedings of the 25th Risø International Symposium on Materials Science: Evolution of Deformation Microstructures in 3D, Ed: Gundlach, C., Haldrup, K., Hansen, N., Huang, X., Juul Jensen, D., Leffers, T., Li, Z.J., Nielsen, S.F., Pantleon, W. Wert, J.A. and Winther, G., Risø National Laboratory, Roskilde, Denmark, 557-562.

Van Houtte, P. and Aernoudt, E. (1975) *Solution of the generalized Taylor theory of plastic flow.* Z. Metallkd. **66**, 202-209.

Van Houtte, P. (1988) *A comprehensive mathematical formulation of an extended Taylor-Bishop-Hill model featuring relaxed constraints, the Renouard-Wintenberger theory and a strain rate sensitivity model.* Textures Microstruct. **8-9**, 313-350.

Van Houtte, P. (1994) *Application of plastic potentials to strain rate sensitive and insensitive anisotropic deformation textures.* Int. J. Plasticity **10**, 719-748.

Van Houtte, P. (1995a) *Manual of the MTM-FHM software*, Department MTM, KULeuven.

Van Houtte, P. (1995b) *Heterogeneity of plastic strain around an ellipsoidal inclusion in an ideal plastic matrix*. Acta Metall. Mater. **43**, 2859-2879.

Van Houtte, P., Delannay, L. and Samajdar, I. (1999) *Quantitative prediction of cold rolling textures in low-carbon steel by means of the Lamel model.* Textures Microstruct. **31**, 109-149.

Van Houtte, P., Hiwatashi, S., Hoferlin, E., Peeters, B. and Teodosiu, C. (2003) *Physics-based material modeling of the deformation process in deep drawing of IF steel*. In: Proceedings of the international forum for the properties and application of IF steels, Ed.: Takechi, H., The Iron and Steel Institute of Japan (ISIJ), Tokyo, Japan, 82-91.

Van Houtte, P. and Van Bael, A. (2004) *Convex plastic potentials of fourth and sixth rank for anisotropic materials.* Int. J. Plasticity **20**, 1505-1524.

Van Houtte, P., Li, S., Seefeldt, M. and Delannay, L. (2005) *Deformation texture prediction: from the Taylor model to the advanced Lamel model.* Int. J. Plasticity **21**, 589-624.

Van Houtte, P., Yerra, S.K. and Van Bael, A. (2009) *The facet method: a hierarchical multilevel modeling scheme for anisotropic convex plastic potentials*. Int. J. Plasticity **25**, 332-360.

Verlinden, B., Driver, J., Samajdar, I. and Doherty, R.D. (2007) *Thermo-mechanical processing of metallic materials*. Elsevier, Amsterdam, ISBN: 978-0-08-044497-0.

Vincze, G., Rauch, E.F., Gracio, J.J., Barlat, F. and Lopes, A.B. (2005) *A comparison of the mechanical behaviour of an AA1050 and a low carbon steel deformed upon strain reversal*. Acta Mater. **53**, 1005-1013.

Wagoner, R.H. and Laukonis, J.V. (1983) *Plastic behavior of aluminum-killed steel following plane-strain deformation*. Metall. Trans. A **14**, 1487-1495.

Wang, J., Levkovitch, V., Reusch, F., Svendsen, B., Huétink, J., and van Riel, M. (2008) *On the modeling of hardening in metals during non-proportional loading*. Int. J. Plasticity **24**, 1039-1070.

Wert, J.A., Liu, Q. and Hansen, N. (1995) *Dislocation boundaries and active slip systems.* Acta Metall. Mater. **43**, 4153-4163.

Wilson, D.V. (1965) *Reversible work hardening in alloys of cubic metals*. Acta Metall. **13**, 807-814.

Wilson, D.V., Zandrahimi, M. and Roberts, W.T. (1990) *Effects of changes in strain path on work-hardening in CP aluminium and an Al-Cu-Mg alloy*. Acta Metall. Mater. **38**, 215-226.

Wilson, D.V. and Bate, P.S. (1994) *Influences of cell walls and grain boundaries on transient responses of an IF steel to changes in strain path*. Acta Metall. Mater. **42**, 1099-1111.

Winther, G., Juul Jensen, D. and Hansen, N. (1997) *Modelling flow stress anisotropy caused by deformation induced dislocation boundaries.* Acta Mater. **45**, 2455-4265.

Winther, G., Huang, X. and Hansen, N. (2000) *Crystallographic and macroscopic orientation of planar dislocation boundaries – correlation with grain orientation.* Acta Mater. **48**, 2187-2198.

Winther, G. (2005) *Effect of grain orientation dependent microstructures on flow stress anisotropy modelling.* Scripta Mater. **52**, 995-1000.

Wu, H.-C. (2003) *Effect of loading-path on the evolution of yield surface for anisotropic metals subjected to large pre-strain*. Int. J. Plasticity **19**, 1773-1800.

Wu, T.-Y., Bassani, J.L. and Laird, C. (1991) *Latent hardening in single crystals I. theory and experiments.* Proc. R. Soc. Lond. A **435**, 1-19.

Yakou, T., Hasegawa, T. and Karashima, S. (1985) *Stagnation of strain hardening during reversed straining of prestrained aluminium, copper and iron*. T. Jpn. I. Met. **26**, 88-93.

Yoshida, F. and Uemori, T. (2002) *A model of large-strain cyclic plasticity describing the Bauschinger effect and workhardening stagnation*. Int. J. Plasticity **18**, 661-686.

Zaiser, M. and Hähner, P. (1999) *The flow stress of fractal dislocation arrangements.* Mater. Sci. Eng. A **270**, 299-307.

Zandrahimi, M., Platias, S., Price, D., Barrett, D., Bate, P.S., Roberts, W.T. and Wilson, D.V. (1989) *Effects of Changes in strain path on work hardening in cubic metals*. Metall. Trans. A **20**, 2471-2482.

Appendix A

The Taylor factor in multiple slip with different τ

1. Taylor factor for a single orientation

The Taylor factor or *M*-factor is a geometrical parameter which relates for one grain a scalar equivalent of the externally applied strain rate tensor (in the Taylor theory this is the macroscopic strain rate tensor) with the rate of increase of the total amount of microscopical slip [Gil Sevillano et al.; 1980] :

$$M = \frac{\dot{\Gamma}}{\dot{\varepsilon}_{eq}} = \frac{d\Gamma}{d\varepsilon_{eq}}, \tag{A.1}$$

with $\dot{\Gamma}$ the sum of all slip rates and $\dot{\varepsilon}_{eq}$ a scalar equivalent of the strain rate. The value of the Taylor factor depends on the chosen scalar equivalent for the strain rate, which therefore should be specified. Usually the $\dot{\varepsilon}_{11}$-component is taken for tension, compression and uniaxial deformation, while for simple shear and torsion the macroscopic shear rate $\dot{\gamma}$ (at the outer surface) is used. For other straining modes generally the von Mises equivalent strain rate is used[31].

The plastic work rate of the grain can be expressed as

$$\dot{W} = \sum_j \sum_i \sigma_{ij} \dot{\varepsilon}_{ij} = \sigma_{eq} \dot{\varepsilon}_{eq}, \tag{A.2}$$

---

[31] In most advanced models for polycrstyal deformation (such as e.g. A-Lamel), the von Mises equivalent strain rate is consistently used to define the *M*-factor, regardless of the imposed straining mode

where σ_{eq} is a scalar equivalent of the stress tensor corresponding to the equivalent strain rate $\dot{\varepsilon}_{eq}$. If a certain formulation of $\dot{\varepsilon}_{eq}$ is chosen, then σ_{eq} is defined by this equation.[32] The plastic work rate also corresponds to

$$\dot{W} = \sum_{\alpha} \tau^{\alpha} \left|\dot{\gamma}^{\alpha}\right| = \tau_{ref} \dot{\Gamma}, \tag{A.3}$$

where

$$\tau_{ref} = \frac{\sum_{\alpha} \tau^{\alpha} \left|\dot{\gamma}^{\alpha}\right|}{\sum_{\alpha} \left|\dot{\gamma}^{\alpha}\right|} \tag{A.4}$$

is the weighted average of the critical shear stresses of the slip systems τ^{α}, with the shear rates $\dot{\gamma}^{\alpha}$ as weighting factors. Equating (A.2) and (A.3) and using the definition of the Taylor factor (A.1) results in

$$\dot{W} = \dot{\varepsilon}_{eq} M \tau_{ref} \tag{A.5}$$

$$\text{and } \sigma_{eq} = M \tau_{ref} \,. \tag{A.6}$$

The aim is to use the concept of the Taylor factor to distinguish between the textural and the substructural contribution to the overall work hardening rate. The reference stress τ_{ref} depends on the substructural configuration and can only be changed by substructural hardening. The *M*-factor depends on the tensor which describes the externally imposed straining mode (expressed with respect to the external reference frame) and the orientation of the crystal reference frame with respect to the external reference frame. The *M*-factor thus may change if the straining mode changes or if the crystal orientation changes. This does not mean that *M* and τ_{ref} necessarily evolve independently. To separate the hardening contributions of orientation changes and substructural changes for polycrystals, a careful derivation regarding the involved averaging procedures has to be performed.

---

[32] which means that for the classically defined von Mises strain rate $\dot{\varepsilon}_{vm} = \sqrt{\frac{2}{3}\dot{\varepsilon}_{ij}\dot{\varepsilon}_{ij}}$, the von Mises stress σ_{vm} will be only found if the material follows the von Mises yield criterion.

2. Textural and microstructural hardening in polycrystalline materials

In the Taylor theory, the macroscopic stress is obtained as the average of the stresses of the individual grains, following equation (A.6). This corresponds to

$$\overline{\sigma_{eq}} = \overline{M\tau_{ref}} \, . \tag{A.7}$$

Because in the Taylor theory every grain undergoes the same deformation, the overall work hardening rate can be expressed as

$$\frac{d\overline{\sigma_{eq}}}{d\varepsilon_{eq}} = \overline{M\frac{d\tau_{ref}}{d\varepsilon_{eq}}} + \overline{\tau_{ref}\frac{dM}{d\varepsilon_{eq}}} = \overline{M^2\frac{d\tau_{ref}}{d\Gamma}} + \overline{\tau_{ref}\frac{dM}{d\varepsilon_{eq}}} \, , \tag{A.8}$$

which is the sum of the average of all hardening contributions due to substructural work hardening and the average of the hardening/softening contributions due to changes in the grain orientations.

A common modelling approximation is to assume that τ_{ref} is a unique function of Γ. Equation (A.1) leads to

$$\Gamma = \int_0^{\varepsilon_{eq}} M\left(\varepsilon_{eq}\right) d\varepsilon_{eq} \tag{A.9}$$

and since the deformation is assumed to be equal in each grain

$$\overline{\Gamma} = \int_0^{\varepsilon_{eq}} \overline{M}\left(\varepsilon_{eq}\right) d\varepsilon_{eq} \tag{A.10}$$

Combining equations (A.1), (A.9) and (A.10) leads to

$$d\varepsilon_{eq} = \frac{d\Gamma}{M} = \frac{d\overline{\Gamma}}{\overline{M}} \, . \tag{A.11}$$

Equation (A.9) implies that Γ can be different for every grain, and therefore also τ_{ref} can be different. Nevertheless a good approximation of the average microscopic hardening curve $\tau_{ref}\left(\Gamma\right)$ can be obtained by calculating the curve $\tilde{\tau}_{ref}\left(\overline{\Gamma}\right)$ [Tomé et al.; 1984], where $\tilde{\tau}_{ref}$ is the weighted average of τ_{ref} with the *M*-factors as weighting factors :

$$\tilde{\tau}_{ref} = \frac{\sum M \tau_{ref}}{\sum M} = \frac{\overline{M \tau_{ref}}}{\overline{\overline{M}}}. \tag{A.12}$$

Using equations (A.12) and (A.11), equations (A.7) and (A.8) become

$$\overline{\sigma_{eq}} = \overline{M} \tilde{\tau}_{ref} \tag{A.13}$$

and

$$\frac{d\overline{\sigma_{eq}}}{d\varepsilon_{eq}} = \left(\overline{M}\right)^2 \frac{d\tilde{\tau}_{ref}}{d\overline{\overline{\Gamma}}} + \tilde{\tau}_{ref} \frac{d\overline{M}}{d\varepsilon_{eq}}, \tag{A.14}$$

which are much easier to obtain and give the relative importance of the two hardening contributions as well. There is however a difference with the relative importance of the two terms of equation (A.8), since the true substructural contribution of equation (A.8) can be elaborated by using equations (A.11) and (A.12) to:

$$\begin{aligned} \overline{M^2 \frac{d\tau_{ref}}{d\Gamma}} &= \overline{M \overline{M} \frac{d\tau_{ref}}{d\overline{\overline{\Gamma}}}} = \frac{\left(\overline{M}\right)^2}{d\overline{\overline{\Gamma}}} \left(d\left(\frac{\overline{M \tau_{ref}}}{\overline{\overline{M}}} \right) - \overline{\tau_{ref}\, d\left(\frac{M}{\overline{\overline{M}}} \right)} \right) \\ &= \left(\overline{M}\right)^2 \frac{d\tilde{\tau}_{ref}}{d\overline{\overline{\Gamma}}} - \overline{\tau_{ref}\, \overline{M} \frac{d\left(\frac{M}{\overline{\overline{M}}} \right)}{d\varepsilon_{eq}}} \end{aligned} \tag{A.15}$$

Equation (A.14) can therefore not be used for analyzing the relative importance of textural and microstructural work hardening. The difference between the true substructural contribution and the apparent one of equation (A.14) depends on the spread $\Delta\tau_{ref}$ on the reference critical resolved shear stress τ_{ref} of the different grains, since:

$$\begin{aligned} \overline{\tau_{ref}\, \overline{M} \frac{d\left(\frac{M}{\overline{\overline{M}}} \right)}{d\varepsilon_{eq}}} &= \frac{\overline{M}}{d\varepsilon_{eq}} \overline{\left(\overline{\tau_{ref}} + \Delta\tau_{ref} \right) d\left(\frac{M}{\overline{\overline{M}}} \right)} = \frac{\overline{M}}{d\varepsilon_{eq}} \left(\overline{\overline{\tau_{ref}}\, d\left(\frac{M}{\overline{\overline{M}}} \right)} + \overline{\Delta\tau_{ref}\, d\left(\frac{M}{\overline{\overline{M}}} \right)} \right) \\ &= \frac{\overline{M}}{d\varepsilon_{eq}} \left(\overline{\tau_{ref}} \frac{\overbrace{\overline{\overline{M}\, dM} - \overline{M\, d\overline{M}}}^{=0}}{\left(\overline{M}\right)^2} + \overline{\Delta\tau_{ref}\, d\left(\frac{M}{\overline{\overline{M}}} \right)} \right) = \overline{\Delta\tau_{ref}\, \overline{M} \frac{d\left(\frac{M}{\overline{\overline{M}}} \right)}{d\varepsilon_{eq}}} \end{aligned} \tag{A.16}$$

As a consequence of equation (A.5), grains that have a high *M*-factor will have a high amount of plastic work dissipation. As long as the strain compatibility is maintained this has as consequence that the total amount of slip for these grains is relatively high, which can be seen in equation (A.9). In stage II and early stage III of work hardening this means that the reference stress τ_{ref} for these grains will increase much more rapidly than for grains with a low *M*-factor. If this is not compensated by a drastic lowering of the *M*-factor, it means that the flow stress of this grain will increase likewise. For soft grains (low *M*-factor) the opposite will be observed. This is consistent with findings of [Hansen and Huang; 1998], where they conclude on the basis of microstructural observations that grains with a high Taylor factor have a higher hardening rate and a different substructure than grains with a low Taylor factor. The spread of the average flow stress will become very high in the classical FC Taylor model. If strain relaxations due to grain interactions are taken into account (e.g. A-Lamel) the spread will be presumably lower, because the combinations of a hard grain with a soft grain, solved together in the linear program will favour slip in the soft grain, if the difference of the two τ_{ref} would become rather large. In that respect, one might expect a considerable influence of integrating slip system based hardening models into these codes.

3. Influence of different τ^α on the *M*-factor.

If all τ^α are the same, the Taylor ambiguity problem arrises. There are multiple combinations of $\dot{\gamma}^\alpha$ that lead to the same minimum value of $\dot{W}$. Also the linear combinations of several distinct solutions will result in the same minimum value of $\dot{W}$. Since $\dot{\boldsymbol{\varepsilon}}$ is a macroscopically imposed tensor, $\boldsymbol{\sigma}$ will be the same tensor for all possible solutions of the equations of the Taylor model. If all τ^α are the same and therefore equal to τ_{ref}, the sum of the slip rates $\dot{\Gamma}$ is also a fixed value for all possible solutions.

$$\dot{W} = \sigma_{eq}\dot{\varepsilon}_{eq} = \boldsymbol{\sigma} : \dot{\boldsymbol{\varepsilon}} = \tau_{ref}\dot{\Gamma} \qquad \text{(A.17)}$$

Since the equations of the Taylor model that control the slip rates (equation 4.1) can be reduced to a set of 5 independent equations, in general every solution needs to have at least 5 slip rates different from zero. In the fcc case, some cases of the Taylor ambiguity leads to 6 possibly active slip systems, while others have

8 (the hyperplanes, which represent in deviatoric stress space the bounding planes of the overall flow surface of a single orientation due to the individual slip systems, of 6 or 8 slip systems intersect at a single vertex). Because of the possiblilty to make linear combination, this means that all possible solution to the Taylor ambiguity problem are described by 6 or 8 slip rates that have values within certain intervals.

If the τ^{α} are different for the different slip systems, the ambiguity issue generally disappears (the hyperplanes of all 6 or 8 slip systems are not intersecting at a single vertex anymore). A single solution for the $\dot{\gamma}^{\alpha}$ leading to a minium $\dot{W}$ will be obtained.

$$\dot{W}=\sum_{\alpha}\tau^{\alpha}\dot{\gamma}^{\alpha}=\sum_{\alpha}\left(\tau_{ref}+\Delta\tau^{\alpha}\right)\dot{\gamma}^{\alpha}=\tau_{ref}\sum_{\alpha}\dot{\gamma}^{\alpha}+\sum_{\alpha}\Delta\tau^{\alpha}\dot{\gamma}^{\alpha} \tag{A.18}$$

It can be easily demonstrated that the last term of the previous equation equals 0:

$$\tau_{ref}=\frac{\sum_{\alpha}\tau^{\alpha}\dot{\gamma}^{\alpha}}{\dot{\Gamma}}=\tau_{ref}\frac{\sum_{\alpha}\dot{\gamma}^{\alpha}}{\dot{\Gamma}}+\frac{\sum_{\alpha}\Delta\tau^{\alpha}\dot{\gamma}^{\alpha}}{\dot{\Gamma}}=\tau_{ref}+0 \tag{A.19}$$

Since the $\dot{\gamma}^{\alpha}$ should comply with the macroscopically imposed strain tensor $\dot{\boldsymbol{\varepsilon}}$, the possible solutions of the Taylor ambiguity problem (having a fixed value for $\dot{\Gamma}$ and for M), will satisfy the conditions set by the imposed strain rate, but will not necessarily result in a minimum value of $\dot{W}$. If the found solution for the $\dot{\gamma}^{\alpha}$ that minimises $\dot{W}$, remains however within the solution intervals of the Taylor ambiguity problem, the value of $\dot{\Gamma}$ and for M will not be affected by having different τ^{α}. If the τ^{α} for some of the 6 or 8 slip systems of the solution to the Taylor ambiguity problem are very high, the minimum solution for $\dot{W}$ might be obtained by activating other slip systems that have a low value of τ^{α} and which are not among these 6 or 8 slip systems of the original solution. This new set of slip systems would in case of equal τ^{α} not be an optimal solution (with minimum $\dot{W}$) and consequently the *M*-factor and $\dot{\Gamma}$ will be higher for this solution.

If it is assumed that the τ^{α} of active slip systems remain lower than those of inactive slip systems (due to latent hardening) and that changes of the slip rates due to the reorientation of the crystal lattice are relatively slow compared to the changes in the substructure (the τ^{α}) to comply with the somewhat changed slip rates, it can be argued that the *M*-factors of the individual grains during monotonic straining to moderate strains will only depend on their crystallographic orientation with respect to the straining mode. This means that the average Taylor factor can be calculated from experimentally measured textures obtained at intermediate strains by applying the Taylor model with equal τ^{α} for all slip systems to a representative set of orientations.

After abrupt changes in the straining mode, completely new slip systems can become active and the solution that minimises $\dot{W}$ is not necessarily a solution of the Taylor ambiguity problem. The $\overline{M}$-factor calculated from an experimentally measured texture by the Taylor model with equal τ^{α} will therefore only be a lower estimate value of the true $\overline{M}$-factor which would be obtained if the individual values of τ^{α} would be known.

Appendix B
Microscopic work hardening models

1. Model of Kocks

The Kocks hardening model [Kocks; 1976] is already reviewed in section 2.1.3.b. It is here repeated with a slightly different derivation to take into account a non negligible lattice resistance. This is the case for alloys with substitutional solute atoms and for bcc metals. For the Kocks model it will not make any difference in the obtained stress-strain relationship, but there is a difference in the interpretation of the modelling constants.

With a non negligible lattice resistance, equation (2.8) for the microscopic critical resolved shear stress has to be replaced by

$$\tau = \tau_0 + \alpha G b \sqrt{\rho}\,, \tag{B.1}$$

with G the shear modulus and b the length of the Burgers vector, α a proportionality factor about 0.2 to 0.5 and τ_0 the lattice resistance. The general expression for the work hardening rate remains equal to equation (2.9) :

$$\theta = \frac{d\tau}{d\gamma} = \frac{\alpha G b}{2\sqrt{\rho}} \frac{d\rho}{d\gamma}\,. \tag{B.2}$$

In the Kocks model the evolution equation of the dislocation density is a combination of a storage term and a recovery term (cf. equation (2.10))

$$\frac{d\rho}{d\gamma} = \frac{1}{Kb}\sqrt{\rho} - \frac{L_R}{b}\rho\,, \tag{B.3}$$

with K a proportionality constant and L_R the average length of dislocation line that is recovered in one recovery event. Combining the previous three equations results in :

$$\theta = \frac{d\tau}{d\gamma} = \frac{\alpha G}{2K} - \frac{\alpha G L_R}{2}\sqrt{\rho} = \frac{\alpha G}{2K} - \frac{L_R}{2b}\left(\tau - \tau_0\right) = \theta_0\left(1 - \frac{\tau}{\tau_{sat}}\right), \tag{B.4}$$

which is the same form as equation (2.11) but the hardening rate at $\tau = 0$ and the saturation stress equal now

$$\theta_0 = \frac{\alpha G}{2K} + \frac{L_R}{2b}\tau_0 \tag{B.5}$$

and $\tau_{sat} = \dfrac{\alpha G b}{K L_R} + \tau_0$. (B.6)

Integration of the differential equation (B.4) under the assumption that there is a negligible dislocation density in the undeformed material results in

$$\tau = \tau_{sat} - \left(\tau_{sat} - \tau_0\right)\exp\left(-\frac{\theta_0}{\tau_{sat}}\right). \tag{B.7}$$

2. Model of Estrin and Mecking

The work hardening model of Estrin and Mecking [1984] is a generalisation of the Kocks model which takes also into account the hardening effects in particle strengthened materials. The derivation here again deviates from the one given in the original paper by including a non negligible lattice resistance.

The storage of mobile dislocations is assumed to be inversely proportional to the mean free path length Λ

$$\frac{d\rho^+}{d\gamma} \sim \frac{1}{b\Lambda} \tag{B.8}$$

In the initial stages of the work hardening this mean free path is prescribed by the interparticle spacing and is constant before it gets reduced by the increasing dislocation forest. In their model Estrin and Mecking assume that both contributions to dislocation storage are additive and equation (B.3) is replaced by

$$\frac{d\rho}{d\gamma} = \frac{1}{b l_{part}} + \frac{1}{Kb}\sqrt{\rho} - \frac{L_R}{b}\rho, \tag{B.9}$$

with l_{part} the average interparticle distance. Combined with equations (B.1) and (B.2), the hardening rate equation becomes

$$\theta = \frac{d\tau}{d\gamma} = \frac{(\alpha G)^2 b}{2 l_{part} (\tau - \tau_0)} + \frac{\alpha G}{2K} - \frac{L_R}{2b}(\tau - \tau_0)$$

$$\theta = \frac{L_R}{2b} \left(\frac{\frac{(\alpha G b)^2}{L_R l_{part}} + \frac{\alpha G b}{L_R K}(\tau - \tau_0) - (\tau - \tau_0)^2}{(\tau - \tau_0)} \right) \tag{B.10}$$

The saturation stress τ_{sat} can be found by putting $\theta = 0$ and solving for τ .

$$(\tau_{sat} - \tau_0)^2 - \frac{\alpha G b}{L_R K}(\tau_{sat} - \tau_0) - \frac{(\alpha G b)^2}{L_R l_{part}} = 0$$

$$\tau_{sat} - \tau_0 = \frac{\alpha G b}{2 L_R K} \left(1 + \sqrt{1 + 4 \frac{L_R K^2}{l_{part}}} \right) = \frac{\alpha G b}{L_R K \kappa} \tag{B.11}$$

$$\text{with } \kappa = \frac{2}{1 + \sqrt{1 + 4 \frac{L_R K^2}{l_{part}}}} \tag{B.12}$$

Since

$$1 - \kappa = 1 - \frac{2}{1 + \sqrt{1 + 4 \frac{L_R K^2}{l_{part}}}} = \frac{\sqrt{1 + 4 \frac{L_R K^2}{l_{part}}} - 1}{\sqrt{1 + 4 \frac{L_R K^2}{l_{part}}} + 1} \cdot \frac{\sqrt{1 + 4 \frac{L_R K^2}{l_{part}}} - 1}{\sqrt{1 + 4 \frac{L_R K^2}{l_{part}}} - 1}$$

$$1 - \kappa = \frac{\left(\sqrt{1 + 4 \frac{L_R K^2}{l_{part}}} - 1 \right)^2 l_{part}}{4 L_R K^2} = \frac{\left(\frac{1}{\kappa} - 1 \right)^2 l_{part}}{L_R K^2} = \frac{(1 - \kappa)^2 l_{part}}{\kappa^2 L_R K^2}$$

$$\frac{\kappa^2}{1 - \kappa} = \frac{l_{part}}{L_R K^2} \tag{B.13}$$

If θ_0 is defined by setting the ratio $\frac{\theta_0}{\tau_{sat}} = \frac{L_R}{2b}$ which is analogue to θ_0 of the Kocks model (cf. equation (B.5) divided by equation (B.6)), θ becomes

$$\theta = \frac{\theta_0}{\tau_{sat}} \left(\frac{(1-\kappa)(\tau_{sat}-\tau_0)^2 + \kappa(\tau_{sat}-\tau_0)(\tau-\tau_0) - (\tau-\tau_0)^2}{(\tau-\tau_0)} \right) \tag{B.14}$$

$$\text{with } \theta_0 = \frac{\alpha G}{2K\kappa} + \tau_0 \frac{L_R}{2b} \tag{B.15}$$

if $\kappa = 1$ equation (B.14) becomes equal to equation (B.4) of the Kocks model. This can be easily understood by having the interparticle spacing l_{part} set to $+\infty$ in equation (B.9). The hardening contribution because of the presence of particles is then up to zero. According to equation (B.12) κ indeed becomes 1 in this case.

The opposite case would be if no contribution to the hardening because of interactions with the dislocation forest would occur. In this case l_{part} is the only parameter controlling the dislocation storage rate. In equation (B.9) this can be achieved by putting the value of K to $+\infty$. κ becomes then 0. In case both mechanisms make a contribution to the dislocation storage rate κ will be in between 0 and 1.

It can also be concluded from equation (B.14) that if $\kappa < 1$ initially $(\tau \approx \tau_0)$ the main contribution to the hardening rate is due to the dislocation storage at particles, while with increasing τ the importance of the forest interactions increases as well. Close to the saturation stress τ_{sat} the dominant mechanism is determined by κ. The closer to 1, the more important is forest hardening, the closer to 0, the more important is dislocation storage due to interaction with particles.

To solve the differential equation (B.14), the method of the separation of the variables is applied:

$$\frac{2(\tau-\tau_0)}{(\tau-\tau_0)^2 - \kappa(\tau_{sat}-\tau_0)(\tau-\tau_0) - (1-\kappa)(\tau_{sat}-\tau_0)^2} d\tau = -\frac{2\theta_0}{\tau_{sat}} d\gamma . \tag{B.16}$$

For integrating the left hand side, the equation can be brought back to the form

$$\left(\frac{a_1}{x+a_2}+\frac{1}{x+a_3}\right)dx = a_4 dy \ , \tag{B.17}$$

with $x=\tau-\tau_0$, $y=\gamma$, $a_1=(1-\kappa)$, $a_2=(1-\kappa)(\tau_{sat}-\tau_0)$, $a_3=-(\tau_{sat}-\tau_0)$ and $a_4=-\theta_0(2-\kappa)/\tau_{sat}$.

Integrating equation (B.17) results in

$$\int\frac{a_1}{x+a_2}dx+\int\frac{1}{x+a_3}dx = a_4\int dy\,. \tag{B.18}$$

The first integral can be solved as:

$$\begin{aligned}&\int\frac{1-\kappa}{(\tau-\tau_0)+(1-\kappa)(\tau_{sat}-\tau_0)}d(\tau-\tau_0)\\&=(1-\kappa)\ln\left|(\tau-\tau_0)+(1-\kappa)(\tau_{sat}-\tau_0)\right|+cst\end{aligned} \tag{B.19}$$

The solution to the second integral of equation (B.18) is therefore

$$\int\frac{1}{(\tau-\tau_0)-(\tau_{sat}-\tau_0)}d(\tau-\tau_0)=\ln\left|\tau_{sat}-\tau\right|+cst \tag{B.20}$$

Since $\tau_{sat}>\tau>\tau_0$ and $0\leq\kappa\leq 1$, the absolute value within both logarithmic functions in equations (B.19) and (B.20) can be omitted. Combining equations (B.19) and (B.20) results into

$$\begin{aligned}&\ln\left(\left((\tau-\tau_0)+(1-\kappa)(\tau_{sat}-\tau_0)\right)^{1-\kappa}\right)+\ln(\tau_{sat}-\tau)=-\frac{\theta_0(2-\kappa)}{\tau_{sat}}\gamma+cst\\&\ln\left((\tau_{sat}-\tau)\left((\tau-\tau_0)+(1-\kappa)(\tau_{sat}-\tau_0)\right)^{1-\kappa}\right)=-\frac{\theta_0(2-\kappa)}{\tau_{sat}}\gamma+cst\end{aligned} \tag{B.21}$$

In order to determinate the remaining unknown constant, it is assumed that τ equals τ_0 at a strain of $\gamma=0$.

$$\ln\left((\tau_{sat}-\tau_0)\left((1-\kappa)(\tau_{sat}-\tau_0)\right)^{1-\kappa}\right)=cst \tag{B.22}$$

With equation (B.22) filled in into the solution of the differential equation, equation (B.21) becomes

$$\ln\left(\frac{\left(\tau_{sat}-\tau\right)}{\left(\tau_{sat}-\tau_0\right)}\left(\frac{\left(\tau-\tau_0\right)+\left(1-\kappa\right)\left(\tau_{sat}-\tau_0\right)}{\left(1-\kappa\right)\left(\tau_{sat}-\tau_0\right)}\right)^{1-\kappa}\right)=-\frac{\theta_0\left(2-\kappa\right)}{\tau_{sat}}\gamma \tag{B.23}$$

which is an analytical formulation for the stress-strain curve.

3. Model of Roberts

The model of Roberts [1982] is an alternative to the Kocks model and is mainly used for hot deformation. It assumes a dislocation density evolution equation of the form :

$$\frac{d\rho}{d\gamma}=k_1-k_2\sqrt{\rho}\,. \tag{B.24}$$

The storage term is taken constant, which is explained by Roberts to be a reasonable assumption if a cell or subgrain structure is established early in the deformation process. For the aluminium alloy under consideration at room temperature a more suitable explanation would be the presence of particles at which dislocation gets stored. The dependence of the recovery rate with $\sqrt{\rho}$ is fundamentally different from the two previous models. Unfortunately this is not discussed by Roberts.

In the following derivation the lattice resistance is assumed to be not negligible so equation (B.1) has to be used to translate the dislocation density into the critical resolved shear stress. Equation (B.2) combined with equation (B.24) becomes

$$\theta=\frac{d\tau}{d\gamma}=\frac{\left(\alpha Gb\right)^2}{2\left(\tau-\tau_0\right)}k_1-\frac{\alpha Gb}{2}k_2=\theta_0\left(\frac{\tau_{sat}-\tau_0}{\tau-\tau_0}-1\right)=\theta_0\left(\frac{\tau_{sat}-\tau}{\tau-\tau_0}\right), \tag{B.25}$$

$$\text{with }\ \theta_0=\frac{\alpha Gbk_2}{2} \tag{B.26}$$

$$\text{and }\ \tau_{sat}=\alpha Gb\frac{k_1}{k_2}+\tau_0\,. \tag{B.27}$$

The analytical equation for the stress strain curve can be derived from equation (B.25) :

$$\left(\frac{\tau-\tau_0}{\tau_{sat}-\tau}\right)d\tau=\theta_0 d\gamma$$

$$\int\left(\frac{\tau_{sat}-\tau_0}{\tau_{sat}-\tau}-1\right)d\tau=\theta_0\int d\gamma$$

$$-\left(\tau_{sat}-\tau_0\right)\ln\left|\tau_{sat}-\tau\right|-\tau=\theta_0\gamma+cst$$

$$\left(\tau_{sat}-\tau_0\right)\ln\frac{1}{\tau_{sat}-\tau}-\tau=\theta_0\gamma+cst$$

In order to determinate the remaining integration constant, it is assumed that τ equals τ_0 at a strain of $\gamma=0$.

$$cst=\left(\tau_{sat}-\tau_0\right)\ln\frac{1}{\tau_{sat}-\tau_0}-\tau_0$$

The analytical solution for the stress strain curve becomes

$$\left(\tau_{sat}-\tau_0\right)\ln\frac{\tau_{sat}-\tau_0}{\tau_{sat}-\tau}-\left(\tau-\tau_0\right)=\theta_0\gamma \tag{B.28}$$

4. Phenomenological model

The phenomenological model is inspired by the fact that the work hardening rate-stress curve derived from the experimental stress-strain curve exhibits two nearly linear parts after a exponentially decaying initial stage (in fig. 3-9 (b) respectively between 40 and 60 MPa and between 70 and 90 MPa). For the first linear part of the hardening curve the stress-strain curve can be represented by a Voce type of equation

$$\tau=\tau_A-\left(\tau_A-\tau_0\right)\exp\left(-\frac{\theta_A}{\tau_A}\gamma\right) \tag{B.29}$$

Before reaching the first point of saturation τ_A, the second linear part of the hardening curve increases the stress with further straining with an additional stress which can be represented by

$$\tau-\tau_A=\tau_B-\left(\tau_B-\tau_A\right)\exp\left(-\frac{\theta_B}{\tau_B}\gamma\right) \tag{B.30}$$

If both linear parts of the hardening curve are combined, the stress-strain curve becomes

$$\tau=\tau_B-\left(\tau_B-\tau_A\right)\exp\left(-\frac{\theta_B}{\tau_B}\gamma\right)-\left(\tau_A-\tau_0\right)\exp\left(-\frac{\theta_A}{\tau_A}\gamma\right) \tag{B.31}$$

Of course there will be a linear decreasing contribution to the hardening because of the second slope already from the start of the deformation. Therefore the ordinate and the abscissa of the first linear part are not θ_A and τ_A, but somewhat higher values.

The hardening rate becomes

$$\theta=\frac{d\tau}{d\gamma}=\frac{\theta_B}{\tau_B}\left(\tau_B-\tau_A\right)\exp\left(-\frac{\theta_B}{\tau_B}\gamma\right)+\frac{\theta_A}{\tau_A}\left(\tau_A-\tau_0\right)\exp\left(-\frac{\theta_A}{\tau_A}\gamma\right) \tag{B.32}$$

Expressing θ as a function of stress in order to analyse possible hardening mechanisms is unfortunately impossible.

Appendix C

Texture components for fcc materials

1. Orthorombic sample symmetry

In table C-1 the texture components that have a higher than random intensity after annealing (Cube, ND-RC, Goss, P and RCu) or cold rolling (Brass, S and Cu) of AA3103 are listed. The Euler angles and the Miller indices defining the components are given. In fig. C-1 the positions are indicated in the (90°, 90°,90°) Euler space of all the components and their corresponding equivalent orientations according to orthorhombic sample symmetry.

The relevant components, apart from S, are all found in the φ_2=45°-section. To encompass one full β-fibre (from Cu over S till Brass) the sections from φ_2=45° till φ_2=90° are sufficient. In the figure of chapter 3, three sections (φ_2=45°,65°,90°) are shown, representing the start, the middle and the end of the β-fibre.

Table C-1 : Texture components that are discussed in regard to annealing and cold rolling.textures of AA3103

component	Euler angles $(\varphi_1, \Phi, \varphi_2)$	Miller indices	Symbol
Cube	0°, 0°, 0°	$\{0\ 0\ 1\}\langle 1\ 0\ 0\rangle$	■
18° ND rotated Cube (ND-RC)	18°, 0°, 0°	$\{0\ 0\ 1\}\langle 1\ 3\ 0\rangle$	▰
Goss	0°, 45°, 0°	$\{0\ 1\ 1\}\langle 1\ 0\ 0\rangle$	◆
P	60.5°, 45°, 0°	$\{0\ 1\ 1\}\langle 4\ 5\ 5\rangle$	●
Rotated Copper (RCu)	67.8°, 35.3°, 45°	$\{1\ 1\ 2\}\langle 1\ 3\ 2\rangle$	★
Brass	35.3°, 45°, 0°	$\{0\ 1\ 1\}\langle 2\ 1\ 1\rangle$	▼
S	52.9°, 74.5°, 33.7°	$\{1\ 2\ 3\}\langle 6\ 3\ 4\rangle$	⬟
Copper (Cu)	90°, 35.3°, 45°	$\{1\ 1\ 2\}\langle 1\ 1\ 1\rangle$	○
V	43.1°, 40.3°, 45°	$\{3\ 3\ 5\}\langle 6\ 1\ 3\rangle$	▲

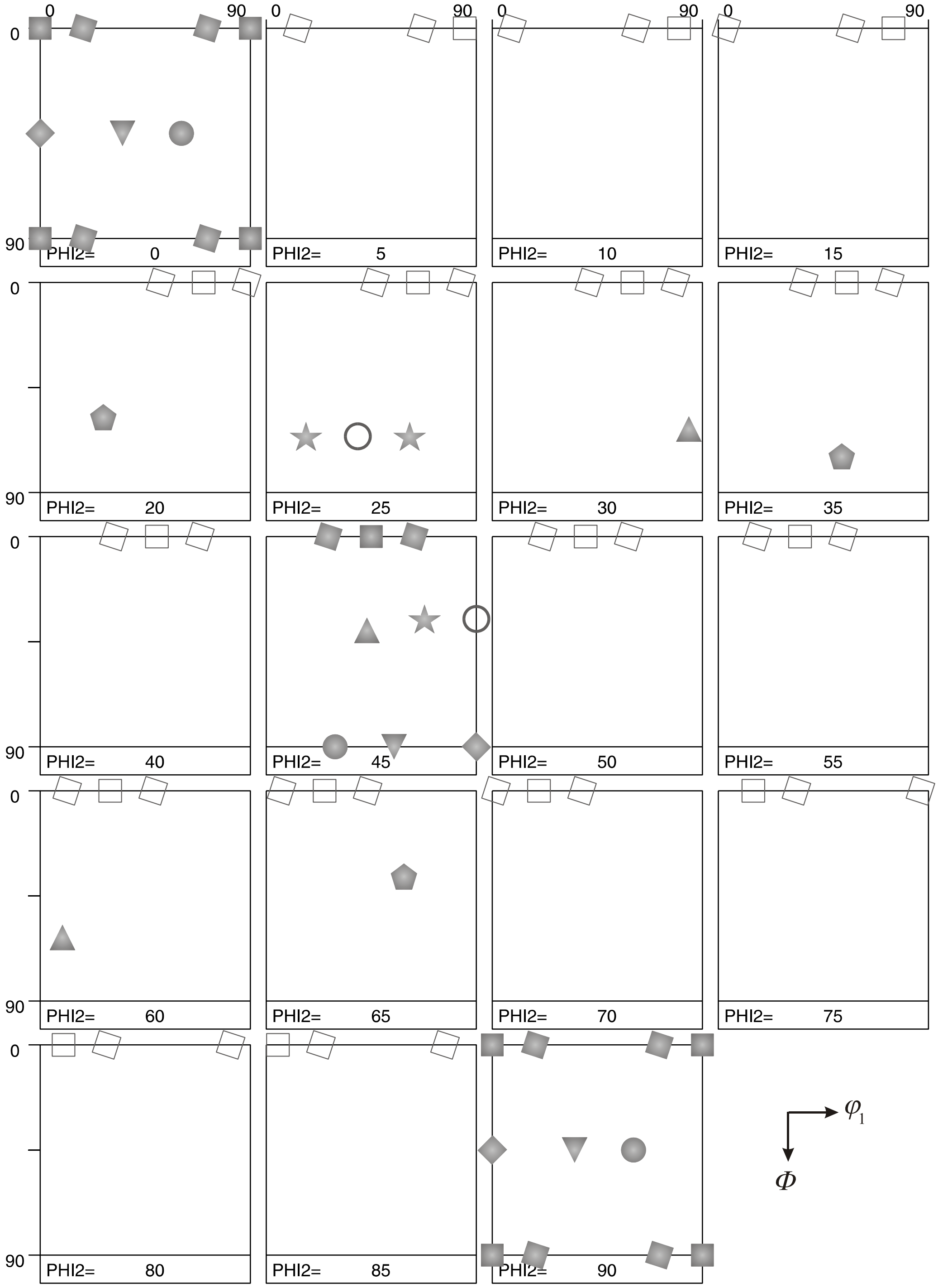

Fig. C-1 : φ_2-sections of (90°, 90°, 90°) Euler space indicating all texture components of table C-1.

2. Monoclinic sample symmetry

For the representation of textures in case of monoclinic sample symmetry deformation, a particular unit zone of the Euler space is selected. All orientations (apart from the ones at the edges of the unit zone) will only occur ones if the Euler space is limited by [Gil Sevillano et al.; 1980] :

$$\begin{aligned} &0° \le \varphi_1 \le 180° \\ &0° \le \varphi_2 \le 90° \\ &0° \le \Phi \le \arctan\left(\sin\left(\varphi_2\right)^{-1}\right) \quad \text{for } \varphi_2 \le 45° \\ &0° \le \Phi \le \arctan\left(\cos\left(\varphi_2\right)^{-1}\right) \quad \text{for } \varphi_2 \ge 45° \end{aligned} \tag{C.1}$$

In table C-2 the texture components and fibres are listed that are discussed in regard to deformation textures obtained after simple shear tests. Due to the lesser degree of sample symmetry compared to the orthorhombic sample symmetry case, some components will have two variants (e.g. P, V). Since only the axes orthogonal to both the shear plane normal (SPN) and the shearing direction (SD) is a dyad axis, a rotation of 180° around this axis (x_3, the normal to the sample surface) will result in an equivalent orientation. Due to their symmetry in respect to the external reference frame, Cube, Goss and Cu will still have only one variant.

The two partial fibres, containing the stable orientations for simple shear are also listed. The $\langle 0\ 1\ 1 \rangle$ // SD fibre is listed in two parts, since it exits the unit zone at $(1\ 1\ 1)[\bar{2}\ 1\ 1]$, but 'continuous' from the equivalent orientation $(1\ 1\ 1)[\bar{1}\ \bar{1}\ 2]$ till Cu. The two parts therefore describe one continuous fibre.

In fig. C-2 all orientation components listed in table C-2 are shown in the unit zone of Euler space described by equation (C.1).

Table C-2 : Texture components that are discussed in regard to the simple shear deformation texture of AA3103

component	Euler angles $(\varphi_1, \Phi, \varphi_2)$	Miller indices	Symbol
Cube	0°, 0°, 0°	$\{0\,0\,1\}\langle 1\,0\,0\rangle$	■
-18° ND rotated Cube (ND-RC$_1$)	72°, 0°, 0°	$(0\,0\,1)[1\,\bar{3}\,0]$	■
Goss	0°, 45°, 0°	$(0\,1\,1)[1\,0\,0]$	◆
Copper (Cu)	90°, 35.3°, 45°	$(1\,1\,2)[\bar{1}\,\bar{1}\,1]$	○
P$_1$	60.5°, 45°, 0°	$(0\,1\,1)[4\,\bar{5}\,5]$	●
P$_2$	119.5°, 45°, 0°	$(0\,1\,1)[\bar{4}\,\bar{5}\,5]$	●
V$_1$	43.1°, 40.3°, 45°	$(3\,3\,5)[1\,\bar{6}\,3]$	▲
V$_2$	136.9°, 40.3°, 45°	$(3\,3\,5)[\bar{6}\,1\,3]$	▲
$\{1\,1\,1\}$ // SP partial fibre	from 125.3°, 45°, 0° till 90°, 35.3°, 45°	$(0\,1\,1)[\bar{1}\,\bar{1}\,1]$ $(1\,1\,2)[\bar{1}\,\bar{1}\,1]$	✱
$\langle 0\,1\,1\rangle$ // SD partial fibre 1	from 180°, 45°, 0° till 150°, 54.7°, 45°	$(0\,1\,1)[\bar{1}\,0\,0]$ $(1\,1\,1)[\bar{2}\,1\,1]$	◆
$\langle 0\,1\,1\rangle$ // SD partial fibre 2	from 90°, 54.7°, 45° till 90°, 35.3°, 45°	$(1\,1\,1)[\bar{1}\,\bar{1}\,2]$ $(1\,1\,2)[\bar{1}\,\bar{1}\,1]$	⬢

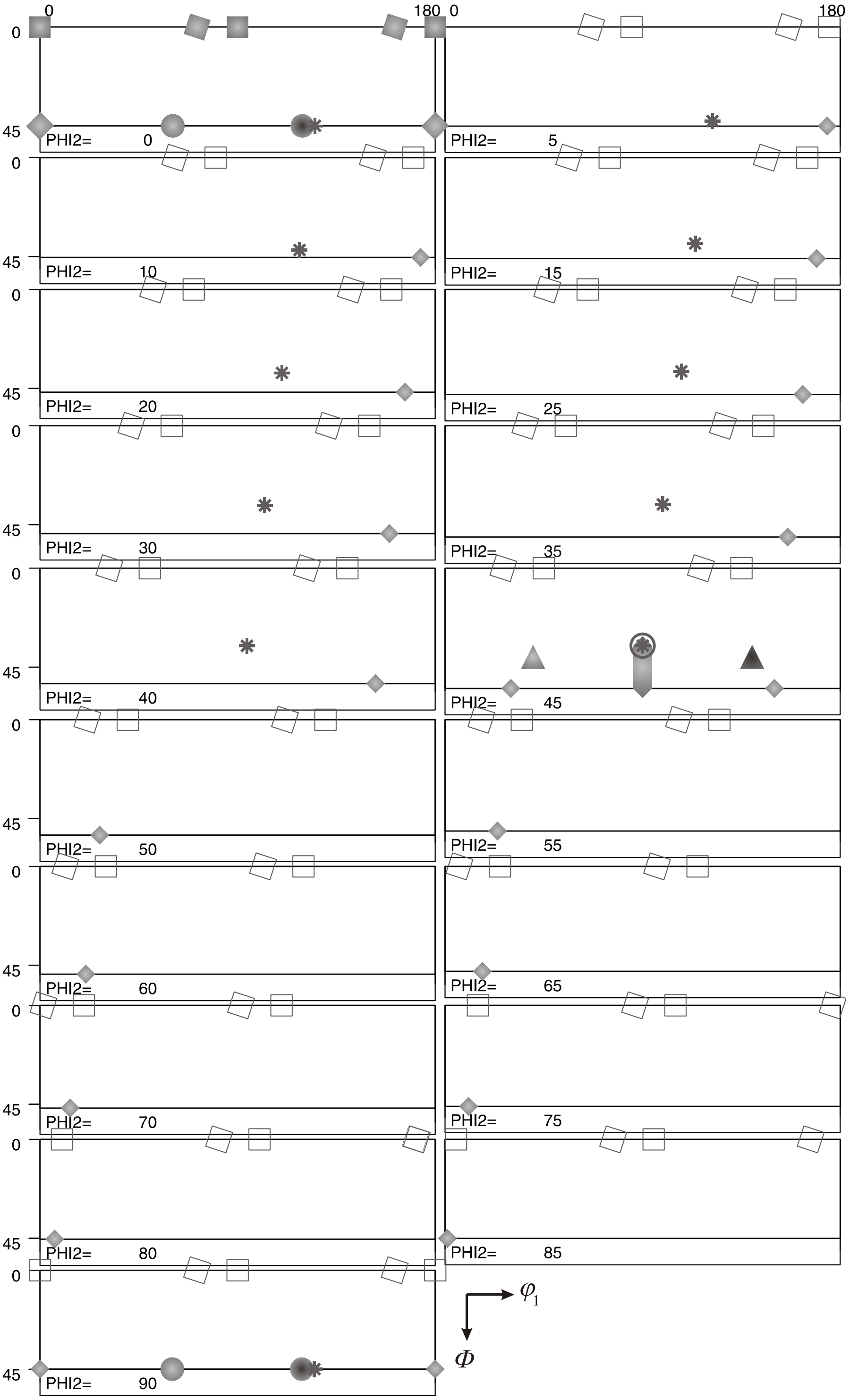

Fig. C-2 : φ_2-sections of (180°, 54.7°, 90°) Euler space indicating all texture components of table C-2.

List of publications

Publications in international journals

Zisman, A., Van Boxel, S., Seefeldt, M. and Van Houtte, P. (2008) *Gradient matrix method to image crystal curvature by processing of EBSD data and trial recognition of low-angle boundaries in IF steel*, Mater. Sci. Eng. A **474**, 165-172.

Zisman, A., Rybin, V., Van Boxel, S., Seefeldt, M. and Verlinden, B. (2006) *Equal channel drawing of aluminium sheet*, Mater. Sci. Eng. A **427**, 123-129.

Van Boxel, S., Seefeldt, M., Verlinden, B. and Van Houtte, P. (2005) *Visualization of grain subdivision by analyzing the misorientations within a grain in EBSD measurements*, J. Microsc. **218**, 104-114.

Proost, J. and Van Boxel, S. (2004) *Large-scale synthesis of high-purity, one dimensional -*Al_2O_3 *structures*, J. Mater. Chem. **14**, 3058-3062.

Publications in preparation

Van Boxel, S., Seefeldt, M., Verlinden, B. and Van Houtte, P. *Development of substructure and anisotropy during cold deformation part I: transient work hardening response after changes of the strain path for an AA3103 aluminium alloy*, in preparation.

Van Boxel, S., Seefeldt, M., Verlinden, B. and Van Houtte, P. *Development of substructure and anisotropy during cold deformation part II: multiscale model for workhardening of aluminium including strain path change effects*, in preparation.

Publications in international conference proceedings

Van Boxel, S., Schmidt, S., Ludwig, W., Zhang, Y.B., Sørensen, H.O., Pantleon, W. and Juul Jensen, D. (2010) *Monitoring grain boundary migration during recrystallisation using topotomography*, in: Proceedings of the 31st Risø International Symposium on Materials Science: Challenges in materials science and possibilities in 3D and 4D characterization techniques, Eds.: Hansen, N., Juul Jensen, D., Nielsen, S.F., Poulsen H.F. and Ralph, B., Risø National Laboratory, Roskilde, Denmark, 449-456.

Zisman, A., Seefeldt, M., Van Boxel, S. and Van Houtte, P. (2008) *Gradient matrix method to image crystal curvature with discrete orientation data: Case study of triple junction in deformed IF steel*, in: Proceedings of the 15th International Conference on Textures of Materials (ICOTOM-15), Ed.: A. Rollett, A., Ceram. Trans. **201**, 803-814.

Zisman, A., Rybin, V., Seefeldt, M., Van Boxel, S. and Van Houtte P. (2008) *Grain interaction and related elastic fields at triple junction in low deformed IF steel: Micromechanical model and reconstruction from EBSD orientation data*, in: Proceedings of the 15th International Conference on Textures of Materials (ICOTOM-15), Ed.: Rollett, A., Ceram. Trans. **201**, 787-802.

Van Boxel, S., Seefeldt, M., Verlinden, B. and Van Houtte, P. (2007) *Slip system based model for work hardening of aluminium including transient effects during strain path changes*, in: Proceedings of the 2nd International Symposium on Physics and Mechanics of Large Plastic Strains, St.-Petersburg, Russia, 111-117.

Zisman, A., Seefeldt, M., Van Boxel, S. and Van Houtte, P. (2007) *Gradient matrix method to image crystal curvature by processing of EBSD data and trial recognition of low-angle boundaries in IF steel*, in: Proceedings of the 2nd International Symposium on Physics and Mechanics of Large Plastic Strains, St.-Petersburg, Russia, 57-67.

Zisman, A., Rybin, V., Seefeldt, M., Van Boxel, S. and Van Houtte, P. (2007) *Detection and micromechanical reconstruction of junction disclinations in low deformed IF steel based on EBSD data*, in: Proceedings of the 2nd International Symposium on Physics and Mechanics of Large Plastic Strains, St.-Petersburg, Russia, 37-50.

Seefeldt, M., Kusters, S., Van Boxel, S., Verlinden, B., and Van Houtte, P. (2007) *Investigating the dependence of grain subdivision on the solid solute content in Al and Cu alloys*, in: Proceedings of the 2nd International Symposium on Physics and Mechanics of Large Plastic Strains, St.-Petersburg, Russia, 30-36.

Van Boxel, S., Seefeldt, M., Verlinden, B. and Van Houtte, P. (2006) *Slip system based model for work hardening and softening of aluminium including strain path change effects*, in: Proceedings of the 3rd International Conference on Multiscale Materials Modeling (MMM 2006), Ed.: Gumbsch, P., Fraunhofer IRB Verlag, Stuttgart, Germany, 567-570.

Van Boxel, S., Seefeldt, M., Verlinden, B. and Van Houtte, P. (2005) *Subdivision morphology and orientation gradients in cold deformed aluminium and aluminium-magnesium polycrystals*, in: Proceedings of the 14th International Conference on Textures of Materials (ICOTOM-14, Eds.: Van Houtte, P. and Kestens, L., Mater. Sci. Forum **495-497**, 1025-1030.

Van Boxel, S., Seefeldt, M., Pantleon, W., Verlinden, B. and Van Houtte, P. (2004) *Study of grain subdivision in aluminium using electron back-scattering diffraction.* In: Proceedings of the 25th Risø International Symposium on Materials Science: Evolution of Deformation Microstructures in 3D, Eds: Gundlach, C., Haldrup, K., Hansen, N., Huang, X., Juul Jensen, D., Leffers, T., Li, Z.J., Nielsen, S.F., Pantleon, W. Wert, J.A. and Winther, G., Risø National Laboratory, Roskilde, Denmark, 557-562.

Presentations without contribution to proceedings

Van Boxel, S., Pantleon, W. and Juul Jensen, D. (2009) *Grain fragmentation in moderately cold rolled AA1050 single crystals*. EBSD meeting, 30-31 March 2009, Swansea, Wales.

Van Boxel, S., Seefeldt, M., Verlinden, B. and Van Houtte, P. (2008) *Multiscale model for anisotropic work hardening of AA3103 including transient effects during strain path changes*. The 15th International Conference on Textures of Materials (ICOTOM-15), 1-6 June 2008, Pittsburgh PA, United States.

Curriculum vitae

Personal information

Name:	Steven Van Boxel
Date of birth:	6 November 1980
Place of birth:	Lommel
Citizenship:	Belgium

Education

1998-2000	Kandidaat burgerlijk ingenieur Katholieke Universiteit Leuven
2000-2003	Burgerlijk materiaalkundig ingenieur Katholieke Universiteit Leuven
2003-2010	Doctor in de Ingenieurswetenschappen Katholieke Universiteit Leuven

Professional

2008-2010	Post-doctoral researcher Risø National Laboratory for Sustainable Energy Technical University of Denmark (DTU)